

Max-Planck-Institut für Biochemie
Abteilung Membran- und Neurophysik

Capacitive stimulation of mammalian cells on silicon chips imaged at optical resolution with voltage-sensitive dyes

Dieter Braun

Vollständiger Abdruck der von der Fakultät für Physik der Technischen
Universität München zur Erlangung des akademischen Grades eines

Doktors der Naturwissenschaften

genehmigten Dissertation.

Vorsitzender: Univ.-Prof. Dr. Dr.h.c. K. Dietrich
Prüfer der Dissertation: 1. Hon.-Prof. Dr. P. Fromherz
2. Univ.-Prof. Dr. M. Stutzmann
3. Univ.-Prof. Dr. F.G. Parak

Die Dissertation wurde am 20.12.1999 bei der Technischen Universität München
eingereicht und durch die Fakultät für Physik am 02.5.2000 angenommen.

Abstract

The electrical contact between mammalian cells and silicon chips was characterized. Cells were capacitively stimulated from a thin spot oxide on a specially designed silicon chip. The resulting membrane potential was imaged at optical resolution with a confocal microscope via voltage-sensitive fluorescence. The detection was accomplished in two ways: either the transfer function of a sinusoidal stimulation to the membrane potential was imaged in amplitude and phase with a software lock-in technique. Or the membrane potential transients in response to a rectangular stimulus were recorded with a time resolution of $0.2\mu\text{s}$ for each pixel. Both measurement methods could be fitted equally well by a spatially resolved planar core-coat conductor theory called the area contact model. The coupling was characterized for erythrocyte ghosts, HEK cells with different shape, confluent HEK cell layers, rat neurons, rat neurons on top of a glia cell layer and adsorbed giant vesicle membrane.

Recorded images were corrected for the transfer functions of the stimulation chip and the photomultiplier. The shape of the cell defined the boundary conditions of the model. All features of the area contact model have been confirmed and fits on lock-in and transient measurements yielded equal parameter values of the model. Transients could also be fitted by the simpler point contact model with a spatially adapted time constant of junction voltage decay.

The junction parameters of fused erythrocyte ghosts measured with transistors were confirmed for the junction of unfused erythrocyte ghosts. They showed a 13-fold reduced specific conductance in the junction cleft as compared to the bulk electrolyte. For mammalian cells grown on fibronectin and poly-lysine there is a 4-fold enhanced specific junction conductance. The measured junction time constant covers the range from $2\mu\text{s}$ to $5\mu\text{s}$ depending on cell size. The sustainable membrane potential can reach values of 600mV . With increased stimulation voltage, the cell membrane is electroporated. The voltage-sensitive fluorescence was shown to be linear with respect to the applied stimulation voltage. Furthermore it could be proved that the membrane of neurons can be stimulated capacitively through a glia cell layer. Confluent cell layers showed a slower junction time constant of up to $10\mu\text{s}$.

Table of contents

<i>Abstract</i>	<i>1</i>
1 <i>Introduction</i>	<i>7</i>
2 <i>Cell on a capacitor</i>	<i>11</i>
<i>Seal resistance and time constant</i>	
2.1 Area contact and Point contact model	12
2.2 Area contact model	13
A Definitions and parameters	13
B Integral equation of the area contact model	14
C Area contact for transistor measurements	16
D Area contact with membrane conductance	16
E Former approximation: localized free membrane	17
2.3 Solving the area contact model	18
A Solving the area contact numerically	18
B Analytical solution for circular junction area	19
2.4 Parameter analysis for circular junctions	20
A Area contact model with characteristic parameters	20
B Comparing area contact and local approximation	22
C Influence of free membrane area [β]	23
D Increasing the spot capacitance [ϵ and c_{ox}]	23
E Influence of membrane conductance [g_{JM}]	24
F Influence of junction membrane conductance [μ]	25
2.5 Point contact model	27
A Point contact model derived from circuit	27
B Formal transition to point contact model	28
C Numerical transition to point contact model	29
D Time domain transition to point contact model	30
E Fitted transition with four point contact models	31
F Point contact model for leaky junction membrane	32
2.6 Measured coupling parameters	33
A Coupling parameters from geometry	33
B Coupling parameters from transistor measurements	36

3	<i>The Chip</i>	37
	<i>Design, Process, Characterization, Usage</i>	
3.1	Chip design	38
	A Thin silicon oxide as stimulation capacitor	38
	B Possible future materials	38
	C Band pass filter of chip and junction	39
	D Chip design	40
3.2	Processing the chips	41
	A Cleaning procedures	42
	B Photolithography	43
	C Doping the stimulation spot and conductor path	43
	D Etching and doping the backbonding pyramids	44
	E Oxidation of the stimulation spot and the chip	46
	F Deposition of chrome and the dicing of the wafer	47
3.3	Characterization of the chips	47
	A Measuring chip parameters with Lock-In amplifier	47
	B capacitance and resistance of a bulk contact	48
	C pn-Junctions between spot and spot	49
	D pn-Junction between bulk and spot	49
	E Bath electrode	50
	F Influence of bath electrolyte and objective	51
	G Summary of the chip data	52
	H Low pass filter characteristic of the chip	53
3.4	Usage of the chip	56
4	<i>Dye in front of silicon</i>	59
	<i>Voltage sensitive fluorescence and interferometry above silicon</i>	
4.1	Voltage sensitive fluorescent dyes	60
	A Voltage sensitivity of BNBIQ	60
	B Wavelengths of voltage sensitivity	60
	C Staining method	61
4.2	FLIC theory for epi-fluorescence	62
	A Electrical field for Köhler illumination	62
	B Transformation to the dye with if-factors	62
	C Transition probability of the dye	63
	D Spectral and aperture integration	64
	E Lifetime correction	64
	F Epi-fluorescence FLIC on adsorbed membrane	65
4.3	FLIC theory for confocal microscopes	66
	A Diffraction forms the focus	66
	B Approximation for polarized excitation	68
	C Transformation to the dye with if-factors	68
	D Transition probability of the dye	69
	E Integration of the focus	69
	F Aperture integration	70
	G Calculation of emission	71
4.4	Using Confocal FLIC	71
	A Confocal FLIC on adsorbed membrane	71
	B Using confocal FLIC to measure the angle of BNBIQ	73
	C Two lambda confocal FLIC	75
4.5	Maximizing the fluorescence signal	76
	A Intensity dependence on oxide thickness and angle	76
	B Fluorescence small-signal better for thicker oxide?	77

5	<i>Confocal microscope</i>	79
	<i>Scanning, Photomultiplier and Software Lock-In</i>	
5.1	Preliminary experiments	80
	A Contacted FLIC-Chip with a locked photodiode	80
	B Conclusions from first experiments	80
5.2	Confocal microscope and LabView interface	81
	A The Laser scanning confocal microscope	81
	B Labview Interface FluoLab	83
5.3	Software lock-in	86
	A Software lock-in from correlation functions	86
	B Testing the software Lock-In	87
5.4	Photomultiplier and amplifier	88
	A Transfer function of the photomultiplier amplifier	88
	B Photon counting	89

6	<i>Lock-In Imaging</i>	91
	<i>Ghosts, HEK cells, neurons, cell layers and vesicle membranes</i>	
6.1	Detailed analysis of a measurement	92
	A Average and small-signal fluorescence images	92
	B The phase image	93
	C The relative amplitude image	94
	D Fitting the point contact model	95
	E Fitting the area contact model	96
6.2	Erythrocyte ghosts	99
	A Preparation of ghosts	99
	B Junction of ghosts	99
	C High membrane conductance or weak coupling?	106
6.3	Single HEK cells	108
	A Cell culture	108
	B Spindle-shaped HEK cells	109
	C Epithelioid HEK cells	113
6.4	Group of HEK cells and Monolayers	116
6.5	Rat neurons and astrocytes	124
	A Hippocampal cell culture	124
	B Rat neuron on poly-lysine	126
	C Rat neuron on top of a glia cell layer	128
6.6	Adsorbed giant vesicle membrane	130
	A Preparation of giant membrane vesicles	130
	B Adsorbed giant vesicle membrane	131

7	<i>Imaging of transients</i>	135
	<i>HEK cells, cell groups and vesicle membranes</i>	
7.1	Detailed analysis of a measurement	137
	A Basic principle and fluorescence image	137
	B Single relative fluorescence transients	138
	C Fitting transients with the Area contact model	139
	D Fitting transients with the Point contact model	141
	E Imaged Sensitivity	142
	F Voltage images with area contact model	143
	G Voltage section versus time	144
7.2	Imaged transients of single HEK cells	144
	A Spindle-shaped HEK cells	144
	B Epithelioid HEK cells	147
7.3	Group of HEK cells	150
7.4	Imaged transients of vesicle membrane	155
8	<i>Specials</i>	157
	<i>Electroporation, Adsorbed dye and Linearity</i>	
8.1	Electroporation of junction membrane	158
8.2	Adsorbed dye on poly-lysine	160
8.3	Linearity of voltage sensitivity	161
	<i>Summary and Outlook</i>	162
	<i>References</i>	165
	<i>Acknowledgements</i>	169

Introduction

Going back to the beginning of the electrical stimulation of nerve cells, we find in the november of the revolutionary year 1789 in Bologna the italian physician Luigi Galvani preparing a broth from frog legs for his ill wife. After he had dissected the legs from the frog's body with his iron knife, an assistant drew a spark from a static electrical machine some meters away. The staggered Galvani saw the legs contract as if they were alive. He had no chance in explaining this effect as electrodynamics was not yet discovered. But he was enough an experimentalist to systematically track down the important ingredients for a successful stimulation. He even stimulated the frog legs with a metal antenna affected from the thunderbolts of a distant storm. By chance he found how a two-part wire made of iron and brass could stimulate the frog's leg by simply touching the spinal nerve with the one and the leg with the other end of the wire. He wrongly assumed that he had found 'animal electricity' generated in the nerve which was shorted by the wire. Most mysterious were seances held by Galvani where many people were arranged in a circle, holding their hands. One of them touched the frog nerves with a brass wire. The person at the other end of the circle held an iron wire to the frog leg. If the circle was closed - no matter where - the 'animal electricity' flowed through all people and the leg of the frog contracted mysteriously. It is even reported that the experiments worked best with wet hands which should not have been a problem under these circumstances. For a long time frog legs were the most sensitive voltmeters and were often used in laboratories as they could detect voltages down to below 100mV. Anyway, it was Alessandro Volta who knew enough more about electrochemistry and batteries to correctly locate the voltage source in the electrochemical contact between both metals.

Much has changed since these times in neuroscience but modern experiments are still very crude compared to the brilliant complexity of neural tissue. For example it is still the most sensitive available technique to stick several glass pipettes into slices of a brain. At the end of the 1960s a more elegant experimental approach was envisaged to directly image the membrane potentials with optical methods. Aside from intrinsic signal detection many efforts have been made to image neuronal activity with fluorescent probes. Most prominent are methods for calcium imaging since slow transients and high dye sensitivities allow for signal detection in many physiologically relevant situations.

Direct detection of the microscopic membrane potential is hampered not only by fast signals, but mainly by poor sensitivities and high phototoxicity. The last two drawbacks can be overcome if large structures with a pixel size of above 100 μm are imaged. Thus only 'activity' is detected, but around 15 recent papers report measurements from such diverse regions as the rat olfactory bulb, the rat geniculate ganglion, the visual cortex, the rat atrium, rabbit hearts, of course the hippocampus and last but not least the auditory cortex. Also the process of electroporation of sea urchin eggs could be imaged ([Hibino 1991], [Hibino 1993]). A more detailed analysis of the stimulation spread from metal electrodes was performed in [Knisley 1995]. But again spatial resolution was very low with 1mm per photodiode.

Monitoring the membrane potential at high spatial and temporal resolution is notoriously difficult. In [Windisch 1995] a measurement of membrane potential generation at a single cell with spatial resolution of 20 μm and time resolution of 20 μs is reported. In our department measurements at axons of Retzius cells [Fromherz 1991b] and of mammalian cells [Meyer 1997] were performed. In the latter the cable properties on linearly grown rat dendrites could be mapped with a resolution of 9 μm and 0.4ms. Recently the good signal to noise ratio of a noise compensated confocal setup with rather low spatial resolution was demonstrated in [Bullen 1997] and [Bullen 1999].

The second development relevant for the present work was the capacitive coupling of neurons to a thin sheet of silicon dioxide on a silicon chip. First experiments were the detection of action potentials of Retzius neurons with field effect transistors ([Fromherz 1991a], review in [Fromherz 1996]). Shortly afterwards [Fromherz 1995a], [Stett 1997] demonstrated the elicitation of action potentials induced by voltage steps applied to the silicon oxide below the Retzius neuron.

But the detection or even stimulation of smaller cells such as rat neurons via a silicon chip turned out to be difficult. The detection of a train of action potentials was achieved with signal averaging ([Vassanelli 1997], [Vassanelli 1998]). The sealing junction resistance of rat neurons is very low and reduces the signal amplitude. This is due to a reduced junction area, a reduced specific membrane capacity and probably also an enhanced distance from cell to substrate as compared to the Retzius neurons. The cell-substrate distance could be measured precisely for rat neurons by FLIC microscopy [Braun 1998] but a reduction in distance was not yet achieved. The junction between rat neurons and transistors could not be spatially resolved and the specific conductance inside the cleft could only be estimated. Therefore a method to characterize the whole coupling process was needed to further optimize the contact between rat neurons and silicon chips.

The present method combines the capacitive stimulation through a thin silicon oxide film with the detection of membrane potential by voltage-sensitive fluorescent dyes. The membrane potential is microscopically imaged either by measuring amplitude and phase of the voltage transfer function in a lock-in mode or by acquiring voltage transients following rectangular stimulation. Concerning resolution, substantial improvements could be achieved with respect to the published methods. Images are acquired at an optical resolution of $0.4\mu\text{m}$. Images of voltage transients can be recorded at a time resolution of $0.2\mu\text{s}$. Since the detection is locked to the passive stimulation of the cell, the signal to noise ratio could be reduced. The method presented can cope with sensitivities as low as $2\%/100\text{mV}$ and light intensities below $10\mu\text{W}$ in the focus.

A further idea underlying this approach is the complementarity between stimulation and detection. Spatially resolved transfer functions from the voltage at the stimulation electrode to the membrane potential are determined with the presented method. These transfer functions exhibit the electrical constraints also involved in the detection of the membrane potential of a single cell. However only passive stimulated membrane potential can be measured with high optical resolution as it is locked to the stimulation. Nevertheless the specific elicitation of an action potential in a single cell in tissue without using patch pipettes is still an unresolved problem. Until now the main interest was focussed on the detection of action potentials but the noninvasive specific stimulation of single cells in tissue may become an important tool to tackle complex theories of the brain functions such as phase locking of neuronal ensembles.

Cell on a capacitor

Seal resistance and time constant

2.1 Area contact and Point contact model **12**

The electrical circuit of a cell on a capacitor can be either described by the spacial resolved area contact model or by the simplified point contact model. Both models will be used in this work.

2.2 Area contact model **13**

In this model the contact of a cell on a capacitor is represented by a flat, two dimensional cable: the resistance of the cleft is isolated by the capacitor (oxide) below the cell and by the junction (lower) cell membrane. The conductive cytosol of the cell is included in the model, resulting in a novel integral-differential equation for the voltage across the junction membrane V_{JM} .

2.3 Solving the area contact model **18**

For periodic time signals it is much more convenient to give the solutions in the frequency domain. An iteration procedure is described which solves the integral equation of the area contact model for arbitrary boundary conditions.

2.4 Parameter analysis for circular junctions **20**

We analyze how the solution of the area contact model depends on the parameters. We define a reference frequency f_0 from junction area A_{JM} and the diffusion constant D .

2.5 Point contact model **27**

The main approximation for the description of the coupling is the point contact model. The junction resistance is approximated by a global junction conductance g_j . Junction oxide and junction membrane potential is averaged.

2.6 Measured coupling parameters **33**

We summarize for various cell types the data from geometry measurements (FLIC-Microscopy) and from transistor measurements.

2.1 Area contact and Point contact model

The electrical circuit of a cell on a capacitor can be either described by the spacial resolved area contact model or by the simplified point contact model. Both models will be used in this work.

We will deal with the situation of a cell grown on a capacitor. Both are separated by a thin cleft, called the junction cleft or for short the junction. The lower membrane in direct contact with the capacitor will be called the junction membrane. The remaining membrane without direct contact to the chip is the free membrane. The cell membranes have a specific capacitance of $1\mu\text{F}/\text{cm}^2$ as one can also guess from its thickness of about 4nm. We will choose the capacitor below to have a similar high specific capacitance. For silicon oxide with a thickness of 10nm we achieve $0.34\mu\text{F}/\text{cm}^2$. If we assume the junction cleft to have a very high resistance and the cell membrane conductance to be zero, any applied voltage at the capacitor will result in voltages across the junction and the free membrane according to the voltage divider of the capacitance of the capacitor, the junction and the free membrane. To model the resistance in the junction cleft we can use the most simple approximation of the point contact model [Fromherz 1991a], [Fromherz 1993b] depicted below in Fig 2.1.

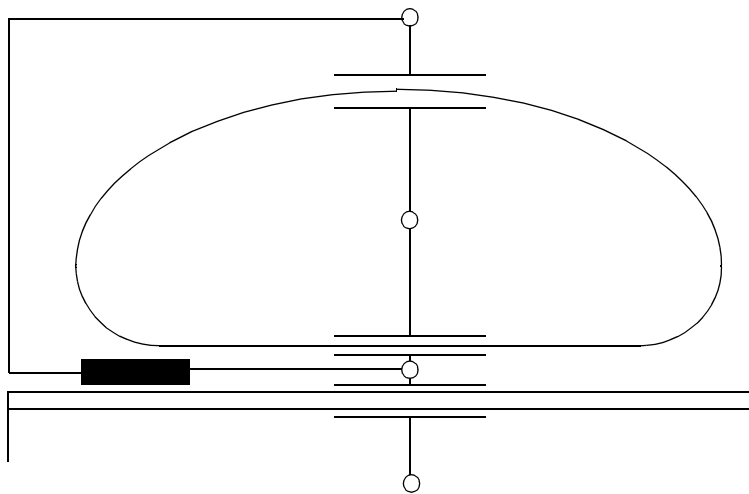


Fig 2.1 Equivalence circuit of the point contact model. The junction resistance is modelled with one resistance. Junction membrane potential is assumed constant as is the voltage at the capacitor below the cell. This simple model will be found to be exact in many situations.

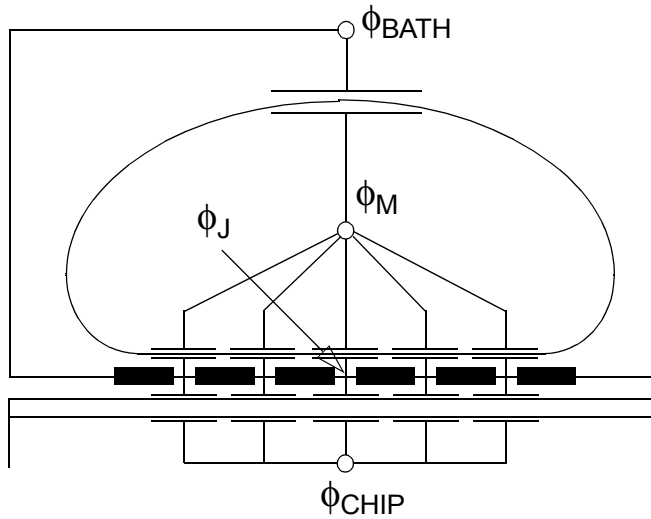
But the junction cleft is a two-dimensional resistance [Weis 1996]. It would be expected that the junction voltage towards the borders shunts already at small frequencies if a sinusoidal voltage is applied to the capacitor under the cell. Therefore the junction membrane potential cannot be constant as assumed in the point contact model. It will be shown how the two-dimensional modelling of the junction resistance between the capacitors of junction membrane and stimulation capacitor leads to a integral-differential equation resembling a 'diffusion' of voltage in the junction. We call this the area contact model which is described and discussed in the next paragraph. Later it will be shown how the point contact model can be derived and approximated from the area contact model.

2.2 Area contact model

In this model the contact of a cell on a capacitor is represented by a flat, two dimensional cable: the resistance of the cleft is isolated by the capacitor (oxide) below the cell and by the junction (lower) cell membrane. The conductive cytosol of the cell is included in the model, resulting in a novel integral-differential equation for the voltage across the junction membrane V_{JM} .

2.2.A Definitions and parameters

Here we define the parameters of the area contact model. We use the physiological definitions for the membrane potentials:



$$\begin{aligned} V_{OX} &= \phi_J - \phi_{CHIP} \\ V_S &= \phi_{BATH} - \phi_{CHIP} \\ V_{JM} &= \phi_M - \phi_J \\ V_{FM} &= \phi_M - \phi_{BATH} \end{aligned}$$

We attribute different area specific conductance g_{JM} , g_{FM} and area specific capacitances c_{JM} , c_{FM} to the lower (junction) and upper (free) membrane of the cell. Often we will use identical membrane properties. The area of both membranes is defined by A_{JM} and A_{FM} :

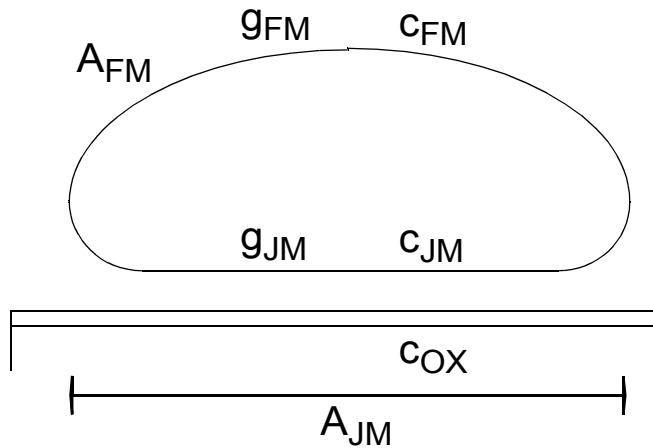


Fig 2.2 Definitions of the capacitances c_{JM} , c_{FM} and conductances g_{JM} , g_{FM} and area A_{JM} , A_{FM} of junction and free membrane.

- $\phi_J, \phi_M, \phi_{\text{BATH}}, \phi_{\text{CHIP}}$ describe the potential in the junction, inside the cell, in the bath and inside the chip.
- V_{OX} defines the voltage across the oxide below the cell $V_{\text{OX}} = \phi_J - \phi_{\text{CHIP}}$
- V_S defines the extracellular stimulation voltage at the spot $V_S = \phi_{\text{BATH}} - \phi_{\text{CHIP}}$
- $V_{\text{JM}}, V_{\text{FM}}$ define the voltage at the junction membrane JM and at the free membrane FM. The sign is determined by $V_{\text{JM}} = \phi_M - \phi_J$ and $V_{\text{FM}} = \phi_M - \phi_{\text{BATH}}$.
- $c_{\text{ox}}, c_{\text{JM}}, c_{\text{FM}}$ [$\mu\text{F}/\text{cm}^2$] define the capacitance per area of the capacitor (oxide), the junction membrane JM and the free membrane FM.
- ν is the ratio of the area specific capacitances of the junction and the free membrane: $\nu = c_{\text{JM}}/c_{\text{FM}}$. Almost always $\nu=1$ is assumed.
- ϵ is the ratio of the area specific capacitance of the oxide and the membrane: $\epsilon = c_{\text{ox}}/c_{\text{JM}}$. Typically this ratio is chosen to match a specific membrane capacitance of $c_{\text{JM}} = 1\mu\text{F}/\text{cm}^2$. For example we find $\epsilon = 0.34$ for 10nm oxide thickness.
- β is the ratio of area between junction and free membrane: $\beta = A_{\text{JM}}/A_{\text{FM}}$. An example is a half spherical cell with $\beta = 0.5$.
- g_{JM} and g_{FM} [mS/cm^2] are the conductances per area of the junction and the free membrane.
- μ is the ratio of specific membrane conductance of the junction and the free membrane: $\mu = g_{\text{JM}}/g_{\text{FM}}$.
- r_j [Ω] is the local sheet resistance of the cleft used in the area contact model. The specific resistance of the cleft material ρ_j [Ωm] can be inferred from $\rho_j = r_j \cdot d$ with the cleft thickness d .
- g_j [mS/cm^2] is the sheet conductance per junction area of the cleft [Vassanelli 1997]. This global quantity of the point contact model is connected to r_j within a rather heuristic approximation presented later.

2.2.B Integral equation of the area contact model

We study the currents through and sideways an infinitesimal area inside the junction. We first neglect the junction membrane conductance and describe the currents at a small infinitesimal area of the junction membrane. All currents used are specific to this area of the junction membrane. From:

$$\begin{aligned} & \text{Capacitive current through junction membrane} = \\ & \text{Capacitive current through oxide} - \text{Current through cleft} \end{aligned}$$

we get:

$$\frac{c_{\text{ox}}}{\epsilon} \partial_t V_{\text{JM}} = c_{\text{ox}} \partial_t V_{\text{OX}} - \frac{1}{r_j} \Delta \phi_J \quad [2.1]$$

The last term is the net sideways current. Due to

$$V_{\text{OX}} = \phi_J - \phi_{\text{CHIP}} \quad \Delta \phi_J = \Delta V_{\text{OX}} \quad [2.2]$$

the Laplace operator is resolved to:

$$\frac{c_{ox}}{\epsilon} \partial_t V_{JM} = c_{ox} \partial_t V_{OX} - \frac{1}{r_j} \Delta V_{OX} \quad [2.3]$$

After changing variables to the junction voltage V_{JM} we find:

$$V_{OX} = V_S - V_{JM} + V_{FM} \quad [2.4]$$

$$\frac{c_{ox}}{\epsilon} \partial_t V_{JM} = c_{ox} \partial_t [V_S - V_{JM} + V_{FM}] - \frac{1}{r_j} \Delta [V_S - V_{JM} + V_{FM}] \quad [2.5]$$

Knowing that V_S and V_{FM} do not depend on the location we find $\Delta V_S = \Delta V_{FM} = 0$. To get rid of the free membrane potential V_{FM} a second equation is necessary. The current through the free membrane can be integrated from the inhomogeneous by distributed currents through the junction membrane. By defining the spatial mean of a quantity x over the junction area A_{JM} with normalized integration

$$\langle x \rangle = \int x dA_{JM} / \int dA_{JM} \quad [2.6]$$

it is possible to express the capacitive current through the free membrane by integrating the capacitive currents through the junction membrane if we assume identical membrane properties:

$$\beta^{-1} \frac{c_{ox}}{\epsilon} \partial_t V_{FM} = -\frac{c_{ox}}{\epsilon} \langle \partial_t V_{JM} \rangle \quad [2.7]$$

The factor β takes into account the different areas of free and junction membrane. It can be proved with Fourier transformation that this implies a direct relationship of V_{FM} and V_{JM} . As the averaging integral is spatial only and the boundary values of V_{JM} are finite we see from the Fourier integration of the right side of [2.7]:

$$\langle i\omega V_{JM} \rangle = i\omega \langle V_{JM} \rangle \Rightarrow \langle \partial_t V_{JM} \rangle = \partial_t \langle V_{JM} \rangle \quad [2.8]$$

Therefore we find:

$$V_{FM} = -\beta \langle V_{JM} \rangle \quad [2.9]$$

and substitute V_{FM} . From this we finally get the integral-differential equation of infinitesimal junction area specific currents:

$$\frac{\Delta V_{JM}}{r_j} - c_{ox}(1 + \epsilon^{-1}) \partial_t V_{JM} - \beta c_{ox} \partial_t \langle V_{JM} \rangle = -c_{ox} \partial_t V_S \quad [2.10]$$

It can be written differently with a diffusion constant D :

$$D \Delta V_{JM} - \partial_t V_{JM} - \beta \frac{\partial_t \langle V_{JM} \rangle}{1 + \epsilon^{-1}} = \frac{-\partial_t V_S}{1 + \epsilon^{-1}} \quad [2.11]$$

$$D = [c_{ox} r_j (1 + \epsilon^{-1})]^{-1} \quad [2.12]$$

Integral equations are typically solved by iteration. We start with a reasonable fixed value for the integral $\langle V_{JM} \rangle$ and solve the differential equation. The solution obtained is used to calculate a new, fixed value of $\langle V_{JM} \rangle$ and so on. We iterate and hope the solution to converge to reasonable values which was no problem in this case. To be precise it would be necessary to prove that there exists only one solution, but the comparison with the localized free membrane solution was satisfactory. The result of the area contact model is often presented in terms of the transfer function $g_{CELL}(\omega=2\pi f, x, y)$ in frequency space. The transfer function for the free membrane is also given:

$$g_{CELL}(\omega, x, y) = \frac{V_{JM}(\omega, x, y)}{V_S(\omega)} \quad g_{CELL}^{FM}(\omega) = \frac{V_{FM}(\omega)}{V_S(\omega)} \quad [2.13]$$

2.2.C Area contact for transistor measurements

It is not possible to formulate the area contact model in terms of the voltage inside the junction $V_J = \phi_J - \phi_{\text{BATH}} = V_{\text{FM}} - V_{\text{JM}}$. This model is needed in the case of transistor measurements without impaling the cells. Starting from the simple case [2.1]

$$\frac{c_{\text{ox}}}{\epsilon} \partial_t V_{\text{JM}} = c_{\text{ox}} \partial_t V_{\text{OX}} - \frac{1}{r_J} \Delta \phi_J \quad [2.14]$$

we would try to express V_{JM} and V_{OX} with V_J [2.4]:

$$V_{\text{OX}} = V_J + V_S \quad \Delta \phi_J = \Delta V_J \quad V_{\text{JM}} = V_J + V_{\text{FM}} \quad [2.15]$$

But with [2.9]

$$\partial_t V_{\text{FM}} = -\beta \langle \partial_t V_{\text{JM}} \rangle \quad [2.16]$$

it would be necessary to solve

$$V_{\text{JM}} = V_J - \beta \langle V_{\text{JM}} \rangle \quad [2.17]$$

which is not possible. This means we have to stick to the area contact model as formulated herein with V_{JM} and transform the result afterwards with [2.4] and [2.9]:

$$V_J = V_{\text{FM}} - V_{\text{JM}} = -\beta \langle V_{\text{JM}} \rangle - V_{\text{JM}} \quad [2.18]$$

In terms of transfer functions we find:

$$g_{\text{JM}}(\omega) = \frac{V_J}{V_{\text{JM}}} = -1 - \beta \frac{\langle g_{\text{CELL}} \rangle}{g_{\text{CELL}}} \quad [2.19]$$

2.2.D Area contact with membrane conductance

We generalize the area contact model for an area specific membrane conductance g_{JM} in the junction and the free membrane. We just have to add the ohmic current on the left hand side of the equation [2.3]:

$$\frac{c_{\text{ox}}}{\epsilon} \partial_t V_{\text{JM}} + g_{\text{JM}} V_{\text{JM}} = c_{\text{ox}} \partial_t V_{\text{OX}} - \frac{1}{r_J} \Delta V_{\text{OX}} \quad [2.20]$$

As the membrane properties of free and junction membrane are the same, the equation [2.7] for the capacitive currents has its ohmic counterpart

$$\beta^{-1} g_{\text{JM}} V_{\text{FM}} = -g_{\text{JM}} \langle V_{\text{JM}} \rangle \quad \text{for} \quad g_{\text{JM}} \neq 0 \quad [2.21]$$

and the generalization [2.9] still holds. We get instead of [2.10] and [2.11]

$$\frac{\Delta V_{\text{JM}}}{r_J} - c_{\text{ox}}(1 + \epsilon^{-1}) \partial_t V_{\text{JM}} - \beta c_{\text{ox}} \partial_t \langle V_{\text{JM}} \rangle - g_{\text{JM}} V_{\text{JM}} = -c_{\text{ox}} \partial_t V_S \quad [2.22]$$

$$D \Delta V_{\text{JM}} - \partial_t V_{\text{JM}} - \beta \frac{\partial_t \langle V_{\text{JM}} \rangle}{1 + \epsilon^{-1}} - \frac{g_{\text{JM}} V_{\text{JM}}}{c_{\text{ox}}(1 + \epsilon^{-1})} = \frac{-\partial_t V_S}{1 + \epsilon^{-1}} \quad [2.23]$$

For different membrane properties of free and junction membrane we have to substitute β with a complex and frequency dependent β^* as shown in the subsequent derivation. We use the factors

$$\mu = \frac{g_{\text{JM}}}{g_{\text{FM}}} \quad \nu = \frac{c_{\text{JM}}}{c_{\text{FM}}} \quad [2.24]$$

The capacitive current and the ohmic current through the free membrane is again defined by the integral currents through the junction membrane:

$$\beta^{-1} \left[\frac{c_{ox}}{v\epsilon} \partial_t V_{FM} + \frac{g_{JM}}{\mu} V_{FM} \right] = - \left\langle \frac{c_{ox}}{\epsilon} \partial_t V_{JM} + g_{JM} V_{JM} \right\rangle \quad [2.25]$$

In the simpler derivations we could solve this for $\partial_t V_{FM}$ and insert it together with [2.4] into [2.20]. Here this is not possible, we have to switch to frequency space with

$$\partial_t \rightarrow i\omega \quad [2.26]$$

to solve [2.25] for V_{FM} - we again argue that the averaging integral can be exchanged with the time derivative and find:

$$V_{FM} = -\beta \left[\frac{g_{JM} + \frac{c_{ox} i\omega}{\epsilon}}{\frac{g_{JM}}{\mu} + \frac{c_{ox} i\omega}{v\epsilon}} \right] \langle V_{JM} \rangle = -\beta v \mu \left[\frac{\epsilon g_{JM} + c_{ox} i\omega}{v\epsilon g_{JM} + \mu c_{ox} i\omega} \right] \langle V_{JM} \rangle = -\beta^* \langle V_{JM} \rangle \quad [2.27]$$

$$\beta^* = \beta v \mu \left[\frac{\epsilon g_{JM} + c_{ox} i\omega}{v\epsilon g_{JM} + \mu c_{ox} i\omega} \right] \quad [2.28]$$

Thus the substitution $\beta \rightarrow \beta^*$ is sufficient to describe different membrane properties of free and junction membrane. Note that the complex number β^* now depends on the frequency. Therefore:

$$\frac{\Delta V_{JM}}{r_J} - c_{ox}(1 + \epsilon^{-1})i\omega V_{JM} - c_{ox}i\omega\beta^* \langle V_{JM} \rangle - g_{JM} V_{JM} = -c_{ox}i\omega V_S \quad [2.29]$$

or written with a diffusion constant D:

$$D\Delta V_{JM} - i\omega V_{JM} - \frac{i\omega\beta^*}{1 + \epsilon^{-1}} \langle V_{JM} \rangle - \frac{g_{JM} V_{JM}}{c_{ox}(1 + \epsilon^{-1})} = -\frac{i\omega V_S}{1 + \epsilon^{-1}} \quad [2.30]$$

$$D = [c_{ox}r_J(1 + \epsilon^{-1})]^{-1} \quad [2.31]$$

2.2.E Former approximation: localized free membrane

Without integrating the currents of the junction membrane to obtain the free membrane potential we obtain the approximation of a localized free membrane used beforehand. Every infinitesimal current through dA_{JM} must also flow through a corresponding element of $dA_{FM} = \beta^{-1} dA_{JM}$. The currents are not allowed to add up in the cytosol of the cell to the current through the free membrane. This approximation is the starting point for the iteration scheme to solve the area contact model. With $v = \mu = 1$, $g_{JM} = 0$ from [2.27] the averaging integral over V_{JM} is now missing:

$$V_{FM}(x, y) = \beta V_{JM}(x, y) \quad [2.32]$$

and we find:

$$\frac{\Delta V_{JM}}{r_J} - c_{ox}(1 + \beta + \epsilon^{-1})\partial_t V_{JM} = -c_{ox}\partial_t V_S \quad [2.33]$$

which is a diffusion equation with a different diffusion constant:

$$\tilde{D}\Delta V_{JM} - \partial_t V_{JM} = \frac{-\partial_t V_S}{1 + \beta + \epsilon^{-1}} \quad [2.34]$$

$$\tilde{D} = [c_{ox}r_J(1 + \beta + \epsilon^{-1})]^{-1} \quad [2.35]$$

2.3 Solving the area contact model

For periodic time signals it is much more convenient to give the solutions in the frequency domain. An iteration procedure is described which solves the integral equation of the area contact model for arbitrary boundary conditions.

2.3.A Solving the area contact numerically

Basis is the relaxation algorithm used to solve a diffusion equation. The diffusion equation

$$D\Delta V_{JM} - \partial_t V_{JM} - gV_{JM} = \text{const} \quad [2.36]$$

is in frequency space $\partial_t \rightarrow i\omega$ with the constants c_1 and c_2 :

$$\begin{aligned} D\Delta V_{JM} + c_1 V_{JM} &= c_2 \\ c_1 &= -(i\omega + g) \end{aligned} \quad [2.37]$$

To solve this equation, we iterate using successive overrelaxation (SOR) algorithm [[*Numerical recipes in C 1992*] Chapter 19.5 page 863ff]. To obtain the voltage at integer position x, y for the next iteration step from the neighbors we use:

$$V_{x,y}^{\text{new}} = \frac{1}{4} \left[V_{x,y-1} + V_{x,y+1} + V_{x-1,y} + V_{x+1,y} + \left(\frac{c_1}{D} - 4 \right) V_{x,y} - \frac{c_2}{D} \right] \quad [2.38]$$

To maintain the boundary conditions, only the values of V inside the boundaries are updated. The above formulation implies that the distance from pixel to pixel is 1. We have to transform the Laplace operator to real lengths by rescaling the diffusion constant D . A typical value of the spectral radius of Jacobi for fast convergence used in the SOR algorithm was around 0.60.

We now have the tool to describe the fast converging iteration scheme to solve the integral-differential equation of area contact in frequency space in its most general form [2.30]:

$$\begin{aligned} D\Delta V_{JM} - i\omega V_{JM} - \frac{i\omega\beta^*}{1+\epsilon^{-1}} \langle V_{JM} \rangle + \frac{g_{JM} V_{JM}}{c_{ox}(1+\epsilon^{-1})} &= -\frac{i\omega V_S}{1+\epsilon^{-1}} \\ D &= [c_{ox} r_J (1+\epsilon^{-1})]^{-1} \end{aligned} \quad [2.39]$$

We use as a starting solution the approximation of the localized free membrane, given here in its most general form and parametrized with the constants of [2.37]:

$$\begin{aligned} D\Delta V_{JM}^0 + c_1^0 V_{JM}^0 &= c_2^0 \\ c_1^0 &= -i\omega \left[1 + \frac{\beta^*}{1+\epsilon^{-1}} \right] - \frac{g_{JM}}{c_{ox}(1+\epsilon^{-1})} \quad c_2^0 = -\frac{i\omega V_S}{1+\epsilon^{-1}} \end{aligned} \quad [2.40]$$

This diffusion equation can be relaxed with the above scheme to the solution V_{JM}^0 . Now the average $\langle V_{JM}^0 \rangle$ can be integrated. If it is held fixed in [2.39] we can again solve a diffusion equation, now with the constants:

$$c_1^1 = -i\omega - \frac{g_{JM}}{c_{ox}(1+\epsilon^{-1})} \quad c_2^1 = \frac{-i\omega(V_E - \beta^* \langle V_{JM}^0 \rangle)}{1+\epsilon^{-1}} \quad [2.41]$$

to get the new solution V_{JM}^1 . We can then update c_1^2 and calculate V_{JM}^2 and so forth. Usually this scheme converges within a few iteration steps. Care must be taken for high values of μ and ν , as this iteration scheme will begin to oscillate at distinct values of ω and will not converge. This is assumed to be an artefact of the iteration scheme. However, the diverging iterations are only obtained for unphysiological parameter values. We must keep in mind that the integral in the area contact integral-differential equation is a global term which in principle could induce resonant behavior.

2.3.B Analytical solution for circular junction area

For a circular junction area it is demonstrated how the iteration scheme can be used to find an analytical solution for the area contact model. From

$$D\Delta V_{JM} + c_1 V_{JM} = c_2 \quad [2.42]$$

we get the well known solution for the transfer function at radius r with the maximal radius a of the junction area:

$$V_{JM} = \frac{c_2}{c_1} \left[1 - \frac{I_0(\Gamma r)}{I_0(\Gamma a)} \right] \quad \Gamma^2 = \frac{-c_1}{D} \quad [2.43]$$

Here $I_0(x)$ denotes the modified Bessel function of order 0. We follow the iteration scheme for solving the integral equation. We use here the more simple form with $\nu=\mu=1$ and $g_{JM}=0$. For the first iteration step we solve the localized free membrane solution from [2.34] directly:

$$\begin{aligned} \tilde{D}\Delta V_{JM} - i\omega V_{JM} &= \frac{-i\omega V_s}{1 + \beta + \varepsilon^{-1}} \\ \tilde{D} &= [c_{ox} r_j (1 + \beta + \varepsilon^{-1})]^{-1} \quad c_1 = -i\omega \quad c_2 = \frac{-i\omega V_s}{1 + \beta + \varepsilon^{-1}} \end{aligned} \quad [2.44]$$

We get the analytical solution

$$\Gamma^2 = \frac{-c_1}{\tilde{D}} \quad V_{JM} = \frac{c_2}{c_1} \left[1 - \frac{I_0(\Gamma r)}{I_0(\Gamma a)} \right] \quad [2.45]$$

Following the iteration scheme for the integral equation we now need the integral over V_{JM} . This can be done according to [Kießling 1999] p.42:

$$\langle I_0(\Gamma r) \rangle = \frac{2\pi}{\pi a^2} \int_0^a I_0(\Gamma r) r dr d\phi = \frac{2I_1(\Gamma a)}{\Gamma a} \quad \langle V_{JM} \rangle = \frac{V_s}{1 + \beta + \varepsilon^{-1}} \left[1 - \frac{2I_1(\Gamma a)}{\Gamma a I_0(\Gamma a)} \right] \quad [2.46]$$

Therefore we get for first iteration from [2.41]:

$$\begin{aligned} c_2^1 &= \frac{-i\omega \left(1 - \frac{\beta}{1 + \beta + \varepsilon^{-1}} \left[1 - \frac{2I_1(\Gamma a)}{\Gamma a I_0(\Gamma a)} \right] \right) V_s}{1 + \alpha^{-1}} \quad \Gamma^2 = \frac{i\omega}{D} \\ V_{JM}^1 &= \frac{c_2^1}{-i\omega} \left[1 - \frac{I_0(\Gamma r)}{I_0(\Gamma a)} \right] \quad V_{FM}^1 = \frac{\beta c_2^1}{i\omega} \left[1 - \frac{2I_1(\Gamma a)}{\Gamma a I_0(\Gamma a)} \right] \end{aligned} \quad [2.47]$$

This solution after the first iteration is not very compact, but with a maximum error of 5% rather precise. We see that the radius dependence of V_{JM} will not be altered by the iteration scheme stays a modified Bessel function of order 0 like in [2.43]. Only the amplitude is refined.

2.4 Parameter analysis for circular junctions

We analyze how the solution of the area contact model depends on the parameters. We define a reference frequency f_0 from junction area A_{JM} and the diffusion constant D .

2.4.A Area contact model with characteristic parameters

To eliminate the junction area dependency we scale the stimulation frequency f by a reference frequency f_0 obtained from junction area A_{JM} and the diffusion constant D :

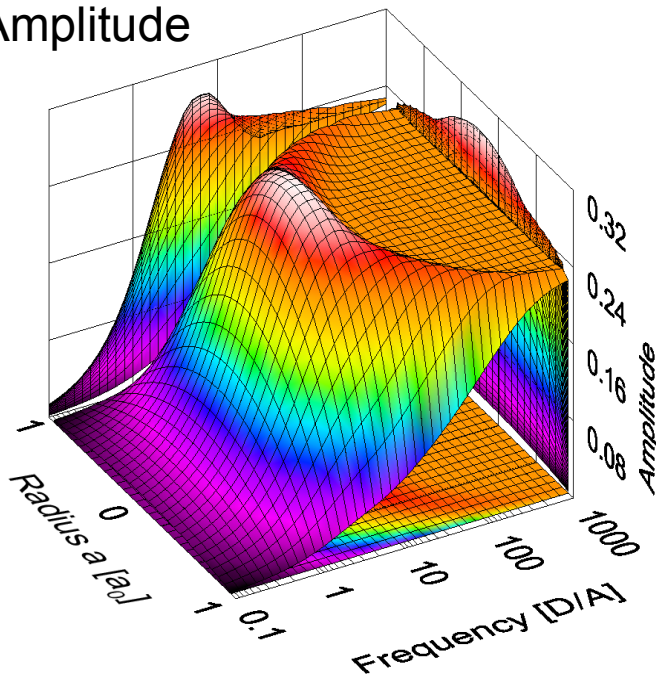
$$f_0 = \frac{D}{A_{JM}} = \frac{1}{c_{ox}r_J(1 + \epsilon^{-1})A_{JM}} \quad [2.48]$$

We choose for the characteristic parameters for the stimulation of a rat nerve cell on 10nm oxide:

TABLE 2.1 Characteristic parameters of the area contact model

c_{ox}	--	$0.34\mu\text{F}/\text{cm}^2$	Specific capacitance of 10nm silicon dioxide
ϵ	$\epsilon=c_{OX}/c_{JM}$	0.34	Chosen to match $c_{JM}=1\mu\text{F}/\text{cm}^2$
β	$\beta=A_{JM}/A_{FM}$	0.5	Chosen for a half spherical geometry
g_{JM}	--	0	No junction membrane conductance assumed
μ	$\mu=g_{JM}/g_{FM}$	1	No different membrane conductance assumed
ν	$\nu=c_{JM}/c_{FM}$	1	No different membrane capacitance assumed

Amplitude



Phase

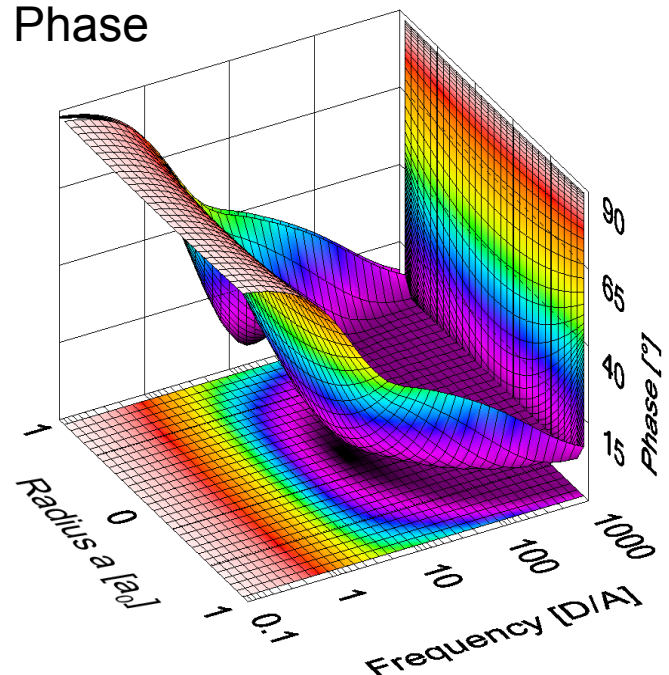


Fig 2.3 Amplitude and phase of the transfer function of the area contact model for the junction membrane $g_{CELL}(f,a)$ versus radius a_0 and the reference frequency $f_0=D/A_{JM}$.

The circular solution for the transfer function $g_{\text{CELL}}(f,r)$ at a given stimulation frequency f is given for the characteristic parameters in Fig 2.3, Fig 2.4 and Fig 2.5. The capacitive coupling between silicon oxide and the cell begins below f_0 and reaches the voltage levels of the capacitively defined voltage divider of oxide, junction and free membrane in the middle of the junction already at $10f_0$ (Fig 2.3). In this transition region we typically see a voltage profile in the junction membrane starting with a hyperbolic shape for low frequencies and ending with a homogenous voltage in the junction for high frequencies. The profile of the phase is similarly bent, though not as pronounced (Fig 2.4).

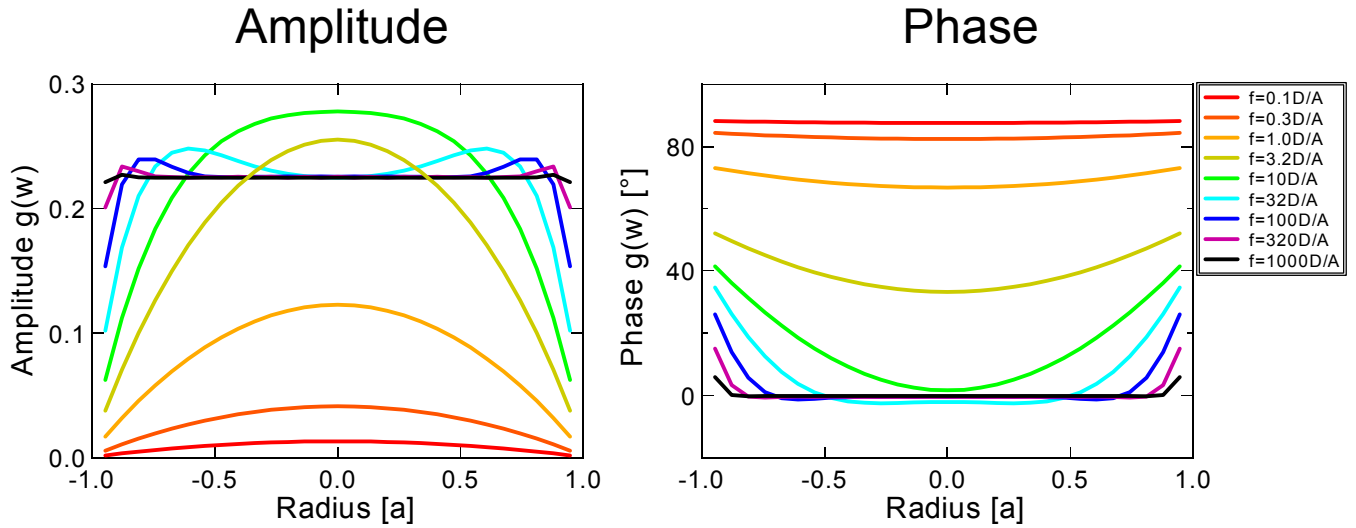


Fig 2.4 Profile of amplitude and phase of the transfer function $g_{\text{CELL}}(f,r)$ of the area contact model for the junction membrane plotted versus the maximum radius a .

By comparing V_{JM} in the center of the junction to V_{FM} for different frequencies (Fig 2.5), we see that V_{FM} does not show the pronounced resonance effect around $f=5f_0$. This is a direct result of the integration over V_{JM} performed in the integral equation of the area contact model.

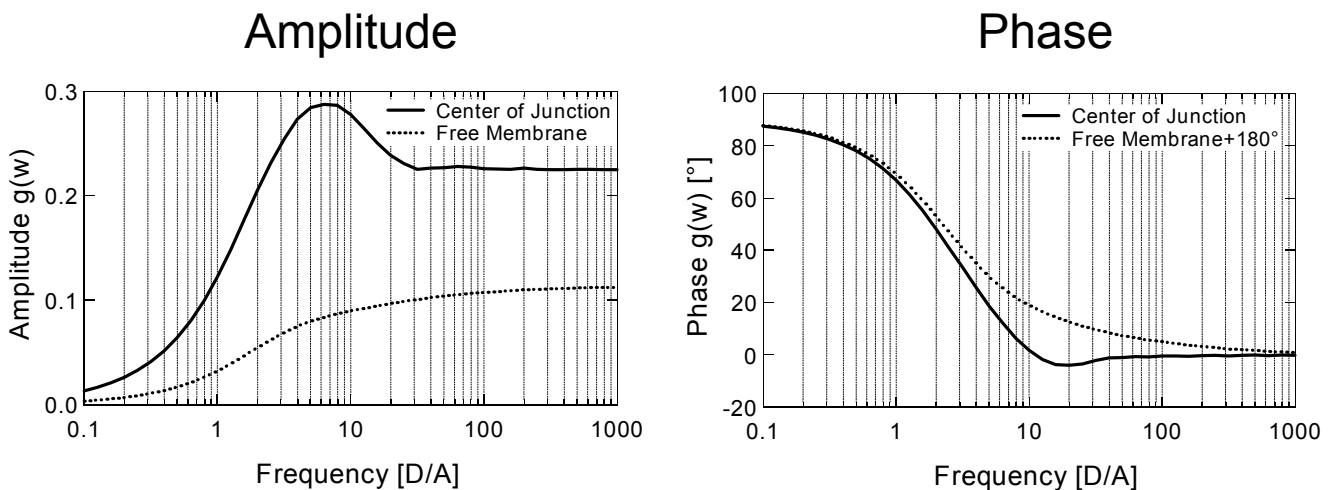


Fig 2.5 Comparison of junction and free membrane potential. Amplitude and phase of the area contact transfer function $g_{\text{CELL}}(f,0)$ in the center of the junction and of the free membrane $g_{\text{CELL}}^{\text{FM}}(f)$ are plotted versus the reference frequency f_0 .

2.4.B Comparing area contact and local approximation

The most prominent difference between the area contact model and its local free membrane approximation occurs in the voltage profile of the free membrane as shown in Fig 2.6. For the local approximation, it does depend on the radius like the junction membrane potential.

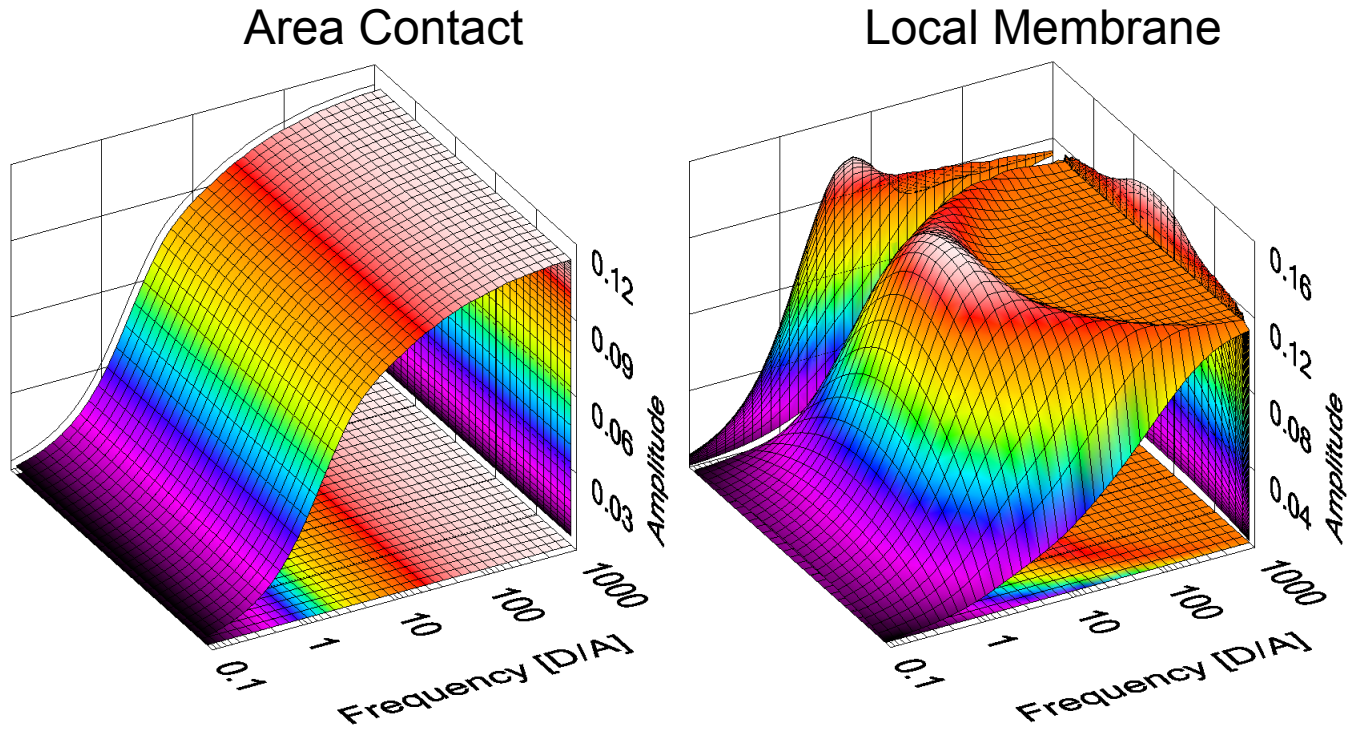


Fig 2.6 Comparison of area contact model (left) and approximation of local membrane used beforehand (right). The amplitude of the transfer function $g_{\text{CELL}}^{\text{FM}}(f,r)$ of the free membrane is plotted versus radius and the reference frequency $f_0=D/A_{\text{JM}}$.

However the amplitude of the junction membrane shows only a small difference (Fig 2.7). Here we can also see the difference in amplitude and phase for the free membrane..

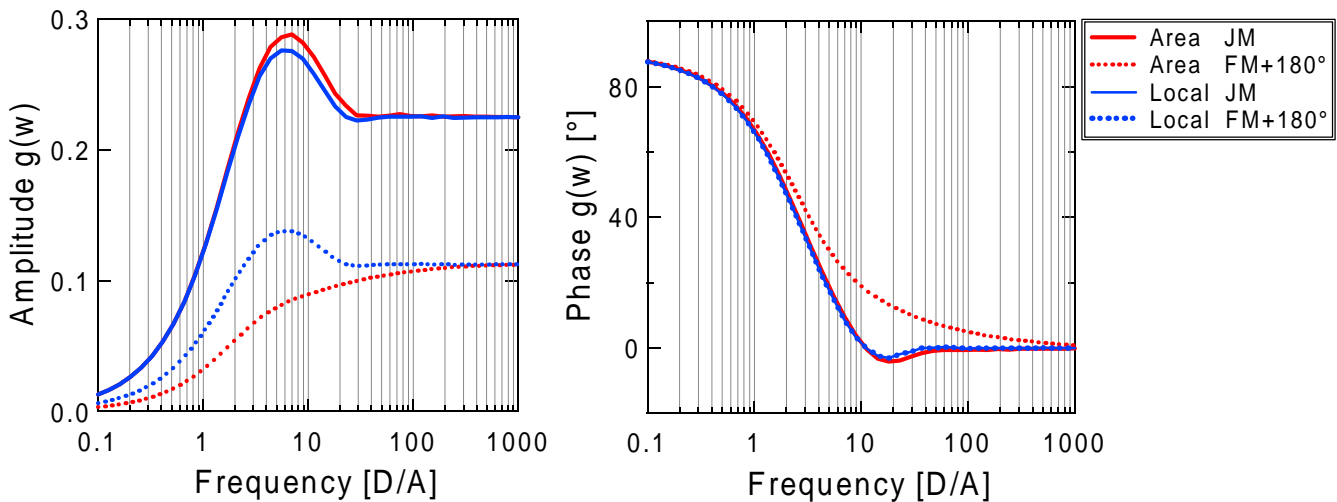


Fig 2.7 Comparison between the area contact model and the local membrane approximation used beforehand. In the middle of the junction the transfer function $g_{\text{CELL}}(f,0)$ is very much the same for the characteristic parameters, but the transfer function for the free membrane $g_{\text{CELL}}^{\text{FM}}(f)$ differs.

2.4.C Influence of free membrane area [β]

The membrane area ratio β mainly influences the amplitude of the free membrane potential whereas the effect on the junction membrane potential is rather small, because the oxide capacitance with $\epsilon=0.34$, the area ratio of junction and free membrane β does only slightly change the overall voltage divider of the capacitances. We do see though a higher voltage in the middle of the junction for low values of β as less voltage is consumed by the free membrane. For very large areas of the free membrane, there is no effect from the free membrane, therefore the parameter $\beta=0$ in this case is also used for single adsorbed vesicle membranes.

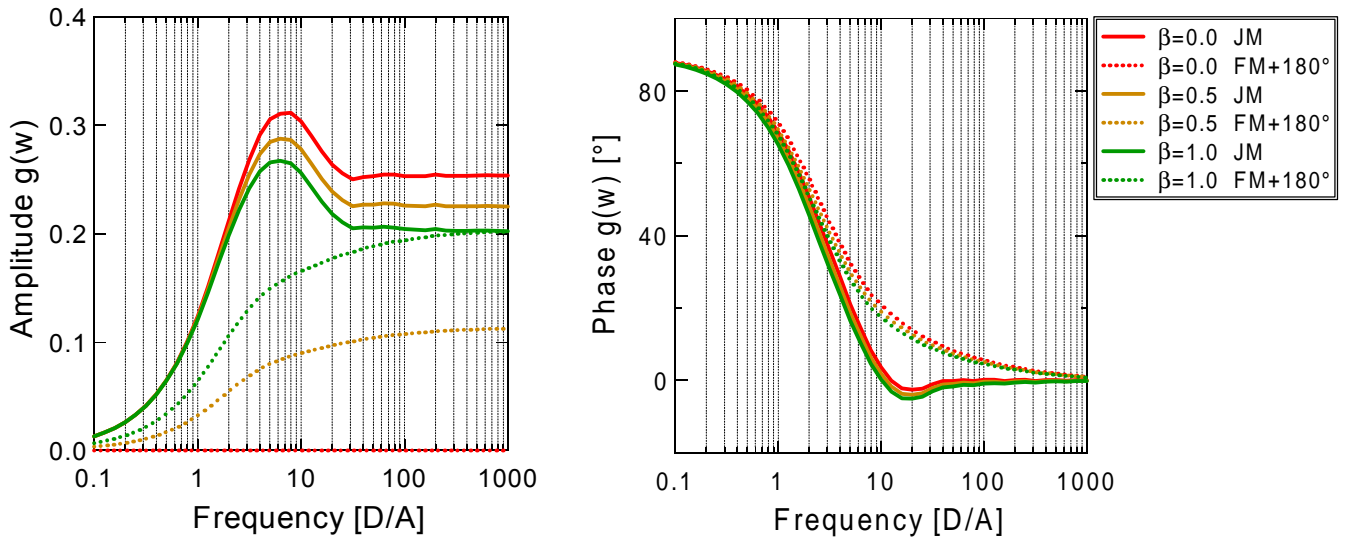


Fig 2.8 Variation of area ratio between junction and free membrane. Amplitude and phase of the area contact transfer function $g_{\text{CELL}}(f,0)$ in the center of the junction and of the free membrane is plotted versus the reference frequency f_0 . The ratio of junction membrane area and free membrane area β was varied from 0 to 1.

2.4.D Increasing the spot capacitance [ϵ and c_{ox}]

Increasing the stimulating capacitance with the parameters ϵ and c_{ox} to values larger than $1\mu\text{F}/\text{cm}^2$ of the cell membrane increases the membrane potential as seen in Fig 2.9 on the next page. The increase of the stimulation capacitance slows down the junction time constant of the point contact model since capacitive coupling is obtained for lower simulation frequencies. As the reference frequency f_0 is proportional to $1/c_{\text{ox}}(1+\epsilon^{-1})$ we will see later from the point contact model in [2.65] that the junction time constant is proportional to:

$$\tau_j \propto c_{\text{ox}}(1 + \beta + \epsilon^{-1}) \propto \alpha(1 + \beta + \epsilon^{-1}) \quad [2.49]$$

Beginning with a typical junction time constant of $\tau_j=2\mu\text{s}$, we get (Table 2.2):

TABLE 2.2 Decrease of junction time constant τ_j with ϵ

ϵ	0.07	0.34	1	3	10	100
τ_j	$1\mu\text{s}$	$2.74\mu\text{s}$	$4.52\mu\text{s}$	$10\mu\text{s}$	$29\mu\text{s}$	$272\mu\text{s}$

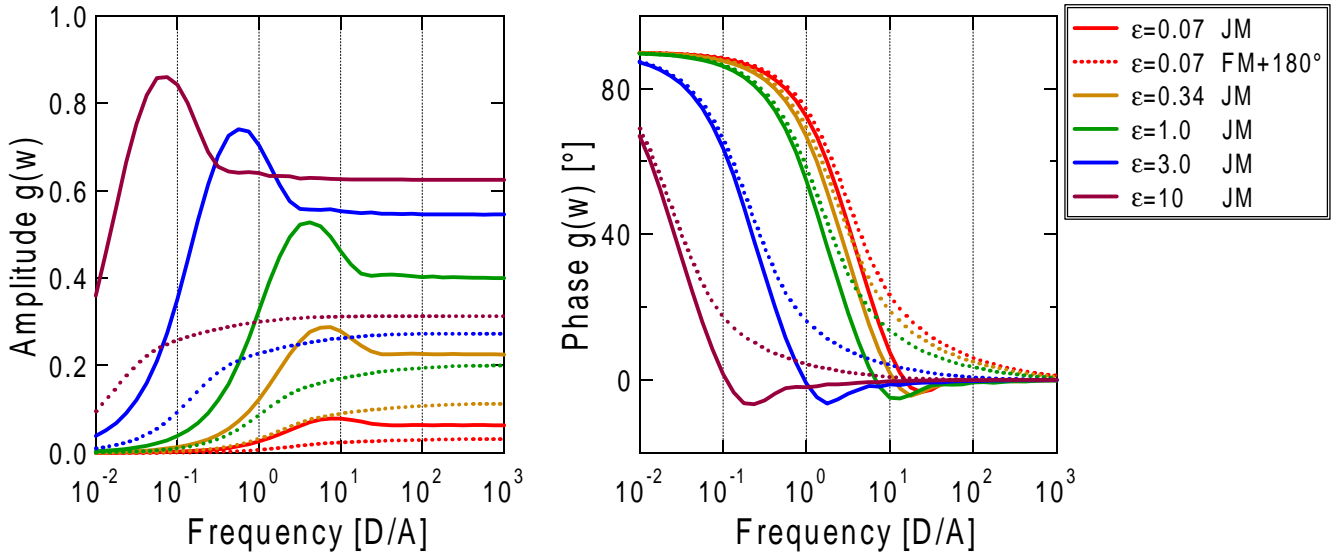


Fig 2.9 Increasing the stimulation spot capacitance. Amplitude and phase of the area contact transfer function $g_{\text{CELL}}(f,0)$ in the center of the junction and of the free membrane $g_{\text{CELL}}^{\text{FM}}(f)$ is plotted versus the reference frequency f_0 . The capacitance of the stimulation spot was increased from $\epsilon=0.07$ to 10 ($c_{\text{ox}}=\epsilon*1\mu\text{F}/\text{cm}^2$).

2.4.E Influence of membrane conductance [g_{JM}]

A highly enhanced membrane conductance flattens the amplitude and phase profile and shifts the capacitive coupling to higher frequencies (Fig 2.10 and Fig 2.11).

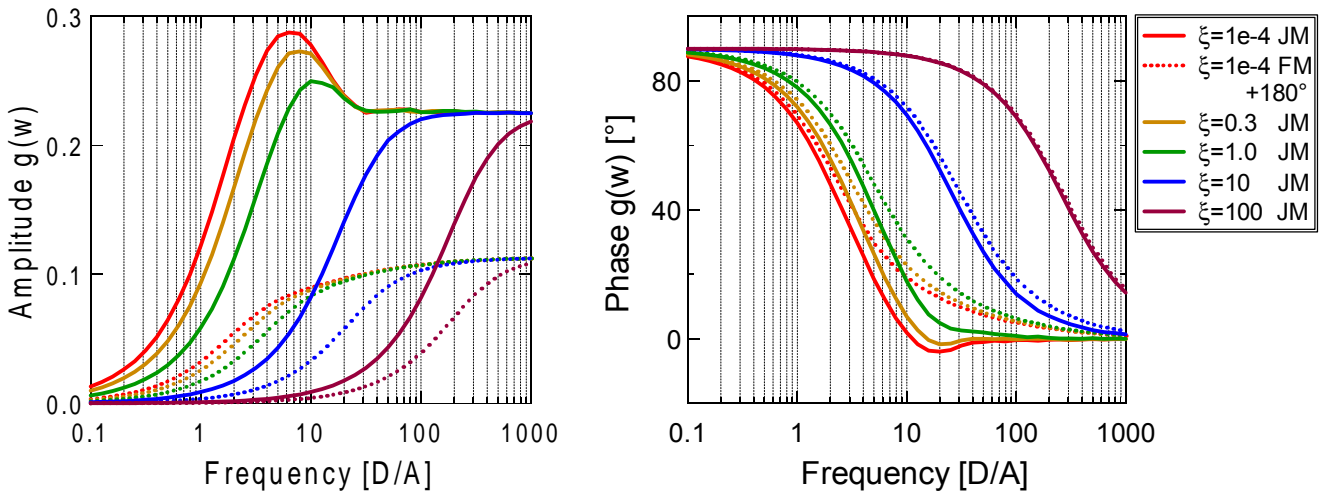


Fig 2.10 Variation of the membrane conductance g_{JM} . Amplitude and phase of the area contact transfer function $g_{\text{CELL}}(f,0)$ in the center of the junction and of the free membrane $g_{\text{CELL}}^{\text{FM}}(f)$ is plotted versus the reference frequency f_0 . The membrane conductance of either junction and free membrane was varied from $1e-4g_j$ to $100g_j$.

We have scaled the junction membrane conductance with the factor ξ from the specific junction conductance g_J explained together with the point contact model in 2.5 on page 27. From [2.48] and the later explained [2.61] we get with $k_\beta=5$:

$$g_J = f_0 k_\beta \pi c_{ox} (1 + \varepsilon^{-1}) \quad g_{JM} = \xi g_J \quad [2.50]$$

Usually in mammalian nerve cells the membrane conductance has values around 0.1 mS/cm^2 and thus is smaller than g_J by four orders of magnitude ($\xi=1e-4$). The effect of the leaky membrane can only be seen with an enhancement of the membrane conductance by some orders of magnitude. Note that although we alter only the membrane conductance of the junction, the membrane conductance of the free membrane is changed accordingly via the ratio $\mu=1$. The voltage profile across the junction becomes flat as the membrane conductance increases (Fig 2.11):

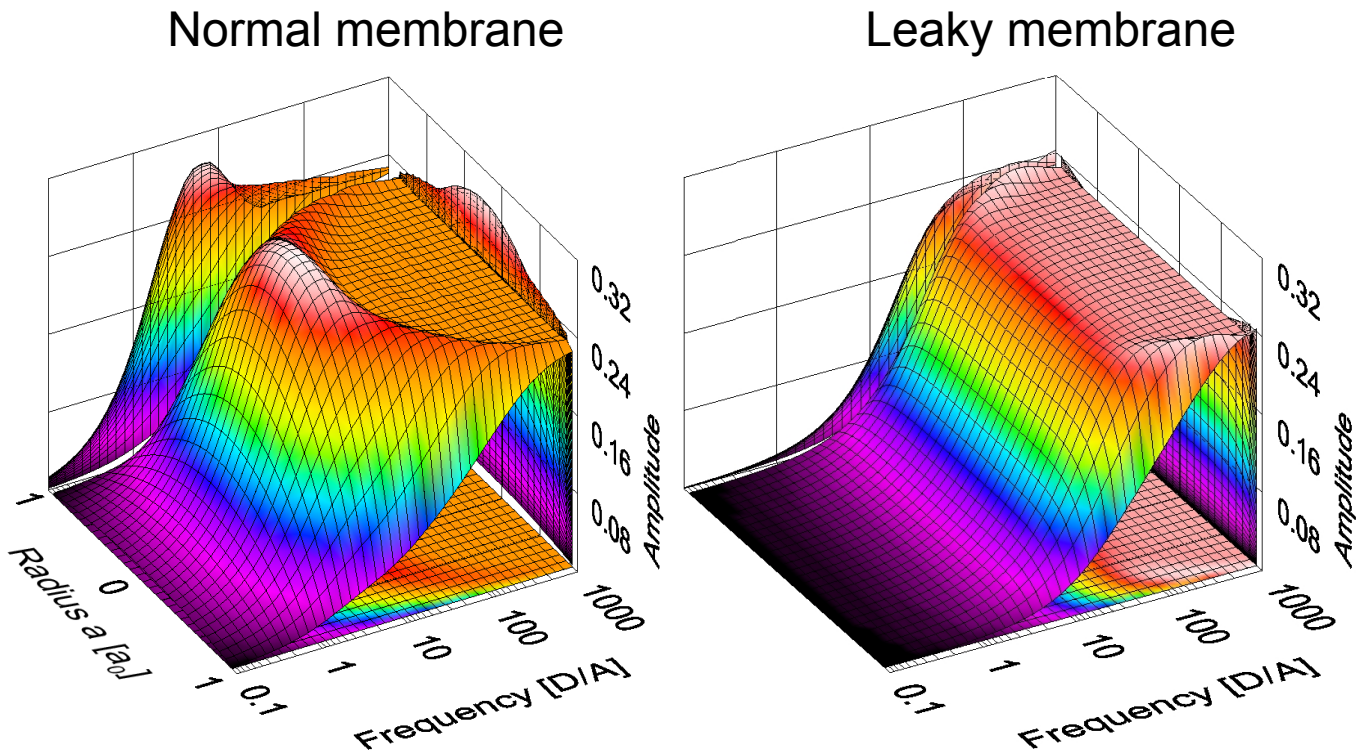


Fig 2.11 The parabolic voltage profile in the junction disappears for leaky membranes. The amplitude of the transfer function $g_{CELL}(f,r)$ for the junction membrane is plotted versus the radius and the reference frequency f_0 . The membrane conductance was increased from $\xi=1e-4$ (left) to $\xi=10$ (right) where $g_{JM}=\xi g_J$.

2.4.F Influence of junction membrane conductance [μ]

For a highly enhanced junction membrane conductance a big phase difference between free and junction membrane can be found together with a very slow time constant in the free membrane. We stick to a conductance of the free membrane of $g_{FM}=1e-4g_J$ and increase the conductance of the junction membrane with the parameter μ from 1 to $1e5$. Like in the case of the leaky membrane the transfer function shifts to higher frequencies, flattening its voltage profile in the junction. It can be seen in Fig 2.12 that for a leaky junction membrane the junction voltage V_{JM} itself is small, but the free membrane potential V_{FM} is stimulated down to very low frequencies.

The reason is that the free membrane can only discharge slowly via the membrane conductance of the free membrane g_{JM}/μ with a membrane time constant of around 1ms. Further estimates for this situation with the point contact model will be given in paragraph 2.5.F on page 32. A variation of the free membrane conductance is comparable to increasing values of β : the voltage divider of the free membrane can be totally neglected for very leaky free membranes. As a further consequence we see that the phases of the junction and the free membrane decouple due to increasing ohmic currents through the junction membrane: the phase difference between junction and free membrane is not 180° any more but $\text{phase}_{JM}-\text{phase}_{FM}=270^\circ$.

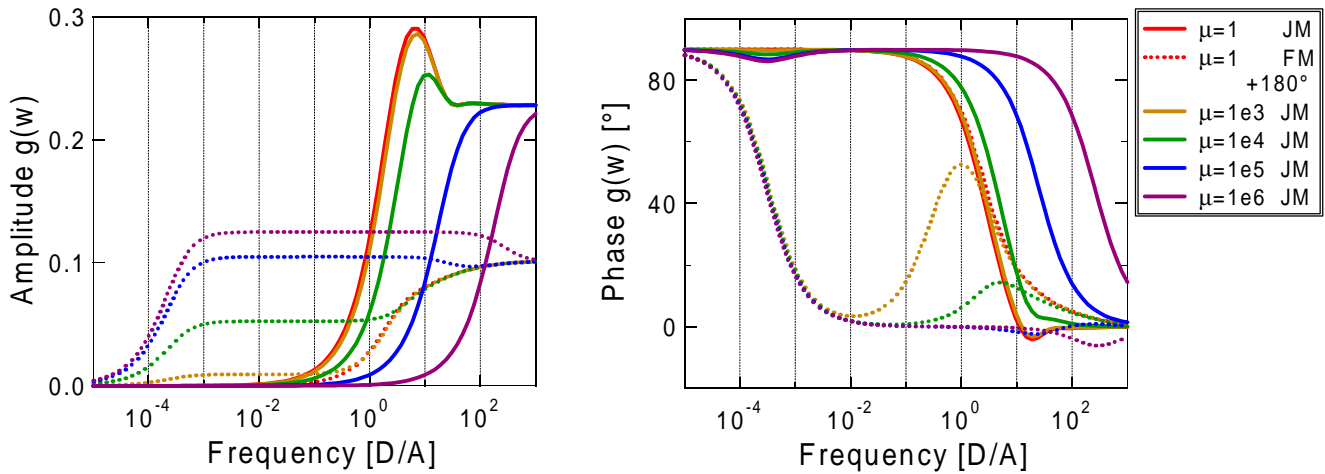
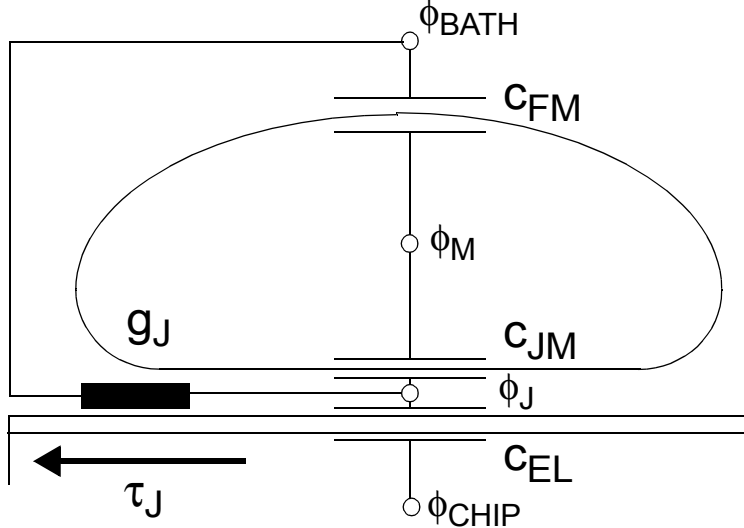


Fig 2.12 Variation of junction membrane conductance. We plot the amplitude and phase of the transfer function $g_{CELL}(f,0)$ for the center of the junction membrane and the transfer function of the free membrane $g_{CELL}^{FM}(f)$ versus the reference frequency f_0 . The junction membrane conductance was increased from $g_{JM}=g_{FM}=1e-4g_J$ to $g_{JM}=1e5g_{FM}$.

2.5 Point contact model

The main approximation for the description of the coupling is the point contact model. The junction resistance is approximated by a global junction conductance g_J . Junction oxide and junction membrane potential is averaged.



$$\begin{aligned}\epsilon &= \frac{c_{ox}}{c_{JM}} & \beta &= \frac{A_{JM}}{A_{FM}} \\ V_E &= \phi_{BATH} - \phi_{CHIP} \\ V_J &= \phi_J - \phi_{BATH} \\ V_{JM} &= \phi_M - \phi_J \\ V_{FM} &= \phi_M - \phi_{BATH}\end{aligned}$$

2.5.A Point contact model derived from circuit

We derive the point contact differential equation from the currents in the junction similar to [2.1]. From

**Capacitive current through junction membrane =
Capacitive current through oxide - Current through cleft**

with a membrane conductance g_{JM} added to the above circuit we get:

$$\frac{c_{ox}}{\epsilon} \partial_t V_{JM} + g_{JM} V_{JM} = c_{ox} \partial_t V_{OX} + g_J (V_{FM} - V_{JM}) \quad [2.51]$$

With the voltage divider

$$V_{FM} = -\beta V_{JM} \quad V_{OX} = V_S - V_{JM} + V_{FM} = V_E - (1 + \beta) V_{JM} \quad [2.52]$$

$$\frac{c_{ox}}{\epsilon} \partial_t V_{JM} + g_{JM} V_{JM} = c_{ox} \partial_t (V_S - (1 + \beta) V_{JM}) - g_J (1 + \beta) V_{JM} \quad [2.53]$$

$$[g_J (1 + \beta) + g_{JM}] V_{JM} + (1 + \beta + \epsilon^{-1}) c_{ox} \partial_t V_{JM} = c_{ox} \partial_t V_S \quad [2.54]$$

$$V_{JM} + \frac{1 + \beta + \epsilon^{-1}}{g_J (1 + \beta) + g_{JM}} c_{ox} \partial_t V_{JM} = \frac{c_{ox}}{g_J (1 + \beta)} \partial_t V_S \quad [2.55]$$

Thus the time constant τ_J of the exponential solution and the high frequency limit g^∞ are:

$$\tau_J = \frac{c_{ox} (1 + \beta + \epsilon^{-1})}{g_J (1 + \beta) + g_{JM}} \quad g^\infty = \frac{1}{1 + \beta + \epsilon^{-1}} \quad [2.56]$$

resulting in a compact differential equation

$$V_{JM} + \tau_J \partial_t V_{JM} = g^\infty \tau_J \partial_t V_S \quad [2.57]$$

In the limit of high frequencies we expect that the junction conductance does not play a role and the voltage of spot oxide, junction and free membrane is determined by their capacitances due to a voltage divider. This can be found for high frequencies when only the time derivatives contribute to the equation [2.57]. The response to a voltage step with amplitude V_S at time $t=0$ is:

$$V_{JM}(t) = V_S g^\infty e^{-t/\tau_J} \quad [2.58]$$

Often we will deal with lock-in measurements and are thus interested in the transfer function of the coupling that is obtained for junction and free membrane by making the transition to frequency space with $\delta_t \rightarrow i\omega$ from [2.57]. It has the form of a high pass filter of order one:

$$g_{CELL}(\omega) = \frac{V_{JM}}{V_S} = \frac{i\omega g^\infty \tau_J}{1 + i\omega \tau_J} \quad g_{CELL}^{FM}(\omega) = \frac{V_{FM}}{V_S} = -\beta \frac{i\omega g^\infty \tau_J}{1 + i\omega \tau_J} \quad [2.59]$$

Plots of the point contact model are in paragraph 3.1.C on page 39. The junction conductance g_J was introduced in [Vassanelli 1997], former papers [Fromherz 1991a], [Fromherz 1993b] dealt with the global junction resistance $R_J = (g_J^* A_{JM})^{-1}$ measured in Ω , not to be confused with the junction resistance of the area contact model.

2.5.B Formal transition to point contact model

We will present a more formal transition from the area contact to the point contact model. In the two following paragraphs further evidence in favour of this kind of transition is given. We have to keep in mind that g_J is an approximation of the whole junction which cannot be applied to infinitesimal area pieces as done with r_J . Since it is a global conductance per junction area it also has to account for the shape of the junction. On the other hand, r_J is strictly defined as a local sheet resistance: $\Delta V_{JM}/r_J$ gives the infinitesimal local current flowing from an infinitesimal piece of junction area dA_{JM} . The transition to the simple point contact model can be most easily achieved by substituting the Laplace operator:

$$-\frac{\Delta}{r_J} \Leftrightarrow g_J(1 + \beta) \quad [2.60]$$

We further have to assume a relationship between g_J and r_J :

$$g_J = k_\beta \frac{\pi}{A_{JM} r_J} = k_\beta \frac{\pi c_{ox}(1 + \epsilon^{-1})}{A_{JM}} D \quad [2.61]$$

The value of the transition constant k_β will be discussed later. In this way we obtain the ordinary differential equation of the point contact directly from the diffusion equations of area contact model in the approximation of localized free membrane. To make the transition from the area contact model to the point contact model we have to reduce the space dependent voltages to their averages:

$$V_{JM} = \langle V_{JM} \rangle \quad V_J = \langle V_J \rangle \quad [2.62]$$

With the substitutions [2.60]&[2.62], starting from [2.22] we find:

$$[g_J(1 + \beta) + g_{JM}]V_{JM} + c_{ox}(1 + \beta + \epsilon^{-1})\partial_t V_{JM} = c_{ox}\partial_t V_S \quad [2.63]$$

or rewriting the point contact model of [2.55]:

$$V_{JM} + \frac{c_{ox}(1 + \beta + \varepsilon^{-1})}{g_J(1 + \beta) + g_{JM}} \partial_t V_{JM} = \frac{c_{ox}}{g_J(1 + \beta) + g_{JM}} \partial_t V_S \quad [2.64]$$

We give here a conversion formula between junction sheet resistance g_J and the junction time constant τ_j [2.56]:

$$g_J = \frac{c_{ox}(1 + \beta + \varepsilon^{-1})}{\tau_j(1 + \beta)} - \frac{g_{JM}}{1 + \beta} \quad [2.65]$$

To make the transition of the general area contact model [2.29] to the general point contact model we have to make the substitution in the frequency domain ($\delta_t \rightarrow i\omega$) with β^* :

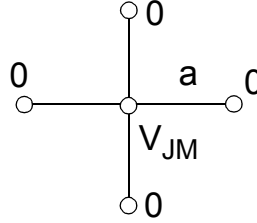
$$[g_J(1 + \beta^*) + g_{JM}]V_{JM} + c_{ox}i\omega(1 + \beta^* + \varepsilon^{-1})V_{JM} = c_{ox}i\omega V_S \quad [2.66]$$

Thus the general substitution is:

$$-\frac{\Delta}{r_J} \Leftrightarrow g_J(1 + \beta^*) \quad [2.67]$$

2.5.C Numerical transition to point contact model

From a discrete Laplace operator we can obtain a crude transition from area to point contact. We approximate the integral equation of the area contact model on a very small grid with finite differences. Starting from a coarse, more computer oriented approximation of a circular junction:



We obtain from finite differencing as e.g. also done for numerically solving in [2.38]:

$$\Delta V_{JM} = \sum_{i=\{x,y\}} \left[\frac{0 - V_{JM}^i}{a} - \frac{V_{JM}^i - 0}{a} \right] / a = -\frac{4}{a^2} V_{JM} \quad \langle V_{JM} \rangle = V_{JM} \quad [2.68]$$

With this we get from [2.10]

$$-\frac{4V_{JM}}{a^2 r_J} - c_{ox}(1 + \beta + \varepsilon^{-1}) \partial_t V_{JM} = -c_{ox} \partial_t V_S \quad [2.69]$$

Comparing this with [2.60] and [2.61] (using $A_{JM} = \pi a^2$) we obtain the following relation between k_β and β :

$$k_\beta = \frac{4}{1 + \beta} \quad [2.70]$$

We will see in the next paragraph that this choice of k_β is very good for describing the phase in the middle of the junction membrane. In numerically fitting the point contact model to the area contact model we will find a more generalized equation than [2.70] with the number 4 exchanged by a free fit parameter k .

We could envisage also more complicated geometries with more base points, but by introducing more values of V_{JM} in the geometry, we only obtain more equations without gaining more insight into the model. Also the selection of base points is by no means evident.

2.5.D Time domain transition to point contact model

In a third way to reveal the similarity of point and area contact model we will solve the area contact model in the localized approximation in the time domain. The goal is to approximate the area contact model by a single exponential solution. Since the former approximation of the localized free membrane is a diffusion equation, we can obtain the solution for circular boundary conditions analytically. Following [Crank 1975] we get from the diffusion equation [2.34] written in cylinder coordinates

$$\frac{1}{r} \partial_r (r \tilde{D} \partial_r V_{JM}) - \partial_t V_{JM} = \frac{-\partial_t V_S}{1 + \beta + \epsilon^{-1}} \quad [2.71]$$

the solution from a circular junction of radius a with $r=0..a$ after a voltage step of height V_S :

$$V_{JM}(r, t) = \frac{2V_S}{1 + \beta + \epsilon^{-1}} \sum_{n=1}^{\infty} \frac{J_0(r\alpha_n) \exp(-\tilde{D}\alpha_n^2 t)}{a\alpha_n J_1(a\alpha_n)} \quad [2.72]$$

with the Bessel function of order n $J_n(x)$ and α_n the n th zero of $J_0(ax)$. This solution is a converging series of exponential functions with time constants

$$\tau_j^n = \frac{1}{\tilde{D}\alpha_n^2} = \frac{c_{ox} r_J (1 + \beta + \epsilon^{-1})}{\alpha_n^2} \quad [2.73]$$

Note that the area dependence is hidden in the zero α_n . As illustrated in Fig 2.13 the first addend of [2.72] is sufficient to obtain a good time approximation of the locally approximated area contact model

$$V_{JM}^1(r, t) = \frac{1.6V_S \exp(-t/\tau_j^1) J_0(r\alpha_1)}{a\alpha_1 (1 + \beta + \epsilon^{-1}) J_1(a\alpha_1)} \quad \text{for times } t > \frac{\tau_j^1}{2} \quad [2.74]$$

If we compare the first time constant of the series with the time constant of the point contact model [2.56] we find the transition factor

$$k_\beta = \frac{\alpha_1^2 / a^2}{1 + \beta} = \frac{5.783}{1 + \beta} \quad [2.75]$$

Again we find the β -dependence of k_β .

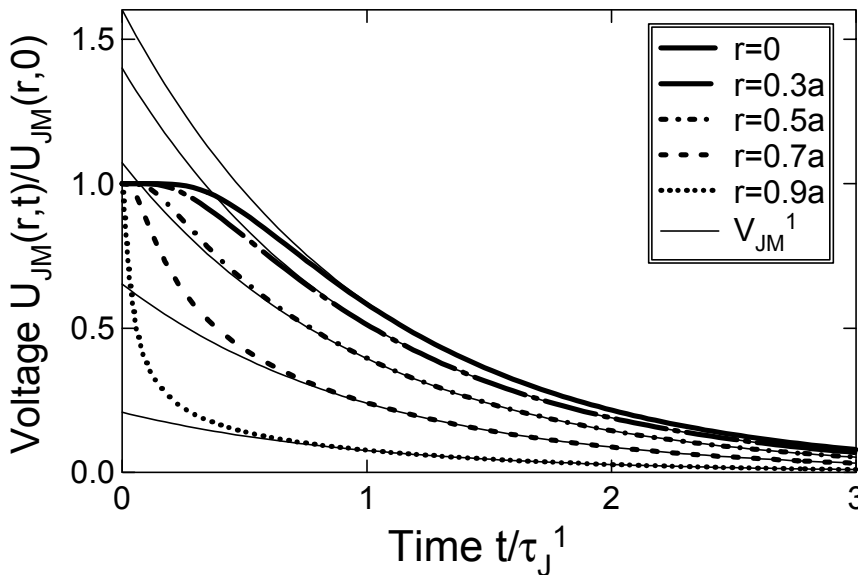


Fig 2.13 Junction voltage decay for local membrane approximation of the area contact model. Transients are plotted for circular boundary conditions at various values of the distance from the center r . For times longer than half of the time constant we get a good single exponential approximation.

2.5.E Fitted transition with four point contact models

We present here numerical estimates for the transition parameter k_β if phase and amplitude would be fitted independently. To describe the transfer function most precisely, we will allow for different k_β for amplitude and phase for the free and for the junction membrane. This demonstrates the compromise of the point contact model both in phase and amplitude.

In comparison with the area contact model the point contact model has a flattened frequency characteristic, very similar to the free membrane in the area contact model. We give here both transfer functions for the characteristic parameters and the transition parameter $k_\beta=5$. With $k_\beta=5$ the point contact model reproduces the amplitude for the free membrane at low frequencies very well (Fig 2.14):

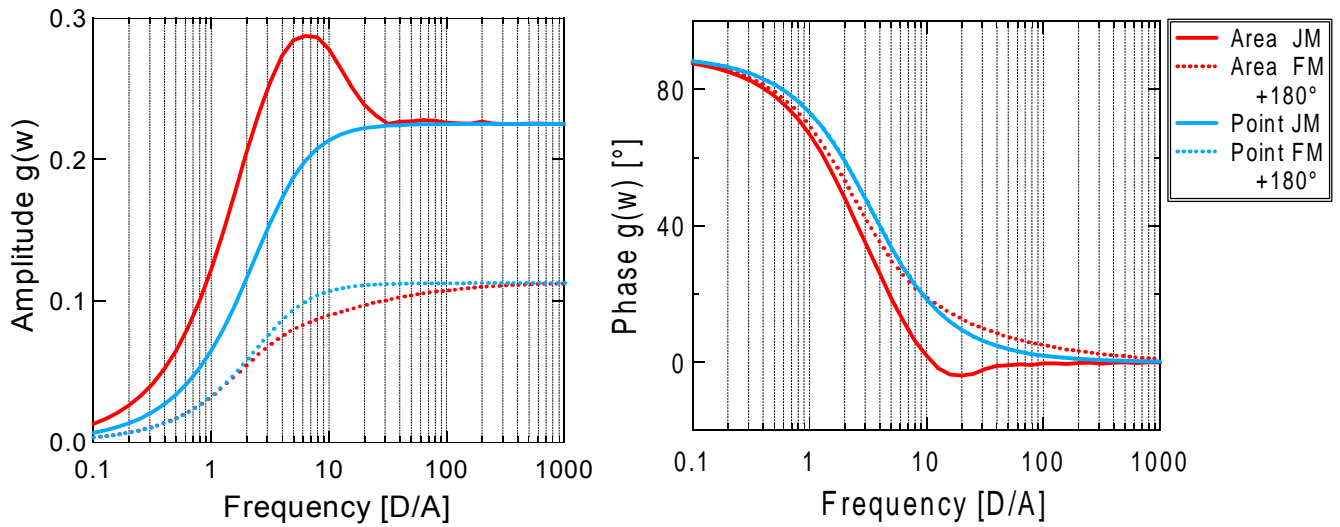


Fig 2.14 Comparison of area and point contact model in amplitude and phase of the transfer function $g_{\text{CELL}}(f,0)$ in the center of the junction and the transfer function for the free membrane $g_{\text{CELL}}^{\text{FM}}(f)$ versus the reference frequency f_0 . The point contact model is inferred from the area contact model with a transition parameter of $k_\beta=5$.

To fit the optimal value of k_β we integrate the difference between both transfer functions over a logarithmic frequency scale in both amplitude and phase of free and junction membrane. These differences are plotted versus k_β and the zeros in these plots are the best fitted values for k_β . Here the negative and positive deviations between both models are balanced. Integration is performed over a logarithmic frequency scale since we are more interested in the low frequency range. The following values of k_β were found in Table 2.3 with different values for the parameter β :

TABLE 2.3 Values of k_β for best linear fitting the area contact on a logarithmic frequency scale.

β value	Amplitude at center of JM	Phase at center of JM	Amplitude in FM	Phase in FM
0.1	2.0	3.5	11.0	6.6
0.5	1.1	2.6	7.8	4.9
1.0	0.8	1.9	5.7	3.6

We have allowed for different transition constants k_β for either amplitude or phase and the free and the junction membrane. Therefore the area contact model is approximated with four point contact differential equations for amplitude and phase with different transition constants. We further find that the β -dependence of k_β follows the proportionality described in [2.70] in a more general way. Assuming

$$k_\beta = \frac{k}{1+\beta} \quad [2.76]$$

A good agreement can be found with the proportionality constants $k=2,4,12$ and 7 as shown in Table 2.4:

TABLE 2.4 Values of k describing with k_β the best linear fit on a logarithmic frequency scale. Values of $k=2,4,12,7$ are found for the amplitude and phase of the center of the junction membrane potential and the amplitude and phase of the free membrane potential.

β value	Amplitude at center of JM	Phase at center of JM	Amplitude in FM	Phase in FM
	$k_\beta = \frac{2}{1+\beta}$	$k_\beta = \frac{4}{1+\beta}$	$k_\beta = \frac{12}{1+\beta}$	$k_\beta = \frac{7}{1+\beta}$
	$k = 2$	$k = 4$	$k = 12$	$k = 7$
0.1	1.8	3.6	10.9	6.4
0.5	1.3	2.7	8	4.7
1.0	1.0	2.0	6	3.5

2.5.F Point contact model for leaky junction membrane

An approximation for high junction membrane conductance within the point contact model is presented. With a high junction membrane conductance and a nonleaky free membrane it is possible to observe high free membrane potentials at low frequencies and high time constants. This was shown for the area contact model in paragraph 2.4.F on page 25. We start from [2.66] with $v=1$ and approximate within a frequency window

$$c_{ox}i\omega \gg \alpha g_{FM} \quad c_{ox}i\omega \ll \alpha g_{JM} \quad g_{JM} = \mu g_{FM} \quad [2.77]$$

$$\beta^* = \beta\mu \left[\frac{\epsilon g_{JM} + c_{ox}i\omega}{\epsilon g_{JM} + \mu c_{ox}i\omega} \right] \approx \frac{\beta\epsilon\mu g_{FM}}{c_{ox}i\omega} \quad [2.78]$$

We translate everything to the free membrane potential and finally get:

$$-\left[g_J \left(1 + \frac{\beta\epsilon\mu g_{FM}}{c_{ox}i\omega} \right) + \mu g_{FM} + c_{ox}i\omega \left(1 + \frac{\beta\epsilon\mu g_{FM}}{c_{ox}i\omega} + \alpha^{-1} \right) \right] \frac{V_{FM}}{\beta\epsilon\mu g_{FM}} = V_S \quad [2.79]$$

With further assuming

$$\frac{\beta\epsilon\mu g_{FM}}{c_{ox}i\omega} \gg 1 \quad \epsilon^{-1} \approx 1 \quad g_J \frac{\beta\epsilon}{c_{ox}i\omega} \ll 1 \quad [2.80]$$

we find a constant transfer function for the free membrane of:

$$g_{CELL}^{FM}(\omega) = \frac{V_{FM}}{V_S} = -\frac{\beta\epsilon}{(1+\epsilon\beta)} \quad [2.81]$$

For the characteristic parameters (Table 2.1 on page 20) this yields $|g_{\text{CELL}}^{\text{FM}}(\omega)| = 0.145$ which is very well the upper limit in Fig 2.12. We see how the point contact model approximates these conditions in Fig 2.15, where comparison is made with $k_{\beta}=5$. We see that the phase is approximated rather precisely whilst the amplitude is systematically overestimated by the point contact model.

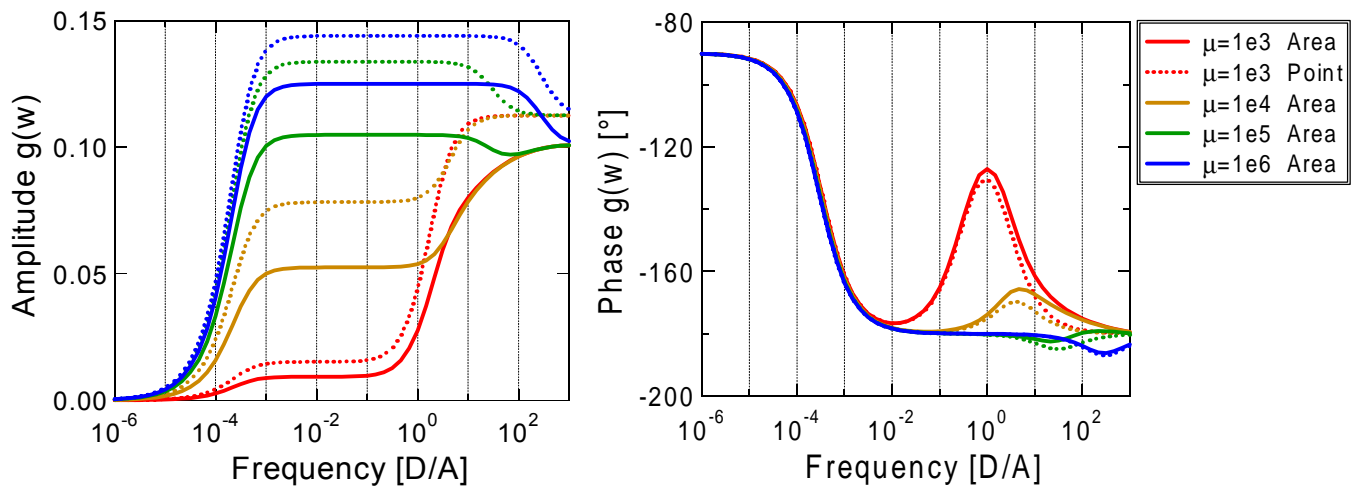


Fig 2.15 Comparison of area and point contact model in the case of leaky junction membrane. We plot the transfer function of the free membrane $V_{\text{FM}}(f)/V_{\text{S}}(f)$ versus the reference frequency $f_0=D/A_{\text{JM}}$.

2.6 Measured coupling parameters

We summarize for various cell types the data from geometry measurements (FLIC-Microscopy) and from transistor measurements.

2.6.A Coupling parameters from geometry

Measurements of the cell-substrate distance can be obtained from FLIC microscopy. Together with the junction membrane area measured simultaneously the geometric parameters of the junction are determined. We will present estimates of junction parameters from geometry.

After the development of the theory and first tests with Langmuir-Blodgett films on chips by [Lambacher 1994], [Lambacher 1996], the method of FLIC microscopy was extended to measure cell-substrate distances on steps of 4 or 16 oxide steps [Braun 1996]. The method was tested on erythrocyte ghosts [Braun 1997] and on various cell types such as HEK cells, neurons and astrocytes [Braun 1998].

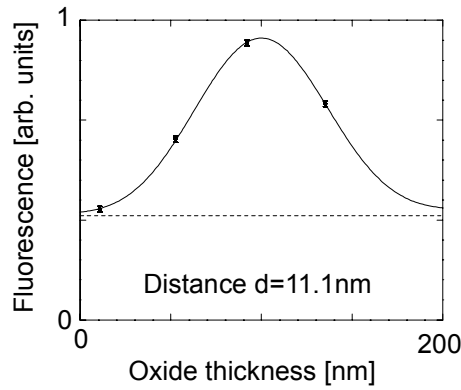
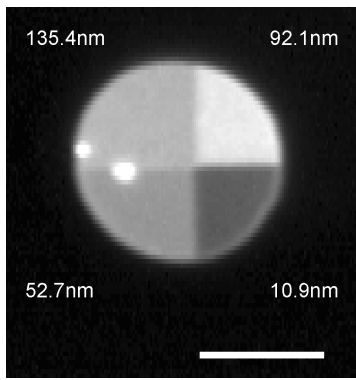


Fig 2.16 Measuring the thickness of the junction cleft d of an erythrocyte ghost in Poly-Lysine with FLIC-Microscopy [Braun 1997]. We see homogeneous fluorescence on 4 oxide steps (left). The intensities are fitted with theory. We get a thickness of the cleft of 11.1nm, in average a value of 11.4 ± 0.7 nm.

The thickness of the junction of erythrocytes ghosts on poly-lysine coated chips is found to be $d = 11.4 \pm 0.7$ nm. A sample measurement is displayed in Fig 2.16. Thicknesses of the junction for neuronal cells on laminin and fibronectin are 105nm and 60nm (Fig 2.17):

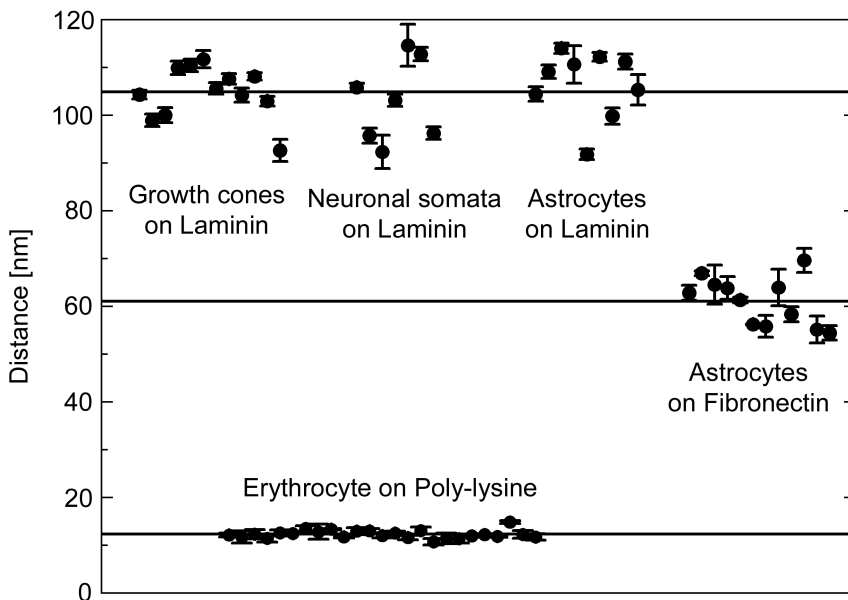


Fig 2.17 Thickness of the cleft d for neuronal cells and ghosts on Laminin, Fibronectin and Poly-Lysine as measured with FLIC microscopy. [Braun 1998]

Rat nerve somata showed a rough cleft on Poly-Lysine (Fig 2.18):

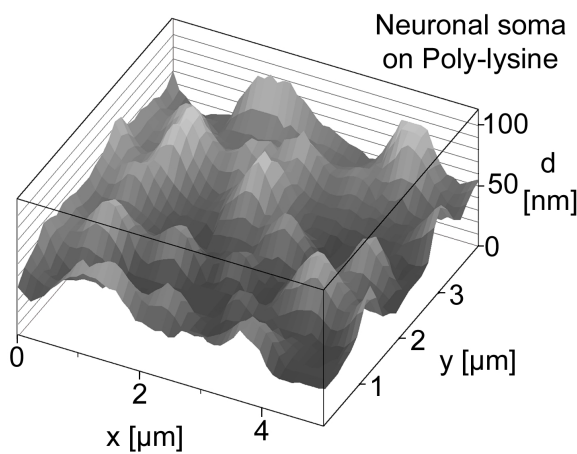


Fig 2.18 Thickness of the cleft d for a rat nerve soma on Poly-Lysine. The distance is very rough, oscillating from 35nm to 85nm. In average we obtain a thickness of around 60nm.

I used in this work not only neuronal, but also human embryo kidney cells (HEK 293). This cell line was first measured on uncoated substrates in [Braun 1996] with a distance of 65nm, but also on coated substrates recently by [Görler 1999] while he was doing an internship in our department. We find mean values for the cleft thickness of $d=97.3\pm 3\text{nm}$ on Laminin coated and $d=50.0\pm 6\text{nm}$ on Fibronectin coated chips (Fig 2.19):

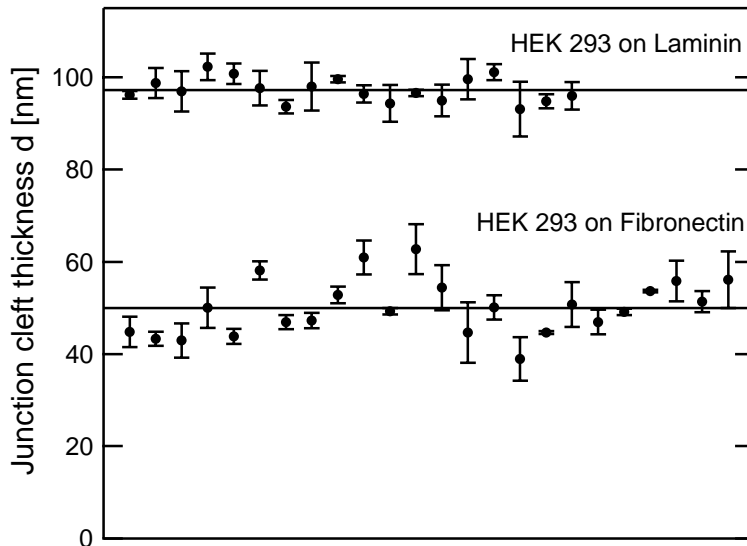


Fig 2.19 Junction cleft thickness d of HEK 293 cells on Laminin and Fibronectin as measured with FLIC microscopy. Error bars indicate the statistical error of a single measurement. Average values are on Laminin $97\pm 3\text{nm}$ and on Fibronectin $50\pm 6\text{nm}$. The measurements are collected from 2 (3) cell cultures on Laminin (Fibronectin)

A much narrower junction cleft of 1.1nm can be achieved with adsorbed giant vesicle membrane on Poly-Lysine as shown in [Fromherz 1999] or here in chapter 4.4.A on page 71. We can use the cleft width d to calculate from the measured sheet resistance of the cleft r_j the bulk conductivity ρ_j of the cleft:

$$\rho_j = r_j d \quad [2.82]$$

Assuming a specific conductivity in the cleft of $\rho_j=74\Omega\text{cm}$ like in the bulk electrolyte, we find values for r_j , g_j and τ_j as listed in Table 2.5.

TABLE 2.5 Values of r_j derived from cleft thickness d and $\rho_j=74\Omega\text{cm}$ ($250\Omega\text{cm}$ for the vesicles). Estimates of g_j are given assuming a circular junction area and a transition constant between area contact and point contact model $k_\beta=5$. Estimates of τ_j further need the parameters $\epsilon=0.34$, $c_{ox}=0.34\mu\text{F}/\text{cm}^2$ and $\beta=0.5$. (PL=Poly-Lysine, FN=Fibronectin, LN=Laminin)

Cell	Ghost on PL	(S mall) HEK 293 on FN	(Small) HEK 293 on LN	Nerve Soma on PL	Astrocyte on FN	Astrocyte on LN	Adsorbed vesicles
Distance d	11nm	50nm	100nm	35..85nm	60nm	110nm	1.1nm
r_j	65MΩ	14MΩ	7MΩ	20..8MΩ	12MΩ	6MΩ	2300MΩ
Area A_{JM}	60 μm^2	600 μm^2	600 μm^2	150 μm^2	1200 μm^2	1200 μm^2	5000 μm^2
g_j [mS/cm2]	400	190	370	520..1300	110	220	0.14
τ_j	2.5μs	5.3μs	3.7μs	1.9..0.8μs	9μs	4.6μs	9500μs

Estimates for the junction conductance g_j and the time constant of the junction τ_j are obtained from [2.61] and [2.56] together with the characteristic parameters $\varepsilon=0.34$, $c_{ox}=0.34\mu\text{F}/\text{cm}^2$ and $\beta=0.5$ on Table 2.1 on page 20. For the adsorbed vesicle membrane in the last column the parameters $\beta=0$ and $\rho_j=250\Omega\text{cm}$ were used since there is no free membrane and the electrolyte has a reduced conductance. It can be seen that besides the junction thickness the junction area A_{JM} is the dominant parameter.

2.6.B Coupling parameters from transistor measurements

Many measurements were done with field effect transistors on Retzius and snail nerve cells [Fromherz 1991a], [Fromherz 1993b], [Weis 1996] and [Stett 1997]. However FLIC microscopy cannot be applied due to the rough membrane of these cells. Transistor measurements on mammalian cells are published for erythrocyte ghosts [Kießling 1999], rat nerve cells [Vassanelli 1997], [Vassanelli 1998] and giant vesicle membranes [Fromherz 1999]. For these small cells it is only possible to obtain data for the point contact model, namely the junction conductance g_j . Measurements for erythrocyte ghosts on poly-lysine approximately from the middle of the junction gave $g_j=130\pm 30\text{mS}/\text{cm}^2$ [Kießling 1999]. For the rat nerve cells on poly-lysine $g_j=700..2900\text{mS}/\text{cm}^2$ was found [Vassanelli 1997].

To infer the junction resistance r_j , the transition to the area contact model has to be performed with the correct value for the junction area A_{JM} and the transition parameter k_β . For the erythrocytes it was concluded with $k_\beta=5$ that the specific resistance of the junction ρ_j is enhanced by a factor of 4 as compared to the bulk electrolyte of $74\Omega\text{cm}$. The larger giant vesicle membranes could be measured precisely with a linear array of field-effect transistors with $r_j=100\text{G}\Omega$, a value which is increased by a factor of 40 relative to the value of $2.3\text{G}\Omega$ in Table 2.5.

The Chip

Design, Process, Characterization, Usage

3.1 Chip design

38

A chip was designed with a big spot area and a time constant well below the junction time constant of the cell. To be able to use high aperture water objectives, a backbonding technique was used.

3.2 Processing the chips

41

The processing of the chips is described. We contact the spot from the backside through pyramidal contacts through the silicon. Various doping steps lay the conductor path with a chrome layer at the end. The front side is oxidized to 1000nm except for the spot oxide of 10nm or 50nm.

3.3 Characterization of the chips

47

We characterized the junctions of the chip by measuring the frequency dependent resistance. This data was used to prove that the chip behaves as a low pass filter.

3.4 Usage of the chip

56

The chips are glued into a petri dish and are contacted with gilded contact springs. AgCl and Pt bath electrodes were used. The bath current is monitored and the bath is held at negative bias. Chips were cleaned with detergent inside the petri dish.

3.1 Chip design

A chip was designed with a big spot area and a time constant well below the junction time constant of the cell. To be able to use high aperture water objectives, a backbonding technique was used.

3.1.A Thin silicon oxide as stimulation capacitor

We discuss the physical properties of thin silicon oxide in contact to an electrolyte. When a silicon chip is isolated from an electrolyte with a thin film of silicon dioxide, it defines a capacitance as the thin film isolates two conductors. It can be easily calculated from

$$c_{ox} = \epsilon\epsilon_0/d = 0.34\mu\text{F}/\text{cm}^2 \quad (d=10\text{nm and } \epsilon_0=3.8) \quad [3.1]$$

But this is not the only capacitance. It is on top of silicon which shows a sheet of a surface depletion region which also behaves as a capacitance and below a double layer in the electrolyte. The latter is subdivided into an inner and a diffusive layer. If we take a highly doped silicon, both of them have a small effective thickness and thus a high specific capacitance. Therefore they can be neglected in the serial configuration. If we use low doped silicon, we get a by far lower capacitance from the depletion region in silicon - this was the error in the first test chip design (5.1.A on page 80). The 10nm silicon dioxide films made with a very similar process as used here by Fred Stett [Stett 1995] exhibited a resistance of $2.4e14\Omega\text{cm}$. The spot oxide does not degrade if a negative voltage to the electrolyte is applied.

3.1.B Possible future materials

The short junction time constant of around $2\mu\text{s}$ for rat neurons poses a big problem in the stimulation or detection of action potentials. We can envisage three strategies:

- We enhance the dielectric constant of the isolator:
This could be done by ferroelectric materials such as barium titanate. Although they are not easy to fabricate, they begin to be used not only for normal capacitances but also in memory chips to lower the refresh rate. Therefore it could be possible to use the processes developed there. The enhancement in τ_j will be proportional to $c_{ox}(1+\beta+\epsilon^{-1})$. Care has to be taken for the frequency dependent capacitance.
- We use the double layer of a metal electrode:
Metal electrodes have a very high specific capacitance of several $10\mu\text{F}/\text{cm}^2$. But much care has to be taken not to induce toxic electrochemical currents.
- We enhance the area of the isolator:
We can do this by etching grooves or dots in the silicon at the spot area. Let's consider a 10-fold increase in junction area with a checkerboard patten of height $1\mu\text{m}$ and a width $0.2\mu\text{m}$ made from electron beam lithography and anisotropic ion etching of silicon. We should consider two possibilities:

(a) the junction membrane follows the rough structure. We enhance the junction area A_{JM} (therefore τ_j by a factor of 10) and we will get a higher value of β (and reduce τ_j by about a factor of 2 depending on ϵ and β). It is not clear how far the cell will allow the enhancement of its membrane area.

(b) the structure is too small for the cell membrane to follow. Here the junction area stays the same, the specific capacitance of the spot oxide is enhanced (therefore we enhance τ_j by a factor of 4 depending on ϵ and β) and the junction thickness is higher (considering a normal junction thickness of 50nm we reduce r_j with a good serial structure by 10 and therefore reduce τ_j by the same factor). Therefore no positive effect is to be expected and a fine structure with low height would be better. But we could consider the effect of a low conducting spacer inside the grooves or different groove geometry.

We must always keep in mind that the chosen material must not be toxic to the cells as a further layer to protect the cells will either enhance the junction cleft thickness if it is a conductor or decrease the capacitance if it is an isolator. But a combination of the methods could be envisaged.

3.1.C Band pass filter of chip and junction

The serial resistance of chip and bath together with the capacitance of the spot does induce a low pass filter. But the junction of the cell is a high pass filter. They must overlap in combination to give a good coupling into the cell membrane. Or to put it in other words: the chip must be faster than the junction of the cell. The low pass filter characteristic of the chip is characterized with the time constant $\tau_C = R_{\text{serial}} C_{\text{spot}}$. The time constant can for example be decreased by a smaller spot size, a smaller serial resistance or a thicker oxide. Also a monolayer of cells can decrease the capacitance of the chip as seen e.g. in [Glaever 1995]. As the cells provide an additional overall serial capacitance they decrease the overall capacitance of stimulation spot and cells. This does not alter the capacitance under the cell as the voltage is readily distributed in the low resistive p++ silicon under the spot oxide.

If we connect the chip with the voltage V_{CHIP} we will get locally under the cell a stimulation voltage of V_S with the transfer function:

$$g_{\text{CHIP}}(w) = \frac{V_S}{V_{\text{CHIP}}} = \frac{1}{1 + iw\tau_C} \quad [3.2]$$

We saw in [2.59] of 2.5.A on page 27 that the junction of the cell is a high pass filter between the stimulation voltage at the oxide spot V_S towards the voltage in the junction membrane V_{JM} (and analogous to the voltage in the free membrane V_{FM}) with the time constant of the junction τ_j :

$$g_{\text{CELL}}(w) = \frac{V_{JM}}{V_S} = \frac{iw\tau_j g_{\infty}}{1 + iw\tau_j} \quad [3.3]$$

So the total transfer function starting from the chip voltage between bath electrode and chip to the junction voltage becomes:

$$g_{\text{COUPLING}} = \frac{V_{JM}}{V_{\text{CHIP}}} = g_{\text{CHIP}}(w)g_{\text{CELL}}(w) = \frac{iw\tau_j g_{\infty}}{(1 + iw\tau_C)(1 + iw\tau_j)} \quad [3.4]$$

We assume $\tau_j=2\mu\text{s}$ and $g^\infty=1$ and plot this transfer function in amplitude and phase for different chip time constants τ_C :

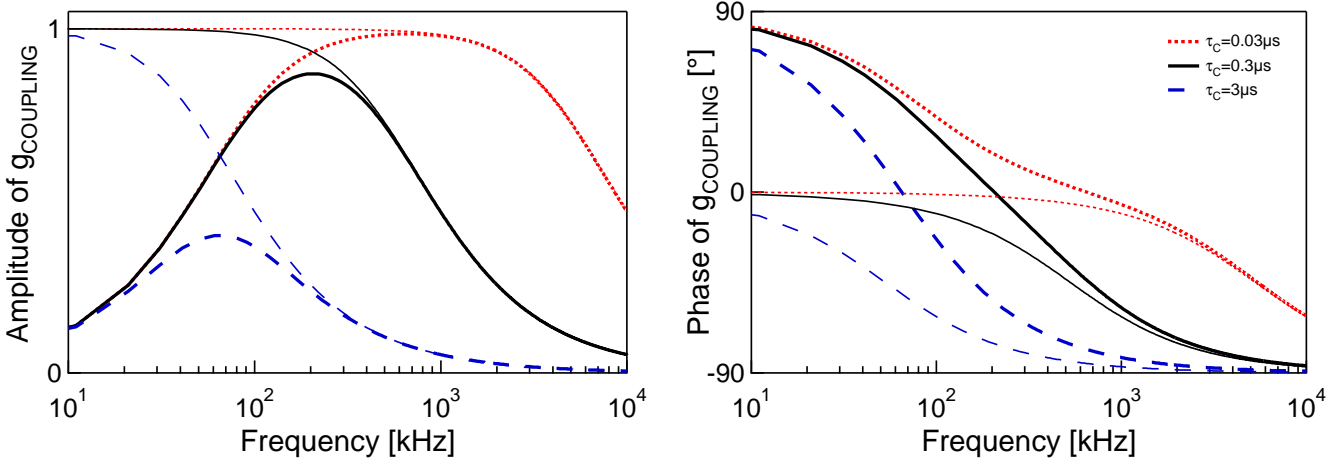


Fig 3.1 Transfer function g_{COUPLING} from chip voltage V_{CHIP} to membrane potential V_{JM} for a junction time constant $\tau_j=2\mu\text{s}$ and different chip time constants τ_C from 0.03..3 μs . Only for $\tau_C \ll \tau_j$ we can neglect the effect of the chip. Correction for the chip transfer function g_{CHIP} (drawn with thin lines) must be done in evaluating the experiments.

We see how a slow chip time constant diminishes the voltage signal in the cell membrane by imposing a right flank on the transfer function. We will correct all measurements for this low pass filtering characteristic of the chip which has a time constant of typically 0.3 μs . Starting from a simulation of the whole chip we will prove later that the chip actually behaved like a low pass (paragraph 3.3.H on page 53).

3.1.D Chip design

We maximize the spot size and keep the chip faster than the junction time constant of the cell. We tried a backbonded design for the following reasons: First we wanted to test for a transparent chip. The cleaning procedure was hoped to improve with backbonding, but the spot membranes were quite vulnerable. The chip should have a small time constant although the bath electrolyte together with the huge objective posed the limiting factor, not the chip. Finally with the backbonded design it was possible to use the high transmission, high aperture water objective.

The main design difference between the chip in this work and to the chip design in [Stett 1995], [Fromherz 1995a] chip design was the insight that, especially in the case when we have no impaling electrodes, the stimulation spot can be much larger than the cell. Therefore the probability to find a nice cell on a spot was enhanced by some orders of magnitude as the cells used could not be positioned. The chip time constant as indicated in the paragraph before is the main design goal. The chip surface is subdivided into a spot area (A_S ; $c_S=0.34\mu\text{F}/\text{cm}^2$; 10nm) with high capacitance and a field area (A_F ; $c_F=0.0034\mu\text{F}/\text{cm}^2$; 1000nm) with low capacitance. Both capacitances add up and with a given serial resistance R_{serial} the design goal is to optimize the areas A_S and A_F to be below a time limit τ_{limit} determined by the coupling time constant of the cell:

$$R_{\text{serial}}(A_S c_S + A_F c_F) \leq \tau_{\text{limit}} \quad [3.5]$$

We used as estimates $R_{\text{serial}}=300\Omega$, $A_S=560\times 560\mu\text{m}^2$ and $A=600\times 600\mu\text{m}^2$. Therefore we get a chip time constant of $t_{\text{limit}}=0.32\mu\text{s}$.

A parallel stray capacitance of the field oxide between the bath and the conductor path was avoided since the whole conductor path was on the back side of the chip. The thin silicon membrane under the spot acted as a mirror for fluorescence interference. The hope that it could be transparent as estimated from visual inspection of formerly created membranes was not fulfilled. This would have increased the fluorescence intensity, but was neither predicted by theory nor later confirmed by inspection of the fluorescence at oxide steps at the edge of the stimulation spot.

Starting from the optimized spot area of $560\times 560\mu\text{m}^2$ we had to find the best number of spots on a chip. From the chip design of [Dertinger 1998] it was known that the silicon membranes were not too stable and could break when cleaning the chips - which was also the case with our chips. As we did not yet know that a broken membrane can be readily filled with silicone glue, we tried to find a minimum number of spots per chip. Moreover since the staining of the cells should not last too long and can only applied to all the cells on a chip at once, the number of spots per chip should not be too large. A number of 6 spots was chosen. One must keep in mind that the pyramids of the backbonding design need at least $800\times 800\mu\text{m}^2$ and must be aligned to the silicon crystal structure. We wanted to have a small chip in order to obtain many chips from one wafer as it was clear that the process had many risks. At the end of the first and only process charge there was only one error free wafer left - starting from 10. But 44 chips could be cut from this wafer. One further boundary condition of chip size was the rather huge objective. Therefore a side length of $12\times 12\text{mm}^2$ was reasonable. Since the spots should be placed more to the middle of the chip and as the pyramids should have a minimum distance to be more stable we chose the setup depicted in Fig 3.2.

Future chip designs should include the possibility of a much more simple chip design: we can just oxidize a p++ wafer with 10 or 50nm spot oxide and 1000nm field oxide at the front side. The whole backside can be covered with a chrome layer. We need a further thick structuring of the field oxide to minimize the chip capacitance to get a small time constant. This could be achieved for example by sticking a sheet of flexiperm (In Vitro Systems) with small holes on the front side of the chip.

3.2 Processing the chips

The processing of the chips is described. We contact the spot from the backside through pyramidal contacts through the silicon. Various doping steps lay the conductor path with a chrome layer at the end. The front side is oxidized to 1000nm except for the spot oxide of 10nm or 50nm.

The chips used in this work were produced by myself in the clean room of the department. I have done the work together with Christian Figger who began with his diploma thesis as the chip design could also be used for his experiments on Retzius cells. We will go through the different steps of the process. A description of the same process is given in [Figger 1999].

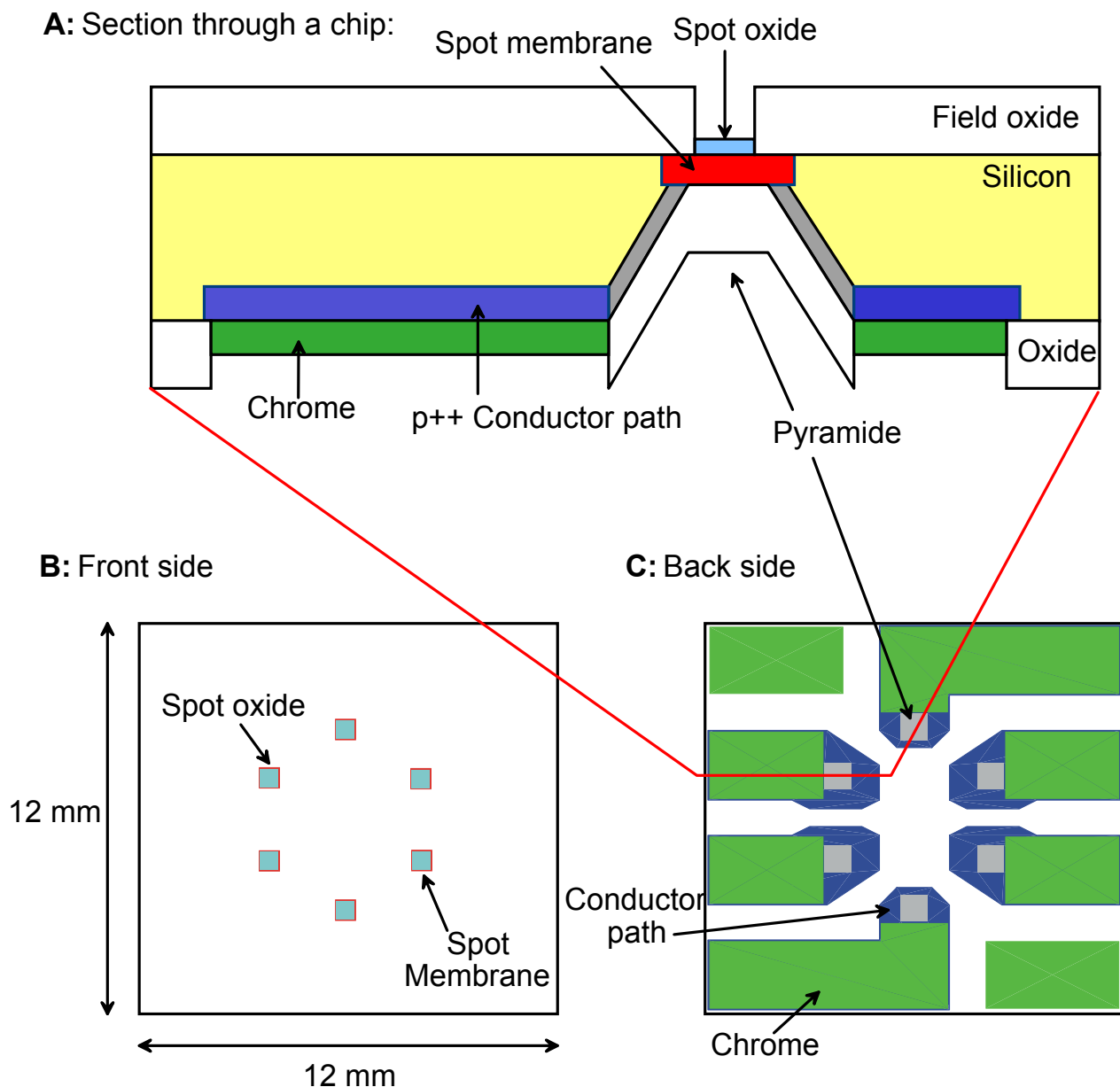


Fig 3.2 Layout of the chip. In A we see a section through a pyramid of a stimulation spot. The current goes from chrome to the p++ conductor path inside the pyramid to the spot oxide. B shows the front side of the chip, C the back side.

3.2.A Cleaning procedures

At various stages of the process we need to clean the wafers. The CARO cleaning is the first step of the RCA-cleaning procedure, often also used as a single cleaning step. CARO cleaning is done in 3750ml 96% H_2SO_4 and 1250ml 31% H_2O_2 . The solution heats up after some seconds and we put the wafers within a teflon holder into the solution. After 10min they were rinsed in millipore water (Quickdump, AST). If we want to continue the RCA cleaning, we prepare RCA1 with 3570ml Millipore water and 720ml 25% ammonia heated to 75°. After pouring 720ml 31% H_2O_2 to the bath and waiting for half a minute the solution bubbles. The wafers are kept in the solution for 10min. Then they were rinsed in Millipore water (Quickdump), put for 15s in 5% unbuffered

HF to remove natural oxide and rinsed again. The HF dip can be also omitted. The RCA2 solution is prepared from 3750ml millipore water, 625ml 37% HCl and also heated to 75°. We then give 625ml H₂O₂ to the solution, wait for bubbling and put the wafers in it for 10min. They were then rinsed in millipore water (Quickdump). At the end the wafers were spun dry under nitrogen. For the double sided wafers it is important to first dry the area where the spin dryer holds the wafer, otherwise we contaminate the wafers.

3.2.B Photolithography

Basis for all structuring processes is the photolithography step. The wafers have to be cleaned by CARO before the lithography. Heating the wafers to 600° in nitrogen environment afterwards increases the sticking of the resist - alternatively we can use 30s of HMDS treatment which is less effective. We used a negative photoresist (1215, micro resist technology) which we spun on the wafers to get a thickness of 1.2µm. We used a special small holder to minimize contamination on the second side of the wafers as it was often necessary to coat the wafer on both sides. The resist is hardened for 30min at 90°. The illumination of the resist was done in a mask aligner (Karl Suss, Martinsried) for 16s at 436nm with an intensity of 21mW/cm². We used 5inch masks (ML&C, Erfurt) made of boron silicate glass structured with chrome-gold. Positioning was achieved at alignment markers between the chips. This area is cut away at the end of the process. The alignment between front and backside of the wafer was accomplished with the special backside alignment mode of the mask aligner and with latent images inside the photoresist only from the illumination of the resist at the front side. The resist is developed for 2 minutes in 750ml AZ Developer (Hoechst) and 4250ml millipore water. The resist can be removed afterwards with CARO cleaning or by rinsing in acetone.

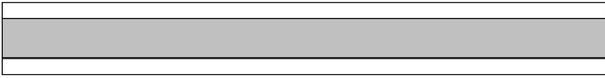
3.2.C Doping the stimulation spot and conductor path

We used 4 inch wafers, polished on both sides (Sico Wafer GmbH, Meiningen). Thickness was specified with 450±15µm, slightly n-doped with phosphor to 2-4Ωcm and with a surface orientation of <100>.

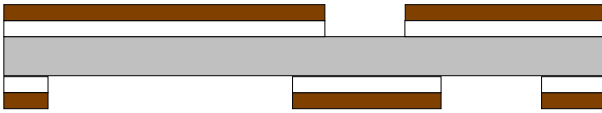
First we dope the stimulation spots on the front side and simultaneously on the backside the conductor paths. The steps of the process are illustrated on the left side of Fig 3.3. The doping of the stimulation spots is not only needed for conductivity to the spot, but also to get a high capacitance of the stimulation spot oxide (thin band bending). Third it is an etch stop for the silicon etching with EDP from the backside. For structured doping we need to mask silicon dioxide as the following doping is diffusing much faster in silicon than in silicon dioxide: 300nm is enough to stand 5h doping with boron at 1100°. We cleaned the wafers with the RCA procedure and made 1000nm oxide by wet oxidation for 5h at 1000°C (Centrotherm, Blaubeuren). The oxide thickness was tested with the ellipsometer (Plasmos). After photolithography we etched away the oxide at the stimulation spot squares on the front side and at the conductor paths on the backside. We removed the oxide with 20minutes of wet etching in 12.5% buffered HF to get the hydrophobic surface of silicon. It was important to fully wet the surface with millipore before, otherwise air bubbles prevent the whole surface from being etched in the HF bath. We removed the resist with CARO cleaning and made a RCA cleaning to prepare for the doping. The boron

Doping spot and conductor path

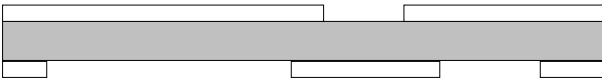
1. Growth of oxide



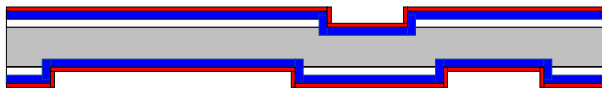
2. Photolithography and oxide etch



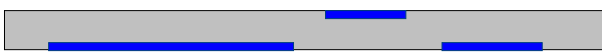
3. Remove photo resist



4. Doping by boron diffusion



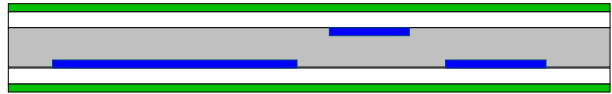
5. Removing all layers



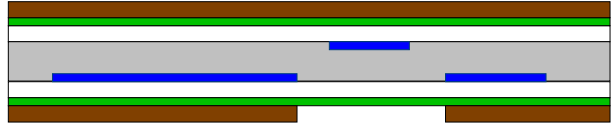
■ Silicon □ Silicon dioxide ■ p++ Silicon ■ Photoresist ■ Nitride ■ boron glass

Etch pyramids with EDP

1. Grow oxide and nitride



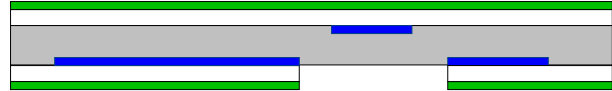
2. Photolithography



3. Etch oxide and nitride



4. Remove resist



5. Etch pyramids in EDP

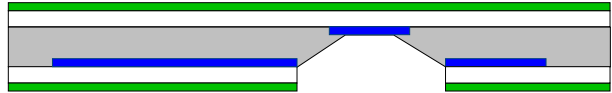


Fig 3.3 Process steps for the doping of both chip sides (left) and for EDP etching of the pyramids (right).

plates must be slowly heated to get dehydrated and are afterwards activated at 900° under oxygen for 30minutes. We put the silicon wafers next to the plates at a distance of 2-4mm with the same distance from both sides. After 40minutes at 900° some 100nm boron glass is transferred to the wafers. We remove the boron plates and heat under nitrogen to 1100° for 5h. This results in about $6\mu\text{m}$ p++ doped silicon as measured with decoration solutions in [Braun 1995]. The silicon oxide is etched away for 40minutes in unbuffered 5% HF. The remaining skin of boron silicon must be removed by 15 minutes of oxidation - after cleaning the wafers with the RCA procedure. With 5minutes of unbuffered 5% HF the wafer is now again hydrophobic.

3.2.D Etching and doping the backbonding pyramids

The etch stop at the front side is now prepared and we are ready to begin with the EDP etching to get pyramids from the backside to the stimulation spot. The process steps around EDP etching can be seen in the right side of Fig 3.3. The surface was first masked with 560nm wet etched oxide. This oxide must also mask a doping process after the EDP etching and was held as thin as possible for not to waste material from the etch stop. Then we put on both wafer sides a nitride layer on the oxide by a CVD-process: for 6minutes at 1Torr, 20W plasma, 1000sccm SiH_4 and 20sccm NH_3 to get 120nm nitride. This was tempered afterwards at 1000° for 1h. The thickness

was thus reduced to 90nm as measured with ellipsometry and adapted refractive indices. In contrast to silicon dioxide the nitride is etched by the EDP only with 2nm/h. We masked the wafer with photoresist and etched on the backside the 760µm squares in the following plasma etch step: 2minutes at 0.5Torr, 50W and 30sccm O₂ to remove rests of the photoresist, then 6minutes at 0.03Torr, 100W, 24sccm CHF₃ and 25sccm O₂ to etch the nitride (and 70nm of oxide below), then 3minutes of the oxide plasma as described above to get rid of a teflon-like skin probably coming from the photoresist. After 500s in 12.5% buffered HF we were back again on the hydrophobic silicon. We removed the photoresist by a CARO cleaning step.

The EDP-S solution consists of 6l ethylene diamine, 790ml millipore water, 960g brenzkatechin and 36g pyracine heated to 95°. This solution has different etching rates in the different crystal directions: only 0.7µm/h along <111>, but 350µm/h along <100> and 400µm/h along <110>. From an flat-aligned square field on the <100> wafer we expect to etch pyramid walls with 54.7° angle to the wafer surface. We begin with a side length of 760µm to obtain with under etching of 19µm a final side length at the front side of the pyramid of 150µm. Due to leakage of the EDP-basin we had changing concentrations in the solution and got a different angle of etching and thus a much bigger side length of around 450µm at the front side. EDP etching needed 10h45min, we had to test the wafers often not to etch through the etch stop as this only slows down the etching rate to 25%. We lost 3 of the 10 wafers in a first etching attempt as the etching rate was much higher as expected. Also the under etching was with 65µm very high and the pyramid angle was 58.2°. After the EDP etching we removed the nitride layer on both sides of the layer with 30minutes of 85% phosphor acid at 160°.

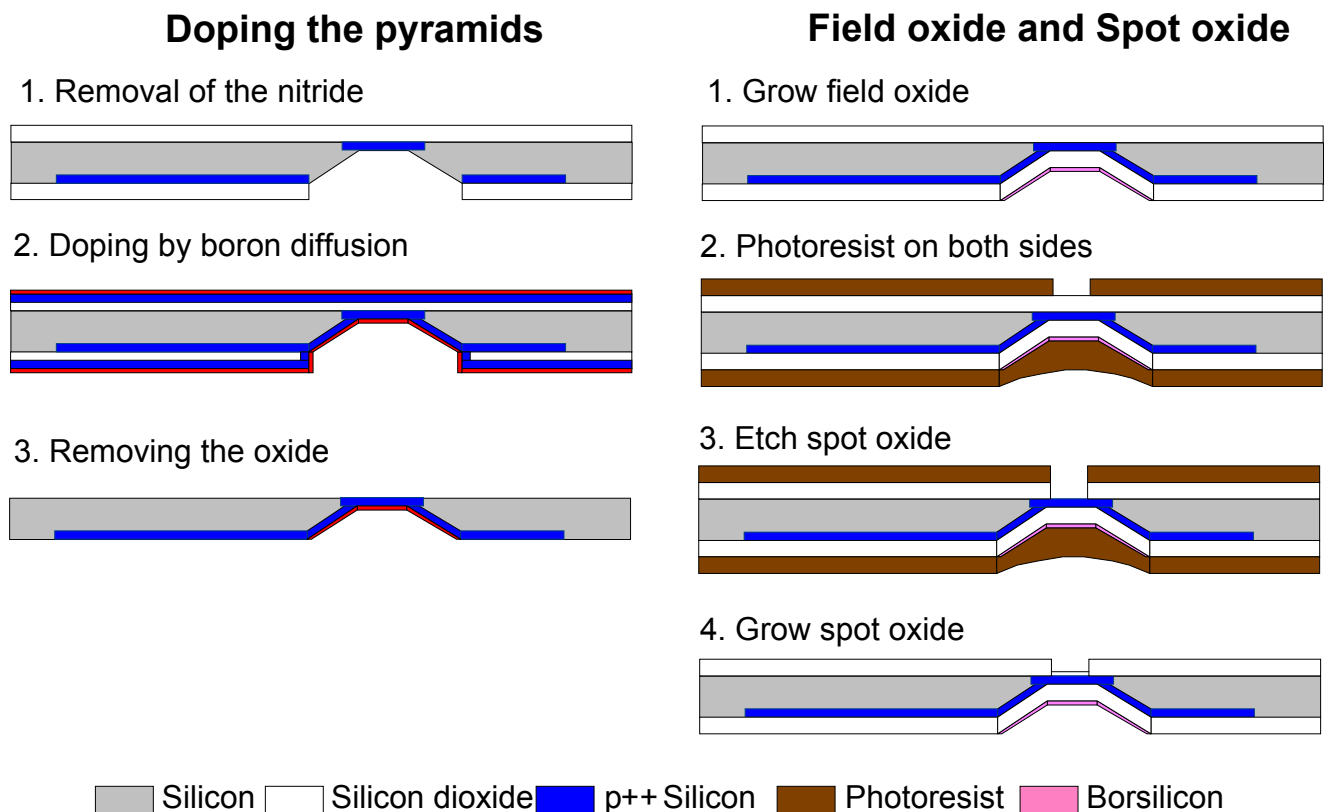


Fig 3.4 Process steps for the doping of the pyramid walls (left) and the growth of field and spot oxide (right).

To connect the conductor paths of the backside with the stimulation spot on the front we doped the walls of the pyramids. The process steps are depicted in Fig 3.4. We only had to dope as the oxide on the back side still provided a doping mask. The doping process was the same as before, but we did not remove the boron silicon as this is done by subsequent oxidation steps on the back side - the front side was not doped. Therefore after removing the silicon dioxide in 12.5% buffered HF in 10minutes the wafer was hydrophilic on the front side but hydrophobic inside the pyramids. We did not want to use the probably low quality mask oxide of the doping process as a field oxide on the front side.

3.2.E Oxidation of the stimulation spot and the chip

The thick field and the thin spot oxide are processed as displayed on the right side of Fig 3.4. First the field oxide is made in a wet oxidation process for 5h30min at 1000° to get 1070nm oxide. We then etch the field oxide down at the stimulation spots on the front side with wet etching in 12.5% buffered HF in 15min. After removal of the resist and a RCA cleaning procedure we are ready to oxidize the spot oxide: after 13s at 1150° in a rapid thermal processing oven (AST, Ulm) we get an average oxide thickness of 9nm. To get 50nm oxide this process was prolonged to 145s and used twice.

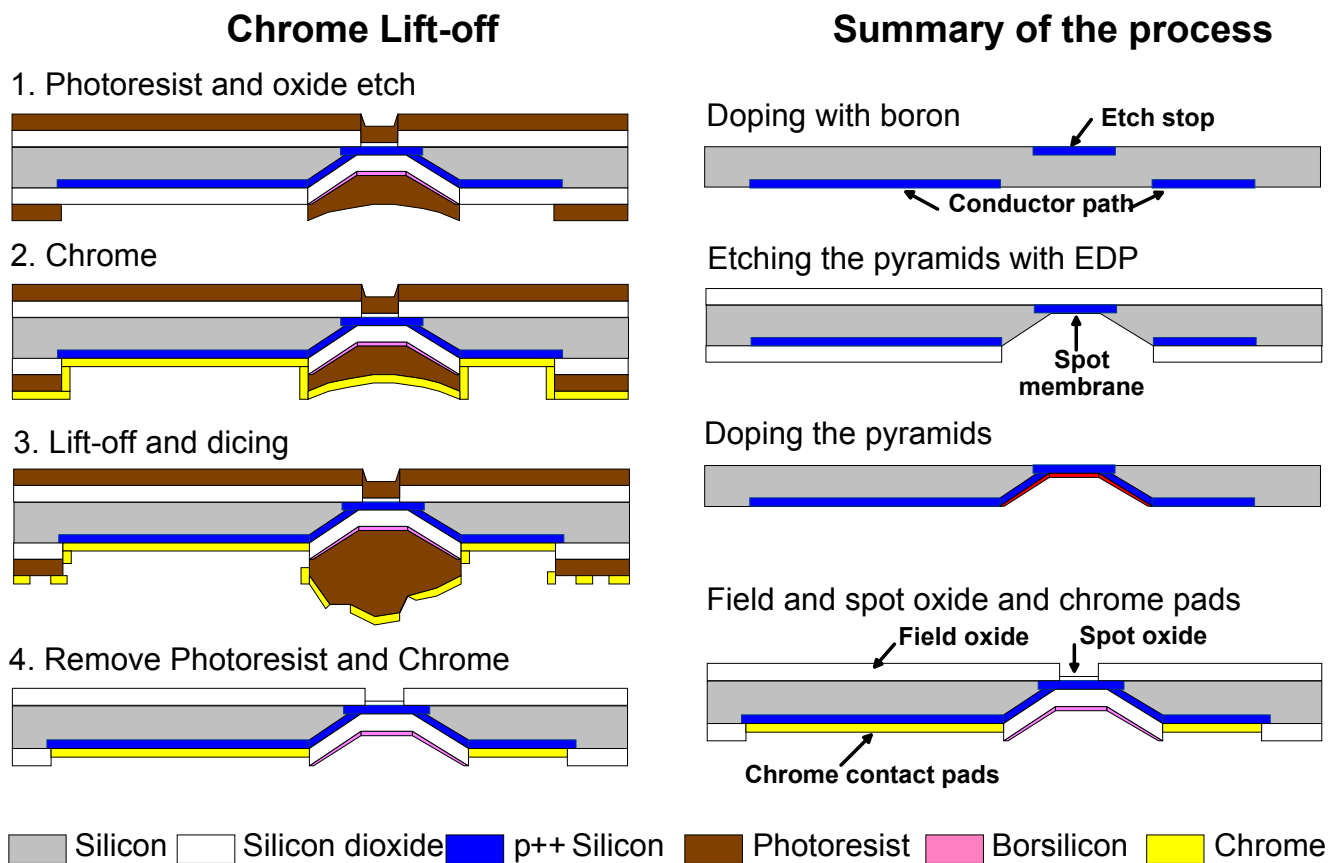


Fig 3.5 Process steps for the lift-off of the backside chrome contact pads (left). Summary of the process is depicted on the right.

3.2.F Deposition of chrome and the dicing of the wafer

In order to deposit at the ends of the conductor paths a chrome pad we again have to coat both sides of the wafer with photoresist. The field oxide on the contact pads is removed by wet etching in 12.5% buffered HF after photolithography. Directly after etching and drying we put the wafers into the vacuum chamber (Univex 450, Leybold) to grow 200nm chrome on the whole wafer. The lift-off was induced by 60min at 120°. But before actually performing the lift-off the wafer was cut into the chips. The photoresist could prevent the thin silicon membrane at the stimulation spot from braking. The wafer had to be placed with the back (chrome) side on the cutting film, otherwise the membranes broke. The resist with the chrome was removed in acetone. A further CARO cleaning process removed further chrome shivers. Pictures of the process can be seen on the left side of Fig 3.5 with an overview over the whole process on the right side. Finally we get the following chip:

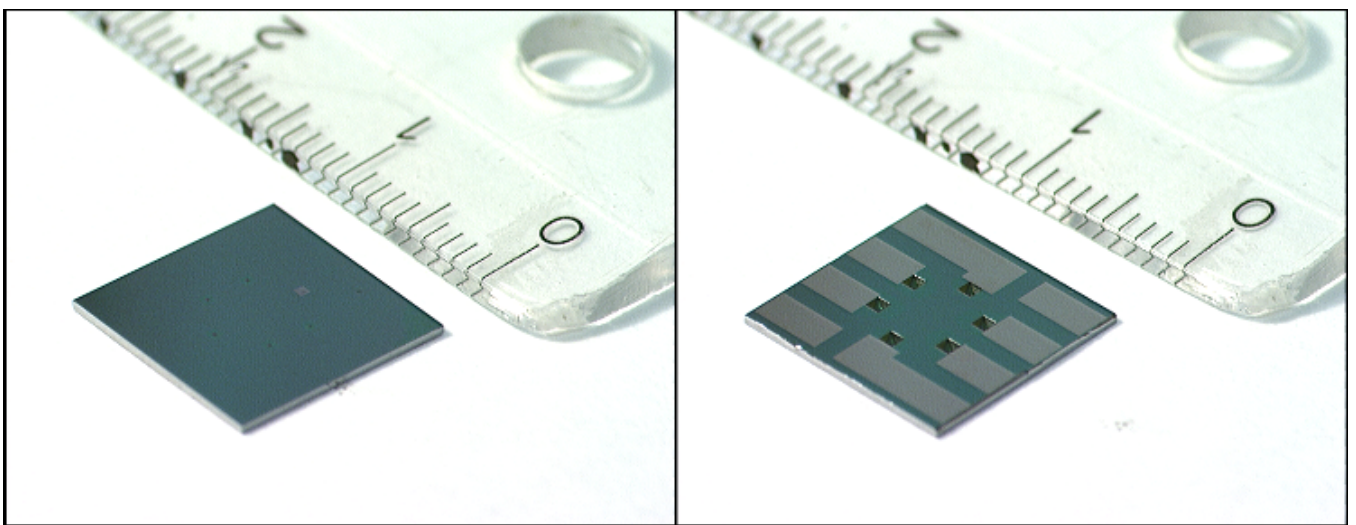


Fig 3.6 Photographs of the final chip from the front side (left) and the back side (right). On the back side we can see the chrome contact pads which lead to the backbonding pyramids. At the front side of the 6 pyramids are the 6 silicon membranes each with one stimulation

3.3 Characterization of the chips

We characterized the junctions of the chip by measuring the frequency dependent resistance. This data was used to prove that the chip behaves as a low pass filter.

3.3.A Measuring chip parameters with Lock-In amplifier

From frequency dependent resistance between different chip contacts we can resolve and check the electrical parameters of the chip. We used a Lock-In amplifier to measure the resistance and the capacitance of various contacts inside the chip: the bulk contact, the pn-junction between a spot conductance path and the bulk, the spot capacitance and the bath electrode.

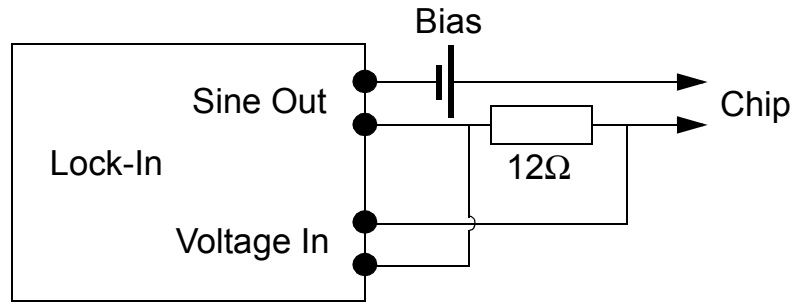


Fig 3.7 Circuitry to measure chip characteristics with a Lock-In amplifier.

We modulated the voltage with the Lock-In by 50mV, added a bias voltage if needed and contacted with this AC/DC combination the chip. The current was measured from the voltage over a 12Ω resistance as the Lock-In amplifier was too sensitive in current measurement mode. The 12Ω did not pose a problem as all fitted resistances were much higher (Fig 3.7). The resulting currents were converted to a frequency dependent complex valued resistance or conductance.

3.3.B capacitance and resistance of a bulk contact

The contact of a single bulk contact can only be measured if we get the characteristic between two bulk contacts. We assume the following circuit and find from the fit:

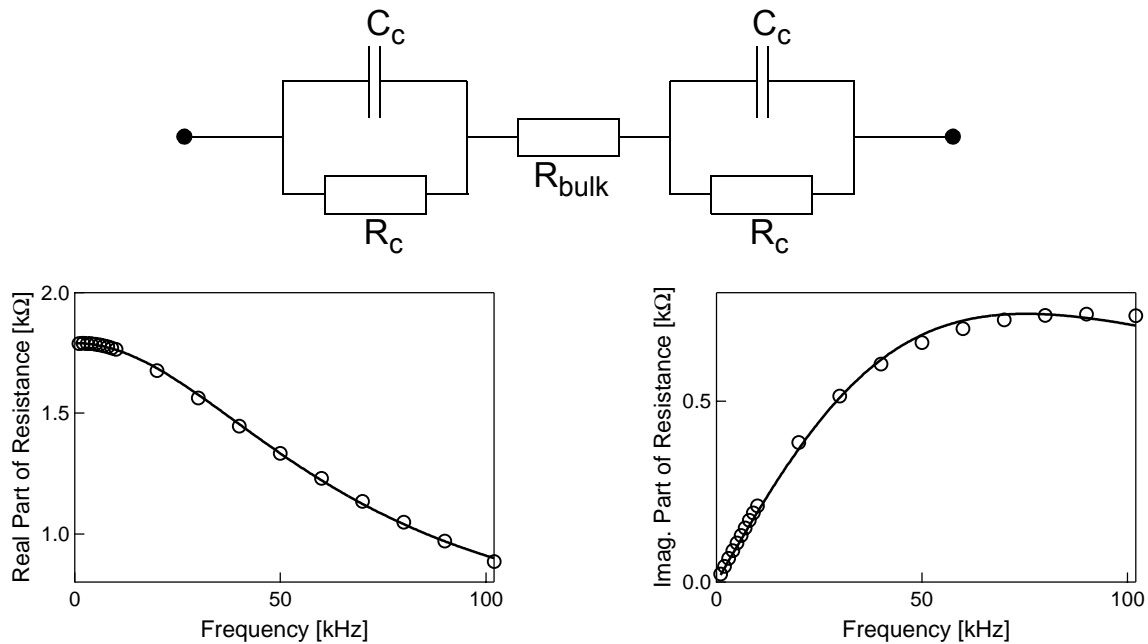


Fig 3.8 Measured impedance versus frequency between the two bulk pads. Real and imaginary part are plotted independently, fitted with $R_C=740\Omega$, $C_C=2.8\text{nF}$, $R_{\text{Bulk}}=400\Omega$

The bulk resistance of 400Ω can be inferred from geometry and a wafer resistance of $2\text{-}4\Omega\text{cm}$. Therefore we see that the contact from low doped n-Si to chrome is not ohmic but behaves similar to a pn-diode as predicted from the literature [Hilleringmann 1996]. We will see later that this property does not harm the chip function.

3.3.C *pn-Junctions between spot and spot*

The pn-junction between bulk and spot is important to isolate different spots from each other and to isolate the stimulated spot from the bulk. We took two neighboring spots and assumed the following circuit in Fig 3.9. It assumes that we have an ohmic contact from chrome to p++ doped silicon as reported in the literature [Hilleringmann 1996] - this we tested also with a bonded version of the chip which showed the same characteristic. Although the junction is not biased we get a high resistance from a single junction of around 830k Ω . The bulk resistance of 120 Ω can be understood with geometry and wafer resistance of 2-4 Ω cm.

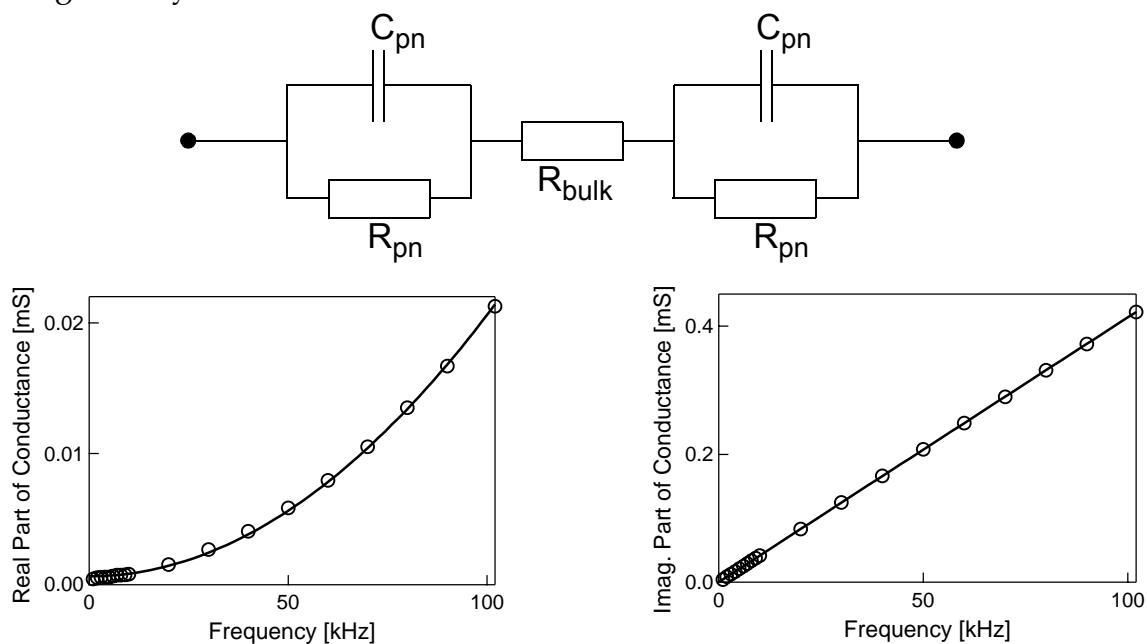


Fig 3.9 Measured complex conductance versus frequency between two neighboring spot pads. Real and imaginary part are plotted independently, fitted with $R_{pn}=830k\Omega$, $C_{pn}=1.32nF$, $R_{Bulk}=120\Omega$

3.3.D *pn-Junction between bulk and spot*

We confirm the previous measurements by measuring between the bulk contact and a neighboring spot contact (Fig 3.10). We cannot fit both values and have to assume the values of the bulk contact of $R_C=740\Omega$, $C_C=2.8nF$. Also we have to assume the resistance of the pn-junction $R_p=830k\Omega$. We then get a further bulk resistance $R_{bulk}=240\Omega$ and the capacitance of the pn-junction $C_p=1.3nF$. The last value nicely confirms the previous measurement with $C_p=1.32nF$.

If we reverse the bias of the pn-junction we get a reduced junction capacitance as the depletion region has broadened. We perform the same measurement as before but now with 5V bias voltage and get a higher junction resistance of $R_p=8M\Omega$ and a lower capacitance of $C_p=0.55nF$. We see that without bias voltage the characteristic does not change very much.

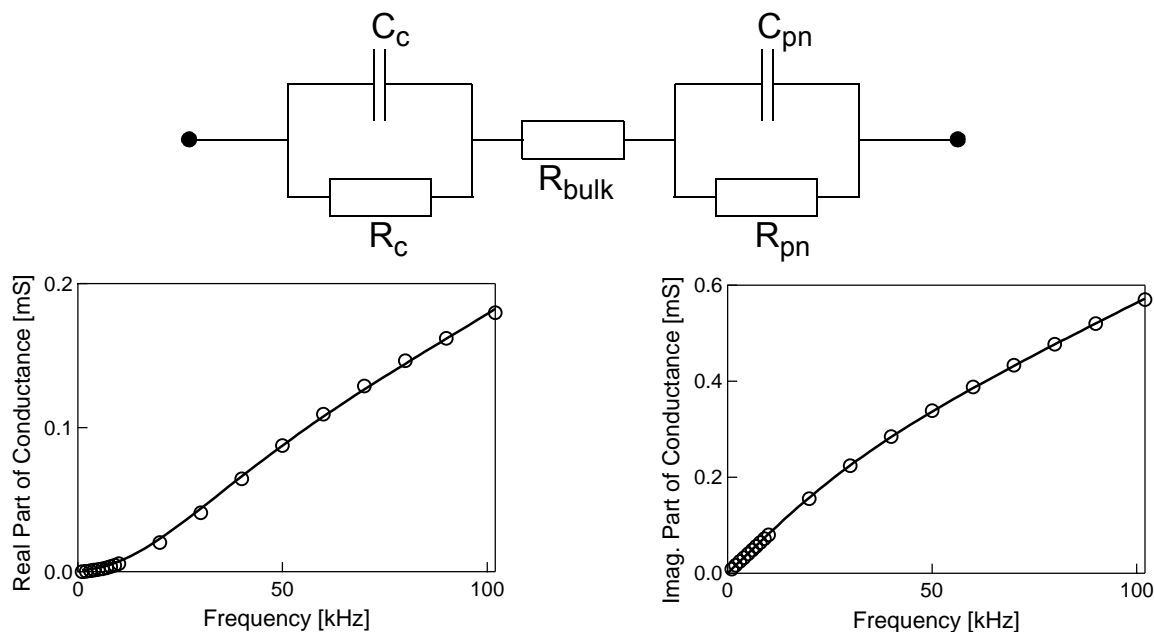


Fig 3.10 Measured complex conductance versus frequency between a bulk contact and the neighboring spot contact. From the values of bulk contact $R_C=740\Omega$, $C_C=2.8\text{nF}$ and $R_{pn}=830\text{k}\Omega$ from the pn junction we fitted a bulk resistance $R_{bulk}=240\Omega$ and the capacitance of the pn-junction $C_{pn}=1.3\text{nF}$.

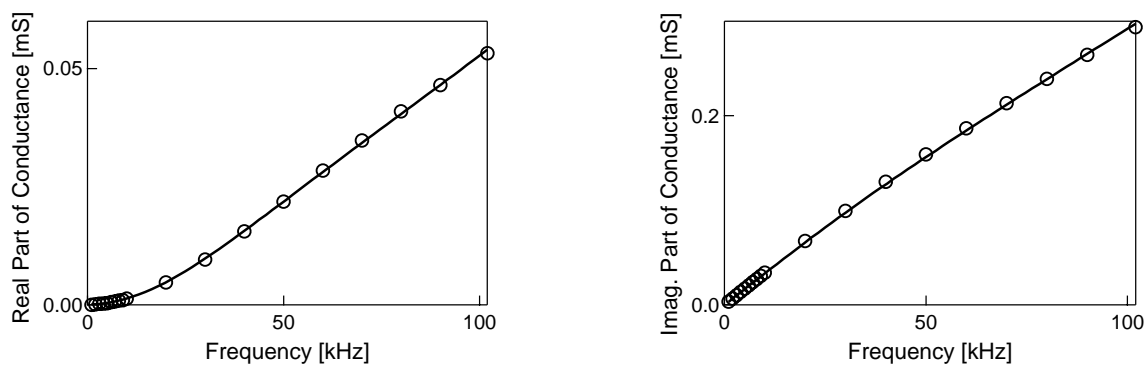


Fig 3.11 Measured complex conductance versus frequency between a bulk contact and the neighboring spot contact under reverse bias of 5V. From the values of bulk contact $R_C=740\Omega$ and $C_C=2.8\text{nF}$ and $R_{bulk}=240\Omega$ we fitted the resistance $R_{pnb}=8\text{M}\Omega$ and the capacitance $C_{pnb}=0.55\text{nF}$ of the pn-junction.

3.3.E Bath electrode

The resistance of both AgCl and Pt electrodes with unbiased small signal voltage showed a very similar characteristic. The capacitive part of the impedance could only be fitted poorly with a simple circuit (Fig 3.12). I switched from AgCl electrodes to Pt electrodes as these ensured a true sinusoidal current for reasons not fully understood. The currents achieved with a Pt electrode was most often perfectly sinusoidal. The geometry of the Pt electrode is further described in Fig 3.22 on page 57. We assume from geometry a 50fold higher surface of this bath electrode as compared to the short wires used in the experiments above. Therefore we will assume $C_{Pt}=3300\text{nF}$,

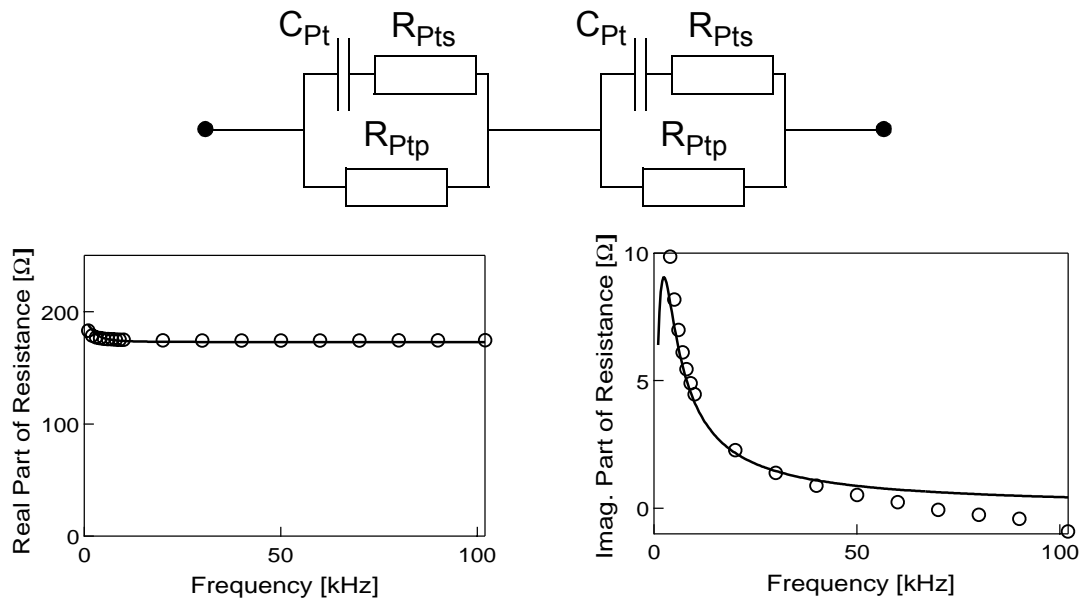


Fig 3.12 Frequency dependent impedance of a neighboring pair of Pt wires (AgCl wires show a very similar characteristic) in TRIS buffer. We see a rather constant real part of the resistance and a decreasing, capacitive imaginary resistance. The measurements could only be fitted poorly with $C_{Pt}=66\text{nF}$, $R_{Pts}=900\Omega$, $R_{Ptp}=95\Omega$

$R_{Pts}=18\Omega$, $R_{Ptp}=1.9\Omega$. We will see later that we can neglect the effects of the bath electrode in the overall circuit. The metal electrodes have a high specific capacitance. Together with the high area with respect to the spot oxide no voltage loss from a capacitive voltage divider has to be expected. AgCl electrodes were prepared from 0.25mm Ag wire, put unto 0.1mM KCl with +1.4V potential against a Pt-electrode for about half an hour to get a grey-brown color. Electrodes were washed with millipore water after usage and held dry in clean conditions.

3.3.F Influence of bath electrolyte and objective

We must deal with further serial resistances in the bath electrolyte mostly induced by the small working distance of the objective. The cell culture media or the PBS solution used for the ghost measurements has a bulk resistance of $74\Omega\text{cm}$ as measured with a resistance meter (WTW LF 96A, Weilheim). The theory of point contact model can be used to find the resistance from the circular Pt electrode to the middle of the petri dish. With an bath height of 2mm we have a sheet resistance of the bath of $r_j=370\Omega$. We use the equation [2.61] on page 28 and a value of $k_\beta=5$ as we are more interested in the phase of the voltage in the low frequency domain as plotted in Fig 2.14 on page 31. We find an equivalence resistance of $R_j=20\Omega$ with

$$R_j = \frac{r_j}{5\pi} \quad [3.6]$$

But the geometry of the microscope objective must not be neglected (Fig 3.13). First it reduces the thickness of the electrolyte in its periphery. This is the reason why we will estimate the bath resistance to $R_{peri}=80\Omega$. But it has a very low working distance of $260\mu\text{m}$ at a big central circular area of 6mm in diameter. Therefore it splits the field oxide of the chip into the field oxide under the objective $C_{F1}=1.0\text{nF}$ and a remaining $C_{F2}=2.4\text{nF}$. For the circular thin sheet we find with [3.6] a

serial resistance of $R_{obj}=180\Omega$. Thus we estimate a bath resistance of $R_{bath}=260\Omega$ and get with the spot capacitance C_S a time constant of the chip of $0.29\mu s$ of 10nm oxide and $0.06\mu s$ for 50nm. We have to note that the small sheet under the objective enhances the current from the spot over the field oxide under the objective (C_{F1}) with a rather low resistance which we estimate to $R_{toField}=50\Omega$. Although this path is not too important it adds another time constant to the system.

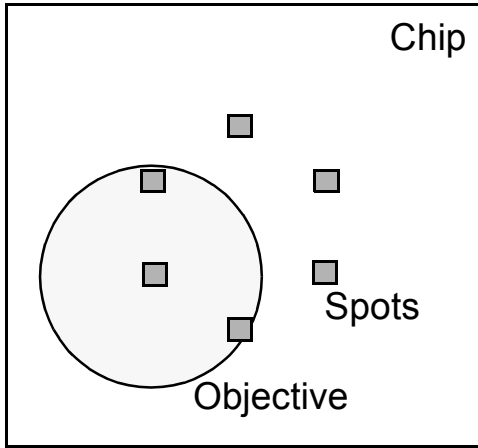


Fig 3.13 The objective imposes a flat sheet of electrolyte above the spot and the chip. This induces a high bath resistance and can provoke a current path through the field oxide, the bulk via the pn-junctions to the other spot conductor paths to ground.

3.3.G Summary of the chip data

TABLE 3.1 Summary of the chip data

	Value	Area	Specific value
Unbiased chrome-n bulk contact resistance R_C	740Ω	$8e-6m^2$	$60\Omega cm^2$
and its capacitance C_C	$2.8nF$	-- " --	$35nF/cm^2$
Unbiased pn-junction between spot conductance path and bulk R_{pn}	$830k\Omega$	$9.2e-6m^2$	$76k\Omega cm^2$
and its capacitance C_{pn}	$1,32nF$	-- " --	$14nF/cm^2$
Reverse biased pn-junction between spot conductor path and bulk R_{pnb}	$8M\Omega$	-- " --	$740k\Omega cm^2$
and its capacitance C_{pnb}	$0.55nF$	-- " --	$6nF/cm^2$
Spot capacitance for 10nm oxide C_S	$1.1nF$	$3.1e-7m^2$	$0.34\mu F/cm^2$
Field capacitances (1: under objective 2:rest)	$C_{F1}=1.0nF$ $C_{F2}=2.4nF$		
Chip bulk resistance	$R_{bulk}=120-400\Omega$ (dep. on geometry)		
Pt or AgCl bath electrode	$C_{Pt}=3300nF$	$R_{Pts}=18\Omega$	$R_{Ptp}=1.9\Omega$
Bath resistances ($\rho=74\Omega cm$)	$R_{peri}=80\Omega$	$R_{obj}=180\Omega$	$R_{toField}=50\Omega$

3.3.H Low pass filter characteristic of the chip

We will demonstrate that within a good approximation the chip is a low pass filter of order 1. The chip data gained so far are given in Table 3.1. We now put the parts together to obtain the most precise equivalence circuit of the chip (Fig 3.14).

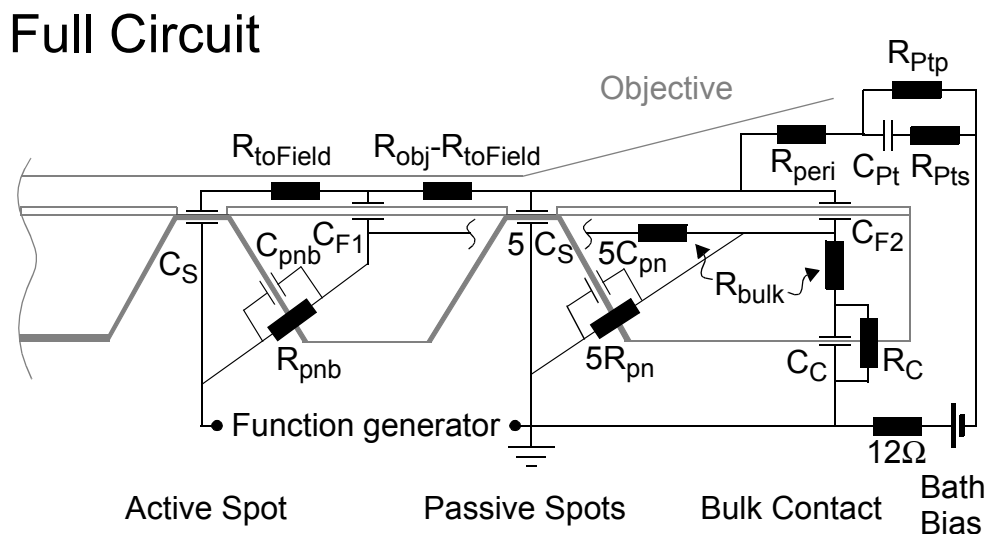


Fig 3.14 Full circuit of the chip. We consider the active and passive spot capacitances, pn-junctions of the conductor paths, the junction of the bulk contact, bulk resistance of the chip, bath resistance and field oxide under the objective, field oxide of the whole chip and in the whole petri dish, the bath electrode and the 12Ω current measurement resistance.

To gain more insight, we will simplify the model down to three, two and one time constant, the last being a very simple low pass filter of order 1. Numerical simulations for all of these approximations are given later in Fig 3.18 and Fig 3.19. We remove all elements which show no effect on the transfer function characteristic. We neglect the bulk contact since it cannot make a short circuit of the bulk to ground and the bath electrode as it has a too high resistance. We remove the pn-junction to the active spot conductor path and the resistance of the pn-junction of the passive spots. Also the field oxide of the whole chip has a rather small effect. We thus obtain a circuit with three time constants as shown in Fig 3.15. Furthermore we also remove the current through the field oxide under the objective and get a circuit with only two time constants. The transfer function simulation (Fig 3.18) shows that the capacitive bath electrode through the nonstimulating spots is very important. The resulting circuit is presented in Fig 3.16. The strongest approximation is to use only the stimulating spot oxide together with the bath resistances. There is only one time constant being a low pass filter of order 1. Its time constant can be gained from $\tau_C=(R_{peri}+R_{obj})C_S=0.29\mu s$ and the circuit is presented in Fig 3.17.

3 time constants

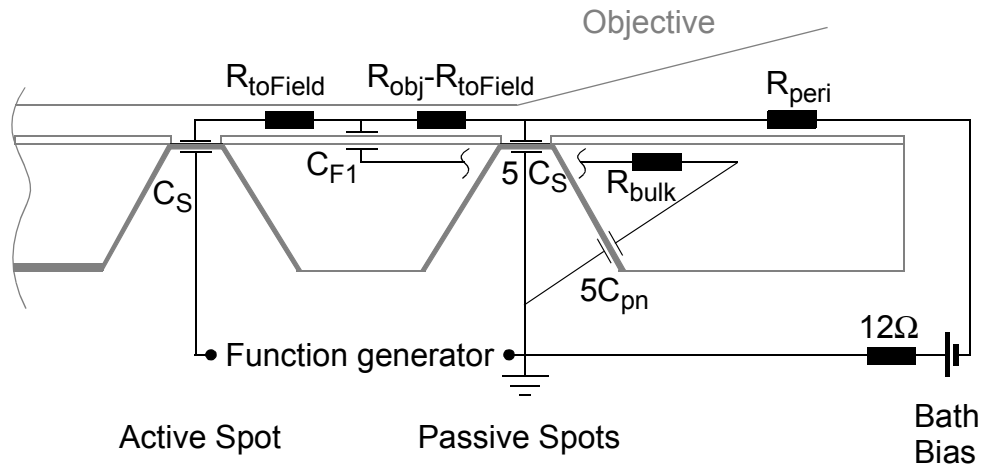


Fig 3.15 A first approximation to the chip with 3 time constants. The bulk contact, the pn-junction of the active spot and the bath electrode have been removed.

2 time constants

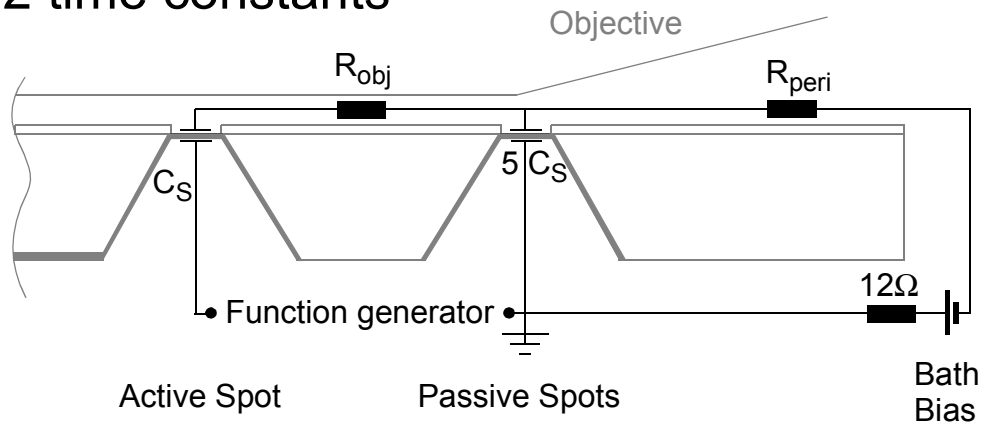


Fig 3.16 We further remove the current through the field oxide under the objective and get a circuit with only two time constants.

1 time constant

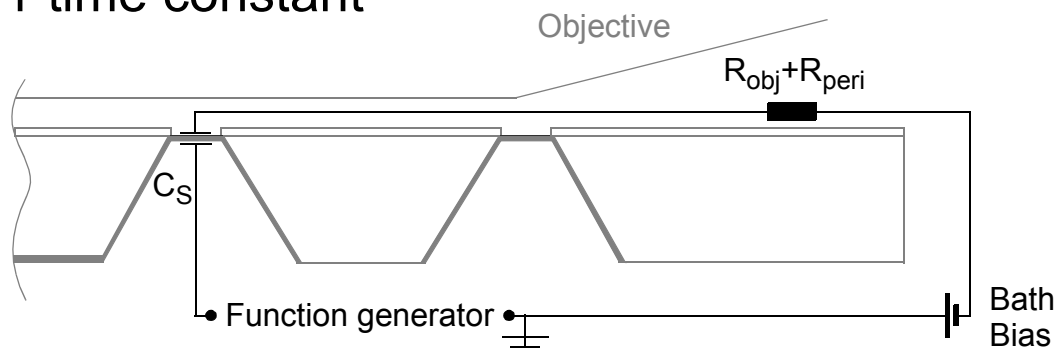


Fig 3.17 The most simple chip model is good enough to account for most of the measurement situations. Here the chip is only a low pass filter of order 1.

All four models of the chip were simulated with the Spice derivate MicroCab by numerical simulation. The transfer function from function generator to the active spot oxide $g_{\text{CHIP}}(f)$ is presented in Fig 3.18:

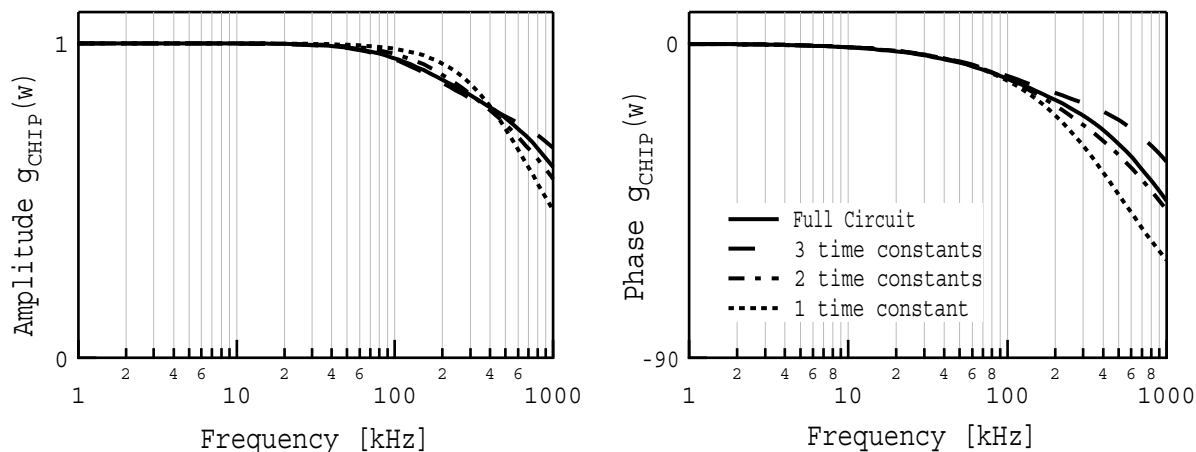


Fig 3.18 Transfer function from function generator to spot oxide $g_{\text{CHIP}}(f)$. The straight plot marks the full chip model, the broken lines are approximations from 3 to 1 time constants as discussed in the figures before. Below 125kHz the approximations do not make any difference in the phase of the transfer function.

There exists further evidence that the full circuit simulation is a good description. As the bath current is in the range of 1mA it can be directly monitored at a 12Ω resistance. Assuming a low pass filter of order 1 (like in Fig 3.17) we can obtain from current amplitude and current phase shift all parameters of the circuit: time constant, serial resistance and capacitance. For 10nm oxide at a stimulation frequency of 125kHz the parameters are typically $1.5\mu\text{s}$, 1200Ω and 1.3nF . This must not be confused with the values of τ_C , $R_{\text{peri}}+R_{\text{obj}}$ and C_S since the bath current is not identical to the current through the spot. But from the simulation of the bath current in the full circuit simulation and the calculation from amplitude and phase the low pass filter parameters, we just find the above parameters of $1.5\mu\text{s}$, 1200Ω and 1.3nF although the chip has a 5-fold smaller time constant.

For lock-in measurements we corrected the phase shift induced by the chip from the most complete chip model of Fig 3.14. Values of the phase are given in Table 3.2.

TABLE 3.2 Phase corrections for lock-in measurements from the complete circuit model of the chip for different chip types at $r=74\text{Wcm}$.

Chip simulation full circuit at:	10nm	50nm
10kHz	-1.0°	0°
25kHz	-3.0°	-0.7°
125kHz	-12.0°	-3.7°
416kHz	-25.7°	-12.2°
625kHz	-33.0°	-16.6°

The phase correction was tested on adsorbed giant vesicle membranes (6.6.B on page 131). Since the strong coupling does not induce a phase shift, we only have to correct for the photomultiplier amplifier (5.4.A on page 88) and obtain the negative phase shift of the chip. In this case there was a thinner spot oxide (6nm) and a bath electrolyte resistance of $250\Omega\text{cm}$. Therefore the resistances in the bath R_{peri} and R_{obj} were enhanced by a factor of 3.4. With these assumptions the full circuit of the chip yielded phase corrections at 125kHz, 417kHz and 625kHz of -35° , -50° and -56° . The measurement results agreed with the simulation values -40° , -53° and -55° .

If we apply transient voltages by imposing a 1V TTL to the function generator we find at the active spot oxide a voltage transient as shown in Fig 3.19. For the transient measurements it is a sufficient approximation to use the most simple model with one time constant of $\tau_C = C_{\text{Spot}} * (R_{\text{peri}} + R_{\text{obj}}) = 0.29\mu\text{s}$ for 10nm spot oxide ($0.06\mu\text{s}$ for 50nm) at $\rho = 74\Omega\text{cm}$. The effects of the transients shortly after the pulse are typically smoothed by the imperfect voltage generator pulses and the photomultiplier amplifier low pass filter.

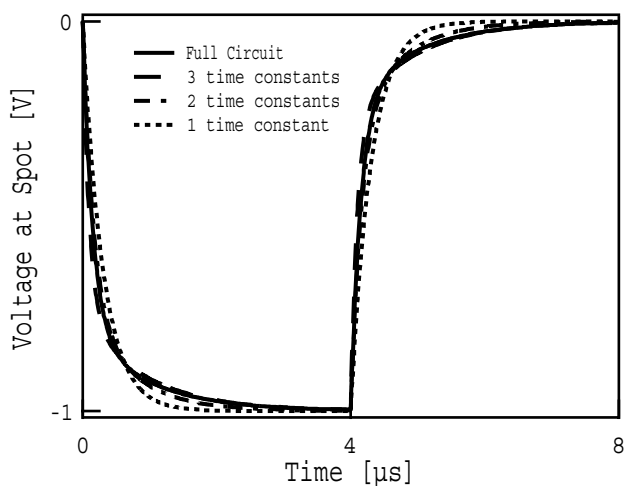


Fig 3.19 Voltage transients at the spot oxide for rectangular voltage pulses of 1V from the function generator. The straight plot marks the full chip model, the broken lines are approximations from 3 to 1 time constants as discussed in the figures before. The approximation of one time constant is chosen in simulations as it describes the voltage transient good enough.

3.4 Usage of the chip

The chips are glued into a petri dish and are contacted with gilded contact springs. AgCl and Pt bath electrodes were used. The bath current is monitored and the bath is held at negative bias. Chips were cleaned with detergent inside the petri dish.

The chip was attached with the silicone glue MK3 (Dr. Osypka GmbH) to a Falcon 3001 petri dish with a square millcut out of the bottom (Fig 3.20). Both petri dish and glue were already tested with cell culture. Another motivation was the the idea to remove the chip out of the dish to clean it by some special procedure, but I did not find a suitable, removable glue. As the chips were very sensitive to harder mechanical treatment, I never tried to break a chip out of the petri dish. The petri dish is fitted into a special holder where gilded contact springs make the contact to the chip. The contacts were connected to a SubD connector on the back side (Fig 3.21). Most often a Pt bath electrode was used made of 0.2mm thick Pt sheet metal, fitting in the outer area of the petri dish (Fig 3.22). In the first experiments on erythrocyte ghosts I also used an AgCl bath electrode prepared from an Ag wire and wound in a spring form to increase the area.

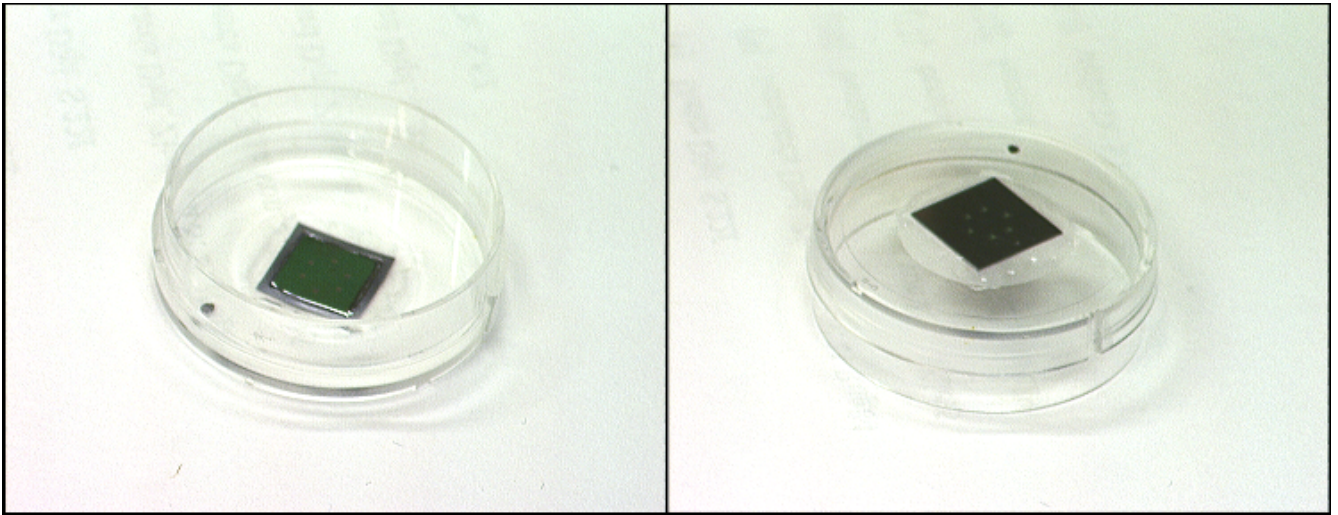


Fig 3.20 The Chip is glued in the bottom of a petri dish.

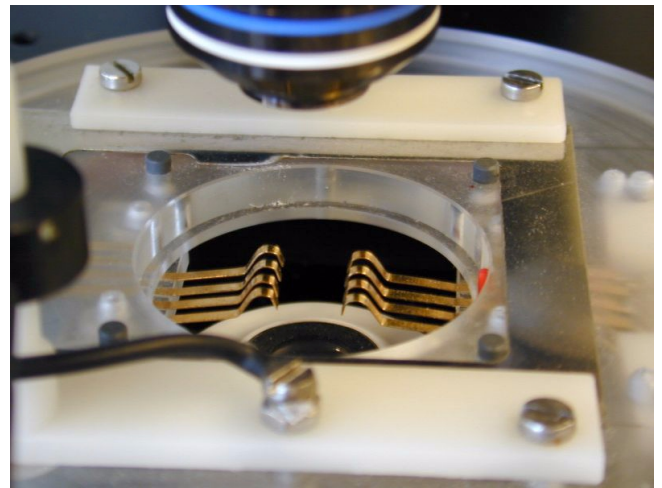
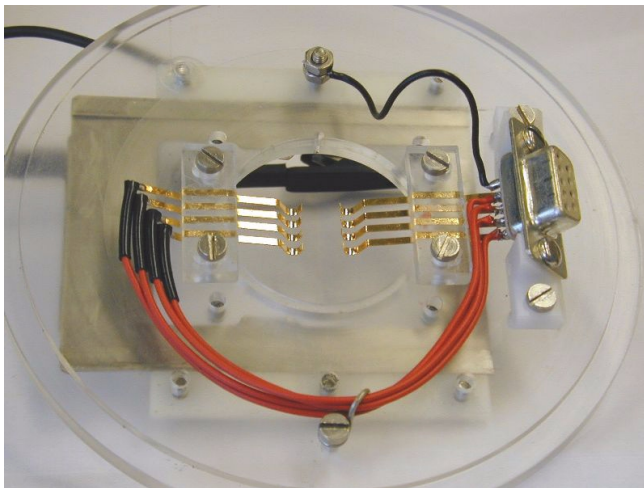


Fig 3.21 Holder for the petri dish from the back side (left) and the front side (right). Contact is made by gilded contact springs.

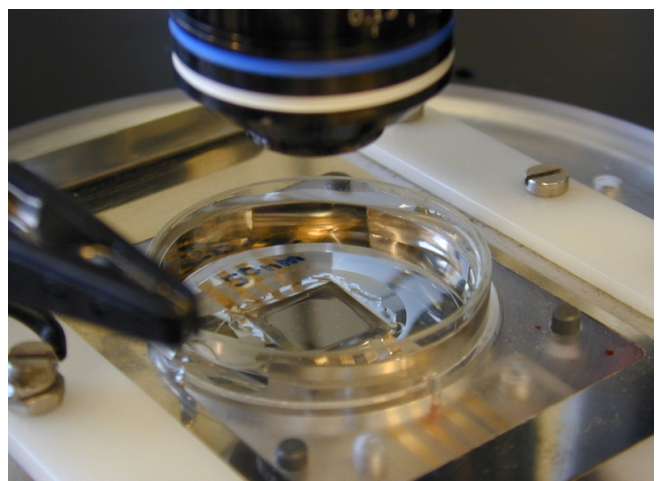


Fig 3.22 A Pt bath electrode (left). Chip in petri dish inserted into the holder. The bath electrode is in the bath and contacted. The objective above will be lowered into the extracellular medium for measurement (right).

The SubD connector of the chip holder was connected to a small switching box where single spots could be switched on and off, the bias voltage and the spot voltage could be applied and the current through the bath electrode could be measured through a 12Ω resistor. The bias voltage came from a separate voltage supply, the spots were connected to a HP33120A function generator (it was switched to 50Ω output resistance but no 50Ω load was applied to get a doubled output voltage to up to 10V) and the current at the 12Ω resistance was measured with a HP54603B oscilloscope (switched to average over 256 values). Both were programmed or read out via a GPIB bus from LabView. To test the contact to the chip I always measured the resistance between the two bulk contacts at the switching box with a digital voltmeter.

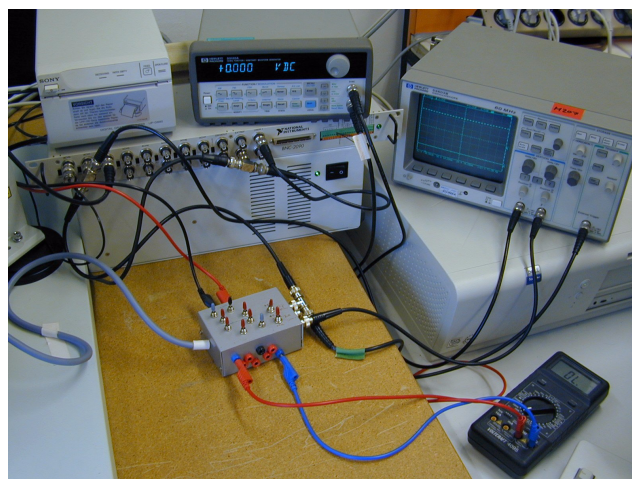
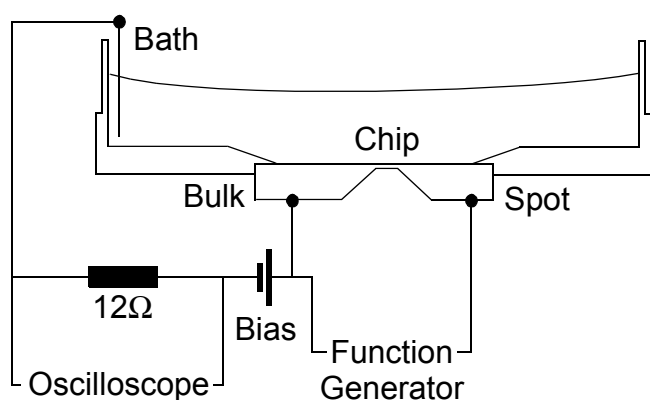


Fig 3.23 Circuitry around the chip (left) and reality (right)

The bias voltage is used to set the a negative potential to the bath with respect to the stimulation spot as required from 3.1.A on page 38. It was taken care that the bias voltage was always higher than the voltage from the function generator. The function generator was programmed as not to apply negative voltages to the spot.

The chips were cleaned inside the petri dish with a solution of 1% dish detergent (Dr. Schnells FOR Spülmittel) in 20ml millipore water wiping with a kimwipe wound around a 1ml eppendorf pipette. The Q-Tips for ear cleaning (Elida Fabege) were also used beforehand but found that they often loose some fibres. The chips were thoroughly rinsed with millipore water and dried under nitrogen. Cleaning was repeated to get a hydrophilic chip surface. If needed, the chips were then held for 30min. under UV light for sterilization. The chip coating and cell culturing is described in the measurement section.

Dye in front of silicon

Voltage sensitive fluorescence and interferometry above silicon

4.1 Voltage sensitive fluorescent dyes **60**

The dye chosen is the annelated hemicyanine dye BNBIQ. It has low phototoxicity and reliable staining properties. Sensitivity can range from 2.5%..9% depending on cell type with the presented filter setup.

4.2 FLIC theory for epi-fluorescence **62**

The dye is in front of the mirror silicon, therefore we must take into account the fluorescence interference of the standing waves. I repeat the derivation of [Lambacher 1996] in order to extend it more easily to confocal illumination in the next chapter.

4.3 FLIC theory for confocal microscopes **66**

We transfer the calculation to the optical situation at a confocal microscope. We must now take into account the diffraction of the focus at excitation. We use the epi-fluorescent FLIC for the emission as the pinhole is rather big. This theory has to use some approximations.

4.4 Using Confocal FLIC **71**

Confocal FLIC theory is tested and used to measure cleft thickness of adsorbed membrane. The dye angle of BNBIQ is measured to 45°.

4.5 Maximizing the fluorescence signal **76**

The dependence of fluorescence intensity on dye angle and oxide thickness is shown. To get a good signal to noise ratio in voltage sensitive fluorescence, the oxide thickness should be small for thick junction clefts and larger for small junction clefts.

4.1 Voltage sensitive fluorescent dyes

The dye chosen is the annelated hemicyanine dye BNBIQ. It has low phototoxicity and reliable staining properties. Sensitivity can range from 2.5%..9% depending on cell type with the presented filter setup.

4.1.A Voltage sensitivity of BNBIQ

Voltage sensitive fluorescence can be achieved by many different mechanisms with different inherent reaction times. As we want to measure at up to stimulation frequencies of 1MHz, a dye with a fast voltage-sensitive mechanism had to be chosen. Therefore a dye was used which is expected to be directly modulated via the Stark effect and not by slow flip-flop reactions.

BNBIQ is an amphiphilic dye (Fig 4.1) with a hydrophilic head group and a hydrophobic tail [Ephardt 1993]. When BNBIQ stains the membrane it is expected and measured in 4.4.B on page 73 or [Lambacher 1994] that its long axis is not parallel to the membrane. Therefore the electrical field induced by the membrane potential has a component along the long axis of the dye molecule. When the dye is excited, the positive charge at the hydrophilic head is moved to the tail. Since this movement happens in the electrical field of the membrane projected along the dye, the electrical field will shift the energy of the excited state and therefore will shift the excitation wavelength. The dye is also sensitive to the dielectric field from the solvent around the dye. The solvent has to rearrange after excitation since the charge has moved in a time scale of ps. This also modulates the excitation spectrum of the dye. A solvent specific shift can be seen in both the excitation and the emission spectrum depending on the polarity of the solvent [Fromherz 1995b]. It is expected that these mechanisms are much more complicated in the membrane of a cell

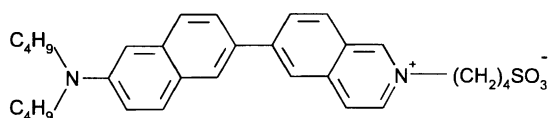


Fig 4.1 Chemical Structure of BNBIQ with hydrophobic tail to the left.

4.1.B Wavelengths of voltage sensitivity

Excitation and emission spectra for BNBIQ in Retzius cells are published in [Fromherz 1993a]. For choosing the appropriate optical filter set we could further rely on the two dimensional voltage sensitive fluorescence spectrum measured for BNBIQ on Retzius cells by [Kuhn 1996] shown (Fig 4.2). We excited BNBIQ with 488nm and masked the emission from 590-700nm with a band pass filter (AHF, Tübingen) further secured by a 510nm long pass filter (Olympus) to measure from the negative sensitivity region. It can be estimated from the spectrum that the sensitivity should be around 10% per 100mV. It must be noted that later and more noisy measurements for HEK cells by Bernd Kuhn showed a slightly shifted spectrum with much lower sensitivities of about 2-3% with the above filter set. In comparing fluorescence amplitudes with theory, measurements yield sensitivities ranging from 2% to 8%/100mV for different cells. This range seems reasonable as the above measurements on HEK or Retzius cells does give a very similar uncertainty in the sensitivity of BNBIQ. It was not envisaged to further optimize the sensitivity as could be easily done e.g. with adsorbed giant vesicle membranes (paragraph 6.6 on page 130)

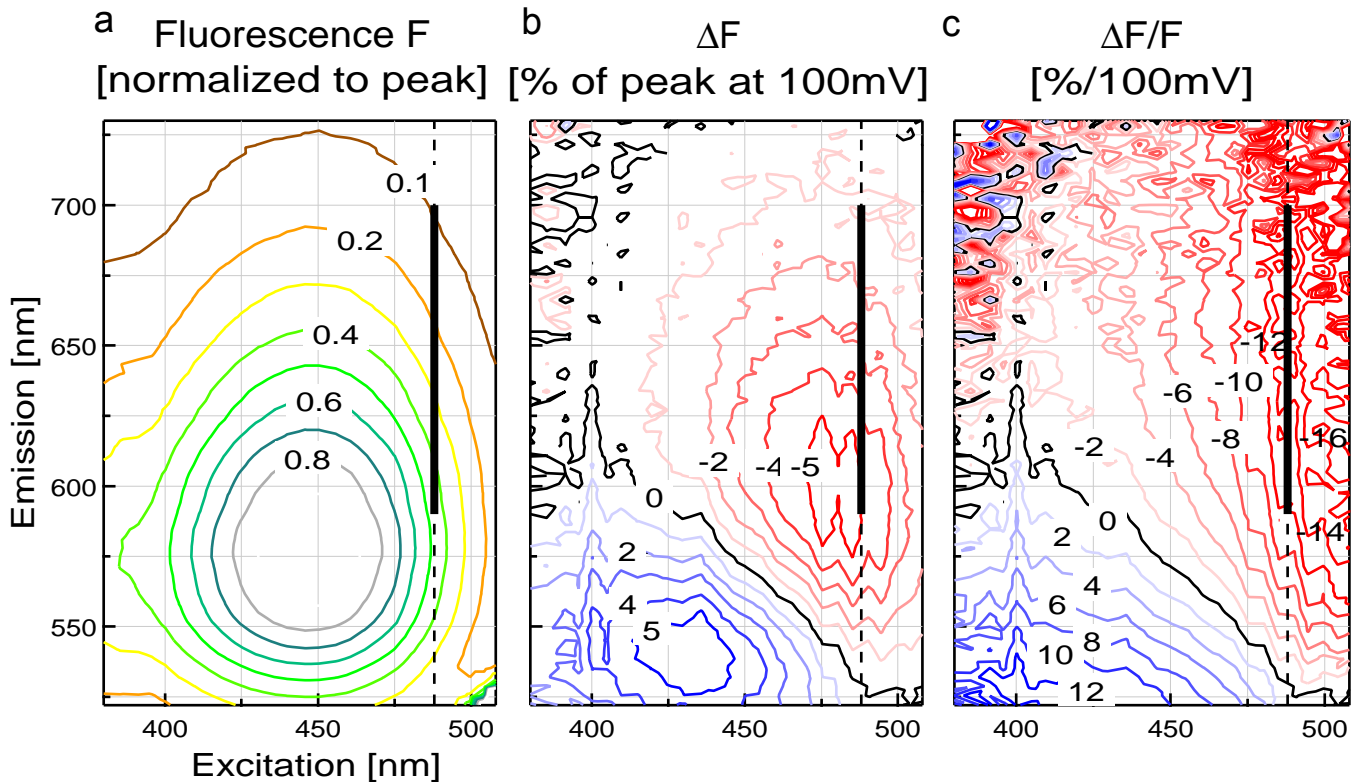


Fig 4.2 2-Dimensional voltage sensitive fluorescence spectrum of BNBIQ in Retzius cells as measured by [Kuhn 1996]. The fluorescence spectrum (a) changes for an applied membrane potential of 100mV by ΔF (b) to yield a sensitivity of $\Delta F/F$ (c). Excitation at 488nm (broken line) and emission 590..700nm (thick line) are displayed. Obtained sensitivity should be 10%/100mV but can be much lower in mammalian cells (about 2-3%/100mV).

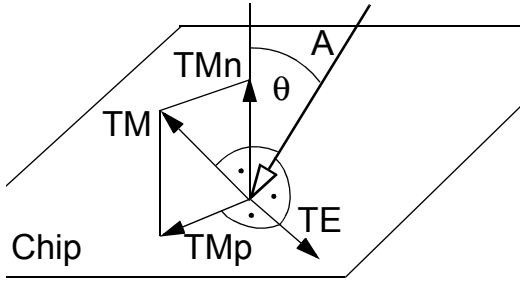
4.1.C Staining method

We prepared in a 1ml eppendorf tube a staining solution of 0.5ml Milli-Q water, 0.5ml fetal calf serum (Sigma) and approximately 2 μ g of BNBIQ. With sucking into a 1ml pipette we broke the brick of BNBIQ into small pieces and performed an ultrasonic bath for 10min. After centrifugation at 500g for 10min the small BNBIQ grains are collected to the ground of the tube. The solution can be kept at room temperature for more than a week. We put 40 μ l of the orange colored supernatant under modest swinging to the medium in the petri dish of the chip. Staining sets in without noticeable delay. It is expected [Prinz 1996] that the dye first binds to the FCS-proteins and is then given to the membrane due its higher affinity. BNBIQ is expected to diffuse in the outer membrane leaflet since the cells membrane is stained homogeneously very fast. Measurements were performed within an hour after staining.

4.2 FLIC theory for epi-fluorescence

The dye is in front of the mirror silicon, therefore we must take into account the fluorescence interference of the standing waves. I repeat the derivation of [Lambacher 1996] in order to extend it more easily to confocal illumination in the next chapter.

4.2.A Electrical field for Köhler illumination



In epi-fluorescent Köhler illumination the dye is excited by defocused plane waves. We describe the electrical field in a coordinate system which rotates with the incoming plane wave: the direction of propagation of the wave and the optical axis perpendicular to the chip defining a plane A. We denote the direction perpendicular to A with TE and the direction parallel to A but perpendicular to the light direction with TM. These are the “natural” coordinates to

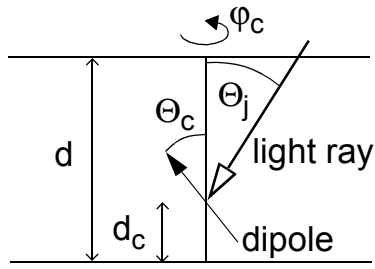
describe reflection coefficients. We further split the TM into components TMn normal to the chip and TMp parallel to the chip: $k=\{TE, TMp, TMn\}$. the incoming wave is polarized with an angle γ relative to the plane A. The incoming electrical field is therefore on the coordinate system k:

$$\vec{E}^0(\Theta) = \begin{bmatrix} E_{TE}^0 \\ E_{TMp}^0 \\ E_{TMn}^0 \end{bmatrix} = \cos\gamma \begin{bmatrix} 0 \\ \cos\Theta \\ \sin\Theta \end{bmatrix} + \sin\gamma \begin{bmatrix} 1 \\ 0 \\ 0 \end{bmatrix} = \begin{bmatrix} \sin\gamma \\ \cos\gamma\cos\Theta \\ \cos\gamma\sin\Theta \end{bmatrix} \quad [4.1]$$

4.2.B Transformation to the dye with if-factors

Transfer matrices are used to describe the multilayer optical system. The multireflection from above the layer system to the dye is described by complex if-factors. The electrical field of the last paragraph must be transformed through the multilayer system to the layer of the dye. We only have to calculate the fresnel reflection coefficients from the layer of the dye upwards r_k^{up} (the reflection coefficient from the objective to the layer of the dye is $-r_k^{up}$) and downwards r_k^{down} to the silicon. Any further prefactors will be discussed in the Poynting correction section below. (I will not describe how these combined fresnel coefficients of reflection can be obtained from multilayer transfer matrix theory. With these coefficients we calculate the multireflection in the layer of the dye to get the electrical field \vec{E} at the position of the dye.) I generalize from the derivation of Armin Lambacher [Lambacher 1994]:

$$if_k = \sqrt{1 - |r_k^{up}|^2} \frac{1 + s_k r_k^{up} e^{i\phi d_c/d}}{1 - r_k^{down} r_k^{up} e^{i\phi}} \quad s_k = \{1, 1, -1\} \quad \phi = \frac{4\pi n_j d \cos\Theta_j}{\lambda} \quad [4.2]$$



The parameters of the stained layer are as depicted to the left with d denoting the thickness of the layer, d_c the low distance of the dye in the layer, Θ_c the angle of the chromophore to the membrane normal, Θ_j the angle of the plane waves and n_j the refractive index. Therefore the electrical field at the chromophore is:

$$\vec{E} = \begin{bmatrix} \text{if}_{\text{TE}} & 0 & 0 \\ 0 & \text{if}_{\text{TMp}} & 0 \\ 0 & 0 & \text{if}_{\text{TMn}} \end{bmatrix} \vec{E}^0(\Theta_j) = \begin{bmatrix} \text{if}_{\text{TE}} \sin \gamma \\ \text{if}_{\text{TMp}} \cos \gamma \cos \Theta_j \\ \text{if}_{\text{TMn}} \cos \gamma \sin \Theta_j \end{bmatrix} \quad [4.3]$$

4.2.C Transition probability of the dye

The scalar product of the dye's transition dipole and the electrical field is proportional to the probability to excite the dye (or to emit light into the mode). We define the dipole of the chromophore with a rotation angle φ_c as

$$\vec{d} = \begin{bmatrix} d_{\text{TE}} \\ d_{\text{TMp}} \\ d_{\text{TMn}} \end{bmatrix} = \begin{bmatrix} \sin \Theta_c \cos \varphi_c \\ \sin \Theta_c \sin \varphi_c \\ \cos \Theta_c \end{bmatrix} \quad [4.4]$$

The matrix element for the transition for excitation and emission is proportional to the squared scalar product of the dipole and the electrical field: $P \sim |\vec{E}\vec{d}|^2$. The remaining question is: do we have to first integrate the electrical field inside and square afterwards or vice versa? As the interference must be realized by a single photon this corresponds to the question whether the paths of the single photon interfere on the way to the chromophore. As the light for excitation is not focussed to a point in Köhler illumination, a photon arrives at the dye only from one direction without interference and approximated by a plane wave. Therefore we must first square and then integrate the different photon directions. For the emission we assume that the whole energy of the emitted dipole wave from the chromophore (after transfer with the if-factors) will be directed to the detector by the objective. Here the different directions are assumed not to interfere and we also first square and then integrate the different directions of energy transport. The symmetry of excitation and emission was explicitly calculated in [Lambacher 1994]. Poynting vector corrections will be discussed later. We thus first square and neglect terms with an odd power of sin or cos as these will integrate to zero afterwards:

$$\sim |\vec{E}\vec{d}|^2 = |\text{if}_{\text{TE}}|^2 \sin^2 \gamma \sin^2 \Theta_c \cos^2 \varphi_c + |\text{if}_{\text{TMp}}|^2 \cos^2 \gamma \cos^2 \Theta_j \sin^2 \Theta_c \sin^2 \varphi_c + |\text{if}_{\text{TMn}}|^2 \cos^2 \gamma \sin^2 \Theta_j \cos^2 \Theta_c \quad [4.5]$$

Integrating over the chromophores' rotation angle φ_c and the polarization γ and dividing by π^2 results in:

$$U = |\text{if}_{\text{TE}}|^2 \sin^2 \Theta_c + |\text{if}_{\text{TMp}}|^2 \cos^2 \Theta_j \sin^2 \Theta_c + 2|\text{if}_{\text{TMn}}|^2 \sin^2 \Theta_j \cos^2 \Theta_c \quad [4.6]$$

4.2.D Spectral and aperture integration

For integration over the wavelength in the case of excitation we need the excitation spectrum of the dye and the intensity of the light source, both multiplied into the spectral weight of excitation $W_{\text{ex}}(\lambda)$. For emission we need the emission spectrum of the dye and the spectral sensitivity of the detector, both multiplied into the spectral weight of emission $W_{\text{em}}(\lambda)$.

After further integrating over the aperture we obtain the probability of exciting the dye or emitting light from the dye. We consider Poynting vector corrections since we have described only with the term $1 - |r_k^{\text{up}}|^2$ in the if-factors how the electrical field was transferred without transforming of the angle element $d\Theta$. The different light velocities are not considered as they only yield a constant factor. When transferring light energy from medium 1 to medium 2 we obtain for the transmission of energy T [Hecht 1987]:

$$T_{12} = 1 - R_{12} = 1 - |r_{12}|^2 \quad R_{12} = |r_{12}|^2 \quad r_{12} = -\bar{r}_{21} \quad [4.7]$$

This description is correct for excitation if the integration is performed with the Θ -variables of the layer of the medium and for emission if Θ is used in the layer of the dye for emission. As we integrate with the variables of the medium, we do not have correct in excitation:

$$C_{\text{poynting}}^{\text{ex}} = 1 \quad [4.8]$$

For emission we assume that all energy leaving the layer of the dye will reach the detector. We describe the emission as a spherical wave from the chromophore, splice it into plane waves in the layer of the dye and ask for the energy which will leave the layer. This is fully described with the if-factors. But to switch from integration in the layer of the dye to the integration in the layer of the objective we get from the substitution $\Theta_j \rightarrow \Theta$:

$$\int n_j \sin \Theta_j d\Theta_j \rightarrow \int \frac{n \cos \Theta}{n_j \cos \Theta_j} n \sin \Theta d\Theta \quad \text{from} \quad n \sin \Theta = n_j \sin \Theta_j \quad [4.9]$$

the Poynting correction factor of

$$C_{\text{poynting}}^{\text{em}} = \frac{n \cos \Theta}{n_j \cos \Theta_j} \quad [4.10]$$

We thus obtain for the full integration of the probability of excitation ($i=\text{ex}$) or emission ($i=\text{em}$):

$$P_i = \int W_i(\lambda) d\lambda \int_0^{\Theta_{\text{max}}} UC_{\text{poynting}}^i \sin \Theta d\Theta \quad i = \{\text{ex}, \text{em}\} \quad [4.11]$$

If we neglect the distance dependent lifetime correction [Lambacher 2000], we can just combine the probabilities of excitation and emission to the fluorescence intensity:

$$I_{\text{fluorescence}} = P_{\text{ex}} P_{\text{em}} \quad [4.12]$$

4.2.E Lifetime correction

Especially for a small distance to the silicon, we have to correct for a distance dependent modulation of the quantum efficiency. An excited dye can also decay without emitting a photon. If the mirror for example inhibits the dye's emission, it will need more time to emit the photon. The chance to decay in the meanwhile without emitting the photon is higher as the dye is longer in the excited state, therefore the overall quantum efficiency will be lower and in general be modu-

lated by the interface. In [4.12] we assumed that the quantum efficiency is constant. From the calculations of Armin Lambacher in [Lambacher 2000] we derive rate constants for the layer system used. From the rate constants for emission in normal (N) and parallel (P) directions

$$k_N(d_{\text{oxide}}, d_{\text{cleft}}) \quad k_P(d_{\text{oxide}}, d_{\text{cleft}}) \quad [4.13]$$

which are referred to values for very thick oxide

$$k_N^{\infty}(d_{\text{cleft}}) \quad k_P^{\infty}(d_{\text{cleft}}) \quad [4.14]$$

we obtain the correction for the quantum efficiency q

$$q' = \frac{(1 + qk_N^{\infty})\sin^2\Theta_c + (1 + qk_P^{\infty})\cos^2\Theta_c}{(1 + qk_N)\sin^2\Theta_c + (1 + qk_P)\cos^2\Theta_c} \quad [4.15]$$

and thus finally get the fluorescence intensity with

$$I_{\text{fluorescence}} = q'P_{\text{ex}}P_{\text{em}} \quad [4.16]$$

For the quantum efficiency of DiI (approximately 0.34) we obtain about 1nm smaller distances between membrane and substrate for FLIC measurements with 4 different oxide steps or even less from measurements with 16 oxide steps.

4.2.F Epi-fluorescence FLIC on adsorbed membrane

We test the epi-fluorescence FLIC theory on adsorbed giant vesicle membranes. As a reference for the following measurements I once more ([Lambacher 1994], [Lambacher 1996], [Braun 1996], [Braun 1997], [Zeck 1997], [Braun 1998], [Fromherz 1999]) used the epi-fluorescence FLIC theory to measure the distance from the membrane to the substrate here. I used adsorbed giant vesicle membrane which I stained after the adsorption. I prepared giant lipid vesicles like in [Fromherz 1999] and let them adsorb on FLIC-Chips with 16 oxides. The processing of the FLIC-Chips used is described in [Braun 1997] and [Braun 1998]. The chips were cleaned in a CARO solution, measured under the ellipsometer and dried under nitrogen as described in [Braun 1997]. Coating, and adsorption of the vesicles were done as described in paragraph 6.6.A on page 130. The vesicles were stained after adsorption with 3 μ l 5mM DiI_{C12} in EtOH added to the 3ml TRIS-Glucose solution. Therefore I assume that only the upper leaflet of the membrane was stained as this dye is reported not to make a flip-flop reaction before 4h [Wolf 1985]. The remaining optical parameters were taken from [Zeck 1997]:

TABLE 4.1. Optical parameters for FLIC on adsorbed giant vesicle membrane

Refractive Indexes		Dye angle to membrane normal Θ_C	90°
Silicon at 633nm	3.87	Numerical aperture of excitation	1.0
Silicon dioxide at 633nm	1.460	Numerical aperture of emission	0.985
Cleft and Medium	1.333	Membrane thickness	3.7nm
		Quantum efficiency q	0.34

From fluorescence images grabbed with a CCD-Camera. Fluorescences intensities are averaged on each oxide steps and their standard deviations are obtained [Braun 1997]. Evaluating with the above constants and fits the thickness of the cleft to 2.3 \pm 0.9nm (Fig 4.3):

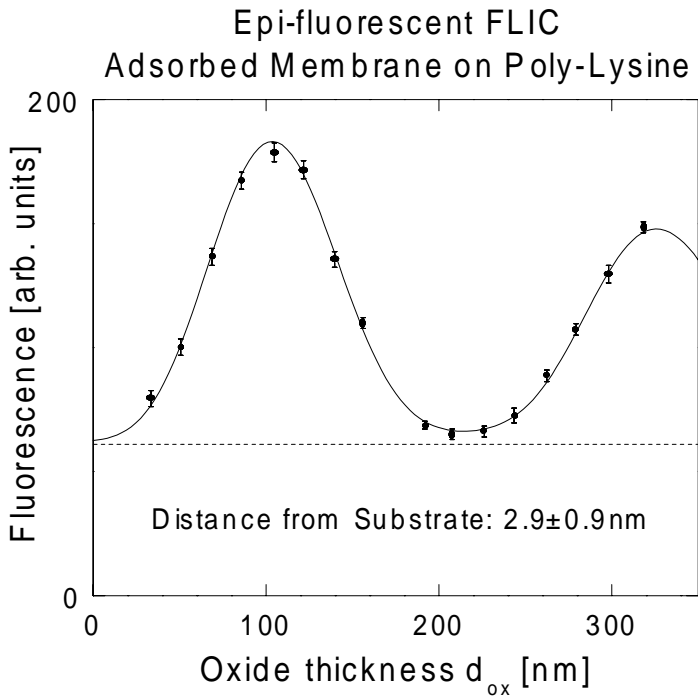


Fig 4.3 FLIC measurement on 16 oxides with epi-fluorescence theory. After fitting for absolute intensities and a background fluorescence we obtain a thickness of the cleft between membrane and silicon oxide of $2.9\pm 0.9\text{nm}$.

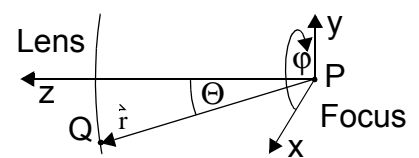
4.3 FLIC theory for confocal microscopes

We transfer the calculation to the optical situation at a confocal microscope. We must now take into account the diffraction of the focus at excitation. We use the epi-fluorescent FLIC for the emission as the pinhole is rather big. This theory has to use some approximations.

From discussions with Karsten Kottig and Armin Lambacher I try here to give a first attempt of the FLIC theory for confocal microscopes. I will have to deal with a full integration over the dye's plane inside a fully integrated focus using approximations given by [Born 1980] for small objective apertures and scalar fields. Furthermore I have to introduce a reasonable approximation of nonscalar E-Field vectors of polarized light in the focus. Last but not least a trick was used to calculate integral constants in advance to squeeze fitting procedures into acceptable computing times. I am aware that the thoughts given here are not fully developed yet, but the approaches given could be valuable for the future.

4.3.A Diffraction forms the focus

The light path differences from a spherical aperture interfere to a focus similar to single slit interference. We begin with the derivation from [Born 1980] where the phase differences after a lens of small aperture are shown to build the focus geometry. Q is a point on a spherical area of constant phase built up by the lens, parametrized in standard spherical coordinates with φ and Θ . From there we integrate the phases of plane waves at the focus point P, given in cylinder coordinates z, r and ϕ . The amplitude at the focus point P is then given by:



$$U(z, r, \phi) = -\frac{i}{\lambda} E_0 \int_0^{\Theta_{\max}} \exp\left(ikz\left[1 + \frac{\tan^2\Theta}{2}\right]\right) \int_0^{2\pi} e^{-ikr \tan\Theta \cos(\phi - \phi)} \sin\Theta d\Theta d\phi \quad [4.17]$$

with E_0 the amplitude of the electrical field at Q and $k=2\pi/\lambda$. The intensity in the plane of the focus at $z=0$ gives

$$|U(P)|^2 \sim \left(\frac{2J_1(v)}{v}\right)^2 I_0 \quad \text{with } v = kr \tan\Theta_{\max} \quad [4.18]$$

and the Bessel function of first order J_1 . This is the well known formula of Airy for the diffraction from a circular hole. The intensity in z direction for $r=0$ gives

$$\left(\frac{\sin u/4}{u/4}\right)^2 I_0 \quad \text{with } u = kz \tan\Theta_{\max}^2 \quad [4.19]$$

For the FLIC theory we assume that the center of the focus is positioned above the mirror interface (defined by the interface of silicon and silicon dioxide) at z_0 . The dye is at z_{dye} approximately on top of the layer system. Therefore the phase factor will be calculated in the medium above the layer system with $z=z_{\text{dye}}-z_0$. All layer reflections are calculated as if the rays from Q to P used for the interference would be parallel. This is a good approximation since we get most of the interference from 2 rays (multireflection plays a minor role) and since these two rays do not diverge much from each other in the used geometry. Without this approximation we would have to calculate all paths with all reflections to get from Q to the dye position P simultaneously in a ray tracing manner which would require great computation power. Karsten Kottig has envisaged such a method for the simulation of a simple mirror [Kottig 2000]. Therefore z is the real distance from the dye to the focus, k is the wave vector inside the medium and Θ is the angle of the rays in the medium. We get as a phase factor at the dye position inside the focus at $P(r, \phi, z)$

$$U(r, \phi) = -\frac{i}{\lambda} E_0 \int_0^{\Theta_{\max}} \exp\left(ikz\left[1 + \frac{\tan^2\Theta}{2}\right]\right) \int_0^{2\pi} \cos(kr \tan\Theta \cos(\phi - \phi)) f(\Theta) \sin\Theta d\Theta d\phi \quad [4.20]$$

assuming a real valued ϕ integral which is the case after the integration over ϕ . For shortening the following calculations we define

$$H(\Theta) = \exp\left(ikz\left[1 + \frac{\tan^2\Theta}{2}\right]\right) f(\Theta) \quad [4.21]$$

We allow here for an additional weight $f(\Theta)$ of the aperture illumination. Since the intensity over the illuminating aperture can follow a gaussian distribution, we assume for the electrical field

$$f(\Theta) = \exp(-\Theta^2/4\Theta_0^2) \quad [4.22]$$

with the sigma width Θ_0 of the illuminating intensity. We must keep in mind that this distribution is further masked with the maximal aperture Θ_{\max} in [4.20]. But for the confocal microscope used the illuminating laser beam has a broader beam profile than the back objective aperture and we will not use gaussian weighting.

4.3.B Approximation for polarized excitation

As the laser light is polarized, we give an approximation for the electrical field behind the objective. The photon from the laser is linearly polarized. This polarization is assumed to be sustained as the objectives can also be used for polarization microscopy. I give here an approximation for this polarized spherical wave after the objective with \hat{r} the vector from P to Q. From the assumptions:

$$E_y = 0 \quad |\hat{E}| = 1 \quad \hat{E}_r = 0 \quad [4.23]$$

yielding

$$\hat{E}' = \frac{1}{\sqrt{\sin^2\Theta\cos^2\varphi + \cos^2\Theta}} \begin{bmatrix} \cos\Theta \\ 0 \\ -\sin\Theta\cos\varphi \end{bmatrix} \quad [4.24]$$

We further rotate this with an angle of α around the z-axis.

$$\hat{E}^0(\Theta) = \begin{bmatrix} \cos\alpha & \sin\alpha & 0 \\ -\sin\alpha & \cos\alpha & 0 \\ 0 & 0 & 1 \end{bmatrix} \hat{E}' = \frac{1}{\sqrt{\sin^2\Theta\cos^2\varphi + \cos^2\Theta}} \begin{bmatrix} \cos\alpha\cos\Theta \\ -\sin\alpha\cos\Theta \\ -\sin\Theta\cos\varphi \end{bmatrix} \quad [4.25]$$

4.3.C Transformation to the dye with if-factors

The transformation to the dye with the if-factors is now slightly different. We have to describe the electrical field in the coordinate system best suited for the fresnel coefficients. Transformation between $k=\{TE, TM_p, TM_n\}$ and $i=\{x, y, z\}$ is done by:

$$\begin{bmatrix} E_{TE} \\ E_{TM_p} \\ E_{TM_n} \end{bmatrix} = \begin{bmatrix} -\sin\varphi & \cos\varphi & 0 \\ \cos\varphi & \sin\varphi & 0 \\ 0 & 0 & 1 \end{bmatrix} \begin{bmatrix} E_x \\ E_y \\ E_z \end{bmatrix} \quad [4.26]$$

$$\begin{bmatrix} E_x \\ E_y \\ E_z \end{bmatrix} = \begin{bmatrix} -\sin\varphi & \cos\varphi & 0 \\ \cos\varphi & \sin\varphi & 0 \\ 0 & 0 & 1 \end{bmatrix} \begin{bmatrix} E_{TE} \\ E_{TM_p} \\ E_{TM_n} \end{bmatrix} \quad [4.27]$$

Therefore the electrical field must be rotated into the $k=\{TE, TM_p, TM_n\}$ coordinates, transferred to the dye layer with the if-factors [4.2] and rotated back again. This means we have an electrical field at the chromophore:

$$\hat{E}_{\sqrt{\sin^2\Theta_j\cos^2\varphi + \cos^2\Theta_j}} = \begin{bmatrix} -\sin\varphi & \cos\varphi & 0 \\ \cos\varphi & \sin\varphi & 0 \\ 0 & 0 & 1 \end{bmatrix} \begin{bmatrix} \tilde{f}_{TE} & 0 & 0 \\ 0 & \tilde{f}_{TM_p} & 0 \\ 0 & 0 & \tilde{f}_{TM_n} \end{bmatrix} \begin{bmatrix} -\sin\varphi & \cos\varphi & 0 \\ \cos\varphi & \sin\varphi & 0 \\ 0 & 0 & 1 \end{bmatrix} \begin{bmatrix} \cos\alpha\cos\Theta_j \\ -\sin\alpha\cos\Theta_j \\ -\sin\Theta_j\cos\varphi \end{bmatrix} \quad [4.28]$$

After neglecting the odd powers of sin and cos in φ since these will be integrated to zero afterwards we obtain:

$$\hat{E} = \frac{1}{\sqrt{\sin^2\Theta_j\cos^2\varphi + \cos^2\Theta_j}} \begin{bmatrix} \cos\Theta_j\cos\alpha(\tilde{f}_{TE}\sin^2\varphi + \tilde{f}_{TM_p}\cos^2\varphi) \\ -\cos\Theta_j\sin\alpha(\tilde{f}_{TE}\cos^2\varphi + \tilde{f}_{TM_p}\sin^2\varphi) \\ 0 \end{bmatrix} \quad [4.29]$$

Please note that we have to use different if-factors as we are not dealing with Poynting vectors any more: we are integrating first the electrical fields and square afterwards. Therefore we must switch to transmission coefficients of the electrical field t_{12} :

$$T_{12} = 1 - R_{12} = 1 - |r_{12}|^2 = \frac{n_2 \cos \Theta_2}{n_1 \cos \Theta_1} |t_{12}|^2 \quad |t_{12}|^2 = \frac{n_1 \cos \Theta_1}{n_2 \cos \Theta_2} (1 - |r_{12}|^2) \quad [4.30]$$

and therefore get for excitation

$$\tilde{f}_k = \sqrt{\frac{n \cos \Theta}{n_j \cos \Theta_j}} \sqrt{1 - |r_k|^2} \frac{1 + s_k r_k^{\text{up}} e^{i\phi_{d_c/d}}}{1 - r_k^{\text{down}} r_k^{\text{up}} e^{i\phi}} \quad s_k = \{1, 1, -1\} \quad \phi = \frac{4\pi n_j d \cos \Theta_j}{\lambda} \quad [4.31]$$

4.3.D Transition probability of the dye

The scalar product of the dye's transition dipole and the electrical field is proportional to the probability to excite the dye. We calculate the scalar product of the dipole

$$\vec{d} = \begin{bmatrix} d_x \\ d_y \\ d_z \end{bmatrix} = \begin{bmatrix} \sin \Theta_c \cos \varphi_c \\ \sin \Theta_c \sin \varphi_c \\ \cos \Theta_c \end{bmatrix} \quad [4.32]$$

and get

$$\vec{E} \vec{d} = \frac{\sin \Theta_c \cos \Theta_j}{\sqrt{\sin^2 \Theta_j \cos^2 \varphi + \cos^2 \Theta_j}} [\cos \varphi_c \cos \alpha (\tilde{f}_{TE} \sin^2 \varphi + \tilde{f}_{TMp} \cos^2 \varphi) - \sin \varphi_c \sin \alpha (\tilde{f}_{TE} \cos^2 \varphi + \tilde{f}_{TMp} \sin^2 \varphi)] \quad [4.33]$$

We integrate these terms together with the phases from integral [4.20]:

$$U(r, \phi) = -\frac{i}{\lambda} E_0 \int_0^{\Theta_{\text{max}}} H(\Theta) \int_0^{2\pi} \vec{E} \vec{d} \cos(kr \tan \Theta_j \cos(\varphi - \phi)) \sin \Theta_j d\Theta_j d\varphi \quad [4.34]$$

and define two integrals which can be calculated numerically:

$$I_{\{1,2\}} = \int_0^{2\pi} \frac{\cos \Theta_j}{\sqrt{\sin^2 \Theta_j \cos^2 \varphi + \cos^2 \Theta_j}} \{\cos^2 \varphi, \sin^2 \varphi\} \cos(kr \tan \Theta_j \cos(\varphi - \phi)) d\varphi \quad [4.35]$$

to get

$$U = -\frac{i}{\lambda} E_0 \sin \Theta_c \int_0^{\Theta_{\text{max}}} H(\Theta) [\cos \varphi_c \cos \alpha (\tilde{f}_{TE} I_2 + \tilde{f}_{TMp} I_1) - \sin \varphi_c \sin \alpha (\tilde{f}_{TE} I_1 + \tilde{f}_{TMp} I_2)] \sin \Theta_j d\Theta_j \quad [4.36]$$

Now we have integrated all directions and are able to square for the transition probability:

$$P_{\text{dye}} = |U|^2 \quad [4.37]$$

4.3.E Integration of the focus

We still have to integrate over all dye positions in the focus r, ϕ . And we have to consider the dye orientations Θ_c, φ_c . To do this we need a trick and write the square in [4.37] as two integrations over Θ and Θ' . In this way we can derive further integrals which can be computed numerically in advance:

$$\begin{aligned}
P_{\text{dye}}(r, \phi, \varphi_c, \Theta_c, \alpha) &= \frac{E_0^2}{\lambda^2} \sin^2 \Theta_c \left| \int_0^{\Theta_{\max}} H(\Theta) [\cos \varphi_c \cos \alpha (\tilde{f}_{\text{TE}I_2} + \tilde{f}_{\text{TMp}I_1}) - \sin \varphi_c \sin \alpha (\tilde{f}_{\text{TE}I_1} + \tilde{f}_{\text{TMp}I_2})] \sin \Theta_j d\Theta_j \right|^2 \\
&= \frac{E_0^2}{\lambda^2} \sin^2 \Theta_c \int_0^{\Theta_{\max}} H(\Theta) [\cos \varphi_c \cos \alpha (\tilde{f}_{\text{TE}I_2} + \tilde{f}_{\text{TMp}I_1}) - \sin \varphi_c \sin \alpha (\tilde{f}_{\text{TE}I_1} + \tilde{f}_{\text{TMp}I_2})] \sin \Theta_j d\Theta_j \\
&\quad \int_0^{\Theta_{\max}} H(\Theta') [\cos \varphi_c \cos \alpha (\tilde{f}_{\text{TE}I_2} + \tilde{f}_{\text{TMp}I_1}) - \sin \varphi_c \sin \alpha (\tilde{f}_{\text{TE}I_1} + \tilde{f}_{\text{TMp}I_2})] \sin \Theta_j' d\Theta_j'
\end{aligned} \tag{4.38}$$

We integrate over the focus with the substitution $R=kr$ which also eliminates the λ prefactor due to $rdr=(RdR)/k^2$. We define the integrals:

$$M_{n,m}(\Theta, \Theta') = \int_0^{r_{\max}} \int_0^{2\pi} I_n(\Theta) I_m(\Theta') r dr d\phi = \frac{1}{k^2} \int_0^{R_{\max}} \int_0^{2\pi} I_n(\Theta) I_m(\Theta') R dR d\phi \tag{4.39}$$

with the focus radius from [4.18]:

$$v = 0.61 = R_{\max} \tan \Theta_{\max} \Rightarrow R_{\max} = \frac{0.61}{\tan \Theta_{\max}} \tag{4.40}$$

We should note that this is a further approximation. Not only do we neglect all intensity outside the focus radius but we also ignore the z -dependence of the focus radius as this would render the calculation of the integrals M in advance impossible. The computation time would increase tremendously. But the constant focus radius is a good approximation as the correct focus radius would be:

$$R_{\max}(z) = \sqrt{R_{\max}^2 + k^2 z^2 \tan^2 \Theta_{\max}} \tag{4.41}$$

4.3.F Aperture integration

Aperture integration is very quick with the precompiled phase factors M from focus integration. From this we get for the dye in a plane in the focus - after also integrating the polarization α and the dye angle φ_c :

$$\begin{aligned}
P_{\text{plane}}(\Theta_c) &= \frac{1}{k^2} \int_0^{2\pi} \int_0^{2\pi} \int_0^{2\pi} \int_0^{R_{\max}} P_{\text{dye}}(r, \phi, \varphi_c, \Theta_c, \alpha) d\phi d\alpha d\varphi_c R dR \\
&= \sin^2 \Theta_c \int_0^{2\pi} \int_0^{2\pi} [\cos^2 \varphi_c \cos^2 \alpha P_0 + \sin^2 \varphi_c \sin^2 \alpha P_1] d\alpha d\varphi_c = \sin^2 \Theta_c [P_0 + P_1]
\end{aligned} \tag{4.42}$$

with the integrals:

$$P_{\{0,1\}} = \frac{E_0^2}{4\pi^4} \int_0^{\Theta_{\max}} \int_0^{\Theta_{\max}} \overline{H(\Theta)H(\Theta')} X_{\{0,1\}}(\Theta_j, \Theta_j') \sin \Theta_j \sin \Theta_j' d\Theta_j d\Theta_j' \tag{4.43}$$

$$X_0(\Theta, \Theta') = \overline{\tilde{f}_{\text{TE}}(\Theta)\tilde{f}_{\text{TE}}(\Theta')} M_{2,2} + \overline{\tilde{f}_{\text{TMp}}(\Theta)\tilde{f}_{\text{TMp}}(\Theta')} M_{1,1} + \overline{\tilde{f}_{\text{TMp}}(\Theta)\tilde{f}_{\text{TE}}(\Theta')} M_{1,2} + \overline{\tilde{f}_{\text{TE}}(\Theta)\tilde{f}_{\text{TMp}}(\Theta')} M_{2,1} \tag{4.44}$$

$$X_1(\Theta, \Theta') = \overline{\tilde{f}_{\text{TE}}(\Theta)\tilde{f}_{\text{TE}}(\Theta')} M_{1,1} + \overline{\tilde{f}_{\text{TMp}}(\Theta)\tilde{f}_{\text{TMp}}(\Theta')} M_{2,2} + \overline{\tilde{f}_{\text{TMp}}(\Theta)\tilde{f}_{\text{TE}}(\Theta')} M_{2,1} + \overline{\tilde{f}_{\text{TE}}(\Theta)\tilde{f}_{\text{TMp}}(\Theta')} M_{1,2}$$

Therefore for an oriented chromophore we obtain the probability for excitation of

$$P_{\text{ex}} = \sin^2 \Theta_c \int W_{\text{ex}}(\lambda) [P_0 + P_1] d\lambda \tag{4.45}$$

It is easy to see that the chromophore orientation is only scaling the intensity and does not affect the shape of the interference as in FLIC theory for epi-fluorescence.

4.3.G Calculation of emission

The pinhole of the confocal microscope used here has a diameter of $100\mu\text{m}$. Therefore the lateral masking is only $2.5\mu\text{m}$ with the 40fold objective ($\text{NA}=1.15$) and $1.7\mu\text{m}$ with the 60fold objective ($\text{NA}=0.9$) as compared to a lateral resolution of $0.25\mu\text{m}$ and $0.34\mu\text{m}$. Therefore also the z-resolution is only weakly masked and the distortion of the epi-fluorescent z-focus should be negligible and the use of the epi-fluorescent FLIC theory applicable. We therefore calculate the emission P_{em} as given in [4.11] and also correct for the lifetime with [4.16].

4.4 Using Confocal FLIC

Confocal FLIC theory is tested and used to measure cleft thickness of adsorbed membrane. The dye angle of BNBIQ is measured to 45° .

4.4.A Confocal FLIC on adsorbed membrane

It is found that it is necessary to fit the numerical apertures in confocal FLIC to match the experiments. With the fitted numerical apertures, confocal FLIC measures the same distances as epi-fluorescent FLIC on the same vesicle preparation as in 4.2.F on page 65. Two different objectives were used: 40x with $\text{NA}=1.15$ also used to measure all voltage sensitive measurements and 60x with $\text{NA}=0.9$. We stick to the optical constants of Table 4.1 on page 65 but now we excite the dye with 488nm - the emission filter is the same: a bandpass filter from 575-645nm. And we have to adjust the sensitivity of the detector to the spectral sensitivity of the photomultiplier (Fig 4.4). For all calculations we set $z_0=150\text{nm}$ by assuming that we focussed in the middle of the oxide stack. No

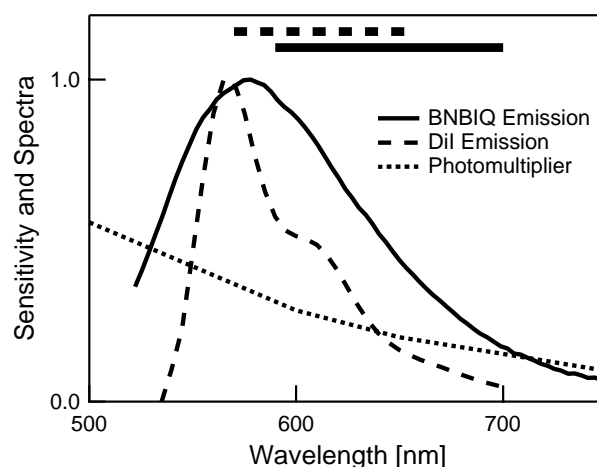


Fig 4.4 Sensitivity of the photomultiplier. Emission spectra used to calculate the confocal FLIC theory for BNBIQ and the standard FLIC dye DiI. The emission filter range is indicated as bar above the plots.

change in the pattern of FLIC intensity was detected when the z-focus is moved although no systematical investigation was undertaken. Obviously the confocal FLIC theory does not describe the measurements with the numerical aperture numbers of the objective (Fig 4.5). It could be speculated that the confocal optics is masking the aperture of the objective. For excitation this is not true as the laser illuminates the whole backside aperture of the objective. I would speculate that the z-shape of the focus is not yet properly modelled (despite of the correct integral [4.17])

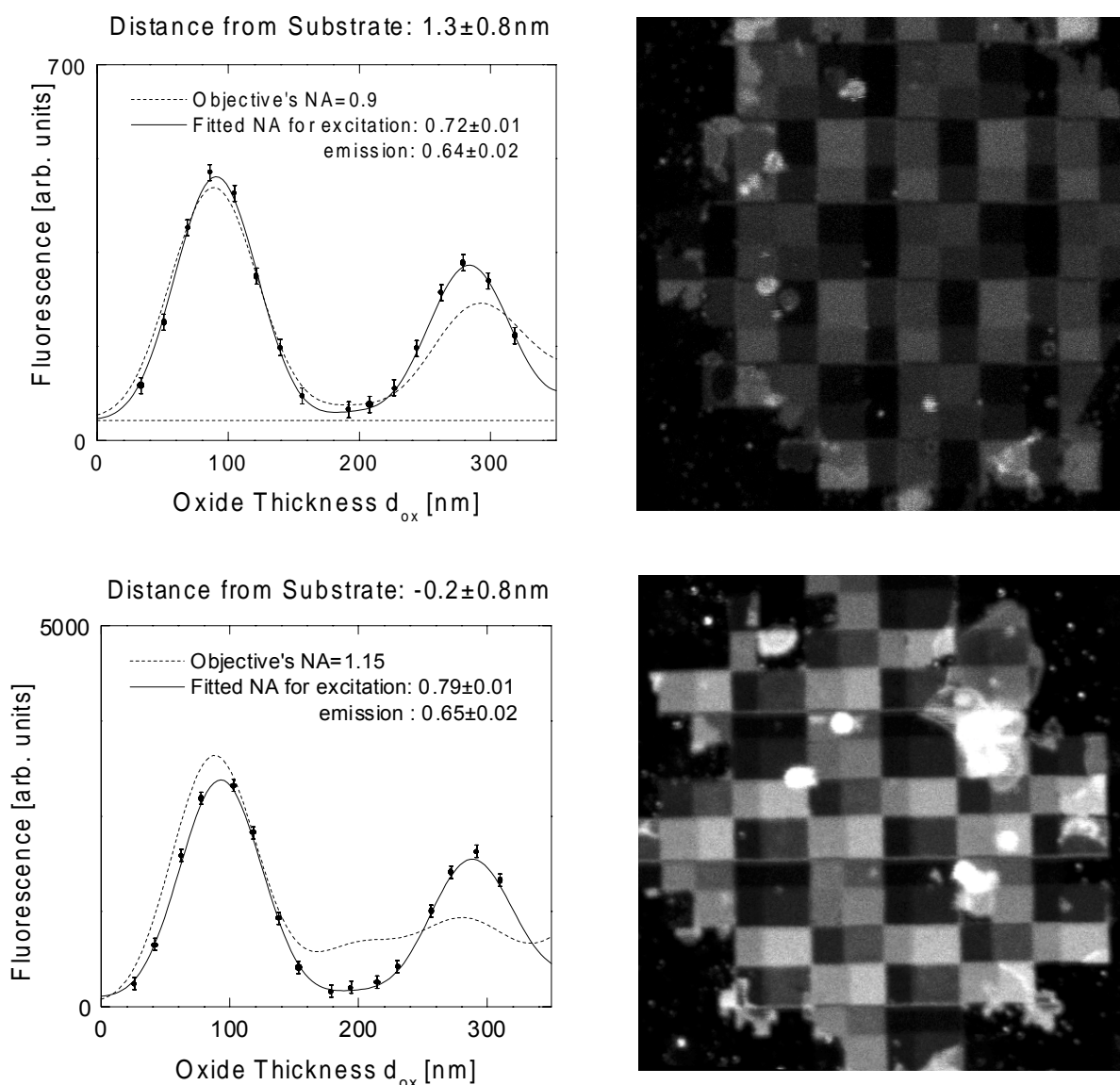


Fig 4.5 Measuring distance of adsorbed giant vesicle membranes with confocal FLIC theory. We have to fit the effective numerical aperture to describe the measurements. We used a 60x objective with numerical aperture 0.9 (above) and a 40x with NA=1.15 (below). But the fitted distances are precise with $1.3\pm 0.8\text{nm}$ (60x, above) and $-0.2\pm 0.8\text{nm}$ (40x, below).

and is only mimicked by the numerical aperture. As the model for the focus in a confocal microscope does explicitly calculate the emission in a coherent way, it might be still necessary to find a coherent calculation also for the emission. But the need to calculate the multilayer interference requests a nonscalar coherent focus model with an electrical field vector. Two other approximations could be envisaged: first we use the epi-fluorescence FLIC and add as an envelope the z-focus intensity for excitation and emission. Or second we use the standard scalar focus integrations using fourier transformation, neglect the multilayer interference and use an electrical field vector parallel to the surface as the electrical field vector perpendicular vanishes in the coherent calculation anyway. I'd suspect that both do not give more convincing theoretical frameworks. It must be noted that all confocal calculations suffer from approximations which are only true for

rather small apertures. The behavior of the objective for high apertures in coherent calculations is not exactly known. We also fitted the epi-fluorescence FLIC theory to the data with fitted numerical apertures as collected in Table 4.2:

TABLE 4.2. Results of Confocal and Epi-Fluorescent FLIC Theory on adsorbed giant vesicle membrane taken with a confocal microscope.

Fitted parameter		Confocal FLIC	Epi-Fluorescence FLIC
60x NA=0.9	NA _{Excitation}	0.72	0.68
	NA _{Emission}	0.64	0.72
	Distance	1.3nm	0.5nm
40x NA=1.15	NA _{Excitation}	0.79	0.83
	NA _{Emission}	0.65	0.79
	Distance	-0.2nm	1.1nm

Nevertheless all fitted distances are very precise - no matter which model we take. Therefore the confocal FLIC theory and the confocal microscope can be used to fit membrane substrate distances.

4.4.B Using confocal FLIC to measure the angle of BNBIQ

With the fitted numerical apertures we can obtain the angle of BNBIQ in adsorbed giant vesicle membrane. Only confocal FLIC theory fits the same angle for different objectives. The adsorbed giant vesicle membrane was now stained with a FCS-BNBIQ solution as described in paragraph 4.1.C on page 61. Confocal images were taken. Since the intensity of the fluorescence images was too dim it was impossible to get pictures from the epi-fluorescence microscope. Thus we cannot compare the confocal results with standard FLIC measurements directly. But from [Lambacher 1994] we have estimates of the dye angle around 40° for the quite similar dye di8-Anepps in a touch-down bilayer.

We now set the numerical apertures to the values fitted in the previous paragraph. Also we set the value of the membrane distance to the value 1.1nm ([Fromherz 1999] and above paragraph). We use the emission spectrum of BNBIQ in HEK cells (Fig 4.2 on page 61). The measurement was performed with the same emission filter from 590-700nm as used for the voltage sensitive fluorescence imaging. No lifetime correction was calculated with BNBIQ. The angle of the dye was the only fitted parameter.

The confocal FLIC theory clearly shows the different dye angle of BNBIQ in the membrane and nicely fits the measurements. We obtain a very similar angle of around 45° independent of the objective used. The aperture-adjusted epi-fluorescence FLIC theory does not give the correct angles (Table 4.3). We must keep in mind that for coherent excitation the angle of the dye is only a scaling factor which does not modify the shape of the FLIC intensity curve (equation [4.45]). Only the emission can account for the angle dependence. This indicates that the emission calcula-

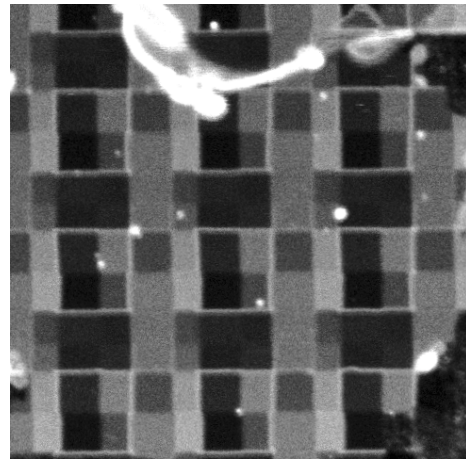
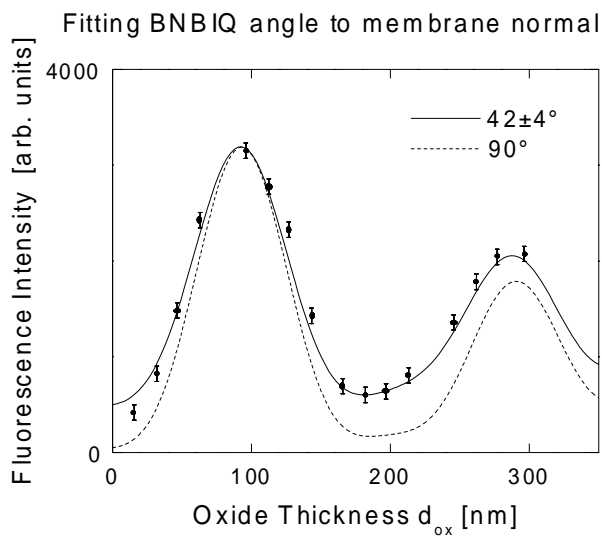
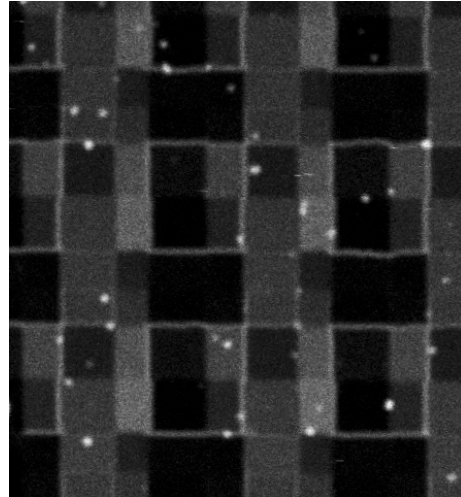
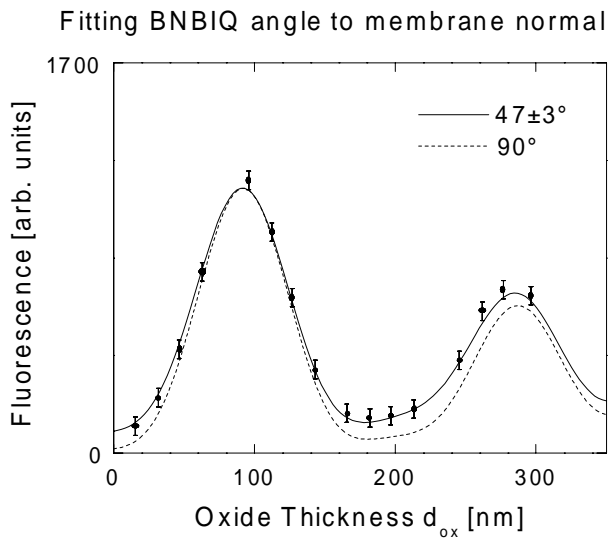


Fig 4.6 Measuring the angle to the membrane normal of BNBIQ in adsorbed giant vesicle membranes with confocal FLIC theory. The dye angle is the only fitted parameter. We find $47\pm 3^\circ$ for the 60x objective (above) and $42\pm 4^\circ$ for the 40x objective (below).

tion is not symmetric to the confocal excitation. On the other hand we see here the limit of the aperture-adjusted epi-fluorescence FLIC theory. It can describe the correct distance but not the correct angle.

TABLE 4.3. Dye angle to the membrane normal of BNBIQ as fitted with Confocal and Epi-Fluorescent FLIC Theory in adsorbed giant vesicle membrane.

		Confocal FLIC	Epi-Fluorescence FLIC
60x NA=0.9	Dye angle	$47\pm 3^\circ$	$49\pm 5^\circ$
40x NA=1.15	Dye angle	$42\pm 4^\circ$	$30\pm 2^\circ$

4.4.C Two lambda confocal FLIC

In extending proposals in [Braun 1996] for the use of FLIC microscopy with different wavelengths, a new approach was envisaged but not yet experimentally implemented. The idea is to get rid of the oxide steps for performing a distance measurement with FLIC. Since the confocal microscope reduces the background intensity from the upper membranes with its pinhole to zero, we only have to deal with two fitting parameters when using FLIC with a confocal microscope: intensity scaling and cleft thickness. Most contrast from different wavelengths could be gained, if we would combine a pulsed femtosecond laser for two-photon imaging and a standard argon ion laser for one-photon imaging within the same confocal microscope. Thus we would be allowed to measure images in both modes shortly after each other. It would be necessary to calibrate the light sources to a fixed intensity ratio. Calibration of the method could be easily achieved with a FLIC chip with different oxide thicknesses and comparing with the standard FLIC method from the same images. Therefore we could gain an intensity ratio from both images and eliminate the second fitting parameter of intensity scaling.

The fluorescence intensity for one and two-photon imaging versus cleft thickness is calculated in Fig 4.7. Good contrast can be obtained for an oxide thickness of 175nm and realistic values of the wavelength for excitation with 488nm and 800nm. Care has to be taken not to use too large wavelengths since the silicon chip becomes transparent in the IR. We used for the calculation the parameters of the 60x objective and a layer system for cells as used in [Braun 1997] or [Braun 1998]. The calculated fluorescence intensity versus cleft thickness can be found in Fig 4.7 on the left side. On the right side of Fig 4.7 the characteristic of fluorescence ratio versus cleft thickness proves that the ratio has a high thickness sensitivity for cleft thicknesses from 0nm to 120nm. On top of a homogeneous oxide thickness of 175nm the intensity ratio has values from 0.04 to 1.2.

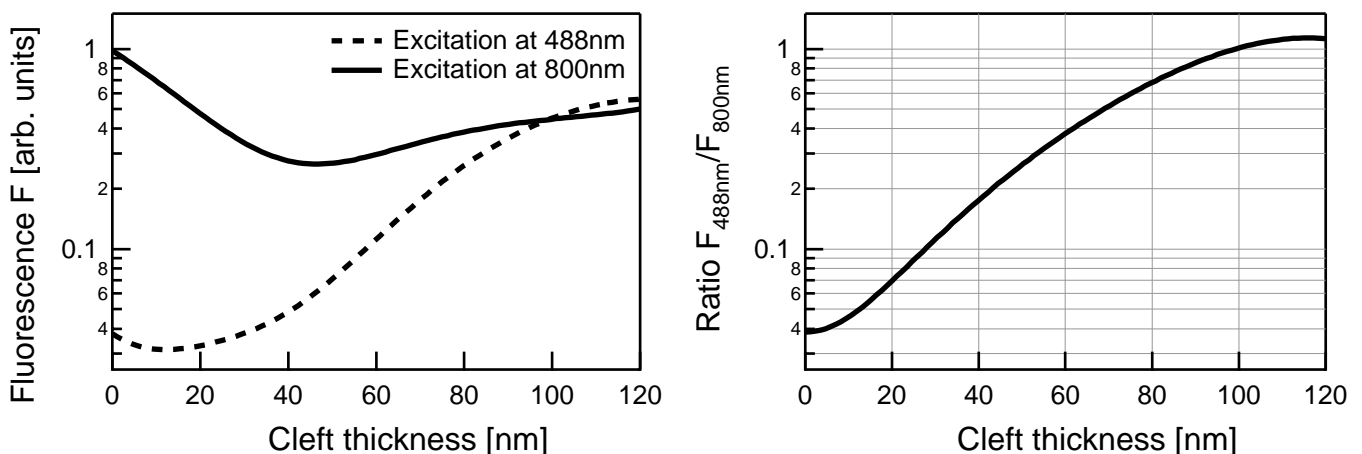


Fig 4.7 Fluorescence ratio characteristic of two-lambda-FLIC. Theoretical estimates show that the image ratio between a one-photon FLIC image excited at 488nm and two-photon FLIC image at 800nm taken above a plane oxide thickness of 175nm exhibits a good contrast for detecting cleft thickness without oxide steps.

4.5 Maximizing the fluorescence signal

The dependence of fluorescence intensity on dye angle and oxide thickness is shown. To get a good signal to noise ratio in voltage sensitive fluorescence, the oxide thickness should be small for thick junction clefts and larger for small junction clefts.

4.5.A Intensity dependence on oxide thickness and angle

The dye angle and the cleft thickness differently modulate the fluorescence intensity on oxide thicknesses of 10nm and 50nm. As the goal is to measure the fluorescence of the lower junction membrane, the fluorescence is always modulated by fluorescence interference due to the mirror of the silicon chip below. Two different chips are used: with 50nm oxide and with 10nm oxide. We plot the fluorescence intensity versus the cleft thickness in Fig 4.8. On 50nm oxide the fluorescence is much higher and less sensitive to the cleft thickness. But the junction membrane potential from capacitive stimulation is diminished also. This relationship is discussed in 4.5.B on page 77.

Here we focus on the dependence of the fluorescence intensity from the angle of the dye's transition dipole to the membrane normal. This is not only an effect of the interference in front of silicon. As voltage sensitive dyes which use the Stark effect are more sensitive if they make a small angle to the membrane normal, we have the problem of small fluorescence intensity for these dyes for the junction membrane. We must also keep in mind that intensity fluctuations in the membrane can very well be angle fluctuations of the dye. Both effects, dependence on cleft thickness and dye angle are plotted in Fig 4.8:

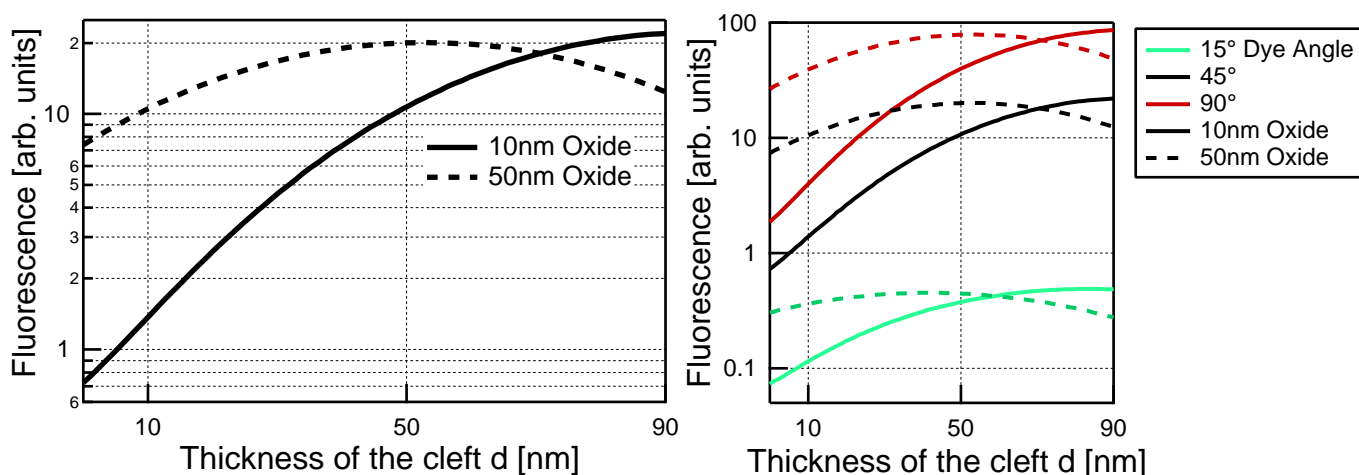


Fig 4.8 Cleft thickness dependence of fluorescence due to interference is higher for 10nm oxide. This dependence is further masked by possible different dye angles to the membrane normal (right). Especially for low angles the fluorescence intensity is diminished dramatically.

4.5.B Fluorescence small-signal better for thicker oxide?

The fluorescence intensity is much higher on 50nm oxide and less sensitive to the cleft thickness, but we cannot excite the membrane potential to too high values since the capacitance of the spot is diminished by a factor of five with respect to a 10nm thick oxide. On 10nm oxide we have a lower fluorescence intensity. The membrane potential is approximately inversely proportional to the oxide thickness. We find for the voltage sensitive fraction of the fluorescence signal ΔF in good approximation:

$$\Delta F = \frac{S \cdot I(d_{\text{ox}}, d_{\text{cleft}})}{d_{\text{ox}}} \quad [4.46]$$

We can plot this for the cleft thicknesses of 10nm and 50nm versus the oxide thickness and find:

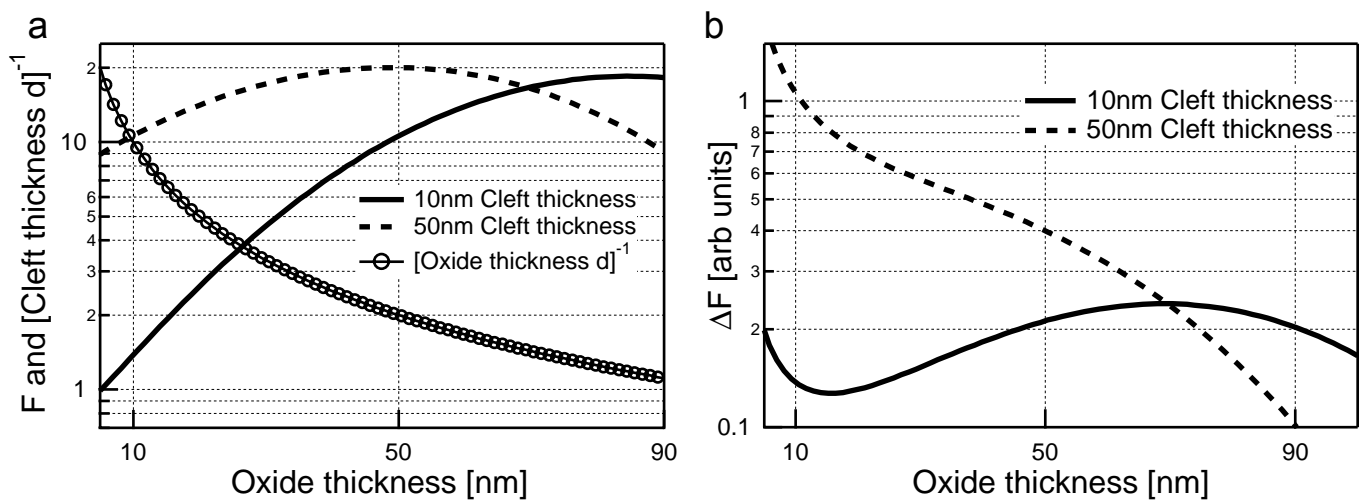


Fig 4.9 (a) For small oxide thickness, we find high membrane potential (circles). But also fluorescence is diminished (lines). (b) Multiplied both together gives an estimation of ΔF and therefore an estimation of signal to noise ratio. Both calculations are done for a small cleft thickness of 10nm (e.g. Ghosts) and 50nm (e.g. HEK cells, rat Neurons, Astrocytes...). For a small cleft thickness it is better to use an oxide of 50-90nm, for wider clefts we better choose a smaller oxide thickness.

But we must keep in mind that we can apply up to 10V at a 50nm oxide and only around 6V to a 10nm oxide. This means that also for small cleft thicknesses a higher oxide thickness has advantages. Furthermore the oxide cannot be cleaned away so easily and does not have much impact on the errors involved. Last but not least the time constant of the chip is accordingly smaller for thicker oxide, an effect which can of course be also achieved with a smaller stimulation electrode.

Confocal microscope

Scanning, Photomultiplier and Software Lock-In

5.1 Preliminary experiments 80

Preliminary experiments were done with a contacted FLIC-Chip and a photodiode mounted on an epi-fluorescence microscope. The goal was to get a first impression of the experimental problems without optimizing a tailored setup.

5.2 Confocal microscope and LabView interface 81

In order to control the Olympus laser scanning confocal microscope by computer, a LabView interface called FluoLab was developed in collaboration with Olympus. An Argon ion laser is coupled to the microscope with fibre optics.

5.3 Software lock-in 86

The real and imaginary part with respect to a sinusoidal reference is calculated by software. Amplitude and phase of relative small-signal fluorescence $\Delta F/F$ is obtained. The lock-in algorithm was tested under conditions typical for subsequent measurements.

5.4 Photomultiplier and amplifier 88

The frequency dependent intensity of an LED was used to measure the transfer function of the photomultiplier amplifier. Photon counting was tested.

5.1 Preliminary experiments

Preliminary experiments were done with a contacted FLIC-Chip and a photodiode mounted on an epi-fluorescence microscope. The goal was to get a first impression of the experimental problems without optimizing a tailored setup.

5.1.A Contacted FLIC-Chip with a locked photodiode

The chip for a preliminary experiment was a post-processed FLIC chip [Braun 1997]. It had oxide steps of height 15,60,100 and 150nm and was metallized with 200nm chrome on the back. The time constant of the chip was around 1 μ s and seemed fast enough for experiments. Later it turned out that the reason for the fast time constant was a diminished capacitance of the silicon oxide due to a serial capacitance in the silicon. This was produced by the surface depletion region of the low doped silicon below the oxide.

A photodiode with amplifier was adapted to a Zeiss Axioskop microscope and amplified up to a cutoff frequency of 4 μ s. The photodiode detected an area of 11x11 μ m² through a 100x water immersion objective. The diode signal was measured with a SR-830DSP Lock-In amplifier (Stanford Research). I cultured GD25 cells for 1-3 days and stained them with 8 μ l of a 1mM solution of RH421 in ethanol. The dye solution was directly injected to 3ml of the medium. The bath was always held at negative potential with respect to the chip. A 100kHz voltage ramp with 1.5V amplitude was applied. The Lock-In showed a fluorescence amplitude of $\Delta F=1\mu V$ when no voltage was applied to the chip and around $\Delta F=3\mu V$ with applied voltage. From a hardly measurable DC diode signal of $F=1mV$ we obtain an amplitude $\Delta F/F=0.2\%$. This was far below the expected value of >20%. But it proved that the signal existed.

5.1.B Conclusions from first experiments

The preliminary experiments showed a very faint signal and indicated the following problems and requirements:

- 1 μ s time resolution seems to be necessary. Detectors with this speed are typically zero dimensional. Therefore a scanning technique has to be used if the imaging of voltage maps should be achieved.
- When using an external Lock-In for measuring ΔF , measuring F could pose a problem. Typically only the small-signal ΔF is measured by lock-in amplifiers.
- It is absolutely necessary to fabricate the spot oxide on highly doped silicon. Otherwise the surface depletion region of the MOS diode below the spot reduces the capacitance of the spot dramatically.
- On flat cells the free cell membrane exhibits a fluorescence signal of almost equal amplitude than the junction membrane, but with inverse sign. If both membranes are not properly separated by the optical setup, the signals could cancel or diminish each other.

5.2 Confocal microscope and LabView interface

In order to control the Olympus laser scanning confocal microscope by computer, a LabView interface called FluoLab was developed in collaboration with Olympus. An Argon ion laser is coupled to the microscope with fibre optics.

5.2.A The Laser scanning confocal microscope

With the requirements listed in the previous paragraph, a confocal laser scanning microscope is the best tool to perform the measurements. It provides a good z-resolution, can scan and image at any rate and has a built in light detector in the 500kHz regime. The laser scanning system FluoView (Olympus) with an upright BX50WI microscope with fixed stage was used (Fig 5.1).

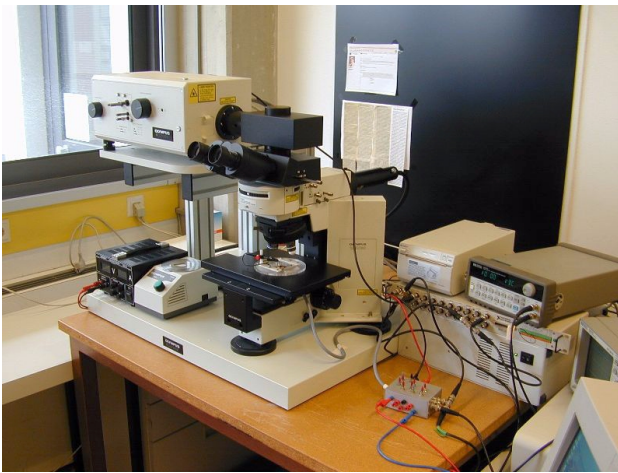


Fig 5.1 Olympus FluoView confocal scanning microscope. The scanning box can be found on the left side of the microscope. It gets the laser light from a fibre, divides emission and excitation, scans both with piezoelectric mirrors, includes the pinhole and can detect the emission with two photomultipliers. It is coupled via tubus optics to the top of the microscope BX50WI. The photomultiplier signal is amplified and delivered via BNC connectors to a 5MHz 12Bit acquisition card. The microscope is controlled through an interface card and a control box.

The computer controls the confocal microscope from LabView with the self-written interface software FluoLab. A separate AD-card acquires the photomultiplier signal and a GPIB interface card other instruments such as a function generator and an oscilloscope is controlled. A signal flow chart of the setup is presented in Fig 5.2.

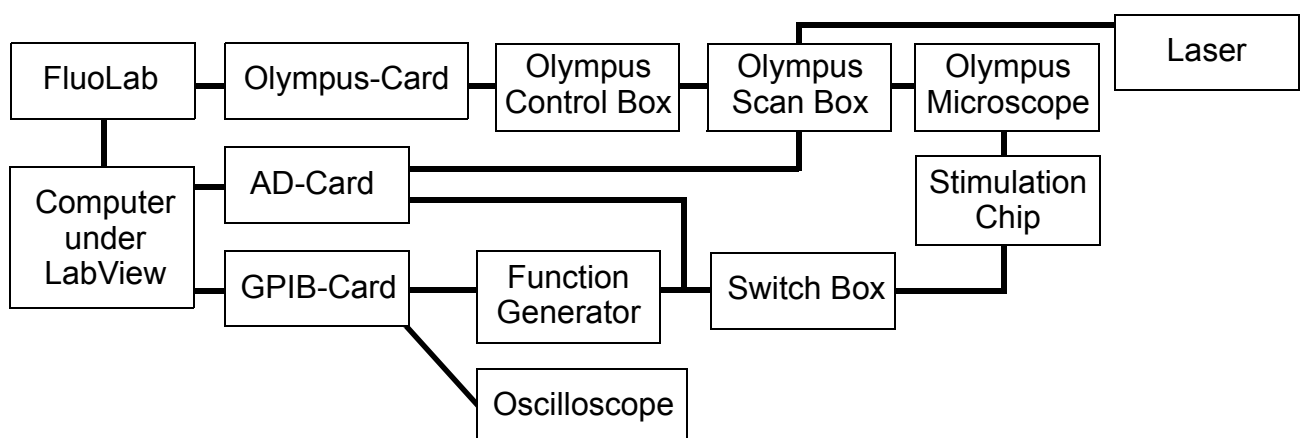


Fig 5.2 Signal flow of the setup. The computer talks with Labview to the setup through three channels: FluoLab controls the confocal microscope, the AD-card reads the photomultiplier and the GPIB-card controls the function generator and the oscilloscope.

The laser beam is delivered into the scanning box from the laser in another room through a single mode fibre. In the scanning box the laser light is dimmed by grey filters, passed through a beam blanker, is scanned with piezo-electric mirrors and runs through a tubus optics to the microscope. The emission light returns from the microscope, is scanned by the same piezo mirrors, split from excitation by a dichroic mirror and passes through two thin glasses into the pinhole. These glasses can be tilted to adjust the emission light through the pinhole. Behind the pinhole we find fluorescence filters and two photomultipliers. The photomultiplier current is amplified in the scanning box to an analog voltage signal from 0V to 5V and delivered via BNC connectors to the Olympus control box. In our measurements, this voltage signal is sampled by a National Instruments PCI 6110E 5MHz 12Bit 4 channel analog digital converter card inside a 200MHz Pentium Windows NT system. The control of the z-scan, Photomultiplier voltage, beam blanker and the mirrors was done by the Olympus control box via the self written LabView interface software FluoLab running on the same computer (Fig 5.2). The upright BX50WI microscope with fixed stage is a complete fluorescence microscope with fluorescent filters, a Xenon high pressure lamp and an Abbe condenser. The Abbe condenser is important for a good contrast on silicon. The Xenon lamp is placed in a separate case and is coupled to the microscope with a thick gel light fibre. It does not need to be adjusted and can be dimmed. Together with the Abbe condenser it was possible to use it both in bright field and in fluorescence mode.



Fig 5.3 High aperture water objective. With 40x magnification, 1.15 numerical aperture without plane correction and a built-in cover slip this objective offers a maximum excitation and emission efficiency. The working distance is 260 μ m. The chip design was heavily influenced by the large size of the objective.

Excitation and emission efficiency is maximized with a special high aperture water objective. Usually these objectives are used with a thin cover slip at inverted microscopes. For upright geometries Olympus offered a prototype where the cover slip was already cemented into the objective. It had a 40x magnification, a numerical aperture of 1.15 and a working distance of 260 μ m. It was not plane corrected to obtain maximum transmission. The chip design had to be adapted to this objective as it is rather broad (11mm) and very flat (17°) at the front (Fig 5.3).

A Stabilite 2017 Argon ion laser (Spectra physics) was used. It can be tuned to different wavelengths for the use with different dyes. The laser was used at 488nm delivering around 1W, dimmed down by several grey glasses. The laser was connected to the confocal microscope with a 10m long single mode fibre (HPC-50.66K 3.1/125/900/2800, Diamond, Gröbenzell). The input coupler was adapted from the input coupler at the setup of Karsten Kottig (Fig 5.4). As the microscope was installed in a different room, coupling had to be adjusted by measuring the light leaving the fibre with a photodiode. The laser power at the focus of the microscope was typically 5-15 μ W.

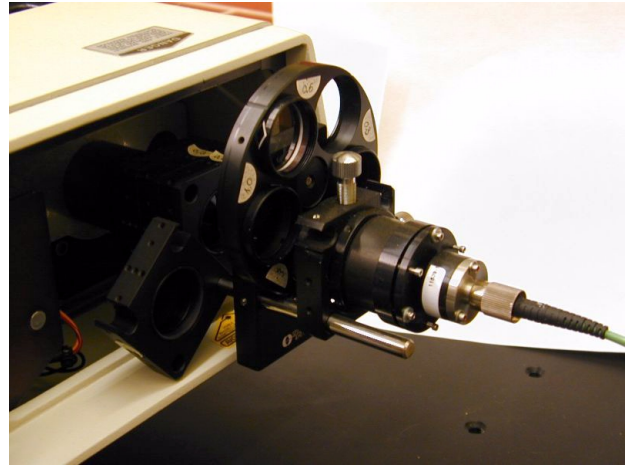


Fig 5.4 Argon ion laser used for the confocal microscope (left). It can be switched to different wavelengths and couples to a single mode fibre (right)

5.2.B Labview Interface FluoLab

The standard scanning software of the confocal microscope generates TTL signals at the control box for each scanned line and each scanned image. Therefore it is possible to synchronize image acquisition from a second computer to obtain the raw photomultiplier signal. But the scanning modes of the standard Fluoview software were much too fast ($<100\mu\text{s}/\text{pixel}$) for acquiring lock-in or transient data with reasonable signal/noise ratio. Therefore control of the microscope had to be performed with self written software. In collaboration with Olympus, I developed a LabView interface, called FluoLab (Fig 5.5) which controls all vital parts of the microscope such as the piezo mirrors, the laser shutter, the photomultiplier voltages and the z-stage. The photomultiplier signal itself is acquired by analog digital converters in the computer and not by the Olympus control box. Within FluoLab all hardware related controls are implemented by calls to the dynamic library gbx.dll found in the Fluoview directory. The calls are documented in Table 5.1. These calls were worked into small LabView VIs (VI is a subroutine under LabView) which include error handling code. They can be found in FluoLab.llb (Fig 5.5) together with some example VIs in FluoLab_Demo.llb.

With the FluoLab interface it was for example possible to write a scanning program My_FluoView.vi which mimicks many of the features of the Olympus Software FluoView. In the context of the measurements it was used as a subroutine to find good cells on the chip. An important feature was the ability to directly scan a region of interest defined in a previous scan. A snapshot of this program is presented in (Fig 5.6).

Basic FluoLab VIs

VIs from FluoLab.lib

Initialize		InitMicroscope.vi Init the software and the hardware.
Close		CloseMicroscope.vi Ends a LSM-Session
Laser shutter control		LaserShutter.vi Does open/close the laser shutter
Photomultiplier voltage		Set PM Voltage.vi Sets the voltage of both PMs.
Move z stage		Step z Motor.vi Relatively moves the z stage
Next Z Move		Next Z Move.vi Performs a Z-Scan (called from a loop)
Basic mirror control X Y		SetMirrorX.vi and SetMirrorY.vi Set the mirror to absolute position
Prepare a scan		CalcScanVoltage.vi Calculates coordinates for bidirectional scan
Prepare Circle / Line Scan		CalcCircleVoltages.vi and CalcLineVoltages.vi Calculates coordinates for a circle or a line scan
Scan		Scan XY Line.vi Scans along an arbitrary line
Extract image		InsertInImage.vi Sets the data along an arbitrary line into an image
Special Scan Next Line		Special Scan Next Line.vi Scans one line from a XYZ-Cube (called from a loop)

Fig 5.5 FluoLab Basic VIs used to control the microscope. These self written control VIs are mainly built interfacing to the dll-calls of Table 5.1.

TABLE 5.1. DLL-Calls of gbx.dll used to control the microscope

<code>int16 idaVbInit(int16 *ConfigVector);</code>	Init the hardware. ConfigVector=0
<code>void lsmMute(int16 arg1);</code>	Mirrors must be unmuted (arg1=0) before any scanning. Otherwise they are blocked.
<code>int16 idaSetDACInitialValue (int16 dac, int16 value);</code>	Sets the mirror position (dac=1 for X, dac=2 for Y) with values X=-16000..16000 and Y=-7000..7000. Too wild movements could collide the mirrors.
<code>void lsmSetPMT1and2 (int16 dac1val, int16 Dac2Val);</code>	Sets PM voltage of PM1 and PM2. Dac values are scaled from a table (see Set_PM_Voltage.vi)
<code>void lsmLaserShutter(int16 MakeOpen);</code>	Move the beam blanker. MakeOpen=1 to open, 0 to close.
<code>void zMotorFree(int16 free);</code>	Free the z-motor (free=1) or prepare it to be moved by software (free=0)
<code>int16 zMotorSpin(int32 nanometers);</code>	Move z-motor relative by nanometers. Values above 10µm are not allowed.

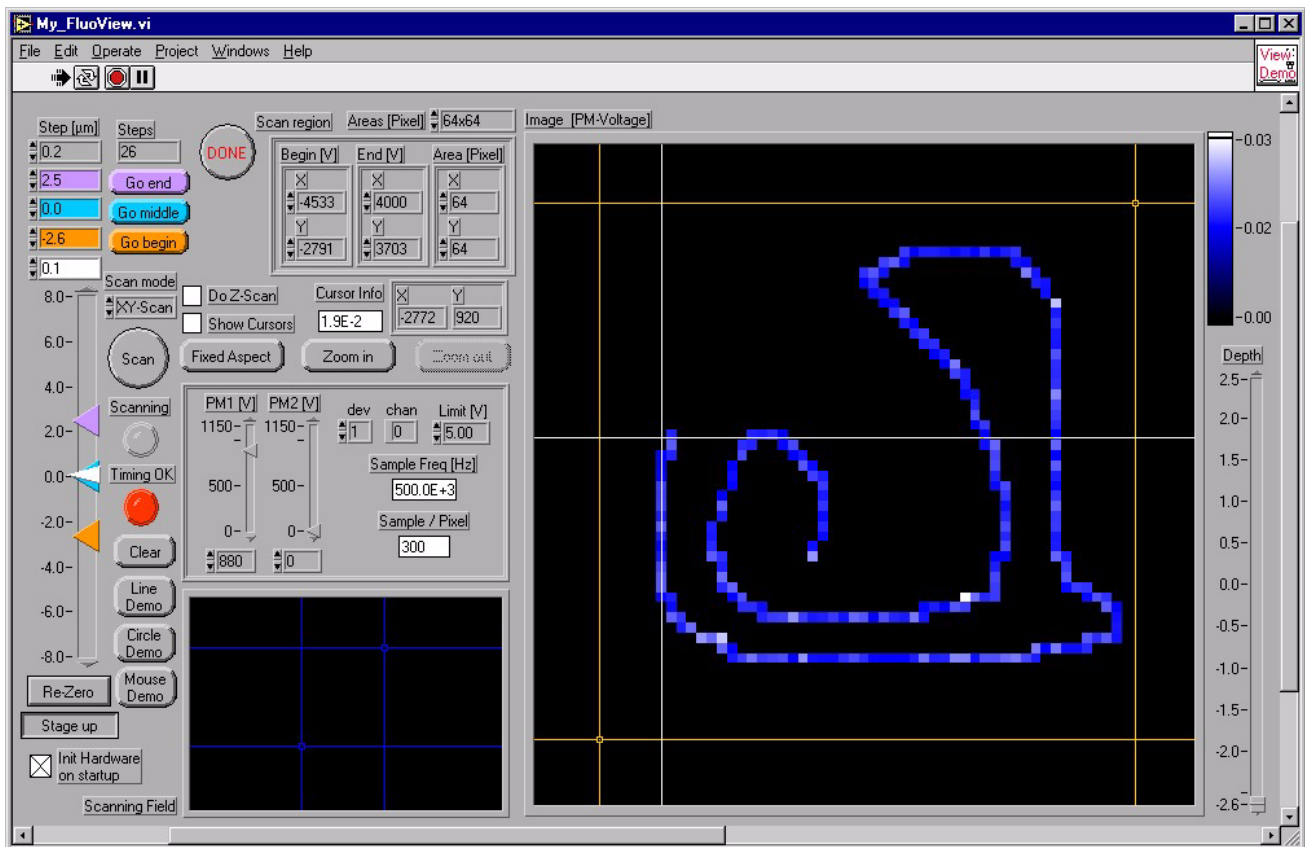


Fig 5.6 Control panel of the MyFluoView.vi used to find the region of interest. It can be used to take 2D or 3D images and to zoom into defined regions. It is used as a sub program to find and select the cells.

The FluoLab software has some minor drawbacks:

- The maximal pixel rate is considerably lower. FLuoLab can only scan up to pixel frequencies of 2kHz whereas FluoView scans rectangles at 250kHz. But FLuoLab can precisely scan along arbitrarily defined lines.
- As the AD-Card and the FluoLab XY-Scan are synchronized either by the AD-Card's counter or by the pentium processor clock, they desynchronize at scans larger than some 256x256 pixels. This problem can be solved with a line-based XY-Scan
- The X-Mirror and the Y-Mirror cannot be controlled simultaneously in the kHz-domain.

On the other hand FluoLab allows to control the whole measurement process centralized within LabView. From the same computer LabView controlled with FluoLab the confocal scanning, with National Instruments routines the acquisition of fluorescence and chip voltage and with GPIB commands the function generator to apply the chip voltage patterns and the oscilloscope to measure the chip current. Programming in LabView was very helpful as it is easy to debug. Although LabView is already very fast, it can be further accelerated at the hot spots with CIN nodes written and compiled in C (Microsoft Visual C++ 4.5) and linked to LabView code.

5.3 Software lock-in

The real and imaginary part with respect to a sinusoidal reference is calculated by software. Amplitude and phase of relative small-signal fluorescence $\Delta F/F$ is obtained. The lock-in algorithm was tested under conditions typical for subsequent measurements.

5.3.A Software lock-in from correlation functions

The way of calculating real and imaginary part of a sinusoidal signal with correlation functions by software is described. An attempt to use a custom lock-in amplifier was not undertaken as synchronization to the imaging process is difficult to achieve. Also our lock-in amplifiers did not reach frequencies above 100kHz. Therefore both price and flexibility of a software solution was superior. The algorithm was programmed in pure C as a code interface node within LabView and thus offered maximum performance.

The amplified photomultiplier current $F_{\text{raw}}(t)$ is sampled at 5MHz with 12bit. The reference sinusoidal with angular frequency ω was additionally sampled in $R_x(t)$. The reference signal is in our case the voltage applied to the chip. From correlating $F_{\text{raw}}(t)$ and $R_x(t)$ the small-signal $\Delta F_x(\omega)$ of $F_{\text{raw}}(t)$ at frequency ω and with zero phase to the reference can be calculated. Care has been taken to be insensitive to offsets in $F_{\text{raw}}(t)$ and to the amplitude of the reference $R_x(t)$ ($\langle \rangle$ is the average over time):

$$\Delta F_x(\omega) = \sqrt{2} \frac{\langle R_x F_{\text{raw}} \rangle - \langle R_x \rangle \langle F_{\text{raw}} \rangle}{\sqrt{\langle R_x R_x \rangle - \langle R_x \rangle \langle R_x \rangle}} \quad [5.1]$$

One might notice that the above calculation scheme is not the fastest as we could also use the fast fourier transform as applied in custom lock-ins. However the above scheme has the main advantage that we don't have to calculate or fit the phase of the reference. Furthermore, possible time drifts between the AD converter and the function generator producing the reference signal do not have an influence.

To obtain the small-signal $\Delta F_y(\omega)$ which has a phase shift of 90° to the reference $R_x(t)$ we use a 90° shifted reference $R_y(t)$ for the calculation:

$$\Delta F_y(\omega) = \sqrt{2} \frac{\langle R_y F_{\text{raw}} \rangle - \langle R_y \rangle \langle F_{\text{raw}} \rangle}{\sqrt{\langle R_y R_y \rangle - \langle R_y \rangle \langle R_y \rangle}} \quad [5.2]$$

Both small-signals are combined into a complex amplitude:

$$\Delta F_{\text{complex}}(\omega) = \Delta F_x(\omega) + i \Delta F_y(\omega) \quad [5.3]$$

with amplitude and phase defined by:

$$\Delta F(\omega) = |\Delta F_{\text{complex}}(\omega)| \quad \Delta F_{\text{phase}}(\omega) = \text{atan} \frac{\Delta F_y(\omega)}{\Delta F_x(\omega)} \quad [5.4]$$

The average fluorescence signal is obtained simply from

$$F = \langle F_{\text{raw}} \rangle \quad [5.5]$$

and therefore it is easy to calculate the relative fluorescence signal $\Delta F(\omega)/F$ which is proportional to the membrane potential in voltage sensitive fluorescence measurements.

5.3.B Testing the software Lock-In

The first test is that $F_{\text{raw}}(t)=R_x(t)$ must result in $\Delta F_x(\omega)=1$ and $\Delta F_y(\omega)=0$ and vice versa with $F_{\text{raw}}(t)=R_y(t)$. A second measurement proved that the lock-in amplitude measures the correct small-signal amplitude from an LED. First the voltage to intensity characteristic of the LED was measured.

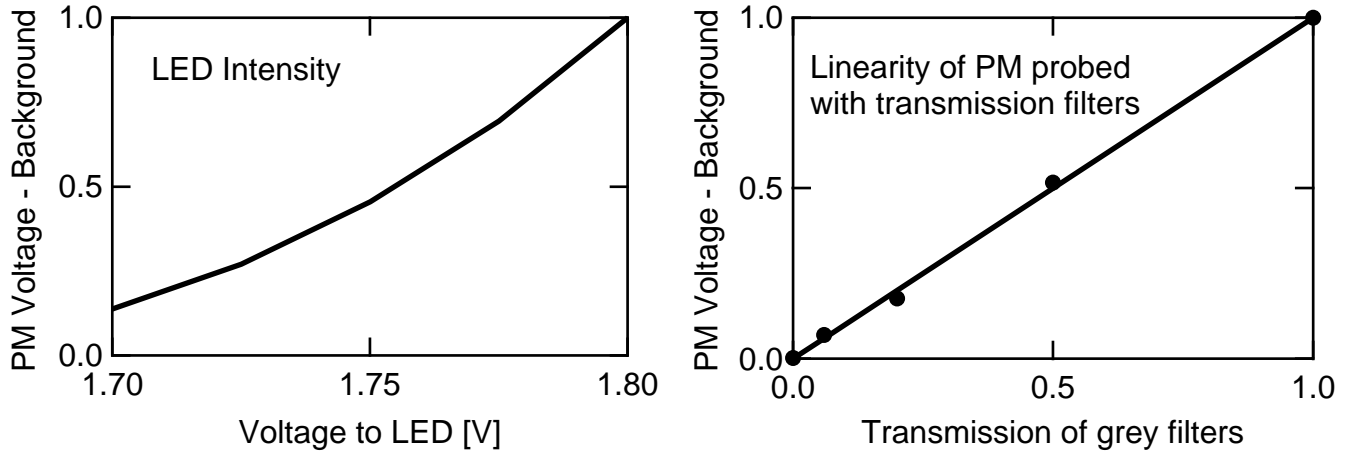


Fig 5.7 Linearity of the Photomultiplier (left) and intensity-voltage characteristic of a red LED (right). Both are preliminary tests for testing the software Lock-In.

The photomultiplier of the laser scan microscope was pointing with a 10x objective and an opened pinhole to a red LED. Voltages from 1.7V to 1.8V were applied to the LED and the averaged photomultiplier voltage signal F was measured (Fig 5.7 right). Linearity of the photomultiplier itself was previously tested while scanning a reflective surface with the laser. Background corrected intensity was proportional to the transmission of the built in grey filters (Fig 5.7 left).

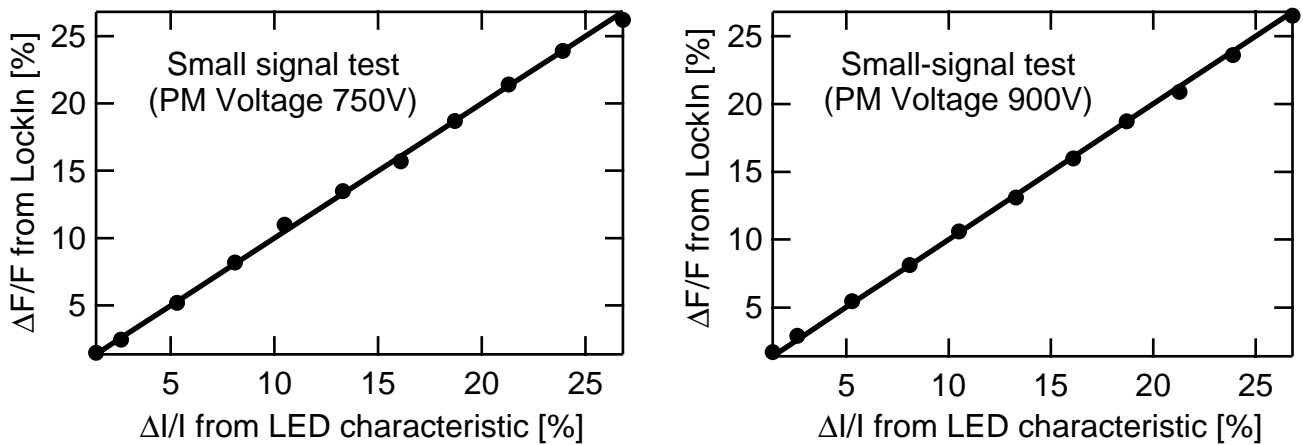


Fig 5.8 Realistic test of photomultiplier and software Lock-In with a red LED. We apply a defined relative intensity variation $\Delta I/I$ at 125kHz and see the same result from the $\Delta F_{\text{amp}}/F$ signal of the software Lock-In.

To test the small-signal amplitude, a defined relative intensity variation $\Delta I/I$ was applied by modulating the LED voltage from 1.2mV to 25mV at 1.75V bias voltage and a frequency of $f=125\text{kHz}$. From the slope of the voltage to intensity characteristic, the voltage variation could be

translated to an intensity variation $\Delta I/I$. The lock-in amplitude $\Delta F/F$ was measured and compared to $\Delta I/I$ in (Fig 5.8). It showed a precise agreement of the lock-in amplitude, independent of the photomultiplier voltage of 750V or 900V.

5.4 Photomultiplier and amplifier

The frequency dependent intensity of an LED was used to measure the transfer function of the photomultiplier amplifier. Photon counting was tested.

5.4.A Transfer function of the photomultiplier amplifier

The transfer function of the photomultiplier amplifier is obtained. Since we have to correct the measurements for the transfer function of the photomultiplier amplifier, this was measured with a red LED directly connected to the function generator. Like for testing the amplitude signal of the software lock-in, a bias of 1.75V was applied to a red LED and the intensity was measured through a 10x with opened pinhole. The LED was modulated with 20mV at frequencies from 20kHz to 1250kHz. The small-signal ΔF and its phase ΔF_{phase} was measured with the software lock-in (Fig 5.9). The amplitude was scaled from low frequency values. It was possible to fit the transfer function with a Bessel low pass filter of order 4 with a limit frequency of $f_0=615\text{kHz}$. A Bessel low pass filter of order 4 is the product of two low pass filters of order 2 with special parametrization of $a_1=0.7743$, $b_1=0.3890$, $a_2=1.3397$, $b_2=0.4889$ and $P=i\omega/f_0$:

$$g_{\text{PM}}(\omega) = \left(\frac{1}{1 + a_1 P + b_1 P^2} \right) \left(\frac{1}{1 + a_2 P + b_2 P^2} \right) \quad [5.6]$$

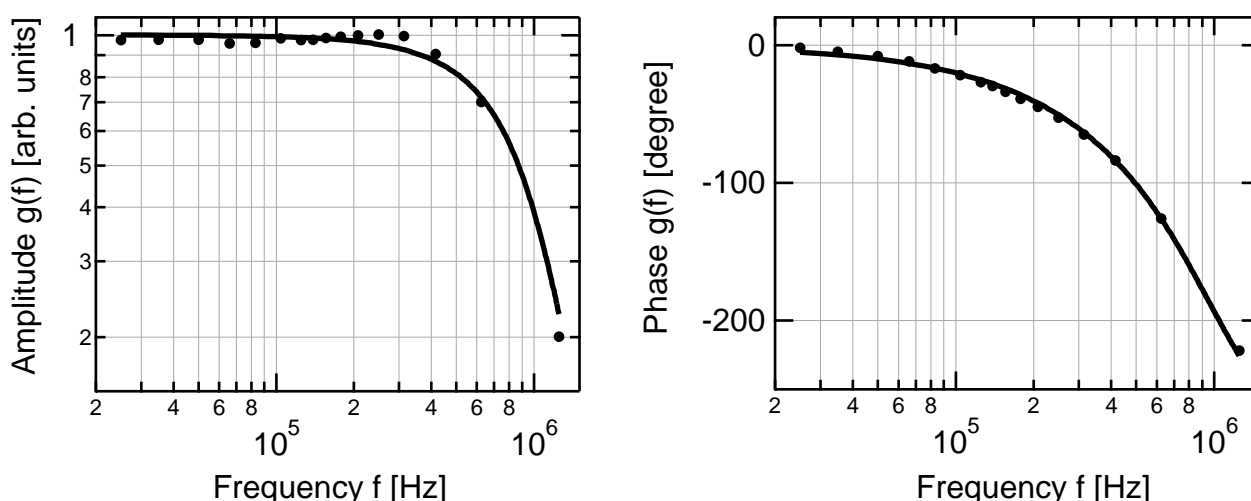


Fig 5.9 Transfer function of the Photomultiplier amplifier as measured with a red LED. It can be fitted with a Bessel low pass filter of order 4 and a limit frequency of 615kHz.

The fitted transfer function is used to correct lock-in and transient measurements. We give often used phase values in Table 5.2:

TABLE 5.2. Phase corrections from photomultiplier amplifier for typical stimulation frequencies.

10kHz	-2.0°	125kHz	-24.6°
25kHz	-4.9°	417kHz	-82.1°
50kHz	-9.9°	625kHz	-122.7°

5.4.B Photon counting

A typical 5MHz sample of the photomultiplier voltage signal at low intensity is given in Fig 5.10a. The peaks are attributed to single photons. The software lock-in technique could also be applied to photon count signals. A peak detector gives a histogram of the peak height which is very typical for photomultipliers (Fig 5.10b). But photon counting did not achieve a better signal to noise ratio, even with the special low background noise tube R2949 (Hamamatsu) specified to use for single photon counting. So I stucked to the analog signal of the R928 delivered with the confocal microscope. Photon counting also yielded a nonlinear characteristic for high intensity as photon peaks could not be separated any more at 5MHz.

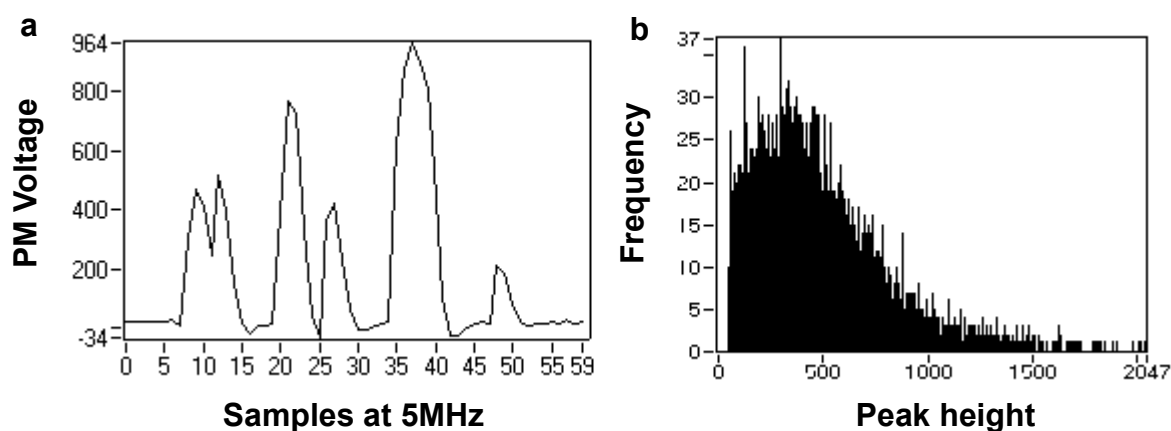


Fig 5.10 (a) Raw signal of the photomultiplier at low light intensity. Peaks are attributed to single photons. Detecting the peaks by software resulted in a typical histogram of the peak height (b). Photon counting was not used as it did not yield a better signal to noise ratio.

Lock-In Imaging

Ghosts, HEK cells, neurons, cell layers and vesicle membranes

6.1 Detailed analysis of a measurement **92**

In order to illustrate the lock-in method in detail, we discuss a measurement of an erythrocyte ghost. The phase and amplitude images are compared with the area and point contact model.

6.2 Erythrocyte ghosts **99**

Measurements of erythrocyte ghosts on poly-lysine yield a junction resistance of $r_j=900\text{M}\Omega$. From 11nm junction thickness we derive a specific junction resistance of $\rho_j=1000\Omega\text{cm}$, increased by a factor of 13 relative to the bulk electrolyte. The time constants are $\tau_j^{\text{JM}}=70\mu\text{s}$ and $t_j^{\text{FM}}=35\mu\text{s}$ at the sustainable junction membrane potential of 650mV.

6.3 Single HEK cells **108**

HEK cells on fibronectin yield a junction resistance of $r_j=3.4\pm 0.9\text{M}\Omega$. From 50nm junction thickness we thus derive a specific junction resistance of $17\pm 5\Omega\text{cm}$, reduced by a factor of 4.4 ± 1.4 as compared to the bulk electrolyte. Junction time constants are $\tau_j=1.5..4\mu\text{s}$, further depending on the junction area. Junction membrane potentials are as high as 500mV.

6.4 Group of HEK cells and Monolayers **116**

Cells in a monolayer enhance the junction time constant by a factor of four. For the junction resistance between the cells $r_{\text{up}}=2.5\text{M}\Omega$ is estimated, a value similar to the junction resistance.

6.5 Rat neurons and astrocytes **124**

Rat nerve cells on poly-lysine yield a junction resistance of $r_j=1.5\text{M}\Omega$. We derive a specific junction resistance of $7.5\Omega\text{cm}$, reduced by a factor of 15 as compared to the bulk. The junction time constant is $\tau_j=1.5\mu\text{s}$ and the junction conductance $g_{\text{JM}}=1500\text{mS}/\text{cm}^2$. Stimulation through a glia monolayer can be performed with similar junction properties.

6.6 Adsorbed giant vesicle membrane **130**

Adsorbed giant vesicle membrane shows a junction resistance above $5\text{G}\Omega$ and a membrane conductance below $0.35\text{mS}/\text{cm}^2$. The dye sensitivity is homogeneous and can be obtained easily.

6.1 Detailed analysis of a measurement

In order to illustrate the lock-in method in detail, we discuss a measurement of an erythrocyte ghost. The phase and amplitude images are compared with the area and point contact model.

6.1.A Average and small-signal fluorescence images

We will analyze a measurement of an erythrocyte ghost. Its preparation is described in 6.2.A on page 99. The pixel width of the scan was $0.17\mu\text{m}$ which together with the scanning rectangle of 64×64 pixel results in an image size of $11\mu\text{m}$ (Fig 6.1 on the left). We have focussed to the lower junction membrane of the cell and subtracted the background fluorescence intensity obtained from a corner of the image. We see a modest intensity in the center of the cell and a very bright border. This border corresponds to the free membrane which is not parallel to the chip surface any more and moves out of focus. Its brightness is both explained with a tilted and thus more excitable dye (emission is also enhanced) and an increase in imaged membrane area since the focus is larger in z-direction than in x-y-direction. Therefore the low fluorescence of the junction membrane contributes only little to the total fluorescence in the bright border. Moreover, in this region the voltage of the junction membrane converges to zero. Therefore we measure the free membrane at the border of the cell and the junction membrane in the center within one scan.

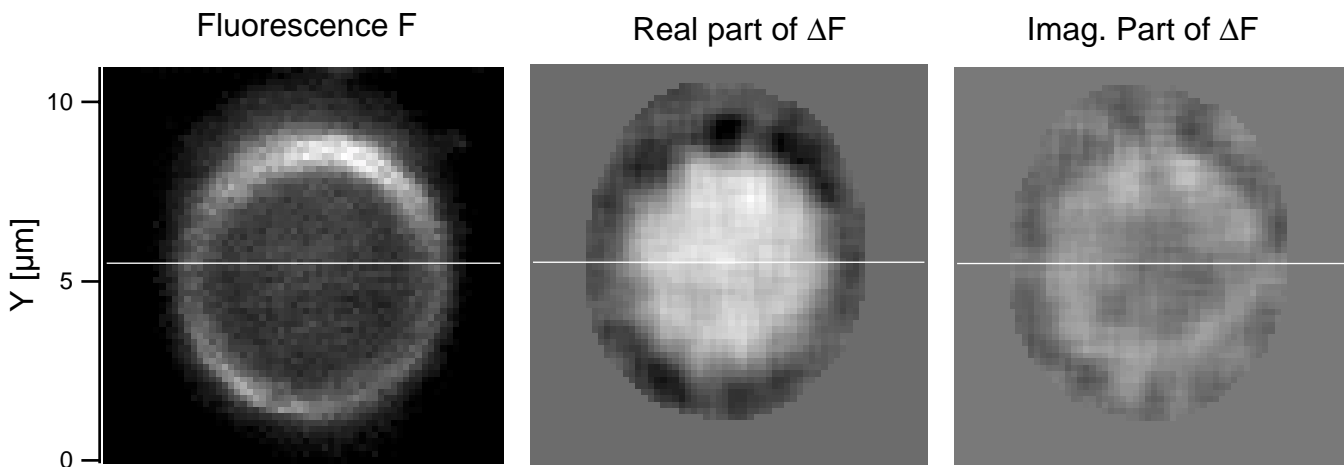


Fig 6.1 Raw images from a Lock-In scan. We see the fluorescence picture of a ghost (left) and the real (middle) and imaginary (right) part of the small-signal fluorescence from voltage sensitivity as excited by the chip at 25kHz. The small-signal images are binned by a 5×5 raster. The pixel size is $0.17\mu\text{m}$ with an image field of 64×64 pixels.

In the middle image of Fig 6.1 we see the fluorescence small-signal oscillation at 25kHz which is in phase with respect to the voltage at the spot oxide. In the right image we see the imaginary part of the small-signal oscillation which is shifted by 90° . Both signals are already corrected for the photomultiplier amplifier (transfer function in 5.4.A on page 88) and for the low pass filter of the chip as discussed in 3.3.H on page 53. The photomultiplier adds a phase of 4.9° to the raw signal at 25kHz and the 10nm chip used here adds a phase of 3° . For the widely used frequency of

125kHz the additional phase from the photomultiplier amplifier is 24.6° , from 10nm oxide chips 12.0° and from 50nm oxide chips 3.7° (Table 3.2 on page 55). The signal is binned over a square of 5×5 pixels to reduce noise. Usually binning is decreased for larger cells.

Obviously, the coupling of the junction membrane in the middle of the cell is almost in phase with the voltage at the spot oxide. Most of the small-signal is contained in the real part. For a high sealing resistance this is what we would expect for strong capacitive coupling with $f \gg f_0$ as compared to the stimulation frequency. At the free membrane measured at the border of the cell we find an inverted small-signal with negative real part. This indicates the different sign in the free membrane with respect to the junction membrane as predicted for the capacitive voltage divider of free and junction membrane. We will describe both with the theoretical models of area and point contact. Beforehand, a more powerful representation is introduced relying on phase and amplitude of the relative fluorescence small-signal.

6.1.B The phase image

We now plot the phase of the small-signal fluorescence ΔF with respect to the voltage at the stimulation spot (Fig 6.2). An additional scaling with F introduced later does not alter the phase signal. The phase is the most reliable and sensitive signal. As described before, this signal is corrected for the low pass of chip and photomultiplier amplifier and binned for noise reduction.

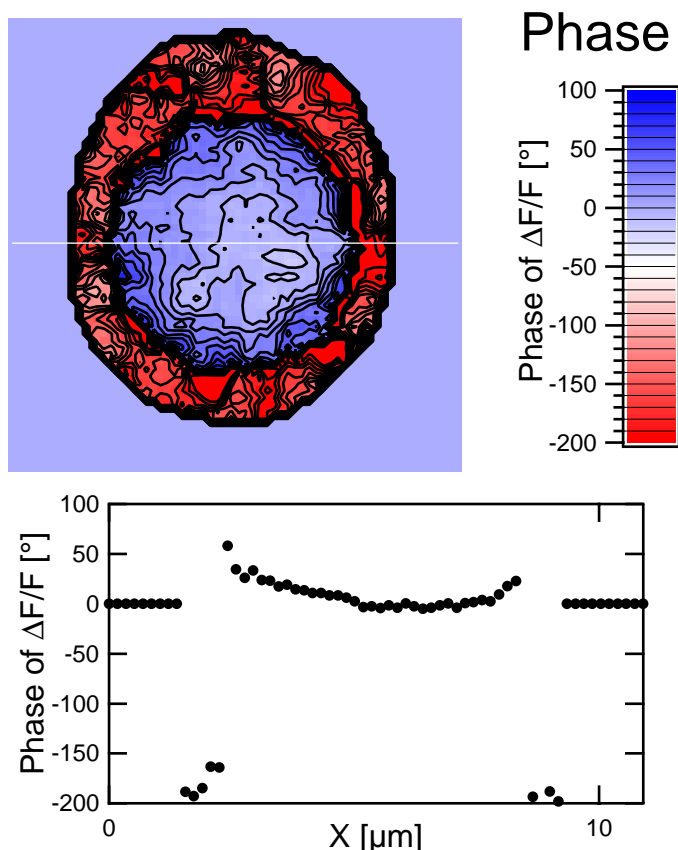


Fig 6.2 Phase of voltage sensitive fluorescence of a ghost's junction membrane. We see the scanned image of the phase and a section at the thin horizontal line below. At the center of the junction membrane the phase is slightly above 0° , slowly increasing to the borders of the cell. At the borders the phase of the free membrane measures about -160° . The cell area is defined with a fluorescence intensity threshold and the image is binned with 5×5 pixels to reduce noise. The scanning region is 64×64 pixels with a size of $0.17 \mu\text{m}$.

For the junction membrane in the center of the cell we observe a phase signal around 0° . It tends to increase to the borders of the cell in a hammock shape. This is expected for values of the stimulation frequency of $f = 15f_0$ with f_0 being the reference frequency of the area contact model (Fig 2.4 on page 21). In the free membrane a phase of around -160° is measured. We expect -180° only for

very strong coupling with $f \gg f_0$, as shown on the right side of Fig 2.5 on page 21. The phase of the free membrane is defined by the integrated current through the junction membrane and we obtain nonzero phase towards the borders of the junction membrane for good coupling as well.

6.1.C The relative amplitude image

As we cannot guarantee a constant fluorescence signal for all parts of the cell, the small-signal amplitude ΔF has to be scaled by the fluorescence F to yield a relative fluorescence change $\Delta F/F$ (Fig 6.3). Both the geometry of the membrane in the microscope focus may be altered, e.g. for the free membrane at the border of the cell (6.1.A on page 92) and the membrane angle might be inhomogeneous. In addition, the possibility of inhomogeneous staining has to be included. The relative fluorescence signal $\Delta F/F$ should be proportional to the membrane potential with a proportionality constant called sensitivity, measured in %/100mV.

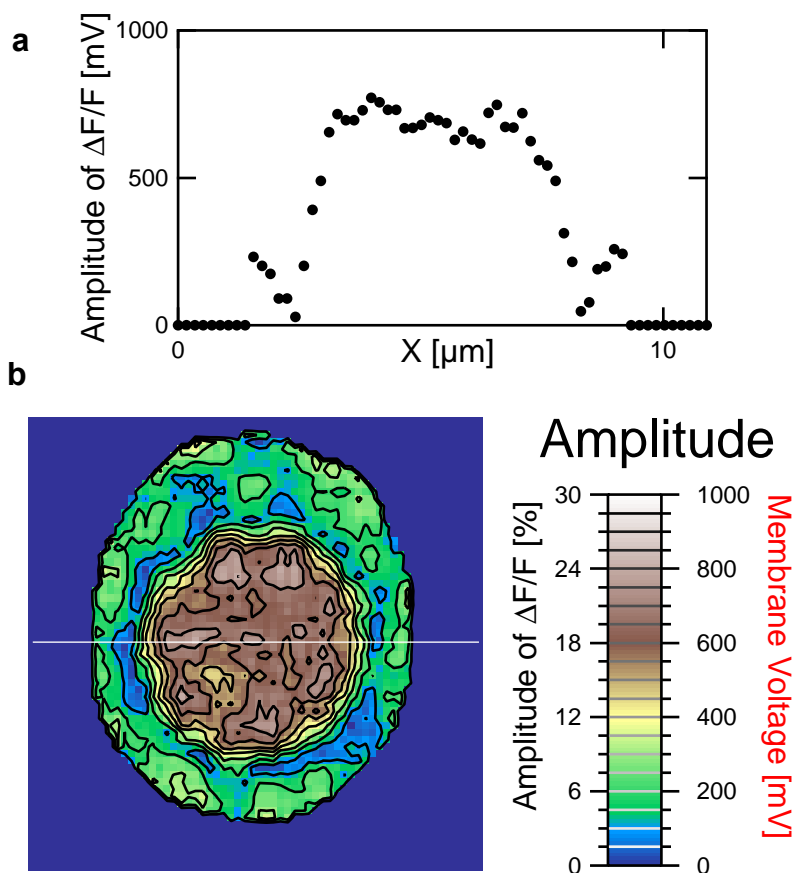


Fig 6.3 Relative small-signal fluorescence amplitude $\Delta F/F$ imaged from the junction membrane of a ghost. (a) Section of amplitude scaled with a sensitivity of 3%/100mV. The junction membrane in the center of the cell yields an amplitude of 21% or 700mV (b) Image of the amplitude. At the borders an amplitude of 7% or 230mV for the free membrane can be found. The white horizontal line indicates the section of (a). The cell area is defined from a fluorescence threshold and the image is binned with 5x5 pixels to reduce noise. The scanning region is 64x64 pixels with a size of 0.17 μ m each.

For the given measurement of a ghost we obtain fluorescence changes of 18-24% in the junction membrane and about 7% in the free membrane. If we assume a sensitivity of 3%/100mV, this corresponds to 600-800mV in the junction and 230mV in the free membrane (Fig 6.3). The cell can sustain these high voltages in the membrane throughout the whole scan of about 30s (pixel time 4ms + online lock-in calculations). The amplitude signal is rather inhomogeneous as compared to the phase signal. It could be possible that a region of much higher membrane conductance is located at the yellow spot of 300mV in the junction membrane. But this effect could also be attributed to sensitivity fluctuations. The rim between junction and free membrane in the amplitude signal is due to an optical mixing of the signals from junction and free membrane: they have dif-

ferent sign and interfere to zero in this region. The voltage in the junction membrane is expected to be rather constant in the center and to slowly fall off at the borders of the cell depending on the junction properties (see Fig 2.4 on page 21 and further discussion).

Comparing different measurements with theory we will find that sensitivity varies between different cells and preparations. With the chosen filter set and BNBIQ a sensitivity range of 2 to 8%/100mV was observed. This variability is already known from measurements of whole cell spectra (4.1.B on page 60). Another source of amplitude variance is the possibility of staining membranous organelles inside the cell. This would increase the total fluorescence F and therefore reduce $\Delta F/F$ and the sensitivity. Thus the amplitude is not used to fit the junction parameters, but only to confirm the fit. We will compare the measurements to the theory in the next two paragraphs.

6.1.D Fitting the point contact model

With the point contact approximation we can directly derive the junction time constant τ_j from the phase of the membrane potential. After transforming the transfer function of the point contact model [2.59]

$$g_{JM}(w) = \frac{V_{JM}}{V_E} = \frac{iwg^\infty\tau_j}{1+iw\tau_j} \quad [6.1]$$

we obtain the junction time constant τ_j from the phase signal ΔF_{phase} with:

$$\Delta F_{\text{phase}}(w) = \text{atan} \frac{\text{Im}(g_{JM})}{\text{Re}(g_{JM})} = \text{atan} \frac{1}{w\tau_j} \Rightarrow \tau_j = \frac{1}{w \tan(\Delta F_{\text{phase}}(w))} \quad [6.2]$$

The relation [6.2] is plotted for $f=125\text{kHz}$ and $f=25\text{kHz}$ ($w=2\pi f$) in Fig 6.4.

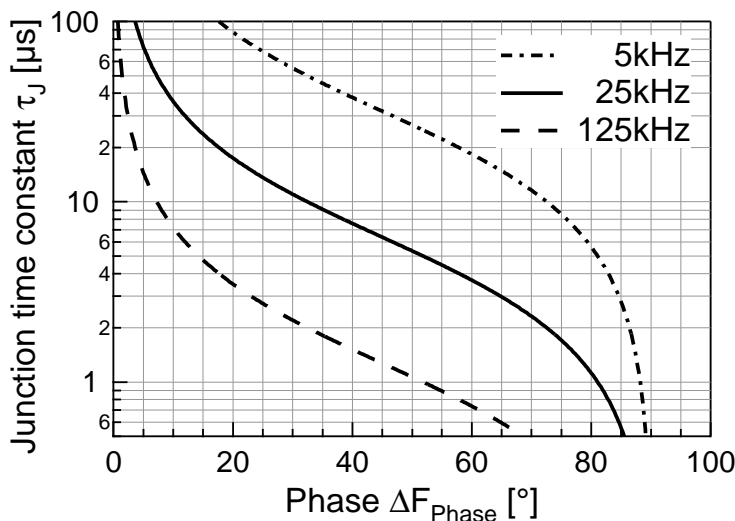


Fig 6.4 From the phase of the fluorescence small-signal we get directly the junction time constant τ_j of the point contact model. The relationship is plotted for stimulation frequencies of 5, 25 and 125kHz. Thus, at 25 kHz values of $\tau_j=2..30\mu\text{s}$ can be resolved properly. For the ghost a junction time constant of $50\mu\text{s}$ is derived from a phase of 30° measured at 5kHz.

With a stimulation frequency of 25kHz, junction time constants of 2..40 μs can be resolved. Constants between 0.5 μs and 5 μs are detectable with the widely used 125kHz. In the center of the cell attributed to the junction membrane we find a phase value of around zero. Thus at this frequency we cannot derive a time constant from the point contact model. But from a measurement at 5kHz on the same cell (Fig 6.6 on page 102) a phase of 30° can be found at the center of the junction, leading to a junction time constant of $\tau_j^{JM}=50\mu\text{s}$. We have seen in 2.5.E on page 31 that a more subtle point contact approximation of the cell junction includes different point contact models for

the center of the junction membrane and for the free membrane. For the latter we find a phase of around -170° , and therewith a time constant of $\tau_j^{\text{FM}}=36\mu\text{s}$. The point contact model yields better estimates for the free membrane than for the junction membrane, since the free membrane potential is already an averaged value calculated from the integral current of the junction membrane. If we want to calculate the area specific junction conductance g_j from the point contact model we have to use the area ratio β and both the capacitances of spot oxide and cell membrane defined by c_{ox} and ϵ . The value of β is estimated from a z-scan of the cell after the measurement, for the ghost we find $\beta=0.5$. The capacitances are determined from a fixed membrane capacitance of $1\mu\text{F}/\text{cm}^2$ and an oxide thickness of 10nm. Therefore the capacitance parameters are $\epsilon=0.34$ and $c_{\text{ox}}=0.34\mu\text{F}/\text{cm}^2$. We set the membrane conductance to zero with $g_{\text{FM}}=g_{\text{FM}}=0$ as published values for this parameter are too small by a factor of 1000 to influence the coupling. Starting from [2.56] we find for the junction conductance:

$$g_j = \frac{c_{\text{ox}}(1 + \beta + \epsilon^{-1})}{\tau_j(1 + \beta)} \quad [6.3]$$

For the junction time constant of the free membrane of $\tau_j^{\text{FM}}=36\mu\text{s}$ we obtain $g_j^{\text{FM}}=30\text{mS}/\text{cm}^2$. Typically the voltage decay of the free membrane is faster than the junction membrane potential decay at the center by a factor of 2 (paragraph 2.5.E on page 31). For the junction membrane we would thus estimate a time constant of $72\mu\text{s}$ and $g_j^{\text{JM}}=15\text{mS}/\text{cm}^2$. This value is confirmed by the measurement at 5kHz with $\tau_j^{\text{JM}}=50\mu\text{s}$ resulting in a junction conductance of $g_j^{\text{JM}}=19\text{mS}/\text{cm}^2$. Having measured all the parameters of the point contact model we can calculate the membrane potential. We obtain a junction membrane potential of 550mV, whereas the free membrane potential is 280mV due to the area ratio β . These values would be estimated from the voltage divider of oxide, junction and free membrane at high stimulation frequencies. Comparing them with the measured relative fluorescence amplitude $\Delta F/F$ of 21% for the junction and 7% of the free membrane we have to assume a sensitivity of 3.8%/100mV for the junction and 2.5%/100mV for the free membrane. The difference between both sensitivities can be attributed to the point contact approximation, as will be clarified by fitting the area contact model. It is mainly due to the fact that the point contact model neglects resonance effects in phase for stimulation frequencies around $f=15f_0$ and in amplitude around $f=8f_0$ (Fig 2.5 on page 21).

6.1.E Fitting the area contact model

The area contact model is fitted on a pixel by pixel basis with the boundary conditions given by the cell shape, which is defined using a fluorescence threshold: free and junction membrane are distinguished by a threshold in phase. Thus we determine areas of free and junction membrane in the image. To fit the measurement with the area contact model, we choose the whole image area of the cell as contact area, since restriction to the junction membrane area results in a crude underestimation of the area contact size and thus the junction resistance r_j . With the additional boundary condition of zero junction membrane potential, the two dimensional integral-diffusion equation of the area contact model is solved at the stimulation frequency. The input parameters are the same as for the point contact model: we need the area ratio β and the capacitance ratio ϵ together with the oxide capacitance of the stimulation spot. As for the point contact model we use $\beta=0.5$, $\epsilon=0.34$ and $c_{\text{ox}}=0.34\mu\text{F}/\text{cm}^2$ in this example. Now the only free parameter in the model is

the junction resistance r_j . It is fitted from the phase image of the junction membrane and accounts for the characteristics of the junction membrane potential. The best fit is obtained with a value of $r_j=900\text{M}\Omega$. The simulated phase and amplitude images can be found at the right side of (Fig 6.5).

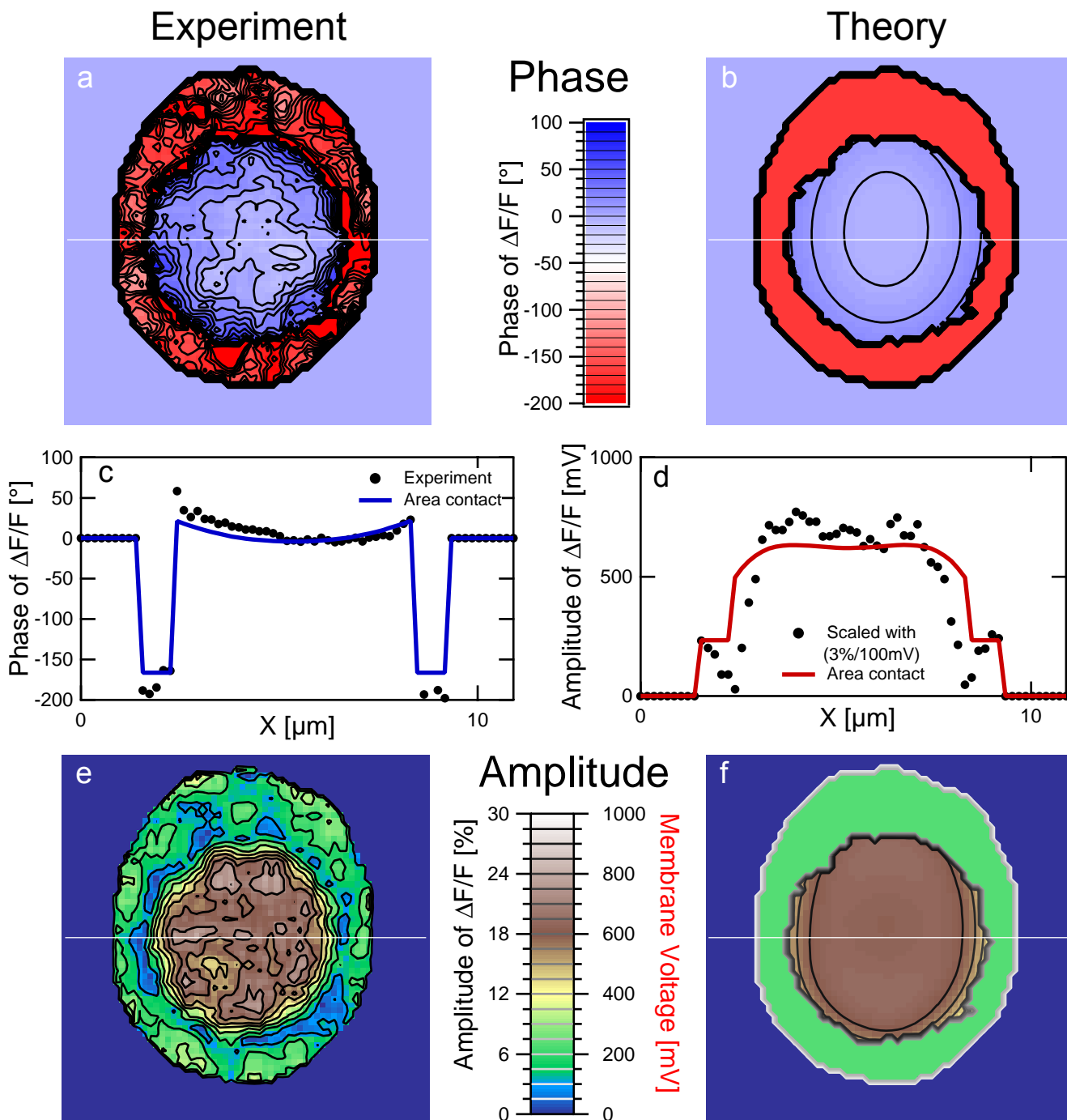


Fig 6.5 The ghost measurement together with the area contact model at $r_j=900\text{M}\Omega$. We define areas from the junction and the free membrane by fluorescence and phase thresholds. The integral-differential equation of the area contact is solved for given ϵ , c_{ox} and β with a fitted junction resistance r_j . The phase agrees very well, the amplitude shows larger variations, probably from different sensitivities of the dye. The amplitude is scaled with a sensitivity of 3%/100mV to describe the membrane potential of up to 650mV in the junction and 230mV in the free membrane.

In the sections of Fig 6.5c,d we find the area contact fit as blue (phase) or red (amplitude) line. The phase image Fig 6.5a is fitted very precisely by the theory (Fig 6.5b), even the hammock shape of the phase in the junction membrane is reproduced. However, there is a shift of the hammock to the right side which could be attributed to an inhomogeneous junction resistance. We also see that the area contact model perfectly predicts the phase of the free membrane with -165° . To compare the amplitude we use a sensitivity of 3.0%/100mV. The amplitude signal appears noisier than the phase (Fig 6.5d,e), but a smoother mean value would follow the theory (Fig 6.5d,f). We obtain a maximum voltage of the junction membrane of 650mV and 230mV for the free membrane. With the relative fluorescence amplitudes of 21% and 7% this yields sensitivities of 3.2%/100mV for the junction and 3.0%/100mV for the free membrane, that agree far better than the values obtained from the point contact model. At the inner border of the free membrane and the outer rim of the junction membrane we see a drop to zero in the measured amplitude. In the fit however, a corresponding drop is missing, since it reflects destructive interference in this region by optical mixing of free and junction membrane fluorescences with different sign. Also the phase signal has the tendency to be increased in this region.

The measured value of r_j can be immediately translated to a bulk resistance of the electrolyte in the junction as the thickness of the junction is known to be 11nm. Therefore we obtain with $\rho_j=r_j*d$ a specific junction resistance of $\rho_j=1000\Omega\text{cm}$ which is enhanced by a factor of 13 relative to the specific resistance of the bulk electrolyte with $\rho=74\Omega\text{cm}$. This effect is probably due to the dense layer of glycolix and poly-lysine in the junction.

In approximating the point contact parameter g_j from the area contact model we have to stick to [2.61] on page 28 and to use a k of Table 2.4 on page 32 and k_β with equation [2.70] on page 29:

$$g_j = k_\beta \frac{\pi}{A_{JM} r_j} \quad k_\beta = \frac{k}{1 + \beta} \quad [6.4]$$

Thus we get for the phase in the middle of the junction membrane a value of $k_\beta=2.7$ (with $k=4$ and $\beta=0.5$), and for the phase of the free membrane $k=7$ and therefore $k_\beta=4.7$. From these k_β and a measured junction area of $A_{JM}=60\mu\text{m}^2$ we find $g_j^{JM}=15\text{mS}/\text{cm}^2$ and $g_j^{FM}=27\text{mS}/\text{cm}^2$. These values are similar to those obtained from the point contact model in the last paragraph. They result in time constants of $\tau_j^{JM}=65\mu\text{s}$ and $\tau_j^{FM}=37\mu\text{s}$.

Thus there are two ways to obtain similar values for g_j and τ_j from the measurements. First directly with the point contact model from the value of the phase via the time constant. And secondly from the phase-fitted r_j by assuming a circular junction and passing the heuristic transition with the k_β -factor. Since the junction voltage is governed by an integral-differential equation we should keep in mind that attributing a single time constant to the whole cell is an approximation.

6.2 Erythrocyte ghosts

Measurements of erythrocyte ghosts on poly-lysine yield a junction resistance of $r_j=900\text{M}\Omega$. From 11nm junction thickness we derive a specific junction resistance of $\rho_j=1000\Omega\text{cm}$, increased by a factor of 13 relative to the bulk electrolyte. The time constants are $\tau_j^{\text{JM}}=70\mu\text{s}$ and $t_j^{\text{FM}}=35\mu\text{s}$ at the sustainable junction membrane potential of 650mV.

6.2.A Preparation of ghosts

The erythrocyte ghosts were prepared according to a standard procedure [Schwoch 1973] with some minor modifications [Braun 1997]. 4ml blood from healthy colleagues were sucked into a tube coated with EDTA to prevent coagulation (Vacutainer 367861, Becton Dickinson, Meyland, France). The blood was centrifuged for 10min at 1600g. The pellet (1.5ml) was collected in a pipette. We washed the erythrocytes three times by resuspension and centrifugation for 10min at 1600g using 20ml of a 300mOsm TRIS buffer (6.05g TRIS, 6.42g NaCl, 420ml 0.1M HCl, 580ml Milli-Q water (Millipore), pH 7.4), 1.5ml of the final pellet were diluted with 1.5ml TRIS buffer and kept at 4° for several hours. Transient lysis of the erythrocytes was performed on ice with precooled solutions. At first we added 15ml of a 30mOsm lysing solution (301mg MgSO_4 , 372mg KCl in 500ml Milli-Q water) to 0.5ml of the cell suspension. Immediately afterwards 1ml of a resealing solution (53.7g KCl, 10.5g NaCl in 400ml Milli-Q water) was added. The suspension was kept on ice for 5min and for 30min at 37°. The ghosts were centrifuged for 10min at 3000g, washed three times with 20ml TRIS buffer and centrifuged for 10min at 3000g. After adding 20ml TRIS buffer this ghost stock suspension was kept at 4°C for several hours before use.

The chips were cleaned inside the petri dish with a 5% solution of detergent (Dr. Schnells FOR Spülmittel) in millipore water by rubbing with a kimwipe wound around a 1ml eppendorf pipette. Q-Tips for ear cleaning (Elida Faberge) were also used but often lost fibres. The chips were thoroughly rinsed with millipore water and dried under nitrogen. Cleaning was repeated to get a hydrophobic chip surface. The chips were coated several hours before use with a solution of 0.5mg/ml poly-L-lysine (MW 10000, Sigma, Heidelberg) in TRIS buffer. They were rinsed three times with TRIS buffer. 1ml of the ghost stock solution was diluted in 20ml TRIS buffer. 3ml of this solution was added to the wet chip. The ghosts were allowed to settle for 20min. Staining was achieved with the procedure described in 4.1.C on page 61.

6.2.B Junction of ghosts

Most of the measurement analysis for the ghosts is described in the introductory paragraph 6.1 on page 92. We now present measurements on the same ghost made at stimulation frequencies of 5,25,50 and 125kHz (Table 6.1 and Table 6.2) presented in Fig 6.6, Fig 6.7, Fig 6.8 and Fig 6.9. All measurements were fitted with a seal resistance of $r_j=900\text{M}\Omega$.

Compared to the junction thickness of 11nm obtained by FLIC microscopy we therefore find a 13-fold enhanced specific junction membrane resistance of $\rho_j=1000\Omega\text{cm}$ as compared to the bulk electrolyte resistance of $\rho=74\Omega\text{cm}$. In a previous work using transistors[Kießling 1999],[Kießling

2000] Volker Kießling found a lower limit of fourfold enhancement but also measured a seal resistance of $r_J=700\text{M}\Omega$ on large fused erythrocyte ghosts similar to the results presented here. The difference is attributed to noncentral transistor locations for the measurement on the ghosts.

The phase profiles at 5kHz (Fig 6.6), 25kHz (Fig 6.7), 50kHz (Fig 6.8) and 125kHz (Fig 6.9) can be compared to area contact calculations for a circular junction presented in Fig 2.4 on page 21 with the corresponding ratio f/f_0 of 3.5, 18, 32 and 90 calculated from $f_0=1.4\text{kHz}$. For 5kHz there is a rather flat phase profile at around 30° . It bends into a hammock shape at 25kHz and flattens again for frequencies of 50kHz and 125kHz. The measured small-signal fluorescence phase is precisely reproduced by the theory, especially the hammock shape for 25kHz. However, the hammock is shifted to the right, perhaps due to slightly asymmetric junction properties or a misinterpreted junction area on the left side. The thickness of the junction is expected to be very homogeneous, according to previous measurements from many ghosts by FLIC microscopy [Braun 1997]. Towards the border of the visible junction membrane the junction phase signal has the tendency to increase due to optical mixing of small-signals from junction and free membrane, best seen in Fig 6.9 at 125kHz. Since at higher frequencies of 50kHz and 125kHz the phase of the junction membrane is slightly above 0° , we can estimate a small systematical error within the phase correction of chip and photomultiplier amplifier of about 5° .

At 5 kHz, the phase of the free membrane is difficult to measure (Fig 6.6). Therefore we can only speculate on an increase due to the enhanced junction membrane phase signal. At 25kHz the phase of the free membrane has an average value of -170° although it seems to be lower at the section position. For the measurement at 50kHz (Fig 6.8) and 125kHz (Fig 6.9) its value is around -175° as predicted by the theory. Since for higher frequencies the junction membrane phase converges to zero, the free membrane phase converges to -180° as predicted (Fig 2.5 on page 21).

The shape of the relative small-signal fluorescence amplitude behaves as predicted (see also Fig 2.4 on page 21). At 5kHz the amplitude image is dominated by a peak voltage of 700mV in the center of the junction (Fig. 6.6). The profile flattens for an increased stimulation frequency of 25kHz in Fig 6.7 and also displays a weak hammock shape for frequencies of 50kHz and 125kHz (Fig 6.8, Fig 6.9). The amplitude is scaled with a sensitivity of $3\%/100\text{mV}$, except for the measurement at 5kHz with a value of $2\%/100\text{mV}$. This can be explained by the fact that this measurement was imaged last and the fluorescence amplitude revealed a significant bleaching, thus probably decreasing the sensitivity. The scaled relative fluorescence precisely follows the theory for 5kHz and 25kHz (Fig 6.6 and Fig 6.7). At 25kHz and 50kHz, again the effect of destructive interference of junction and free membrane fluorescence at the border of the visible junction is reflected in the amplitude drop to zero towards the free membrane. Also the inner border of the free membrane area yields a diminished amplitude. At 125kHz (Fig 6.9) the small rim at the border of the visible junction membrane is predicted by the area contact model. Both in the measurement at 25kHz and 125kHz the amplitude signal shows a small patch of decreased relative fluorescence amplitude. Especially at 25kHz it is accompanied with a lower phase signal, indicating a larger junction time constant. This is paradoxical since a leakage in the junction membrane would decrease the amplitude but also the junction time constant as discussed in 2.4.F on page 25. We will come back to similar observations in spindle shaped HEK cells in 7.2.A on page 144

Image=11 μ m	f=5..125kHz
Pixel=0.17 μ m	V _{Chip} =2.5V
Binning=5x5	ϵ =0.34 (10nm)
A _{JM} =60 μ m ²	β =0.5

TABLE 6.1 Measurement and theory parameter for the erythrocyte ghost measured in Fig 6.6, Fig 6.7, Fig 6.8 and Fig 6.9 at frequencies of 5,25,50 and 125kHz.

f=5kHz=3.5f₀ (Fig 6.6)

Area contact Model		Point contact Model	
r_J=900MΩ	Sens.=2%/100mV	Phase _{JM} =30°	Phase _{FM} =-120°
$\tau_J^{JM}=65\mu$ s	$\tau_J^{FM}=37\mu$ s	$\tau_J^{JM}=50\mu$s	$\tau_J^{FM}=18\mu$s
$g_J^{JM}=15$ mS/cm ²	$g_J^{FM}=27$ mS/cm ²	$g_J^{JM}=19$ mS/cm ²	$g_J^{FM}=60$ mS/cm ²
V _{JM} =660mV	V _{FM} =150mV	V _{JM} =480mV	V _{FM} =140mV

f=25kHz=18f₀ (Fig 6.7)

Area contact Model		Point contact Model	
r_J=900MΩ	Sens.=3%/100mV	Phase _{JM} =-4°	Phase _{FM} =-170°
$\tau_J^{JM}=65\mu$ s	$\tau_J^{FM}=37\mu$ s	---	$\tau_J^{FM}=36\mu$s
$g_J^{JM}=15$ mS/cm ²	$g_J^{FM}=27$ mS/cm ²	---	$g_J^{FM}=30$ mS/cm ²
V _{JM} =620mV	V _{FM} =230mV	V _{JM} =560mV	V _{FM} =280mV

f=50kHz=36f₀ (Fig 6.8)

Area contact Model		Point contact Model	
r_J=900MΩ	Sens.=3%/100mV	Phase _{JM} =0°	Phase _{FM} =-175°
$\tau_J^{JM}=65\mu$ s	$\tau_J^{FM}=37\mu$ s	---	$\tau_J^{FM}=36\mu$s
$g_J^{JM}=15$ mS/cm ²	$g_J^{FM}=27$ mS/cm ²	---	$g_J^{FM}=30$ mS/cm ²
V _{JM} =570mV	V _{FM} =250mV	V _{JM} =560mV	V _{FM} =280mV

f=125kHz=90f₀ (Fig 6.9)

Area contact Model		Point contact Model	
r_J=900MΩ	Sens.=3%/100mV	Phase _{JM} =0°	Phase _{FM} =-175°
$\tau_J^{JM}=65\mu$ s	$\tau_J^{FM}=37\mu$ s	---	$\tau_J^{FM}=15\mu$s
$g_J^{JM}=15$ mS/cm ²	$g_J^{FM}=27$ mS/cm ²	---	$g_J^{FM}=70$ mS/cm ²
V _{JM} =570mV	V _{FM} =260mV	V _{JM} =560mV	V _{FM} =280mV

TABLE 6.2 Results of the fit with point and area contact model for the ghost shown in Fig 6.6 to Fig 6.9. The same ghost is measured at frequencies from 5 to 125kHz.

Erythrocyte Ghost at 5kHz

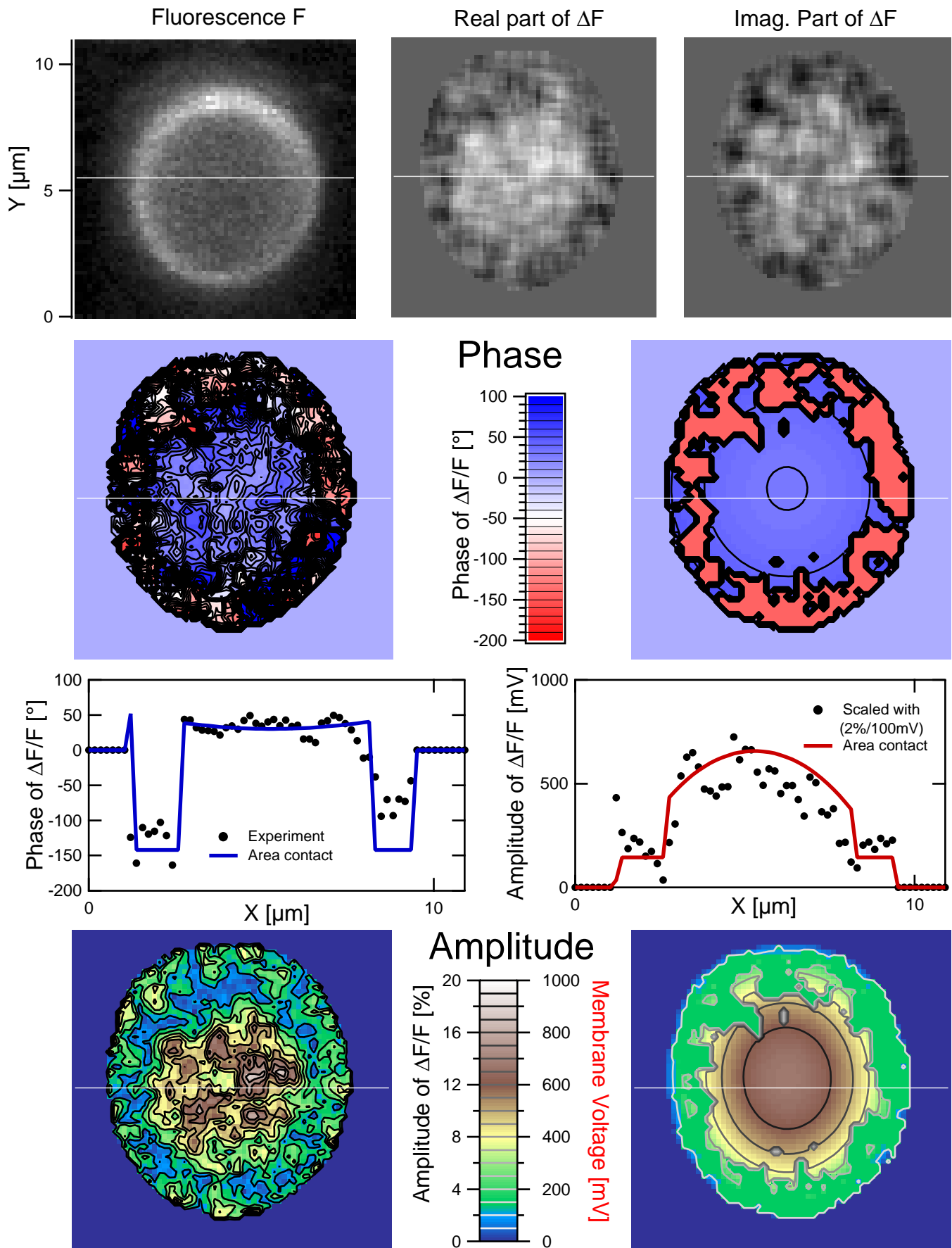


Fig 6.6 Ghost at 5kHz with area contact theory. Parameters from Table 6.1 and Table 6.2.

Erythrocyte Ghost at 25kHz

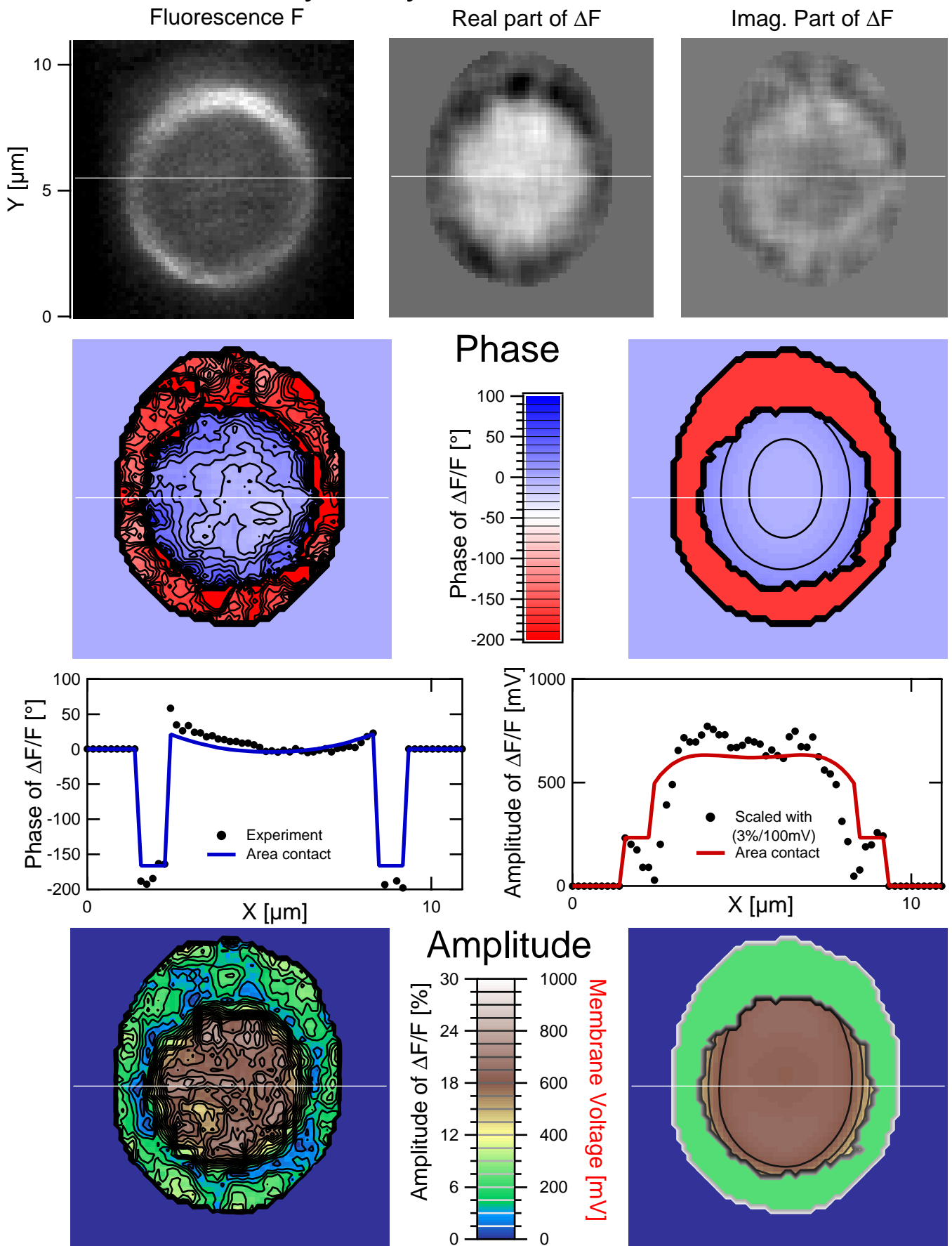


Fig 6.7 Ghost at 25kHz with area contact theory. Parameters from Table 6.1 and Table 6.2.

Erythrocyte Ghost at 50kHz

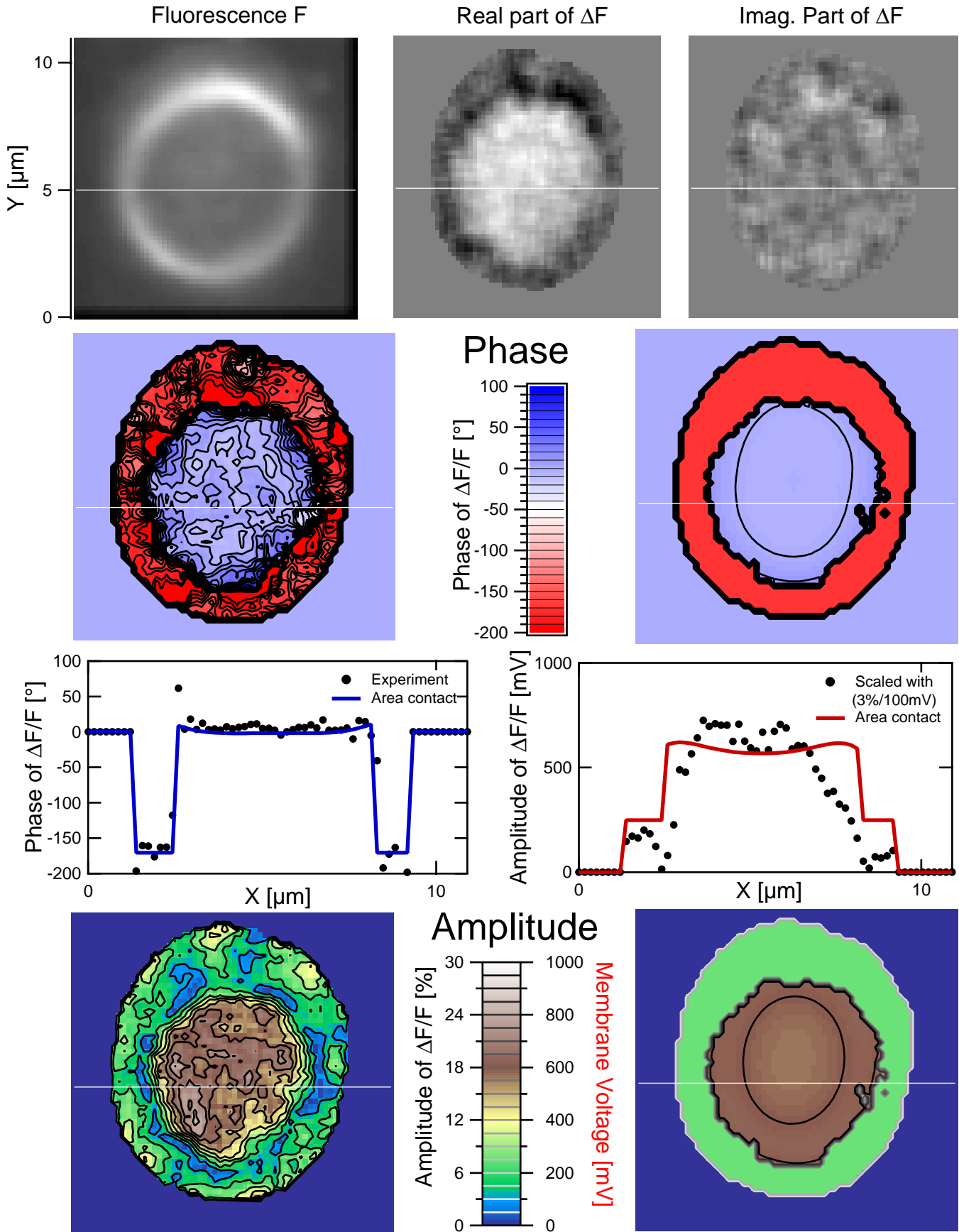


Fig 6.8 Ghost at 50kHz with area contact theory. Parameters from Table 6.1 and Table 6.2.

Erythrocyte Ghost at 125kHz

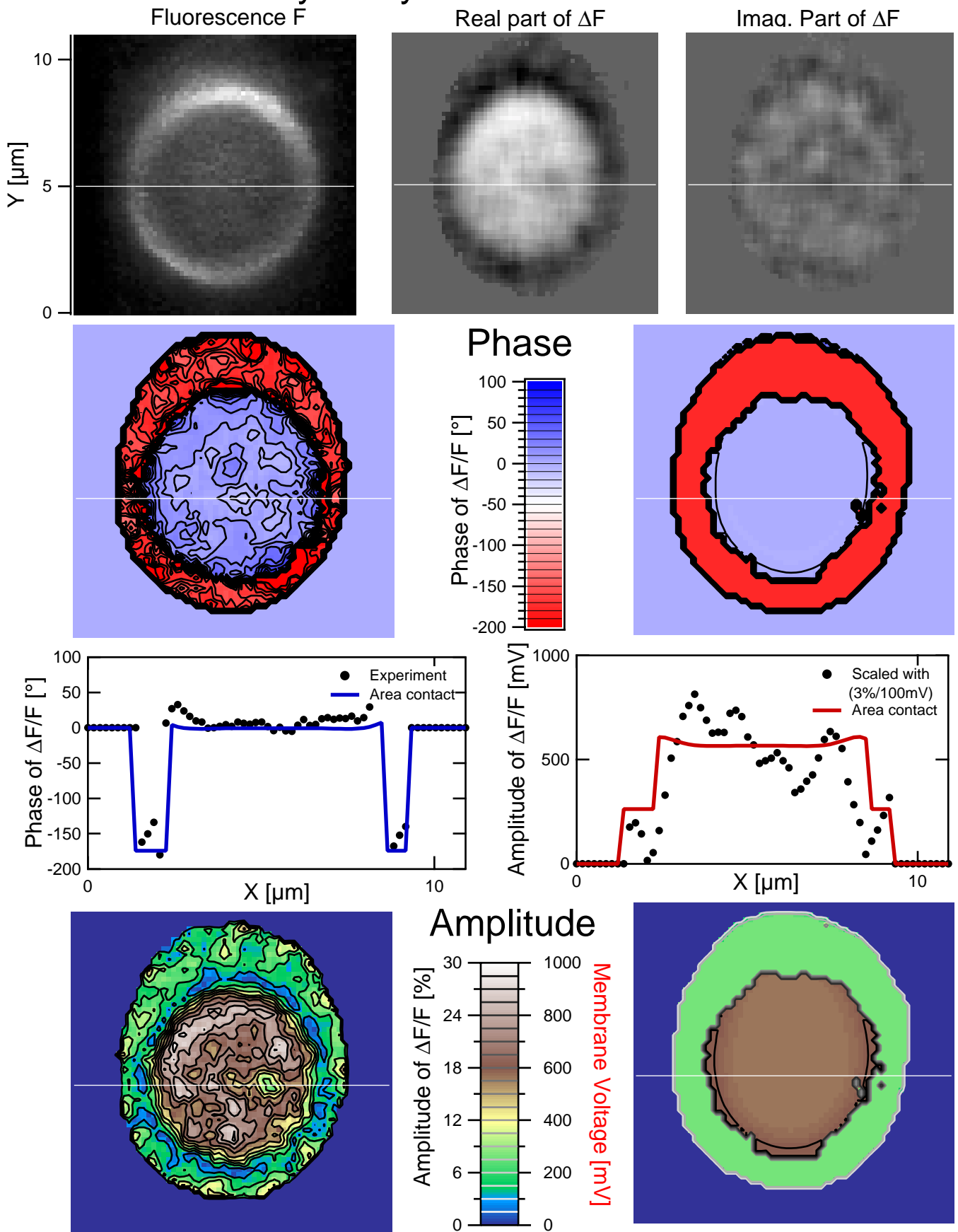


Fig 6.9 Ghost at 125kHz with area contact theory. Parameters from Table 6.1 and Table 6.2.

6.2.C High membrane conductance or weak coupling?

The membrane conductance of erythrocytes is reported to be very low $<10\mu\text{S}/\text{cm}^2$ [Takashima 1988] although the method used is doubtful. However, it only exerts influence on the coupling of ghosts if it is comparable to the measured junction conductance of $15\text{mS}/\text{cm}^2$ as calculated in Fig 2.4.E on page 24 for a circular junction. Nevertheless, the osmotic shock in the preparation of the ghosts could occasionally induce such a high membrane conductance.

We will present a measurement on an ill-shaped ghost with a junction membrane phase of 40° measured at 125kHz . It will be shown that this can be most probably explained with a membrane conductance of $800\text{mS}/\text{cm}^2$. Alternatively, the measurement can also be fitted with a tight membrane but a junction resistance of $r_j=40\text{M}\Omega$. The first case of a leaky membrane is presented in Table 6.3 and Fig 6.10, the case of weak coupling in Table 6.4 and Fig 6.11.

Both fits reveal almost the same phase profile. Therefore only the amplitude signal can distinguish between both cases. The amplitude of the free membrane is reduced by a factor of about 2 relative to the junction membrane. A far better fit is achieved for the leaky membrane as compared to weak coupling. Therefore I would prefer the first case, although it is difficult if not impossible to distinguish between the influence of the junction conductance and the membrane conductance. In the case of living cells however it is easier since the membrane conductance has a defined value of $0.1\text{mS}/\text{cm}^2$ and the junction conductance is typically increased by a factor of 1000 or more.

Area contact Model	
$g_{JM}=800\text{mS}/\text{cm}^2$	Sens.=6%/100mV
$\tau_J^{JM}=1.3\mu\text{s}$	$\tau_J^{FM}=1.3\mu\text{s}$
$g_J^{JM}=15\text{mS}/\text{cm}^2$	$g_J^{FM}=27\text{mS}/\text{cm}^2$
$V_{JM}=230\text{mV}$	$V_{FM}=100\text{mV}$

Image= $11.5\mu\text{m}$	f= 125kHz
Pixel= $0.18\mu\text{m}$	$V_{\text{Chip}}=5\text{V}$
Binning= 4×4	$\epsilon=0.07$ (50nm)
$A_{JM}=60\mu\text{m}^2$	$\beta=0.5$

Point contact Model	
Phase $_{JM}=40^\circ$	Phase $_{FM}=-130^\circ$
$\tau_J^{JM}=1.5\mu\text{s}$	$\tau_J^{FM}=1.1\mu\text{s}$

TABLE 6.3 Results of the fit with point and area contact model if we assume a leaky ghost membrane with an enhanced membrane conductance of $g_{JM}=800\text{mS}/\text{cm}^2$ (Fig 6.10).

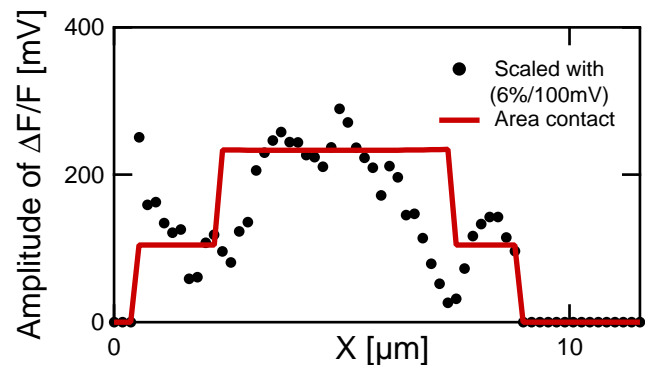
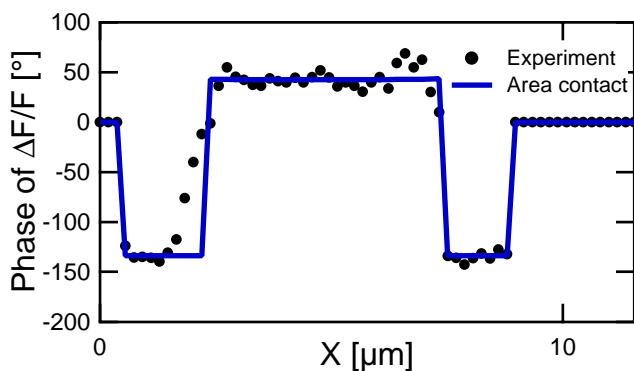


Fig 6.10 Probably leaky ghost with area contact theory. Parameters from Table 6.3.

Ghost with $r_j=40M\Omega$?

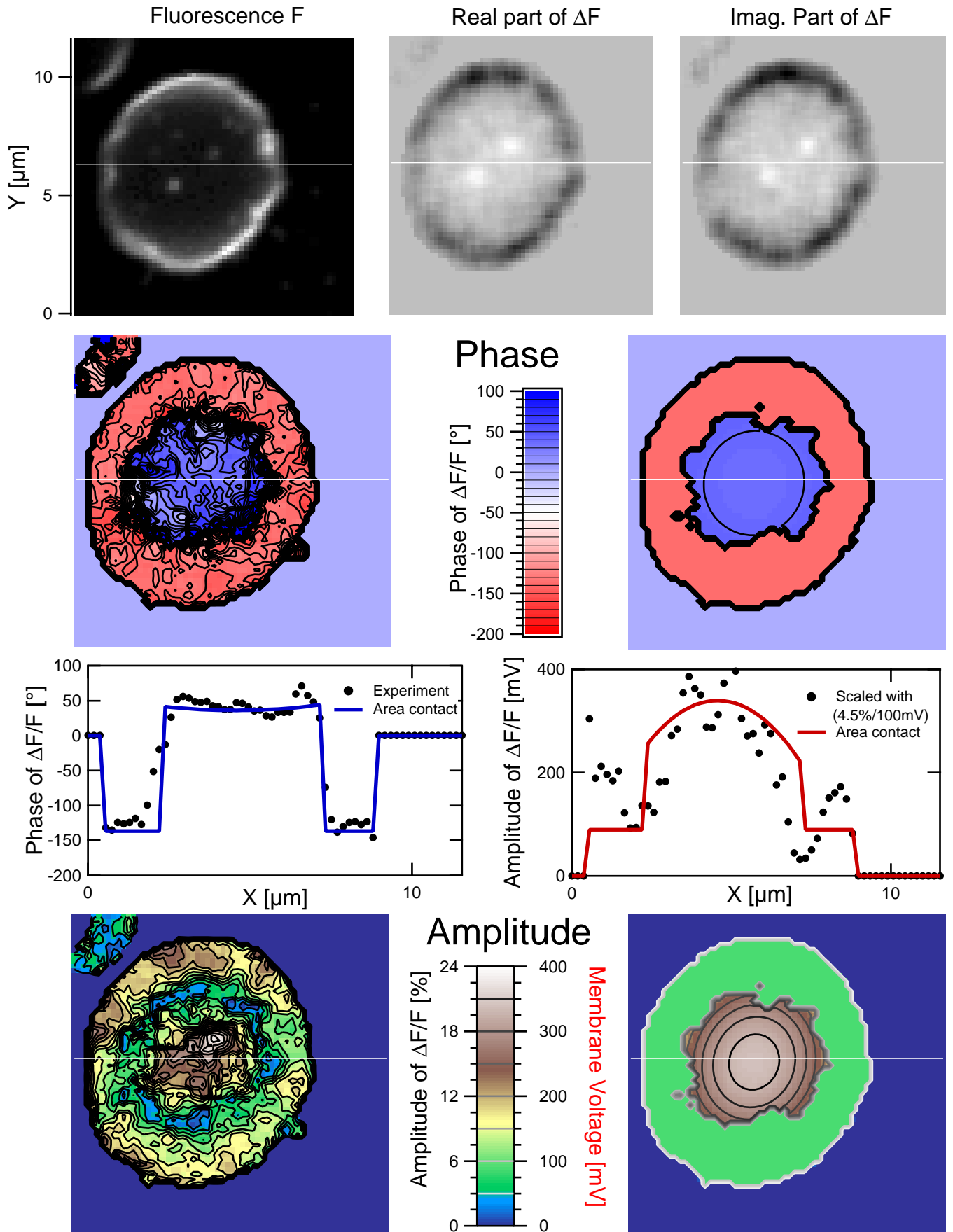


Fig 6.11 Ghost now fitted low coupling of $r_j=40M\Omega$. Parameters from Table 6.4.

Area contact Model		Point contact Model	
$r_J=40M\Omega$	Sens.=4.5%/100mV	Phase _{JM} =40°	Phase _{FM} =-130°
$\tau_J^{JM}=2.2\mu s$	$\tau_J^{FM}=1.2\mu s$	$\tau_J^{JM}=1.5\mu s$	$\tau_J^{FM}=1.1\mu s$
$g_J^{JM}=360mS/cm^2$	$g_J^{FM}=630mS/cm^2$	$g_J^{JM}=500mS/cm^2$	$g_J^{FM}=700mS/cm^2$
$V_{JM}=340mV$	$V_{FM}=90mV$	$V_{JM}=210mV$	$V_{FM}=90mV$

TABLE 6.4 Model parameter values under the assumption of a low seal resistance and a tight membrane (Fig 6.11). With $r_J=40M\Omega$ a 22fold reduced junction resistance is obtained as compared to previous measurements.

6.3 Single HEK cells

HEK cells on fibronectin yield a junction resistance of $r_J=3.4\pm 0.9M\Omega$. From 50nm junction thickness we thus derive a specific junction resistance of $17\pm 5\Omega cm$, reduced by a factor of 4.4 ± 1.4 as compared to the bulk electrolyte. Junction time constants are $\tau_J=1.5..4\mu s$, further depending on the junction area. Junction membrane potentials are as high as 500mV.

6.3.A Cell culture

The HEK cell line was established and described by [Graham 1977]. HEK cells are human embryonal kidney cells, transformed by DNA fragments of the human adenovirus type 5. HEK cells are typically used to express and characterize ion channels from DNA, since they lack any native ion channels and divide themselves frequently. The used cell line was obtained from ATCC (CRL-1573) and cultured on Falcon 3001 petri dishes prior to the growth on the chip. Culture medium was made from 13.89g DMEM (Gibco, 074-02100A, powder), 3.7g NaHCO₃ (Sigma), 1l aqua ad at pH 6.8 with HCl or NaOH. The medium was sterile filtered and 500μl L-Glutamin (Sigma G-2150), 5.5ml Penicillin/Streptomycin (Gibco, 043-05140) and 100ml FKS (C.C.Pro, S-10L, heat deactivated for 1h at 58°) was added. Cells were detached by 0.5ml Trypsin and isolated mechanically. The chips were coated with 25μg/ml Fibronectin in TRIS buffer (6.05g TRIS, 6.42g NaCl, 420ml 0.1M HCl, 580ml Milli-Q water (Millipore), pH 7.4) overnight. The number of cells transferred to the chip was adapted to obtain 50% confluency after 2-3days. Staining was performed in the cell culture medium as described (4.1.C on page 61). Under these conditions (Fig 2.19 on page 35), a junction cleft thickness of 50nm and a specific conductance of the medium 74Ωcm were measured.

6.3.B Spindle-shaped HEK cells

Spindle shaped HEK cells are very similar in size and shape to somata of rat neurons. They have the same junction thickness of 50nm on fibronectin. As discussed in the previous paragraph, a slightly different membrane conductance does not affect the coupling. The reason to choose HEK cells was their easy cell culture. Also the junction properties were of interest for other experiments in our department.

For spindle-shaped HEK cells on fibronectin we find a junction resistance of $r_j=3.7\pm 0.3\text{M}\Omega$. With a junction thickness of 50nm we infer a specific junction resistance of $\rho_j=18.5\pm 1.5\Omega\text{cm}$, reduced by a factor of 4 ± 0.3 relative to the bulk electrolyte. Time constants derived from the point contact model are $\tau_j^{\text{JM}}=1.5\mu\text{s}$ in the middle of the junction and $\tau_j^{\text{FM}}=1.3\pm 0.2\mu\text{s}$ in the free membrane. Estimates of τ_j from the area contact model are expected to be imprecise as they rely on a circular junction area. Sustainable junction membrane potentials are as high as 500mV.

The first measurement is presented in Fig 6.12 on the next page with the model and measurement parameters in Table 6.5. The phase signal in the junction membrane is very flat with a value of 40° . Both the phase of the junction and the free membrane can be described very good with the area contact model with a junction resistance of $r_j=3.5\text{M}\Omega$. Therefore with a junction thickness of 50nm a specific junction conductance of $r_j=17.5\Omega\text{cm}$ is found, reduced by a factor of 4.2 relative to the bulk electrolyte. The point contact fit yields a junction conductance of $750\text{mS}/\text{cm}^2$.

The amplitude signal was fitted with an area ratio of $\beta=0.25$ estimated from a z-scan and a sensitivity of $2.5\%/100\text{mV}$. Again, the amplitude signal of the junction membrane is reduced towards the boundaries of the cell because of the small-signal destructive interference of junction and free membrane. However, the amplitude in the center of the junction membrane and the free membrane is in good agreement with area contact theory although the amplitude section overestimates the amplitude of the free membrane towards the boundary of the cell. At the center of the junction membrane, the chip voltage of 2.0V is attenuated to a membrane potential of 480mV.

The time constants can be estimated from the junction phase of 40° to be $1.5\mu\text{s}$ and the free phase of -140° to $1.5\mu\text{s}$. Estimates of the junction time constant from the area contact model are hampered by the nonsecular junction area.

Image=42 μm	f=125kHz
Pixel=0.65 μm	$V_{\text{Chip}}=2.0\text{V}$
Binning=3x3	$\varepsilon=0.34$ (10nm)
$A_{\text{JM}}=640\mu\text{m}^2$	$\beta=0.25$

TABLE 6.5 Measurement and model parameter values for the spindle-shaped HEK cell in Fig 6.12. We find with $r_j=3.5\text{M}\Omega$ a fourfold reduced specific resistance as compared to the bulk electrolyte. Time constant of junction and free membrane is $\tau_j=1.5\mu\text{s}$ as estimated from phase and point contact model.

Area contact Model		Point contact Model	
$r_j=3.5\text{M}\Omega$	Sens.=2.5%/100mV	Phase _{JM} =40°	Phase _{FM} =-140°
$\tau_j^{\text{JM}}=2.5\mu\text{s}$	$\tau_j^{\text{FM}}=1.5\mu\text{s}$	$\tau_j^{\text{JM}}=1.5\mu\text{s}$	$\tau_j^{\text{FM}}=1.5\mu\text{s}$
$g_j^{\text{JM}}=450\text{mS}/\text{cm}^2$	$g_j^{\text{FM}}=800\text{mS}/\text{cm}^2$	$g_j^{\text{JM}}=750\text{mS}/\text{cm}^2$	$g_j^{\text{FM}}=750\text{mS}/\text{cm}^2$
$V_{\text{JM}}=480\text{mV}$	$V_{\text{FM}}=60\text{mV}$	$V_{\text{JM}}=480\text{mV}$	$V_{\text{FM}}=120\text{mV}$

Spindle-shaped HEK Cell at 125kHz

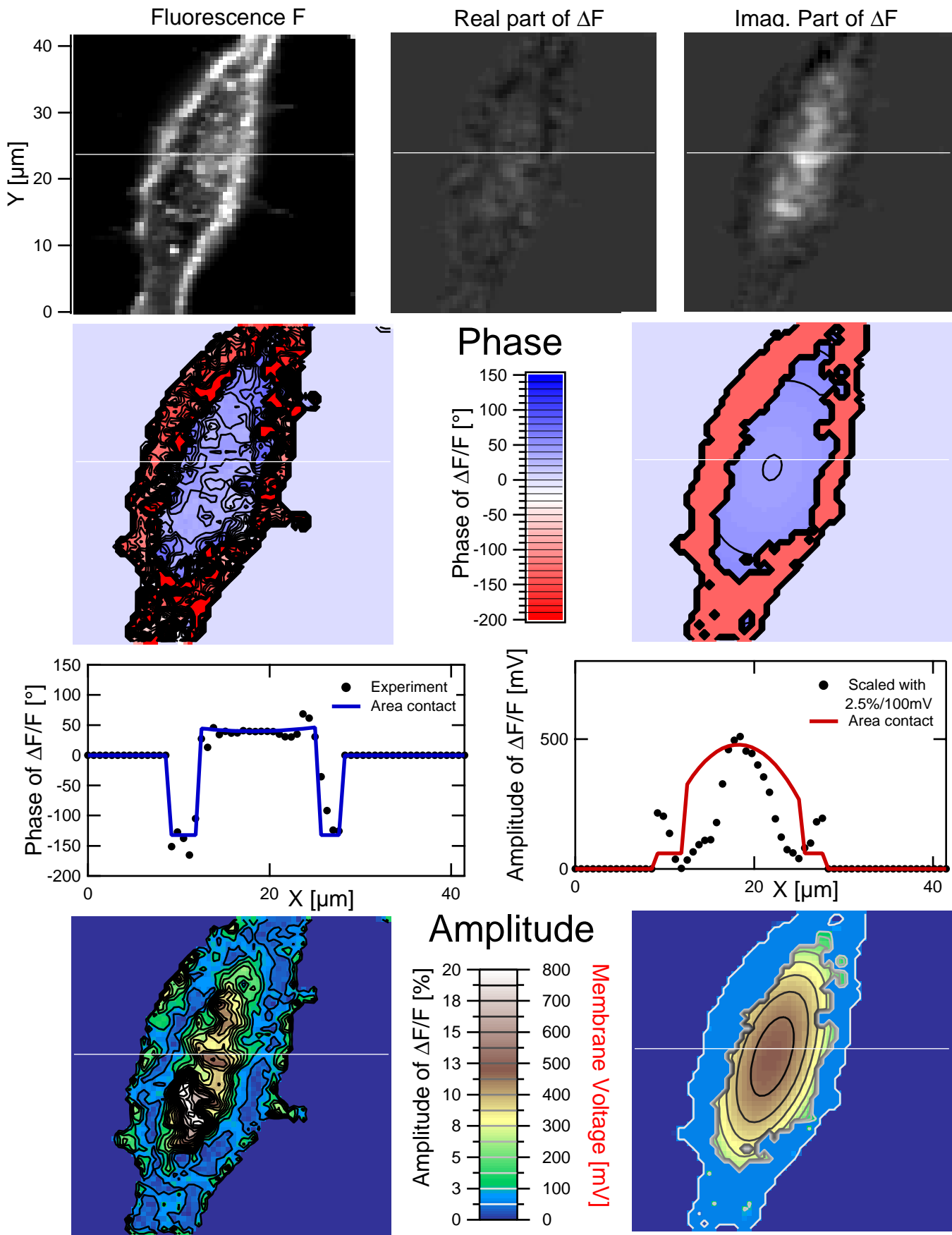


Fig 6.12 Spindle-shaped HEK cell with area contact theory. Parameters from Table 6.5.

The same cell was also measured at 625kHz. In this case, the phase correction from the chip was increased to 33° as derived from chip theory (Table 3.2 on page 55). To match the amplitude signal, sensitivity had to be reduced to a very low value of $0.75\%/100\text{mV}$. Otherwise the same parameters were used. The phase signal corresponds well to the fit as shown in the section in Fig 6.13. The phase of the junction membrane is now decreased to almost zero due to the higher stimulation frequency. Also the amplitude signal is fitted properly, except for the artefacts described beforehand. No small-signal from the dye on the chip could be detected, similar to the poly-lysine coating shown in 8.2 on page 160.

HEK Cell in Spindle Shape at 625kHz

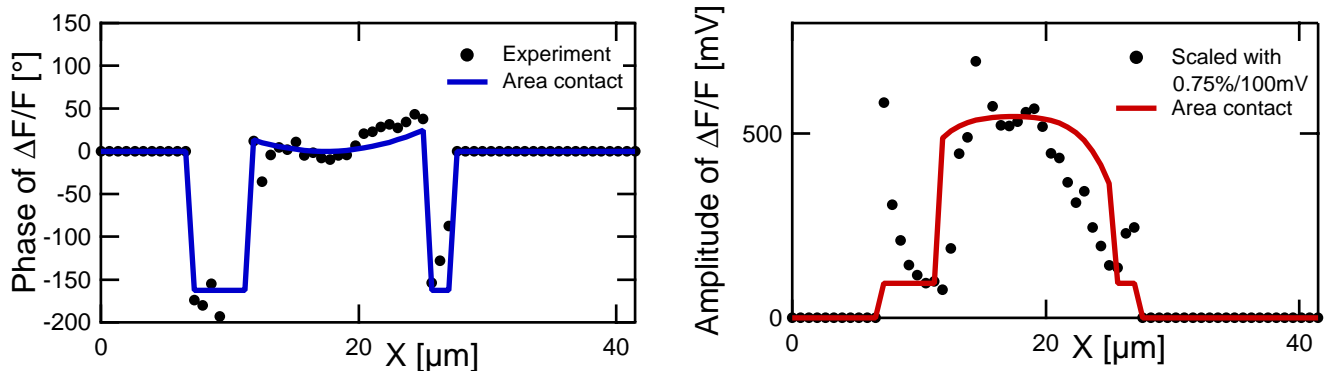


Fig 6.13 Section of the cell in Fig 6.12 now measured at 625kHz. The area contact model used the same parameters, but sensitivity was decreased to $0.75\%/100\text{mV}$.

A second spindle-shaped HEK measured is presented in Fig 6.14 and Table 6.6. The measurement yields junction data that are similar to those from the spindle-shaped HEK cell shown in Fig 6.12 with the parameters of Table 6.5 except for a dye sensitivity of $6\%/100\text{mV}$. From the phase signal and the point contact model we derive $\tau_J^{\text{JM}}=1.5\mu\text{s}$ and $\tau_J^{\text{FM}}=1.1\mu\text{s}$. Slightly higher values are obtained from transient measurements on the same cell (paragraph 7.2.A on page 144).

Image= $36\mu\text{m}$	$f=125\text{kHz}=4f_0$
Pixel= $0.57\mu\text{m}$	$V_{\text{Chip}}=1.5\text{V}$
Binning= 3×3	$\epsilon=0.34$ (10nm)
$A_{\text{JM}}=600\mu\text{m}^2$	$\beta=0.25$

TABLE 6.6 Measurement and model parameter for the spindle-shaped HEK cell in Fig 6.14. We find with $r_J=4\text{M}\Omega$ a fourfold reduced specific resistance relative to the bulk electrolyte. The time constant of the junction membrane is $\tau_J^{\text{JM}}=1.5\mu\text{s}$ as estimated from phase and point contact model.

Area contact Model		Point contact Model	
$r_J=4.0\text{M}\Omega$	Sens.= $6\%/100\text{mV}$	$\text{Phase}_{\text{JM}}=40^\circ$	$\text{Phase}_{\text{FM}}=-130^\circ$
$\tau_J^{\text{JM}}=2.7\mu\text{s}$	$\tau_J^{\text{FM}}=1.6\mu\text{s}$	$\tau_J^{\text{JM}}=1.5\mu\text{s}$	$\tau_J^{\text{FM}}=1.1\mu\text{s}$
$g_J^{\text{JM}}=440\text{mS}/\text{cm}^2$	$g_J^{\text{FM}}=750\text{mS}/\text{cm}^2$	$g_J^{\text{JM}}=750\text{mS}/\text{cm}^2$	$g_J^{\text{FM}}=1070\text{mS}/\text{cm}^2$
$V_{\text{JM}}=350\text{mV}$	$V_{\text{FM}}=45\text{mV}$	$V_{\text{JM}}=290\text{mV}$	$V_{\text{FM}}=70\text{mV}$

Spindle-shaped HEK cell at 125kHz

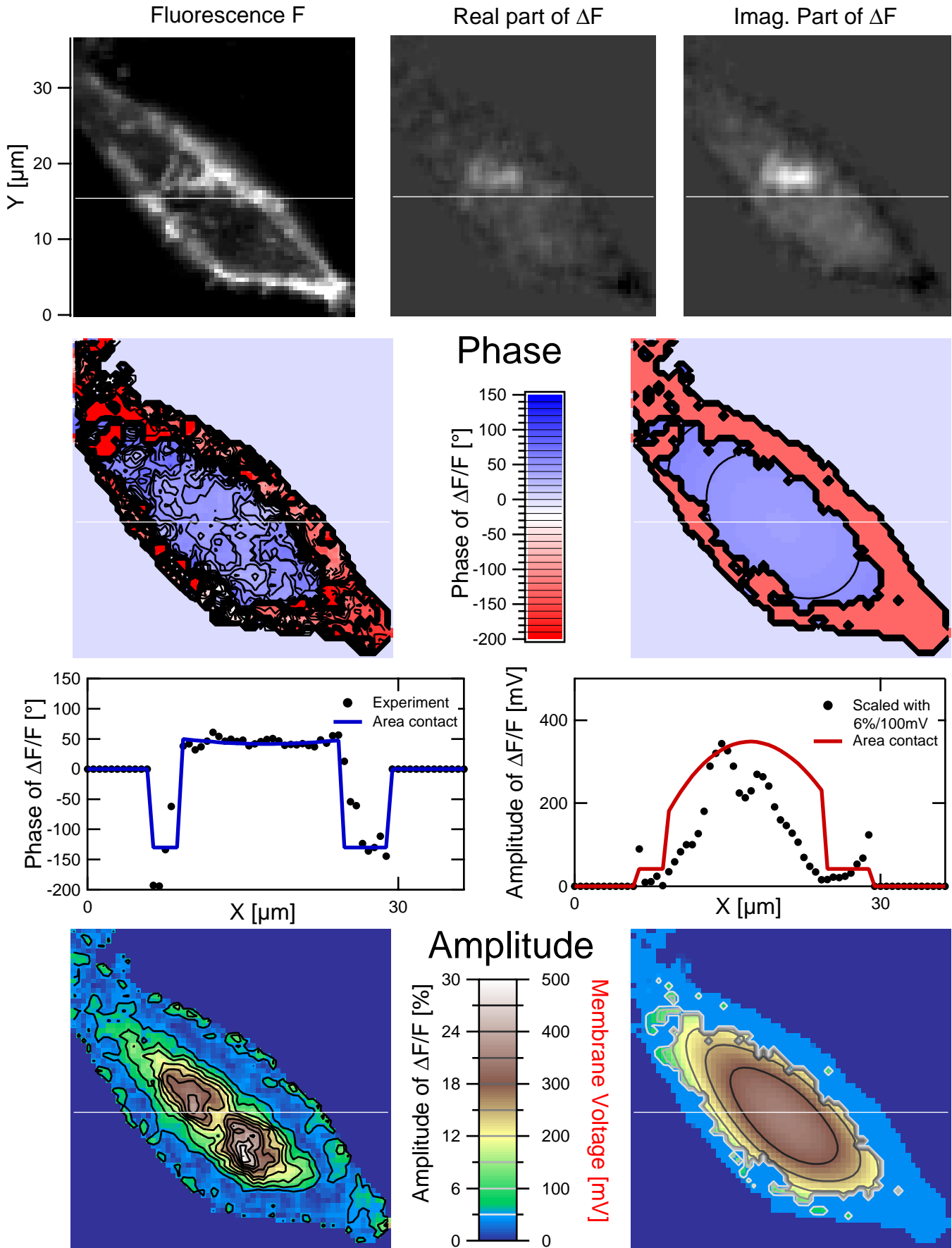


Fig 6.14 Spindle-shaped HEK cell with area contact fit. Parameters from Table 6.6.

6.3.C Epithelioid HEK cells

We also find large epithelioid cells in the HEK cell culture. Their increased size allows for improved measurements of the junction membrane. They have the same junction thickness as spindle-shaped HEK cells, shown with FLIC [Görler 1999]. Therefore we expect similar junction properties. We present two measurements on epithelioid HEK cells in Fig 6.15 and Fig 6.16 on the next two pages. Transient measurements of these cells can be found in paragraph 7.1 on page 137 and in paragraph 7.2.B on page 147.

The measurement and model parameter values of the first measurement are shown in Table 6.7, the measurement in Fig 6.15. Both the phase in the junction and free membrane can be fitted very precisely with a junction resistance of $r_J=4M\Omega$. This corresponds to a resistance reduction relative to the bulk medium by a factor of 4. Therefore we obtain identical junction properties of spindle-shaped and epithelioid HEK cells, apart from a slower time constant in the epithelioid cell due to the larger junction area. Using the point contact model the phase of around 20° in the center of the junction yields a junction time constant of $\tau_J^{JM}=3.5\mu s$, whereas $\tau_J^{JM}=1.5\mu s$ for the spindle-shaped HEK cells. For the free membrane the phase of -145° results in a time constant of $\tau_J^{FM}=1.8\mu s$. Both values are precisely confirmed from a subsequent transient measurement (7.1 on page 137). For the center of the junction membrane, values $g_J^{JM}=200mS/cm^2$ are obtained both from the phase and from the point contact approximation of the area contact model. With respect to the amplitude measurement, the hammock shape in the junction membrane is slightly enhanced in the experiment relative to the area contact fit. The destructive interference effect towards the boundary of the visible junction membrane is reduced.

Image=42 μm	f=125kHz=5f ₀
Pixel=0.66 μm	V _{Chip} =3.0V
Binning=3x3	$\epsilon=0.07$ (50nm)
A _{JM} =1000 μm^2	$\beta=0.5$

TABLE 6.7 Measurement and model parameter for the epithelioid HEK in Fig 6.15. We obtain with $r_J=4.0M\Omega$ a fourfold reduced specific resistance relative to the bulk electrolyte. The time constant of the junction membrane is $t_J=3.5\mu s$ as estimated from the phase and the point contact model.

Area contact Model		Point contact Model	
$r_J=4.0M\Omega$	Sens.=6%/100mV	Phase _{JM} =20°	Phase _{FM} =-145°
$\tau_J^{JM}=3.5\mu s$	$\tau_J^{FM}=2.0\mu s$	$\tau_J^{JM}=3.5\mu s$	$\tau_J^{FM}=1.8\mu s$
$g_J^{JM}=200mS/cm^2$	$g_J^{FM}=350mS/cm^2$	$g_J^{JM}=200mS/cm^2$	$g_J^{FM}=470mS/cm^2$
V _{JM} =230mV	V _{FM} =60mV	V _{JM} =170mV	V _{FM} =70mV

The 50 nm oxide yields a capacitance ratio $\epsilon=0.07$. A sensitivity of 6%/100mV is used to match the amplitude in the free membrane and also the average amplitude in the junction membrane. For some parts of the junction membrane the sensitivity is higher than that, especially where the junction fluorescence is low. The bright spot in the center of the junction membrane reduces the amplitude of $\Delta F/F$. Probably it is due to a staining of the cell nucleus which does not contribute to the voltage signal. These sensitivity fluctuations impair the amplitude profile measurement.

Epithelioid HEK Cell at 125kHz

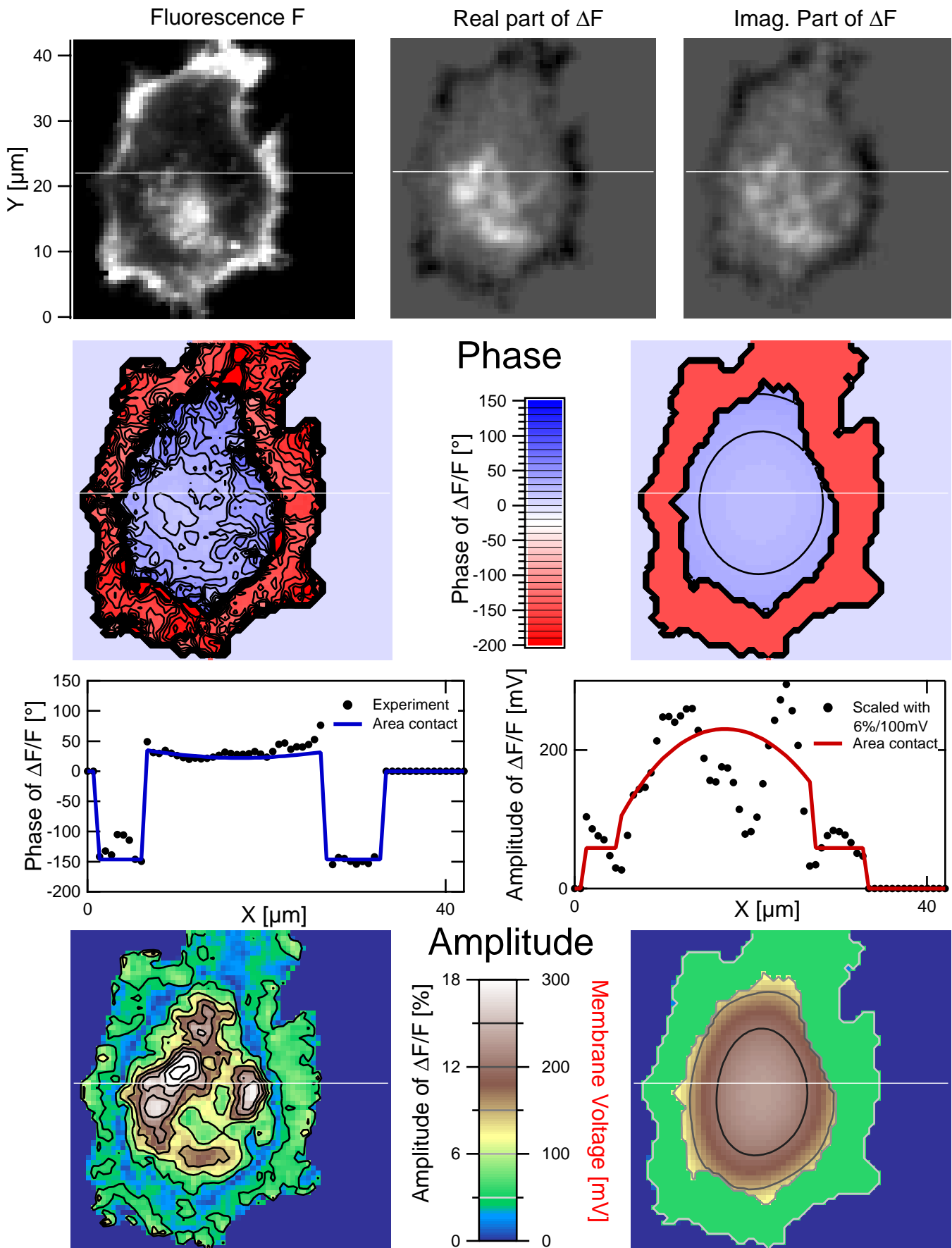


Fig 6.15 Epithelioid HEK cell with area contact theory. Parameters from Table 6.7.

Epithelioid HEK Cell at 125kHz

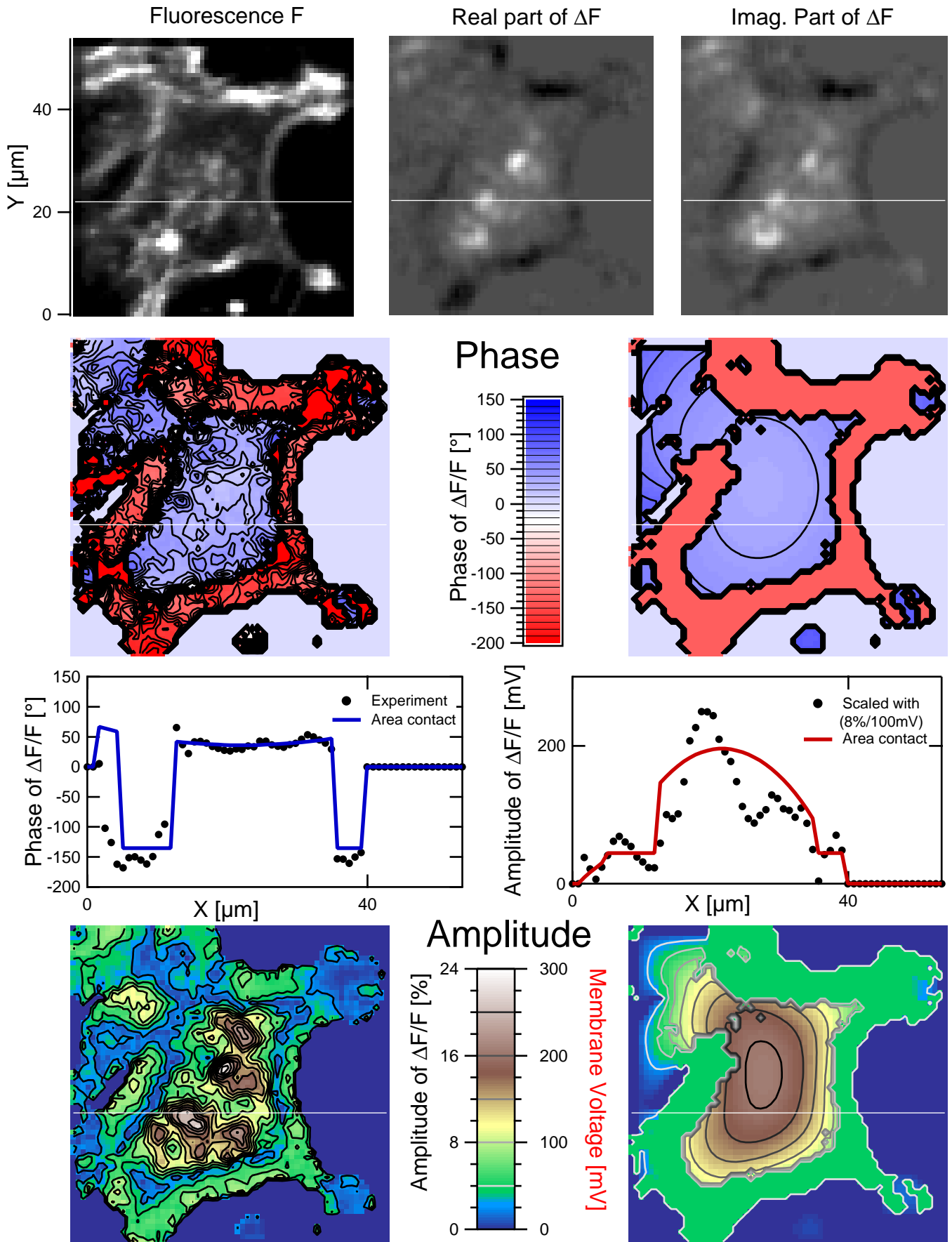


Fig 6.16 Epithelioid HEK cell with area contact theory. Parameters from Table 6.8.

The second measurement on epithelioid cells is presented on the previous page in Fig 6.16, measured and fitted with the parameters in Table 6.8:

Image=54 μ m	f=125kHz=5f ₀
Pixel=0.84 μ m	V _{Chip} =3.0V
Binning=3x3	ϵ =0.07 (50nm)
A _{JM} =1900 μ m ²	β =0.5

TABLE 6.8 Measurement and model parameter for the epithelioid HEK in Fig 6.9. We find with $r_J=2.0M\Omega$ a sevenfold reduced specific resistance as compared to the bulk electrolyte. Time constant of the junction membrane is $\tau_J=2.7\mu$ s as estimated from phase and point contact model.

Area contact Model		Point contact Model	
$r_J=2.0M\Omega$	Sens.=8%/100mV	Phase _{JM} =25°	Phase _{FM} =-150°
$\tau_J^{JM}=3.3\mu$ s	$\tau_J^{FM}=1.9\mu$ s	$\tau_J^{JM}=2.7\mu$ s	$\tau_J^{FM}=2.2\mu$ s
$g_J^{JM}=220$ mS/cm ²	$g_J^{FM}=380$ mS/cm ²	$g_J^{JM}=270$ mS/cm ²	$g_J^{FM}=330$ mS/cm ²
V _{JM} =200mV	V _{FM} =45mV	V _{JM} =150mV	V _{FM} =75mV

In this case a further reduced junction resistance of $r_J=2M\Omega$ is found. The discrepancy between the specific junction and bulk resistance is rather high with a factor of 7. Within the point contact framework, the phase values of around 25° in the center of the junction yield a time constant $\tau_J^{JM}=2.7\mu$ s. For the free membrane we find $\tau_J^{FM}=2.2\mu$ s from a phase of -150°. Both values are precisely confirmed by a subsequent transient measurement (7.2.B on page 147). Values around are found For the center of the junction membrane $g_J^{JM}=250$ mS/cm² is obtained either from the phase or from the point contact approximation of the area contact model.

The amplitude is matched to theory with a sensitivity of 8%/100mV. Again, there is an inhomogeneous amplitude of the relative small-signal fluorescence, probably due to dye binding to internal membranes that are not affected by the stimulation. However, the amplitude may be reconstituted by simply neglecting regions of high fluorescence. The area ratio $\beta=0.5$ is both confirmed by the z-stack taken after the measurement (data not shown) and the fluorescence amplitude signal. The voltage amplitude of 3.0V at the chip is reduced to 200mV in the center of the junction and to 45mV in the free membrane.

6.4 Group of HEK cells and Monolayers

Cells in a monolayer enhance the junction time constant by a factor of four. For the junction resistance between the cells $r_{up}=2.5M\Omega$ is estimated, a value similar to the junction resistance.

As demonstrated before, the junction time constant of a single HEK cell is very low. It is an intriguing question whether the junction time constant can be enhanced by using cell monolayers since they might form very tight cell-cell contacts. The best way to tackle the problem would be to measure z-stacks of cell monolayers. This is not possible because of photodamage. Therefore we derive estimates from measuring either the junction membrane or the membrane between the cells at a height of 5 μ m above the chip surface, which is about a quarter of the cell height, and at

$z=0\mu\text{m}$. If the cell-cell contact had a highly increased junction resistance, it could perfectly isolate the lower junction membrane from the electrolyte. This would result in an increased junction time constant, limited only by the membrane time constant of the cell. The area contact model could be applied to more than one cell and we would expect to find the same junction resistance as for single cells. We will see that this assumption holds for a small group of HEK cells, measured at $0\mu\text{m}$ and $5\mu\text{m}$ above the chip surface. Furthermore, the cell-cell contact has junction properties similar to the cell-chip contact derived from measurements of cell monolayers. Here a junction time constant of $9\mu\text{s}$ was measured, yielding a cell-cell cleft resistance $r_{\text{up}}=2.5\text{M}\Omega$.

As mentioned above, a small group of HEK cells was measured. Assuming a high resistance between the cells, we substitute the group by one huge cell described with the area contact model. The cell group is measured at $0\mu\text{m}$ shown in Fig 6.17 and at $5\mu\text{m}$ relative to the chip surface shown in Fig 6.18 with the measurement and model parameter values for both in Table 6.9 below:

Image= $50\mu\text{m}$	$f=125\text{kHz}=12f_0$
Pixel= $0.61\mu\text{m}$	$V_{\text{Chip}}=1.5\text{V}$
Binning= 3×3	$\epsilon=0.34$ (10nm)
$A_{\text{JM}}=1800\mu\text{m}^2$	$\beta=0.7$

TABLE 6.9 Measurement and model parameter for a group of HEK cells in Fig 6.17 and Fig 6.18 on the next two pages. Images were taken $0\mu\text{m}$ and $5\mu\text{m}$ above the surface of the chip. By applying the area contact model we obtain $r_{\text{J}}=3.0\text{M}\Omega$. The time constant of the junction cannot be obtained as the phase is zero in the center of the cells.

Area contact Model		Point contact Model	
$r_{\text{J}}=3.0\text{M}\Omega$	Sens.=4%/100mV	Phase $_{\text{JM}}=-10^\circ$	Phase $_{\text{FM}}=-160^\circ$
$\tau_{\text{J}}^{\text{JM}}=6.8\mu\text{s}$	$\tau_{\text{J}}^{\text{FM}}=3.9\mu\text{s}$	---	$\tau_{\text{J}}^{\text{FM}}=3.6\mu\text{s}$
$g_{\text{J}}^{\text{JM}}=130\text{mS}/\text{cm}^2$	$g_{\text{J}}^{\text{FM}}=230\text{mS}/\text{cm}^2$	---	$g_{\text{J}}^{\text{FM}}=260\text{mS}/\text{cm}^2$
$V_{\text{JM}}=400\text{mV}$	$V_{\text{FM}}=170\text{mV}$	---	$V_{\text{FM}}=200\text{mV}$

Indeed there is a rather homogeneous phase signal in the center of the cell group for both scans. A typical free membrane phase of about -160° is only measured at the border of the cell group and not for the membranes between the cells. Thus the group behaves like a single cell. All the membranes between the cells show a phase close to the phase of the junction membrane. This is especially obvious in the real part of the small-signal ΔF where the parts inside the cell group are bright with a dark border around the cell group and can be found for both scans at $z=0\mu\text{m}$ and $z=5\mu\text{m}$. At $5\mu\text{m}$ the signal of the junction membrane is not expected to contribute to the signal. The voltage signal at $5\mu\text{m}$ is 25% lower than at $0\mu\text{m}$. Thus the junction voltage has decreased slightly with increasing distance to the chip. For unknown reasons, the phase signal displays slightly negative values of -10 to -20° in the center of the cell. This deviation is larger for the scan at $0\mu\text{m}$. The area contact properties of this cell group are confirmed by transient measurements (7.3 on page 150).

Group of HEK Cells measured 0 μ m above the Chip

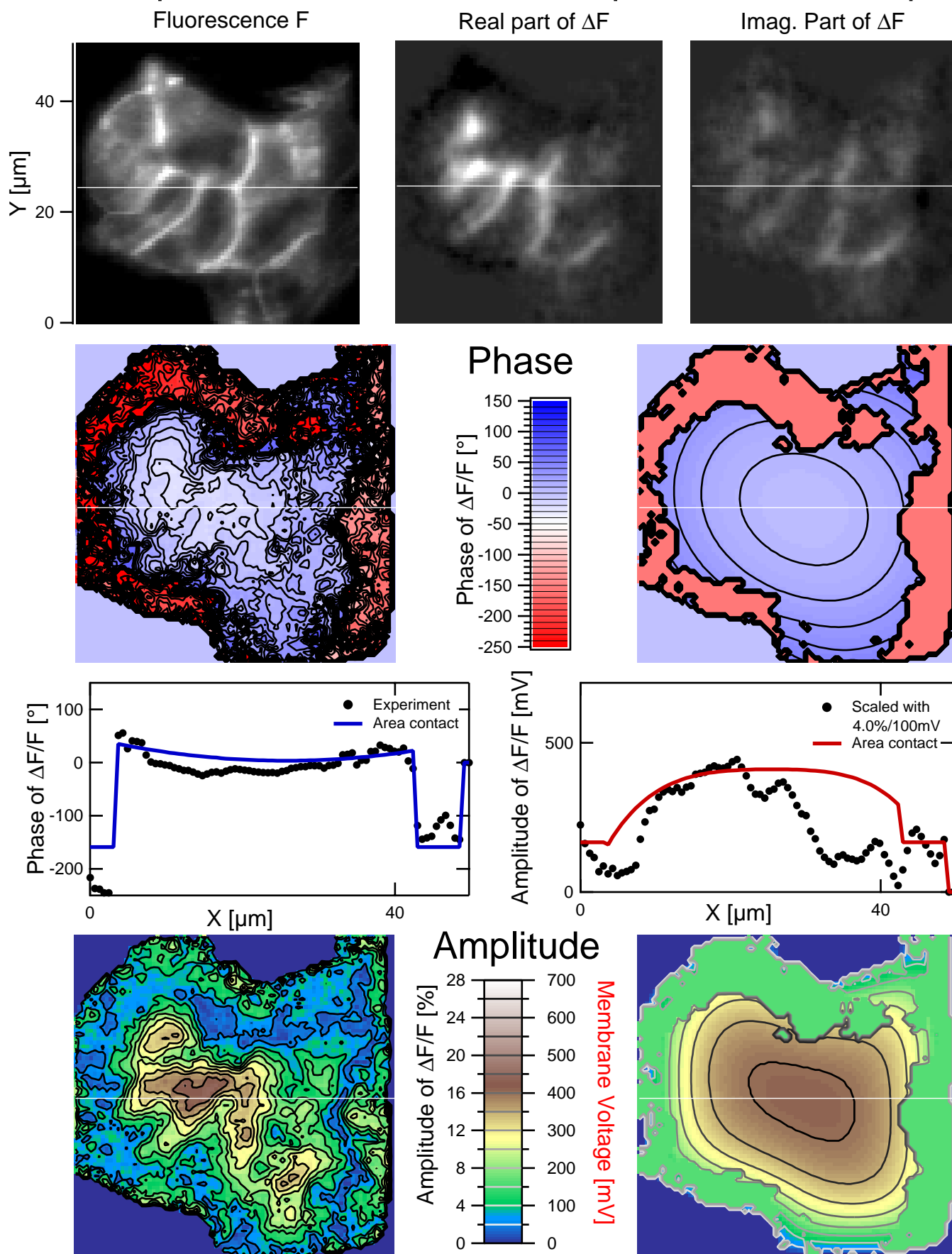


Fig 6.17 Group of HEK cells at $z=0\mu\text{m}$ with theory. Parameters from Table 6.9.

Group of HEK Cells measured 5 μ m above the Chip

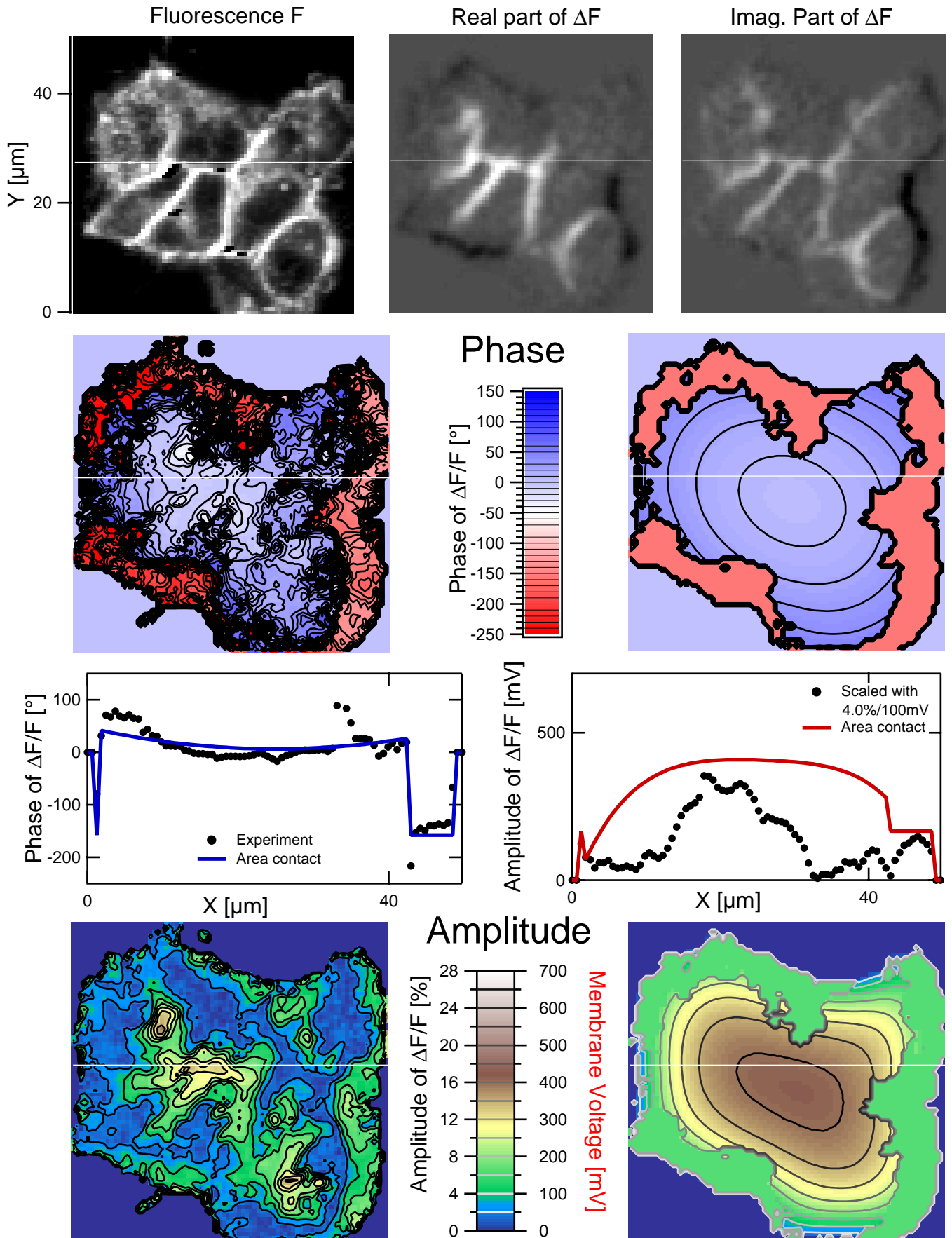


Fig 6.18 Group of HEK cells at $z=5\mu\text{m}$ with theory. Parameters from Table 6.9.

For discussion of the cleft resistance between the cells we consider the simplified equivalence circuit shown in Fig 6.19:

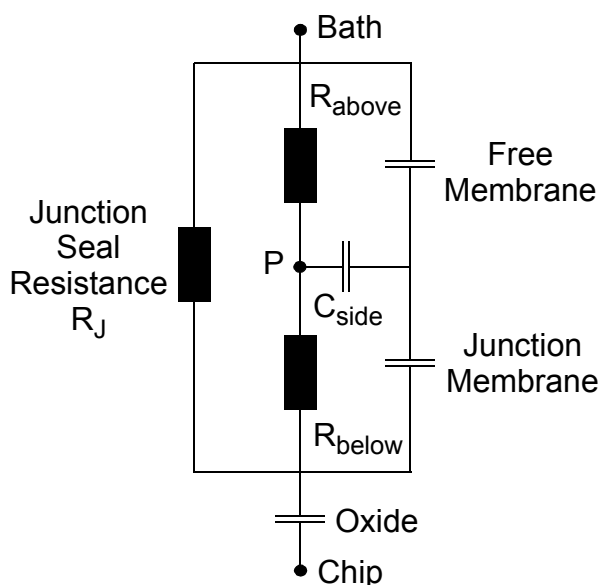
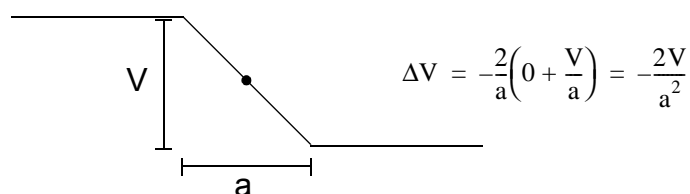


Fig 6.19 Simplified circuitry describing the voltage across the membranes between the cells embedded in a group of cells or a cell monolayer. The voltage is measured across C_{side} at the point P. With $R_{below}=0\Omega$ we obtain the same voltage sign in the membrane between the cells and the junction membrane (with $R_{above}=0\Omega$ the sign is reversed). The voltage at C_{side} reflects the voltage divider of R_{below} and R_{above} and hence the z-position of P. A full model would include an area contact model also in z-direction creating a voltage profile across the membranes between the cells. But we can estimate $R_{up}=R_{below}+R_{above}$ as it behaves like the seal resistance R_J from the time constant of the junction membrane.

The voltage across the cells is merely determined by the voltage divider of R_{below} and R_{above} and therefore the z-position of the point P. $R_{up}=R_{below}+R_{above}$ competes with the junction resistance R_J . According to the measurement of a small cell group (Fig 6.17 and Fig 6.9) the junction resistance of $r_J=3M\Omega$ is similar to that of single HEK cells. However, the cells behave like a huge single cell. Therefore it can be concluded that the resistance R_{up} is at least higher than the junction seal resistance R_J below the whole cell group. To estimate its magnitude we calculate a junction seal resistance $R_J=0.45M\Omega$ with $g_J^M=130mS/cm^2$ and $A_{JM}=1800\mu m^2$. Then the seal resistance between the cells must hold $R_{up}>0.45M\Omega$. The cell-cell contact is approximated as two rectangular membrane sheets of area $A_{up}=20\mu m*40\mu m$ (cell height * length of cell-to-cell walls) with the specific capacitance $c_M=1\mu F/cm^2$. The cleft between the cells defines a 2-dimensional cable with a sheet resistance r_{up} :

$$-\frac{\Delta V}{r_{up}} = 2c_M\partial_t V \quad [6.5]$$

Using a rough numerical approximation (like in 2.5.C on page 29) for the Laplace-operator:



we find:

$$\frac{-2V}{a^2 r_J} = 2c_M\partial_t V \quad \tau = c_M a^2 r_J = C_M R_{up} = 2A_{up} c_M R_{up} \quad [6.6]$$

With the cell height $a=20\mu m$ this results in $r_{up}=2A_{up}R_{up}/a^2$. Thus a lower limit of the sheet resistance between the cells can be derived from the HEK cell group measurement: $r_{up}>1.8M\Omega$

Semi-confluent HEK Cell layer at 125kHz

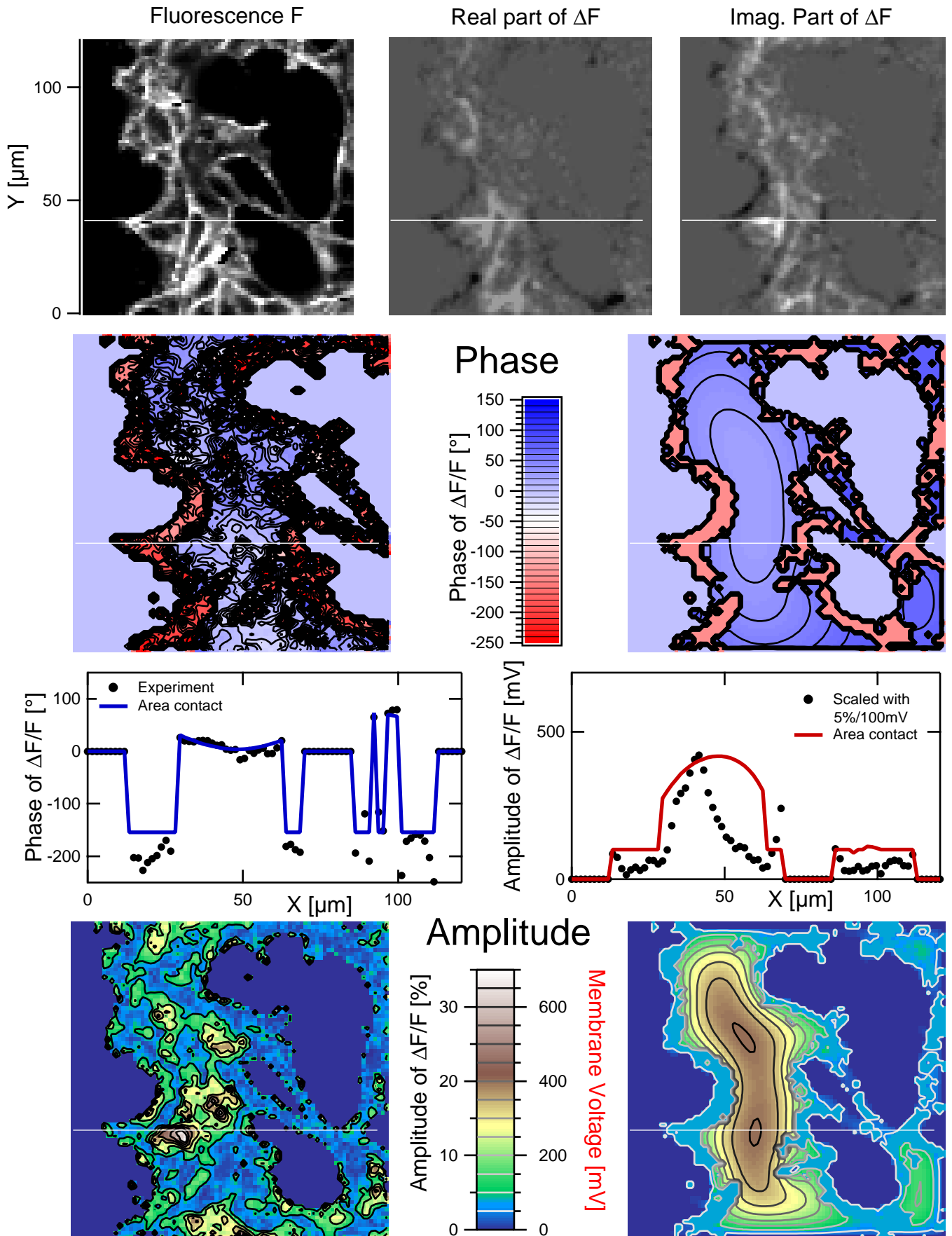


Fig 6.20 Semi-confluent HEK cell layer with theory. Parameters from Table 6.10.

The equivalence of small cell groups and single huge cells is also apparent in the measurement on a semi-confluent HEK cell layer shown on the previous page in Fig 6.20. The parameter values are given below in Table 6.10. The measurement can be precisely fitted with a junction resistance of $r_J=2.5M\Omega$

Image=120 μ m	f=125kHz=8f ₀
Pixel=1.47 μ m	V _{Chip} =1.5V
Binning=2x2	$\epsilon=0.34$ (10nm)
A _{JM} =8600 μ m ²	$\beta=0.5$

TABLE 6.10 Measurement and model parameters for a semi confluent HEK cell monolayer measured 0 μ m above the surface of the chip in Fig 6.20 on the previous page. By applying the area contact model we obtain $r_J=2.5M\Omega$. A time constant of the junction cannot be specified due to phase values around zero.

Area contact Model	
$r_J=2.5M\Omega$	Sens.=5%/100mV
V _{JM} =400mV	V _{FM} =100mV

Point contact Model
Phase _{FM} =-175°
$\tau_J^{FM}=15\mu$ s
$g_J^{FM}=70$ mS/cm ²
V _{FM} =170mV

Another estimate of the cell-cell seal resistance can be obtained by inspecting the phase of the junction membrane in a fully confluent cell monolayer. Such a measurement is presented in Fig 6.21 on the next page with the parameter values listed in Table 6.11 and Table 6.12 below:

Image=120 μ m	f=25kHz
Pixel=1.47 μ m	V _{Chip} =1.5V
Binning=1x1	$\epsilon=0.34$ (10nm)
A _{JM} =8600 μ m ²	$\beta=1.0$

TABLE 6.11 Measurement and model parameters for a monolayer of HEK cells shown in Fig. 6.21 on the next page measured 5 μ m above the surface of the chip.

Point contact Model	
Phase _{JM} =35°	Phase _{FM} =-135°
$\tau_J^{JM}=9\mu$ s	$\tau_J^{FM}=9\mu$ s
$g_J^{JM}=90$ mS/cm ²	$g_J^{FM}=90$ mS/cm ²
V _{JM} =310mV	V _{FM} =310mV

TABLE 6.12 The monolayer of HEK cells is fitted with a homogeneous point contact model to reveal the time constant of the membrane. This gives an estimate of the seal resistance between the cells R_{up} . A sensitivity of 4%/100mV was used

Here, we have switched to a lower stimulation frequency of 25kHz in order to match the expected lower time constant (see Fig 6.4 on page 95), and found a phase value of 35° for the voltage across the membranes between the cells. Assuming a monoexponential decay as implied by the point contact model a time constant of 9 μ s is obtained, increased by a factor of about 4 relative to the time constant of 2 μ s for single HEK cells with the same size as the cells in the group. Amplitude values are 300mV and below with a sensitivity of 6%/100mV matching the theoretical voltage that is obtained with $\beta=1.0$. We assume a cell height of a=20 μ m and neglect the resistance

HEK Cell Monolayer measured 5 μ m above the Chip

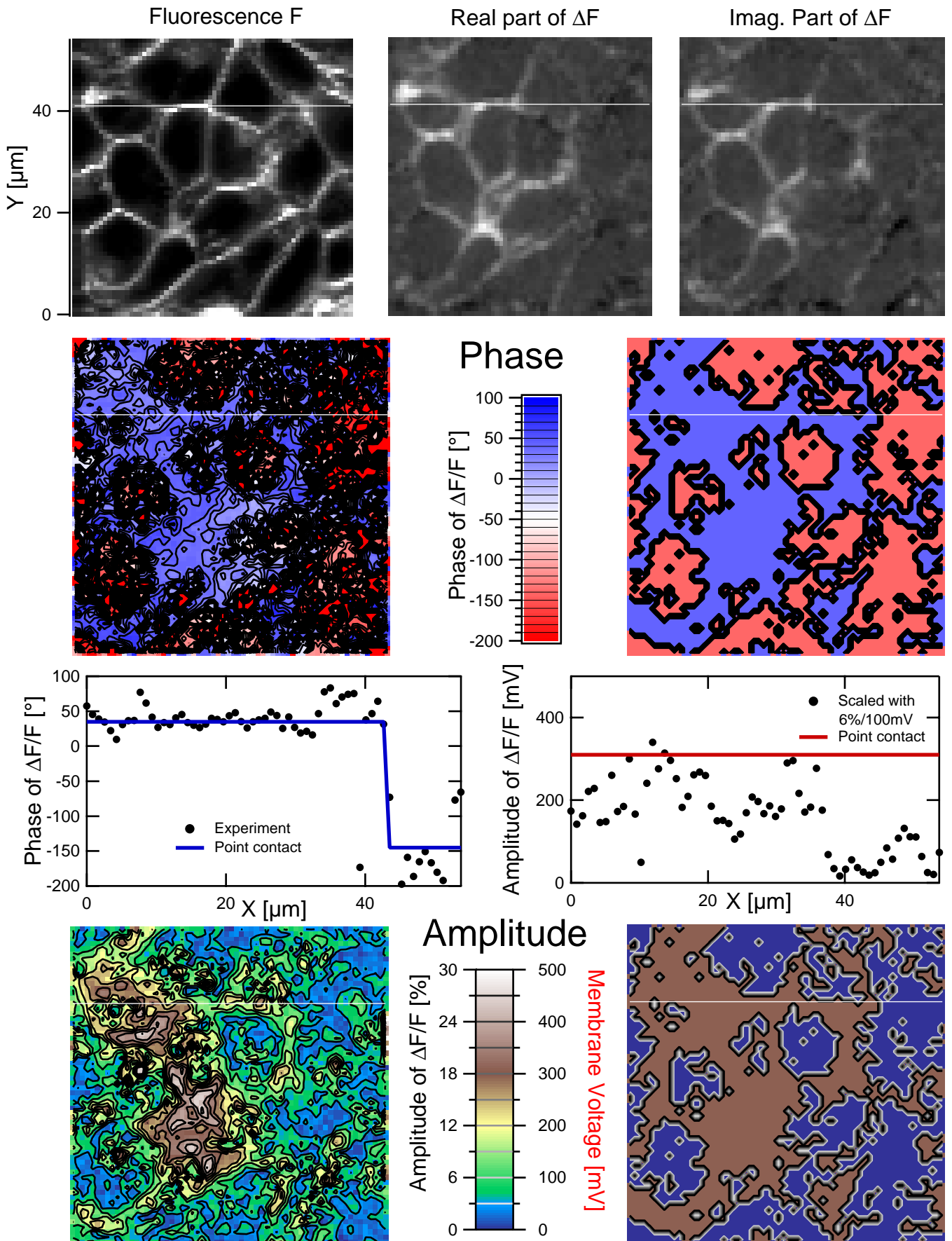


Fig 6.21 Confluent HEK cell layer with theory. Parameters from Table 6.11 and Tab

of the junction at the bottom side of the cells. With [6.6] this yields a rough estimate of the sheet resistance between cells of $r_{up}=9\mu\text{s}/(a^2c_M)=2.3\text{M}\Omega$, only slightly above the lower limit from the measurement in Fig 6.9 on page 117.

Upon analyzing the experiment in more detail, we observe an inhomogeneous distribution of the phase signal. Mainly in the bottom right corner there are cells with a phase signal below zero. The phase increases slightly towards this region indicating a decreasing coupling quality and a possible short circuit to the bath due to an imperfect cell monolayer at this location. A phase below zero is expected for cells with a very loose contact to neighboring cells, thus yielding a free membrane phase similar to that of single cells. Flat cells could also induce a negative phase signal with their free membrane. However, this appears less probable since the image of the cell-cell membrane is very sharp in contrast to images of the free membrane of flat cells at $z=5\mu\text{m}$.

Lines of imperfection in confluency can be seen in the measurement of Fig 6.22 marked by dark cell-cell membranes in the real part of the ΔF signal.

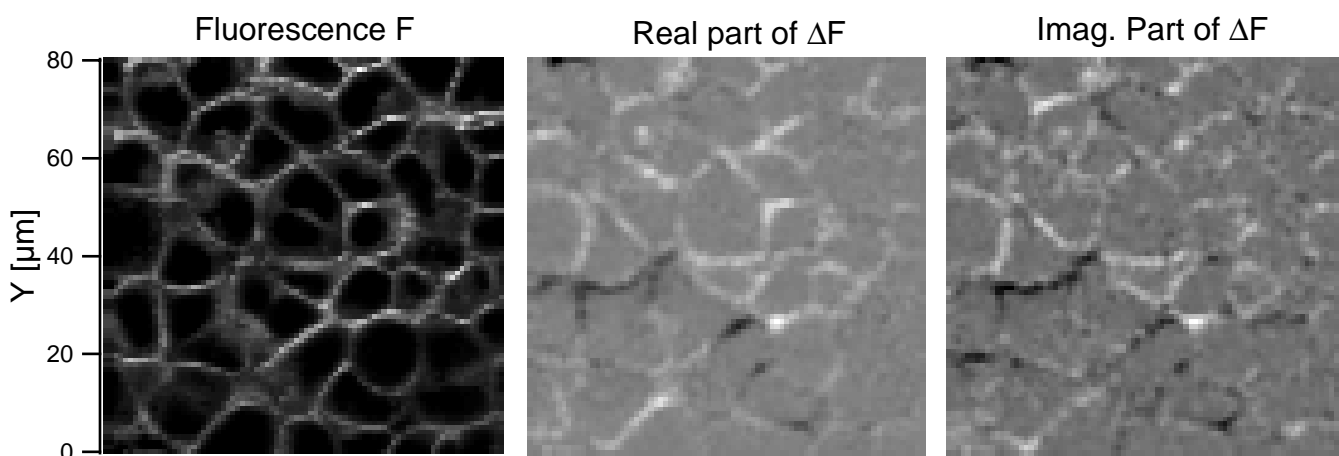


Fig 6.22 HEK cell monolayer with imperfection in confluency. The dark signal in the real part of ΔF indicates a voltage sign of the free membrane. It is most probable resulting from a short circuit to the bath due to large cell-cell contacts.

6.5 Rat neurons and astrocytes

Rat nerve cells on poly-lysine yield a junction resistance of $r_j=1.5\text{M}\Omega$. We derive a specific junction resistance of $7.5\Omega\text{cm}$, reduced by a factor of 15 as compared to the bulk. The junction time constant is $\tau_j=1.5\mu\text{s}$ and the junction conductance $g_{JM}=1500\text{mS}/\text{cm}^2$. Stimulation through a glia monolayer can be performed with similar junction properties.

6.5.A Hippocampal cell culture

The surface of the chip was wiped with a 1-vol% solution of a liquid dish detergent, rinsed with milli-Q water (Millipore, Bedford, MA, USA), dried, and sterilized with UV light as described in paragraph 3.4 on page 56. The chips were coated with poly-L-lysine (MW 375 500, Sigma, Heidelberg, Germany) by adsorption from a 10-mM aqueous solution for 1 h and dried.

Preparations of hippocampal neurons from embryonal rat brain were accomplished by Doris Eckerlein according to protocols of [Banker 1977] as published in [Vassanelli 1997] and [Vassanelli 1998]. Neurons were dissociated from the hippocampi of Wistar rats (Thomae, Biberach, Germany) at 18 days gestation. They were preplated to remove some of the glia cells and suspended in Dulbecco's medium (DMEM with glutamax I, Gibco, Eggenstein, Germany, No. 61965026) supplemented with 10-vol% foetal bovine serum (Gibco, 10106078) and 1-vol% penicilline/streptomycine (Gibco). The final concentration was 350 000 cells/ml. 1ml of the cell suspension was applied to the chip with 2ml of Dulbecco's medium. The chips were kept at 37°C and 10% CO₂ for 2h. Afterwards the medium was removed and the cells were cultured in 3ml of Dulbecco's medium without penicilline/streptomycine for six days. Cells were stained (4.1.C on page 61) in the culture medium and measured within 15min. Neurons tend to cluster if cultured for more than twelve days (shown in Fig 6.23a). After six days already neurons usually grow on a monolayer of astrocyte glia cells shown in Fig 6.23b/c. Glial cell growth is promoted by the foetal bovine serum contained in the medium. Glia cells can be seen on the flat chip by optical inspection. An example is shown in Fig 6.23c with glia present only on the left side of the chip.

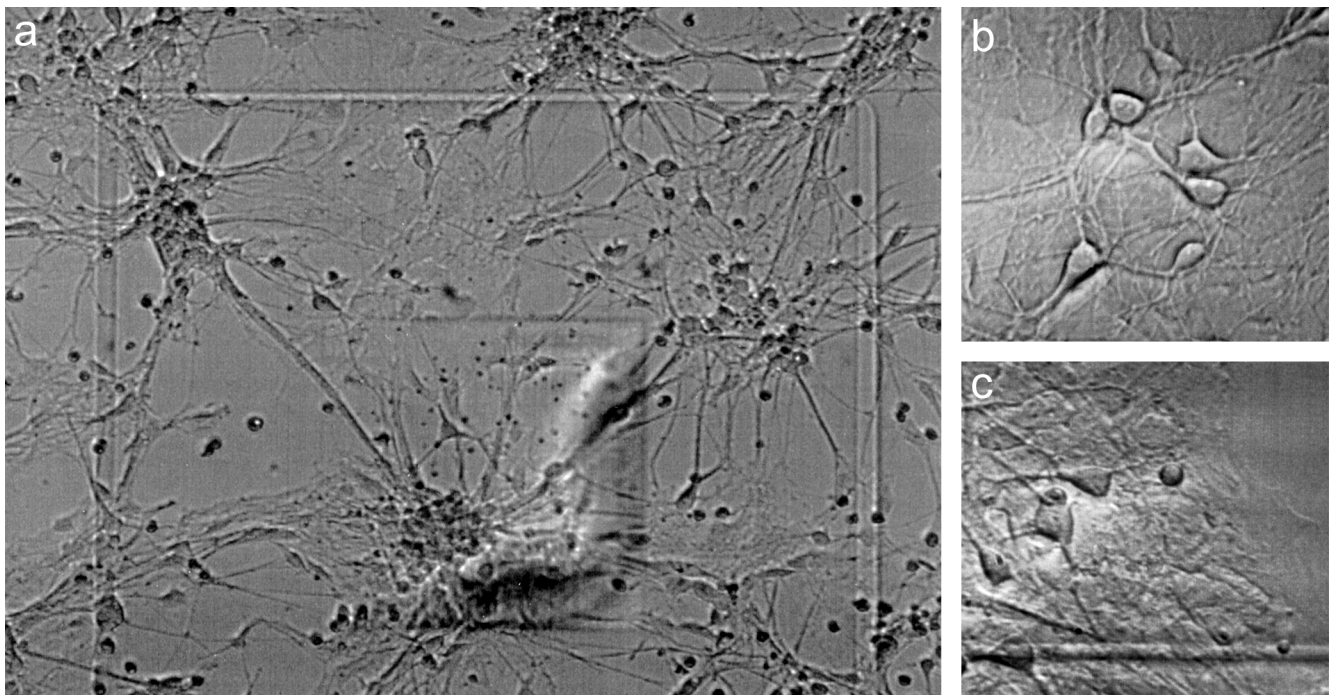


Fig 6.23 Rat nerve cell culture on the stimulation spot. In (a) neural clusters are shown that occur after twelve days in culture. After six days neurons usually grow on a monolayer of astrocyte glia cells illustrated in (b,c). Glia cells can be seen below the neurons in c on the left side as compared to the right side where glia cells are absent.

6.5.B Rat neuron on poly-lysine

In cell cultures with reduced astroglia growth, it was possible after six days to find single neurons in direct contact to the chip. The measurement is presented on the next page in Fig 6.24 with the model and measurement parameter values in Table 6.13:

Image=27 μ m	f=125kHz=4f ₀
Pixel=0.42 μ m	V _{Chip} =2.5V
Binning=4x4	ϵ =0.07 (50nm)
A _{JM} =400 μ m ²	β =0.5

TABLE 6.13 Measurement and model parameters for a rat neuron on poly-lysine shown in Fig 6.24. By applying the area contact model we find $r_j=1.5M\Omega$. The phase of the junction membrane corresponds to a junction time constant of $t_j=1.5\mu$ s and a specific sealing resistance of around $g_j=2000mS/cm^2$.

Area contact Model		Point contact Model	
$r_j=1.5M\Omega$	Sens.=7%/100mV	Phase _{JM} =40°	Phase _{FM} =-130°
$\tau_j^{JM}=0.6\mu$ s	$\tau_j^{FM}=0.3\mu$ s	$\tau_j^{JM}=1.5\mu$ s	$\tau_j^{FM}=1.0\mu$ s
$g_j^{JM}=1500mS/cm^2$	$g_j^{FM}=2600mS/cm^2$	$g_j^{JM}=2300mS/cm^2$	$g_j^{FM}=3300mS/cm^2$
V _{JM} =150mV	V _{FM} =35mV	V _{JM} =110mV	V _{FM} =50mV

We observe a homogeneous phase in the junction membrane and lower phase values for the free membrane and also the dendritic processes. It can be fitted precisely with the area contact model using a value $r_j=1.5M\Omega$. According to the point contact model, the phase of the junction membrane of around 40° yields to a junction time constant $t_j=1.5\mu$ s. Therefore the specific membrane conductance of the junction membrane is $g_j=2300mS/cm^2$. Both values fit well into the range of values measured with a transistor in [Vassanelli 1997], where the weak coupling is explained by a small junction membrane area of 20 μ m². In the present case, there is weak coupling and a large area of the junction membrane. The bulk electrolyte is the neurobasal medium with a measured resistance of 115 Ω cm. Together with the average distance of 50nm ([Braun 1998] and Fig 2.18 on page 34) we obtain $\rho_j=1000\Omega$ cm and have to assume a 15-fold reduced specific junction resistance. The factor could be overestimated by approximately 30% as the area of several dendrites was added to the total area of the junction. In addition the neuron might enrich the junction cleft with conducting ions. Another, although less conceivable possibility would be an enhanced electrolyte conductivity for high frequencies of about 100kHz. The free membrane yields phase values of around -130° which correspond to a time constant $t_j^{FM}=1.0\mu$ s.

In order to match the junction voltage of 150mV to the fluorescence amplitude we have to assume a rather high sensitivity of 7%/100mV. However, this value is comparable to the 9%/100mV obtained for retzius cells (paragraph 4.1.B on page 60). The area contact amplitude profile is in poor agreement with the relative fluorescence amplitude due to fluctuating sensitivities within the inhomogeneously stained junction membrane.

Rat Neuron on Poly-Lysine

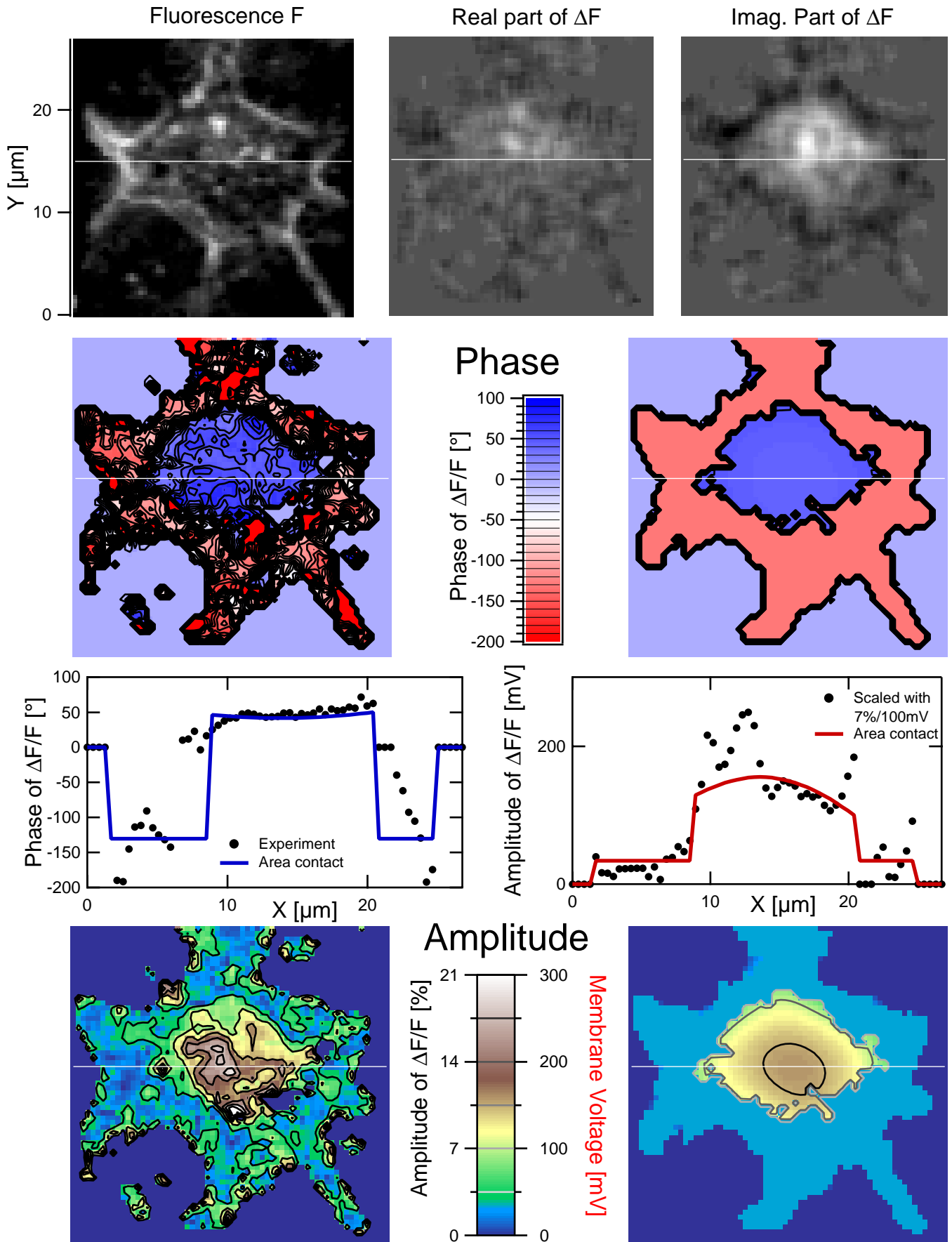


Fig 6.24 Rat neuron on poly-lysine with theory. Parameters given by Table 6.13.

6.5.C Rat neuron on top of a glia cell layer

In cell culture rat neurons have the tendency to grow on a monolayer of astrocyte glia cells unless special techniques are applied. Long-term culture of neurons free of glia cells seems to be difficult. For example prosthetics are typically also covered with a layer of glia cells. Therefore we tried to stimulate the membrane of neurons on top of a glia monolayer by the chip underneath:

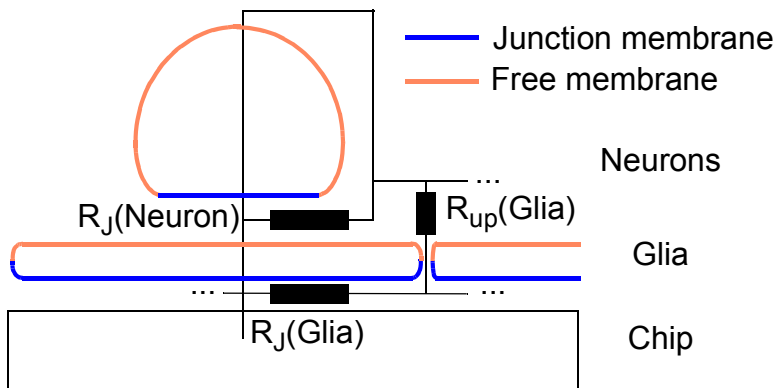


Fig 6.25 Stimulation of a neuron via a monolayer of glia cells. The voltage across the free membrane of the glia cells can stimulate the neuron if the time constant of $R_J(\text{Glia})$ and $R_{up}(\text{Glia})$ is larger than the time constant of $R_J(\text{Neuron})$. With $\beta=1.0$ for glia cells no loss in stimulation voltage due to the glia cell layer is expected.

A sketch of the geometrical situation is given in Fig 6.25. Glia cells are flat and can cover an area about $1600\mu\text{m}^2$ or more. Together with their neighboring cells they form a confluent layer. Measurements on stained cells showed that their cell-cell contacts are not necessarily tight although glia cells form gap junctions in tissue. But even with single cells we can apply high voltages across the free membrane of the glia cells. With a reasonable value of $\beta = 1.0$ the upper membrane potential of the glial cell should adopt the same amplitude (but with reversed sign) as its junction membrane potential. In the case of a neuron sitting on top of the glia cell the voltage across the upper glial membrane can also excite the membrane of the neuron.

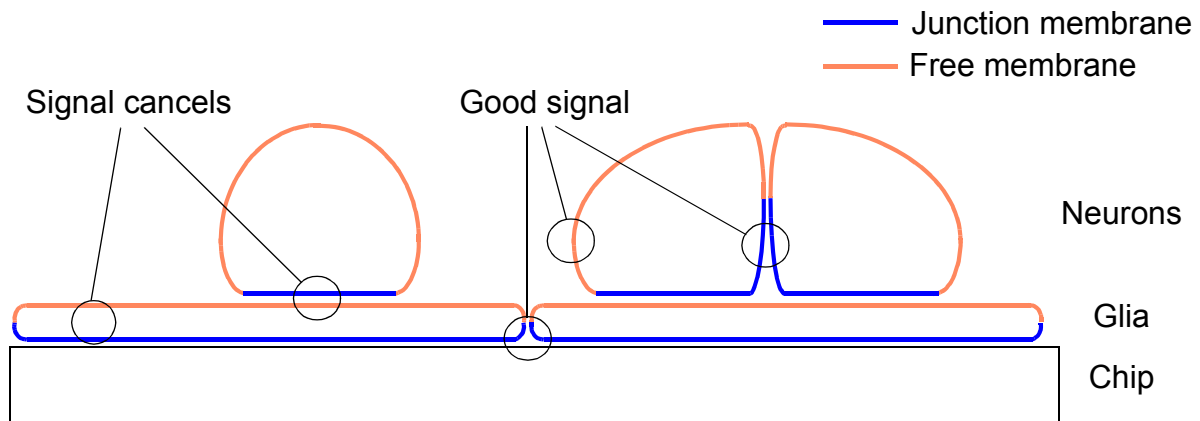


Fig 6.26 Signal interference for neurons on a monolayer of glia cells. The signal from the junction and the free membrane of a glia cell superimposes to signal zero. Also the voltage across the junction membrane of the neurons and the free membrane of the glia cell cannot be detected. Glia cells yield detectable signals only at their cell-cell contacts. Neurons have to be detected at their free membrane or at the membrane between two cells.

For high frequencies we would expect a voltage divider of spot oxide, junction and free membrane of the glia cells, and junction and free membrane of the neuron. In case of the same junction properties between spot oxide, glia and neuron, the junction voltage should be diminished due to

junction resistances $R_J(\text{Glia})$ and $R_{\text{up}}(\text{Glia})$ in the glia cell and furthermore with $R_J(\text{Neuron})$ in the neuron. But the junction resistance $R_J(\text{Glia})$ is assumed to be higher than $R_J(\text{Neuron})$ due to the large junction area of the glia cell. Since the focus height of the microscope is $1.5\mu\text{m}$ and the glia height is around $2\mu\text{m}$ some measurement spots are cancelled by superposition of the small-signal fluorescence from the free and the junction membrane. Especially for the junction of the neuron we don't expect any signal because the sign and amplitude of junction membrane of the neuron and free membrane of the glia cell cancel out each other perfectly as proved experimentally. The signal superposition is explained in Fig 6.26.

Thus the best way was to measure two neurons at their cell-cell contact or to measure the free membrane of the neurons. Both cases are visible in the measurement shown in Fig 6.27.

Rat Neuron on Astrocyte Monolayer

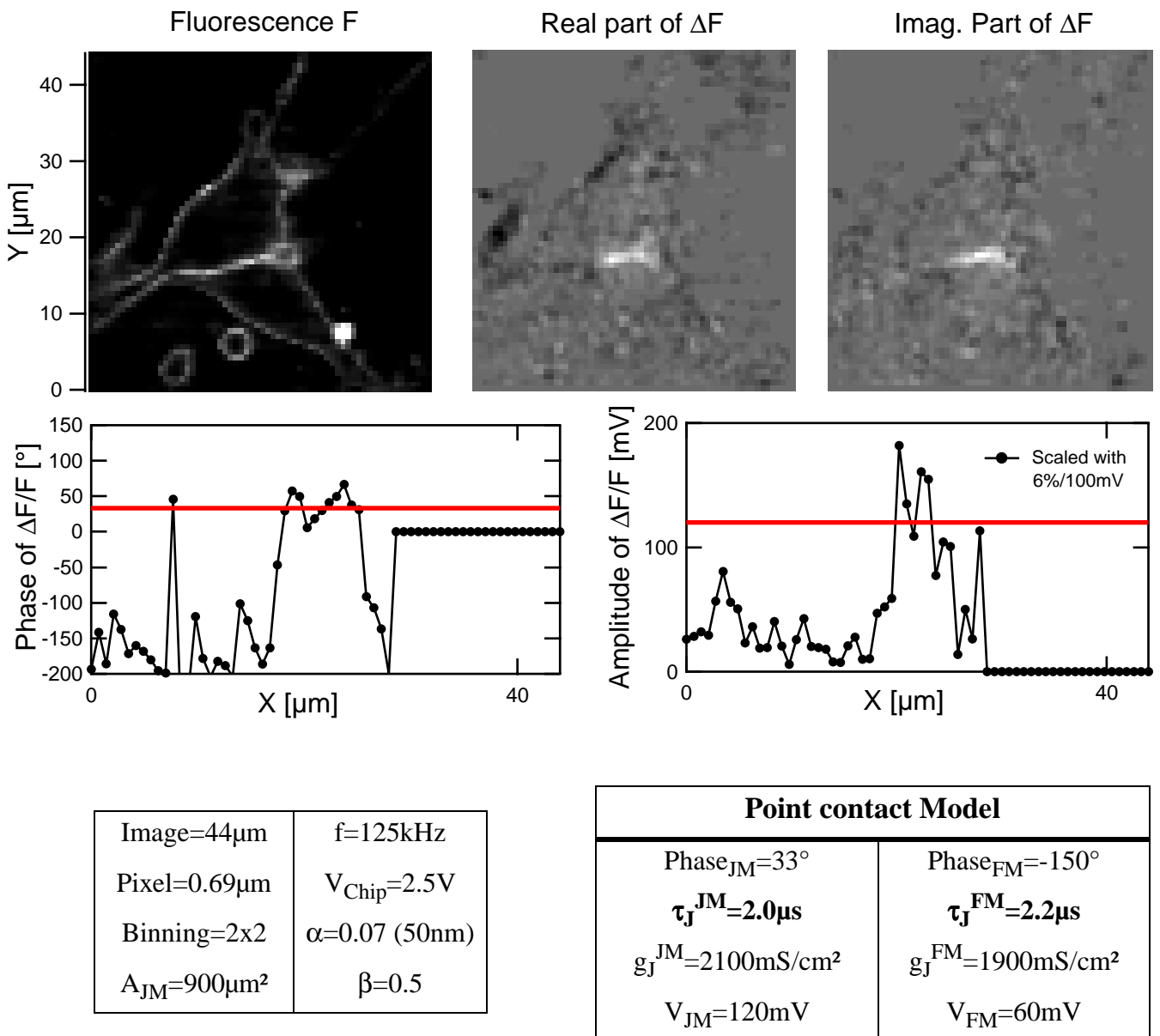


Fig 6.27 Measurement and model parameter for a rat neuron cell grown on a monolayer of astrocyte glia. The phase of the junction membrane corresponds to a junction time constant of $t_j=2\mu\text{s}$ and a specific sealing resistance of $g_j=2000\text{mS}/\text{cm}^2$.

As expected there is no signal from the junction membrane of the neuron. Assuming a larger time constant of the glia cell we discuss the measurement only in terms of the point contact model for junctions between neuron and glia. The phase of the neuron junction is 33° and results in a time constant of $2.0\mu\text{s}$. The phase of the free membrane is estimated with less precision to be -150° corresponding to a time constant of $2.2\mu\text{s}$. Therefore we obtain a specific junction conductance of around $2000\text{mS}/\text{cm}^2$, similar to the value of a direct junction between neuron and silicon. With a sensitivity of $6\%/100\text{mV}$ there is a good agreement between the measured amplitude and a junction voltage of 120mV as calculated from the point contact model. Therefore we conclude that neurons sitting on top of glia cells can be excited by capacitive stimulation. However it has to be emphasized that the reverse path, i.e. the detection of a signal from the neuron above a glia cell, is hampered by the stray capacitance of the glia's free membrane.

6.6 Adsorbed giant vesicle membrane

Adsorbed giant vesicle membrane shows a junction resistance above $5\text{G}\Omega$ and a membrane conductance below $0.35\text{mS}/\text{cm}^2$. The dye sensitivity is homogeneous and can be obtained easily.

6.6.A Preparation of giant membrane vesicles

Swelling of giant vesicle membranes was performed with the method further refined by [Kottig 2000]. In contrast to the description given in [Fromherz 1999] I used pure POPC vesicles stained after adsorption in order to incorporate the dye only into the upper leaflet of the membrane bilayer - a precondition for obtaining voltage sensitivity. Giant vesicles were prepared from the lipid palmitoyl-oleoyl-phosphatidyl-choline (POPC, Avanti Polar Lipids, Alabaster) by the method of electroswelling [Dimitrov 1988], [Mathivet 1996]. The vesicles contained 300mM sucrose and were suspended in 300mM glucose. The different densities of glucose and sucrose solutions promoted sedimentation. POPC (2mM) was dissolved in diethylether/methanol (volume ratio 9:1). 5ml of the solution were applied to a pair of planar electrodes of indium tin oxide coated with 70nm of silica. After drying, we added 1.25ml of 300mM sucrose and applied an AC voltage of 10Hz , ramping the peak-to-peak amplitude from 100mV to 6V within 2h . The attached vesicles were dissociated by applying an AC voltage of 4Hz and 6V amplitude for 20min , with 1Hz for 10min and with 0.1Hz for 10min . 0.5ml of the suspension was sucked into a wide pipette and added to 2.5ml of 300mM glucose. 10ml of that dispersion were applied to 2ml of 300mM glucose with 40mM NaCl and 10mM TRIS/HCl buffer at pH 7.4 on a chip. The chips were cleaned as described in 3.4 on page 56 and coated with poly-L-lysine (MW 10 000, Sigma, Heidelberg) in milli-Q water ($25\text{mg}/\text{ml}$) for 30min at room temperature and rinsed 5 times with 300mM glucose, 40mM NaCl, 10mM TRIS/HCl at pH 7.4. The coating overcompensated the negative surface charge of silica [Burns 1995]. Then the vesicle suspension was applied. After 2h the vesicles settled and many of them adsorbed on the chip. FLIC measurements on these adsorbed membranes can be found in 4.2.F on page 65 and 4.4.A on page 71. Staining was performed as usual (4.1.C on page 61).

6.6.B Adsorbed giant vesicle membrane

We present two measurements in Fig 6.28 and Fig 6.29 together with the model and measurement parameter values in Table 6.14 and Table 6.15.

Image=43 μ m	f=10kHz>40f ₀
Pixel=0.67 μ m	V _{Chip} =1.5V
Binning=3x3	ϵ =0.07 (50nm)
A _{JM} =780 μ m ²	β =0.0

Area contact Model	
r_J>0.5GΩ	ρ_J >55 Ω cm
τ_J >0.3ms	Sens.=8%/100mV
g_J^{JM} <3.2mS/cm ²	V _{JM} =85mV

TABLE 6.14 Measurement and model parameters for an adsorbed giant vesicle membrane measured at 10kHz in Fig 6.28. We find a lower limit for r_J >0.5G Ω and an upper limit for the membrane conductance of g_M <3.2mS/cm² from the flat profile of the phase around zero. Sensitivity is homogeneous at 8%/100mV.

Image=64 μ m	f=1kHz>40f ₀
Pixel=1.0 μ m	V _{Chip} =1.5V
Binning=3x3	ϵ =0.34 (10nm)
A _{JM} =670 μ m ²	β =0.0

Area contact Model	
r_J>5GΩ	ρ_J >550 Ω cm
τ_J >3.6ms	Sens.=3.75%/100mV
g_J^{JM} <0.35mS/cm ²	V _{JM} =380mV

TABLE 6.15 Measurement and model parameter for an adsorbed giant vesicle membrane measured at 1kHz in Fig 6.29. We find a lower limit for r_J >5G Ω and an upper limit for the membrane conductance of g_M <0.35mS/cm² from the flat profile of the phase around zero. Sensitivity is homogeneous at 3.75%/100mV.

With respect to the previous measurements the fluorescence small-signal has changed sign because now the membrane is stained in the top leaflet and thus the phase signal is shifted by 180°. The measurements can only yield a lower limit for the junction resistance r_J : since we measured a phase of roughly -180° at both stimulation frequencies of 10kHz and 1kHz, there is total capacitive coupling with f >40f₀. We obtain a lower limit of r_J >0.5G Ω at 10kHz and of r_J >5G Ω at 1kHz. Photodamage and bleaching did not allow for slower stimulation rates although I think the lower limit could be extended with improved equipment. Anyway, the limit is compatible to the known values r_J =50..130G Ω measured with transistor arrays for this membrane preparation [Fromherz 1999]. The phase of -180° also provides an upper limit of the membrane conductance. For leaky membranes we would expect a phase of -90° in the limit f >40f₀. Therefore, including the specific junction conductance g_J <0.35mS/cm² at 1kHz we can directly derive an upper limit for the membrane conductance g_M <0.35mS/cm² as discussed in 2.4.E on page 24. Sensitivity is homogeneous as expected, but for unknown reasons it differs substantially between both measurements (with 8%/100mV and 3.75%/100mV). The junction parameters are confirmed by a subsequent transient measurement in Fig 6.29 presented in paragraph 7.4 on page 155.

Adsorbed Vesicle Membrane at 10kHz

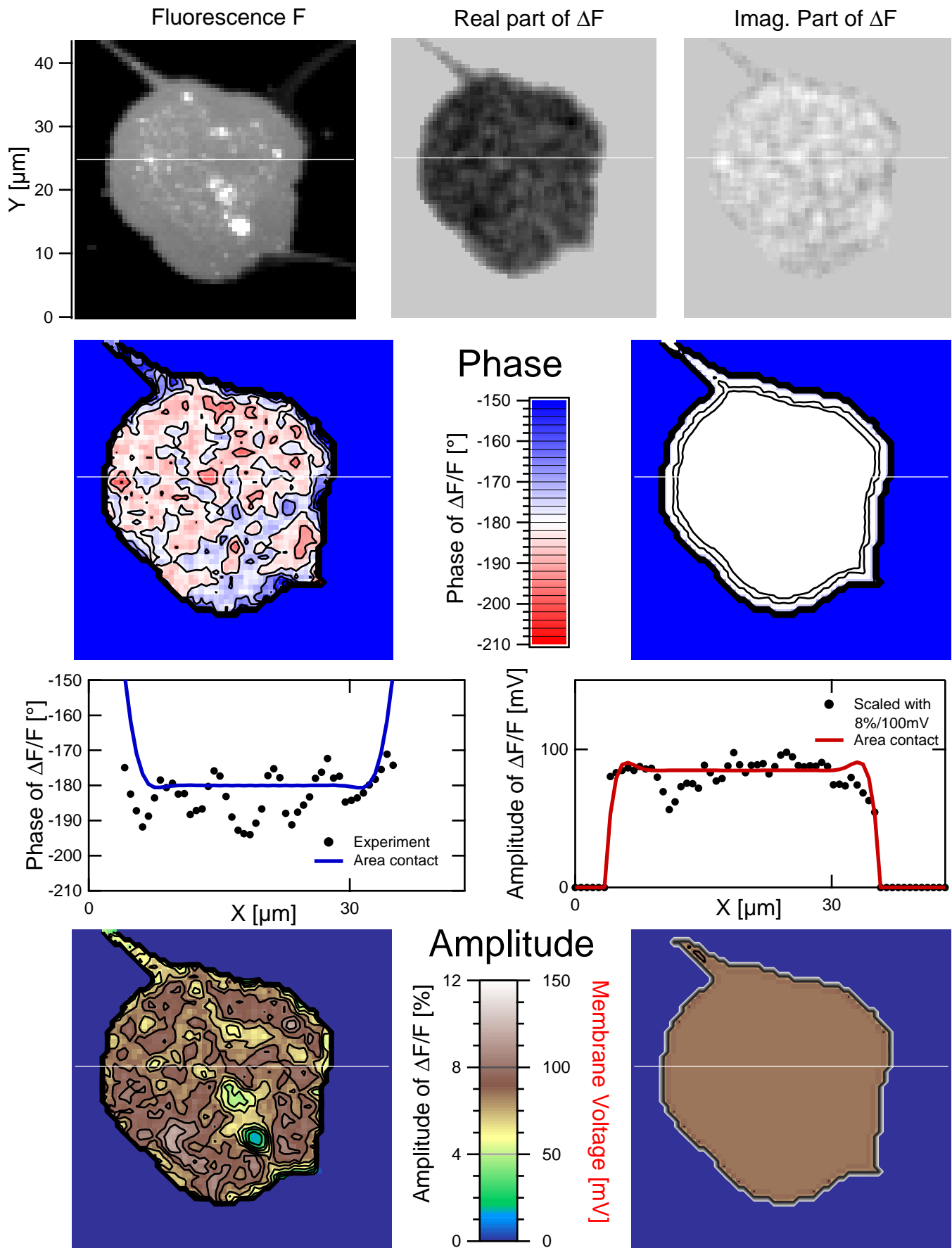


Fig 6.28 Adsorbed vesicle membrane with theory limit. Parameters given by Table 6.14

Adsorbed Vesicle Membrane at 1kHz

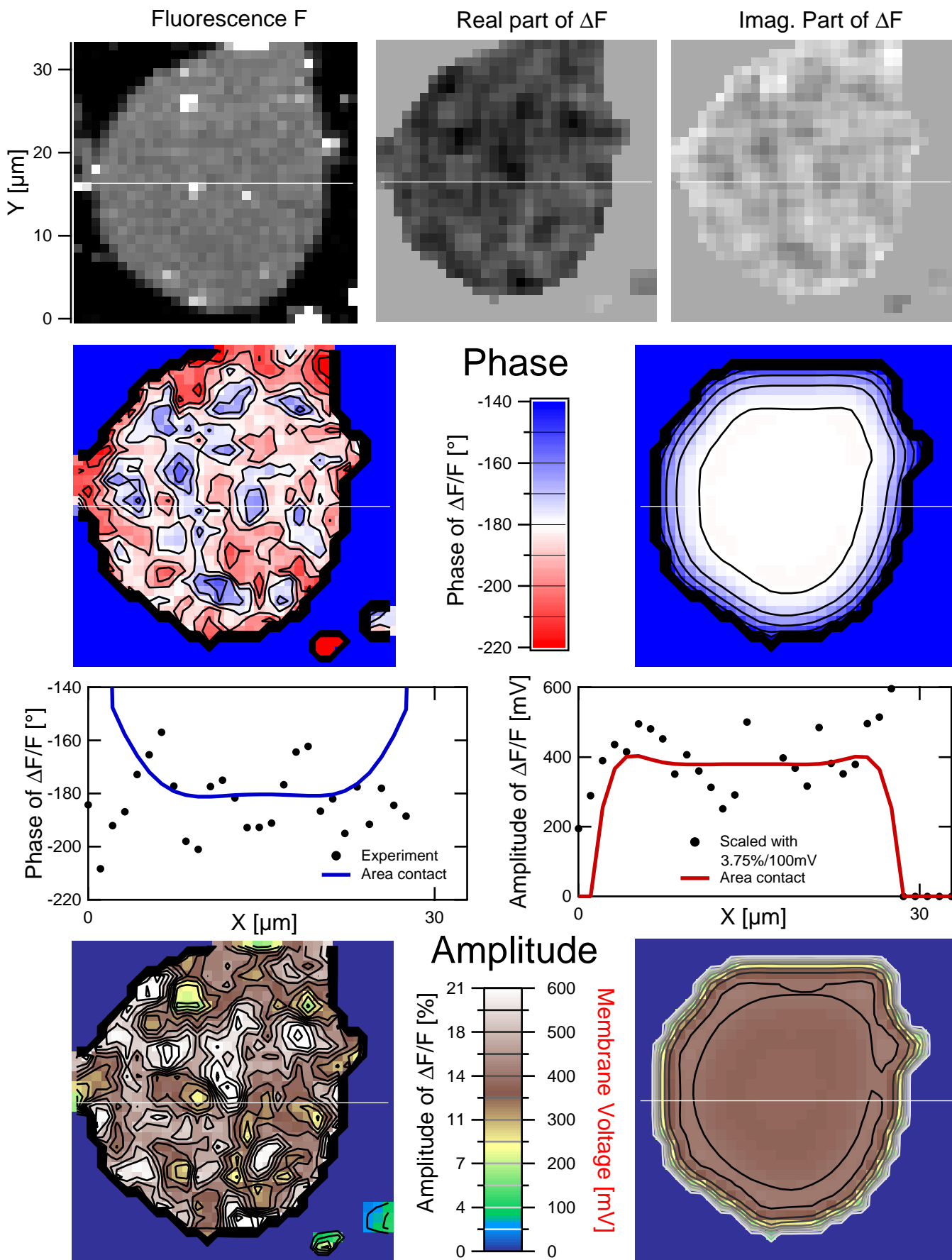


Fig 6.29 Adsorbed vesicle membrane with theory limit. Parameters given by Table 6.1

Imaging of transients

HEK cells, cell groups and vesicle membranes

7.1 Detailed analysis of a measurement ***137***

We discuss a transient measurement of an epithelioid HEK cell in detail. The relative fluorescence transients are compared to the theory fit of area and point contact model.

7.2 Imaged transients of single HEK cells ***144***

Imaged transients of HEK cells confirm the area contact parameters previously obtained from lock-in measurements of the same cells. The junction time constants fitted with the point contact model cover the range of $\tau_j=1.5$ to $5\mu\text{s}$ depending on cell size.

7.3 Group of HEK cells ***150***

The group of HEK cells previously measured with lock-in imaging is reexamined with transient imaging. Junction time constants of up to $6\mu\text{s}$ are confirmed.

7.4 Imaged transients of vesicle membrane ***155***

Imaged transients of adsorbed giant vesicle membranes confirm previous lock-in measurements. Junction time constants are limited to $>3\text{ms}$ with both methods.

7.1 Detailed analysis of a measurement

We discuss a transient measurement of an epithelioid HEK cell in detail. The relative fluorescence transients are compared to the theory fit of area and point contact model.

7.1.A Basic principle and fluorescence image

Supplementary to the lock-in imaging technique another averaging scheme was developed. Voltage transients at a given pixel are measured by averaging over a train of rectangular voltage pulses applied to the chip at usually 125kHz. This induces a train of membrane potential transients and therefore with voltage sensitive dyes a train of fluorescence transients. With a pixel dwell time of 10 μ s we are able to gather 1250 stimulation periods at the time resolution of the sampling rate of 5MHz. From averaging we obtain both the fluorescence transient $\Delta F(t)$ inside one period and the overall fluorescence intensity F . This yields for each pixel a relative fluorescence transient $\Delta F(t)/F$ with 40 values over a period length of 8 μ s and a fluorescence image F of the cell.

The lock-in imaging principle presented in chapter 6 on page 91 is a very similar averaging method. Using the lock-in scheme, the voltage transients are not resolved, but averaged internally with the correlation functions (paragraph 5.3 on page 86) to obtain only the amplitude and the phase of the resulting sinusoidal transient. This further reduction to two parameters is also the reason why the lock-in imaging is much more sensitive. Usually only cells imaged at a good signal to noise ratio with the lock-in technique were used to measure transients.

We will present in this paragraph an epithelioid HEK cell measured with the transient imaging scheme as sketched above. The same cell was previously measured with lock-in (Fig 6.15 on page 114). The fluorescence image measured is shown on left of Fig 7.1.

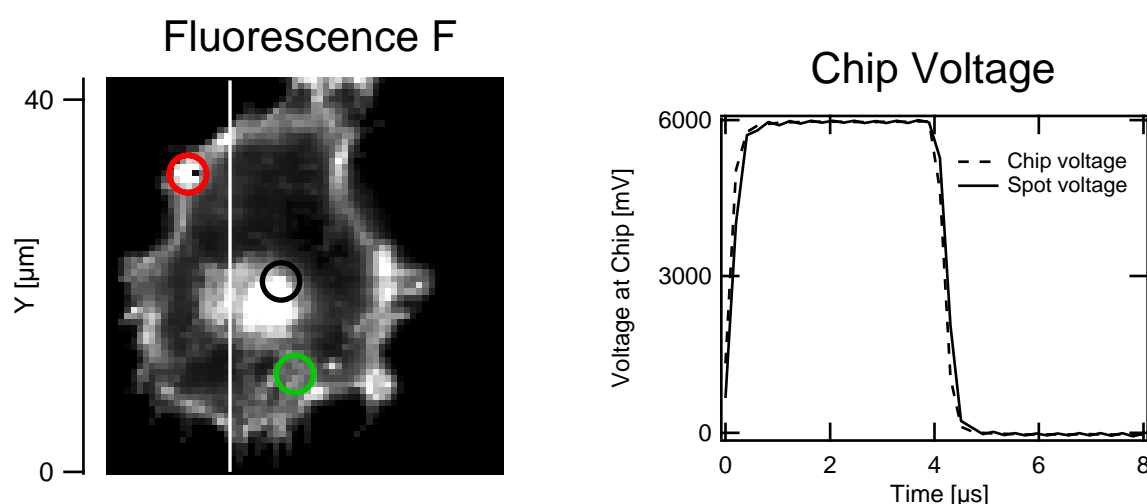


Fig 7.1 Fluorescence image and chip voltage from a transient measurement on an epithelioid HEK cell. The chip voltage is recorded and transformed to the spot voltage with the low pass transfer function of the chip.

On the right side of Fig 7.1 we find one period of the train of rectangular chip voltage V_{CHIP} applied with 125kHz. As the current through the chip is as high as 1mA the function generator cannot generate the voltage steps properly in an ideally rectangular shape. Therefore the chip voltage was recorded and used for all theoretical calculation of voltage transients. Already included in Fig 7.1 is the effect of the low pass filter of the chip (3.1.C on page 39). Since the chip has an oxide thickness of 50nm, its time constant is $\tau_C=0.06\mu\text{s}$ (3.3.H on page 53). To obtain the voltage transient at the stimulation spot V_S , the chip voltage is transformed into a fourier series, multiplied with the transfer function of the chip. After fourier back transformation we obtain the voltage at the stimulation spot. As seen from the bold line in the right plot of Fig 7.1, the delay induced in the spot voltage due to the low pass filter of the chip is very small.

7.1.B Single relative fluorescence transients

Examples of relative fluorescence at the center of the junction membrane (black circle in Fig 7.1) and at the free membrane (red circle) are given in Fig 7.2 with the corresponding color. At the center of the junction membrane we find for an upward step in the stimulation spot voltage a significantly delayed downward transient of the relative fluorescence signal with an amplitude of around 15%. The fluorescence transient decays with a time constant of some μs . The downward step in stimulation voltage gives a delayed increase in relative fluorescence which decays again. The relative fluorescence transient from the free membrane shows an inverted sign and possibly a different time constant. Also the amplitude is reduced to about 5% in the maximum.

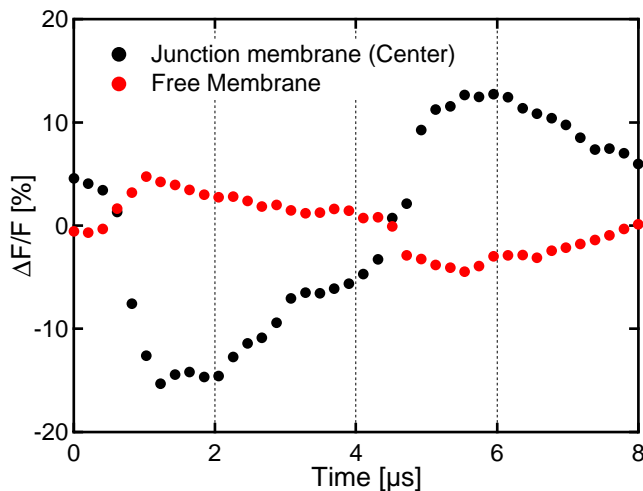


Fig 7.2 Relative fluorescence transients in the center of the junction membrane and the free membrane. The rectangular stimulation voltage stimulates the membrane capacitively. Afterwards the voltage decays within time constants of some μs through the junction. The sign of the free and the junction membrane is different as expected. The photomultiplier amplifier delays the transients significantly which has to be considered when comparisons with theory are made.

Without the delays this is what would have been expected for the point contact model as presented in paragraph 2.5.D on page 30. The voltage step loads the applied voltage into the cell membrane with no delay. The amplitude is defined by the capacitive voltage divider of spot, junction and free membrane. Afterwards the voltage decays due to the resistance in the junction. Only directly after the voltage step in the center of the junction membrane the models of area and point contact could be discriminated as shown in 2.5.D on page 30.

The already mentioned delay is introduced to the system by the low pass filter of the photomultiplier amplifier. The characteristic of the amplifier is known (5.4 on page 88). Deconvolution of the true fluorescence signal from the noisy transient has proved to be impossible. Therefore the theoretical transients calculated from point and area contact model have to be transformed with the amplifier characteristic to be compared with the experiment.

The main advantage of measuring fluorescence transients is that we can directly monitor the membrane potential decay. Lock-in imaging could accomplish this task only if a contact model was assumed. Therefore only the transient measurements can confirm the area contact model without further assumptions. Also the various phase corrections in lock-in measurements could have introduced very easily an error in the contact model fits as these rely on absolute phase values.

The scaling of the transients will be handled differently as compared to lock-in imaging. In the latter we have assumed a fixed sensitivity and have discussed the deviations. Now we will assign to every pixel a fitted sensitivity which is derived from the scaling between the theoretical membrane potential transient and the measured relative fluorescence transient. This results in maps of sensitivity, depending on the contact model used as shown in paragraph 7.1.E in Fig 7.6.

With the obtained sensitivity we scale all relative fluorescence transients to a membrane potential. Thus the discussion of membrane potential transients is somehow restricted to the discussions of the shape of the transients. This is reasonable since the sensitivity was already found to be undetermined within 50% and we are mostly interested in the decay characteristic of the fluorescence transients. Nevertheless the scaling can lead to misunderstandings since the measured fluorescence transients will be also given in terms of membrane potential, but they could in principle be only given as relative fluorescence due to the effects of the low pass filter of the photomultiplier. With this trick it is possible to keep the less interesting sensitivity out of the discussions and concentrate on the shape of the voltage transients.

It must be further noted that both the images of $\Delta F(t)$ and of F have been binned with 4x4 pixels to enhance the signal to noise ratio. Therefore the binning size was comparable to those used with the lock-in measurements. The signal to noise ratio needed for the transient measurements was mostly gained from an increased pixel dwell time of 10ms as compared to 2-4ms in lock-in imaging.

7.1.C Fitting transients with the Area contact model

The scheme for calculating theoretical transients from the area contact model is straightforward. The measured chip voltage V_{CHIP} is fourier transformed into a finite fourier series as it is a periodical signal. In fourier space we multiply at each frequency the transfer function of the chip $g_{\text{CHIP}}(\omega)$ (3.1.C on page 39) and the transfer function of the contact model $g_{\text{CELL}}(\omega, x, y)$ (2.2.B on page 14). When we fourier back transform now, we obtain the real membrane potential transient. But to correct for the photomultiplier we stay in the fourier space and multiply the transfer function of the photomultiplier $g_{\text{PM}}(\omega)$ (5.4.A on page 88). After the fourier back transformation we obtain the photomultiplier signal as if the cell would have been stimulated with the given chip voltage, low pass filtered with the given chip, high pass filtered according the used area contact model and finally low pass filtered from the photomultiplier amplifier.

It is already known from lock-in measurements how to calculate the voltage of junction and free membrane for a given cell geometry. This geometry was determined by a fluorescence threshold and a phase threshold. The latter threshold is exchanged as following. We will average the relative fluorescence transient $\Delta F(t)/F$ for times $0.4\mu\text{s}$ and for times $4.8\mu\text{s}$. If the first average is larger than the second, we attribute the pixel to the junction membrane, otherwise to the free

membrane. By means of this distinction of the measured image into visible junction area, visible free membrane area and boundary conditions of the cell, we can calculate the transfer function of area contact model for each pixel of the image at a given frequency as described for the lock-In measurements. This calculation has to be done for all the frequencies of the fourier series. The results of the calculation for the three circled positions in Fig 7.1 can be found below in Fig 7.3:

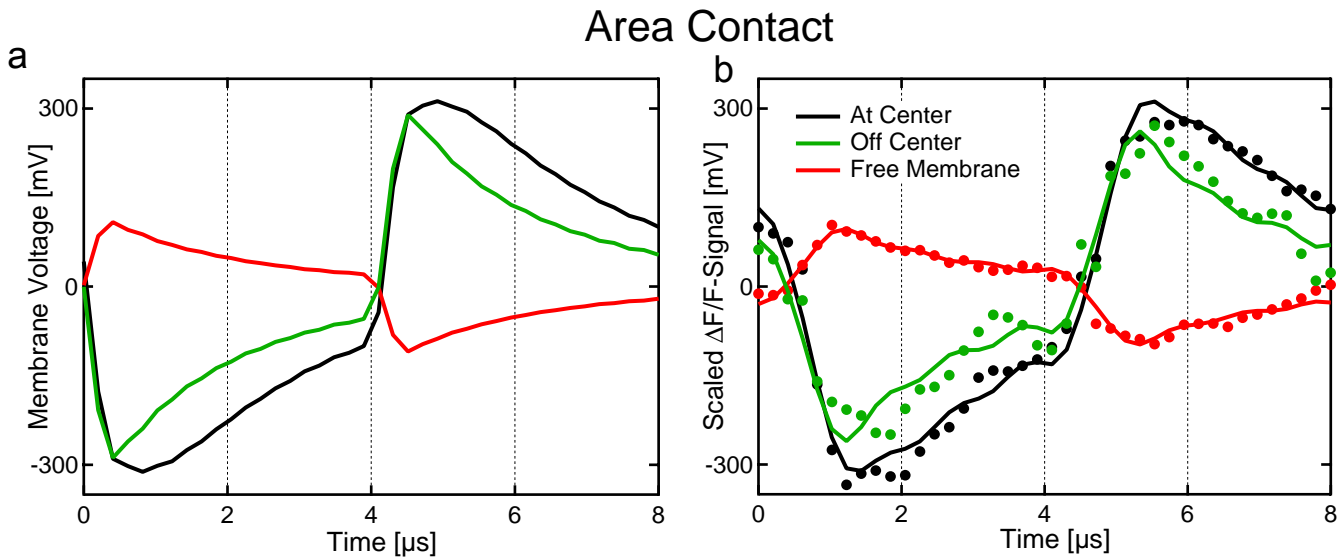


Fig 7.3 Transients from area contact model. (a) Membrane potential transients from different locations of the cell marked in Fig 7.1 calculated from chip voltage V_{CHIP} with the transfer functions of the chip $g_{\text{CHIP}}(\omega)$ and the area contact model $g_{\text{CELL}}(\omega, x, y)$. (b) Comparison with measured relative fluorescence transients. The calculated membrane potential was further filtered with the photomultiplier amplifier transfer function $g_{\text{PM}}(\omega)$. After scaling with the sensitivity the transients agree very well with the measured relative fluorescence transients (dots).

In Fig 7.3a we find the membrane potential transients as calculated from the area contact model with the procedure described. The parameters of the area contact model were taken from the previous measurement of same the cell with the lock-in imaging technique (Table 6.7 on page 113). We find a fast charging of the membranes, decaying with a time constant of some μs afterwards. The characteristic is different in the center of the junction membrane (black) and towards the border of the cell (green) as at the center of the membrane the exponential decay is initially delayed. In terms of the diffusion part of the integral equation of the area contact model, the membrane potential needs time to diffuse outside towards the boundary of the junction membrane area. After correcting for the transfer function of the photomultiplier amplifier, the transients have the shape as shown in Fig 7.3b. We already have applied scaling with the sensitivity to present all transients as membrane potential. The transients measured from different parts of the cell (defined by circles in the fluorescence image of Fig 7.1) are predicted precisely by the area contact model. Especially we can see the slight difference between the transient in the center and towards the border of the cell as predicted. Also the free membrane is described by the integral-differential equation of the area contact model. We have taken the same parameters as in Table 6.7 on page 113 where the identical cell was measured and fitted by lock-In imaging. Therefore fitting from the phase signal as done within the Lock-In measurements is confirmed perfectly. We will further see that the relative fluorescence transients can also be described with a fitted point contact model:

7.1.D Fitting transients with the Point contact model

Within the point contact model the junction properties are described as a high pass with the junction time constant τ_j . We will fit the point contact model to the measured image of transients by allowing each pixel to have a junction time constant of its own. Therefore we find a junction time constant and a sensitivity for each pixel. As compared to the lock-in measurement scheme which also calculates for each pixel a phase and an amplitude, the parameters sensitivity and junction time constant are adapted to the problem. They yield a comparable signal to noise ratio. But we first have to check whether the transients can be fitted with the point contact model.

The calculation scheme for the point contact model is the same as for the area contact model. Again the chip voltage is transformed to a fourier series, multiplied with $g_{\text{CHIP}}(\omega)$ and $g_{\text{CELL}}(\omega)$ of free or junction membrane to obtain after back fourier transformation the membrane potential transient. Staying in the fourier space and further multiplying $g_{\text{PM}}(\omega)$ we obtain after back transformation the expected relative fluorescence transient. To fit the junction time constant τ_j , the calculation is repeated and the resulting fluorescence transient is matched with the sensitivity to the measured transient until a minimal quadratic difference is obtained. Some of the resulted transients are shown in Fig 7.4 below:

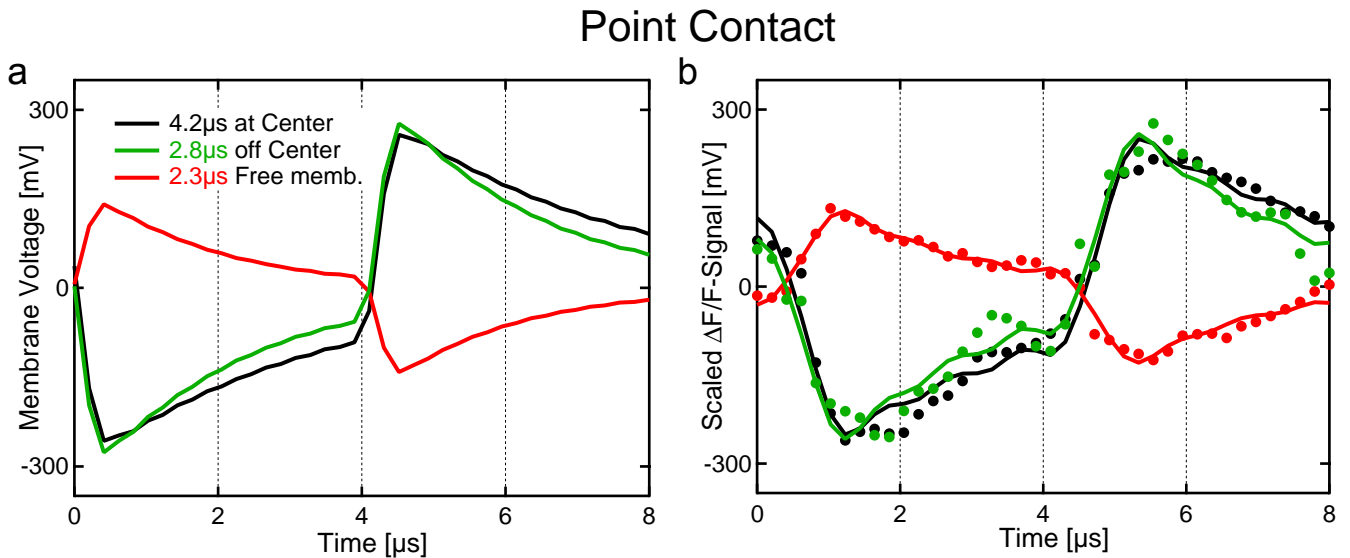


Fig 7.4 Transients from point contact model with fit of τ_j . (a) Membrane potential transient with time constants τ_j from different locations of the cell marked with circles in Fig 7.1. They are calculated from chip voltage V_{CHIP} with the transfer functions of the chip $g_{\text{CHIP}}(\omega)$ and the point contact model $g_{\text{CELL}}(\omega)$. (b) Comparison with measured relative fluorescence transients (dots) yields both the junction time constant τ_j and the sensitivity. The calculated membrane potential was filtered with the photomultiplier amplifier transfer function $g_{\text{PM}}(\omega)$. After scaling with the sensitivity the transients agree very well with the measured relative fluorescence transients (dots). The photomultiplier amplifier has washed away the differences in membrane potential between area and point contact model.

It is found that also the point contact model predicts the fluorescence signal very precisely. As the photomultiplier amplifier smears out the fluorescence transients shortly after the steep flank, we cannot distinguish between area and point contact model as both models show the difference only there. But the area contact model does not need to fit a time constant at each pixel, all the transients are defined by the junction resistance r_j alone and match the experimental data. The locally fitted junction time constant τ_j is plotted and discussed in Fig 7.5 below:.

Time constant (Point Contact)

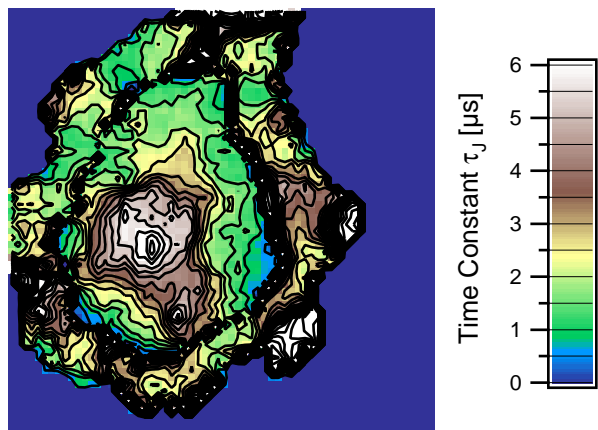


Fig 7.5 Junction time constant τ_j as fitted from the point contact model. The increase in time constant towards the center reflects the area contact model behavior of the junction. As the voltage 'diffuses' away towards the boundaries of the junction membrane, the junction decay is fast ($2\mu\text{s}$) at the border and slow ($5\mu\text{s}$) in the center of the junction. The junction time constant of the free membrane is an average of both ($2..3\mu\text{s}$) as predicted from the integral equation of the area contact model.

7.1.E Imaged Sensitivity

The local fitting of transients yields the sensitivity of the dye, both for the area contact and the local point contact. The sensitivities that match the area contact model are more homogeneous towards the border or the cell. Since the point contact model predicts identical amplitudes of membrane potential transients all over the junction area, the sensitivity is increased towards the borders of the cell. This effect can be seen in Fig 7.6 below:

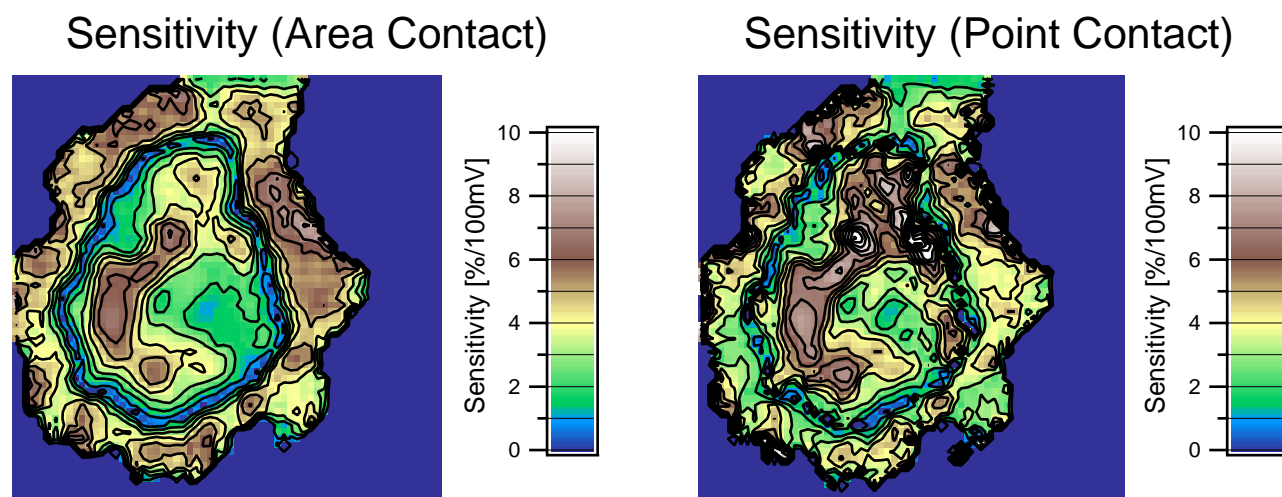


Fig 7.6 Sensitivities that match the voltage transients with area (left) and point contact model (right). As the point contact model predicts a constant membrane potential of the junction, its sensitivity is higher towards the border of the cell. Sensitivity in the free membrane is comparable.

7.1.F Voltage images with area contact model

A transient image consists of a three dimensional stack of relative fluorescence. It can either be visualized as transients at each pixel of the image or as a stack of images at fixed times. Images of relative fluorescence at times 0,2,4,6 μ s (from 40 possible) are presented in Fig 7.7 below:

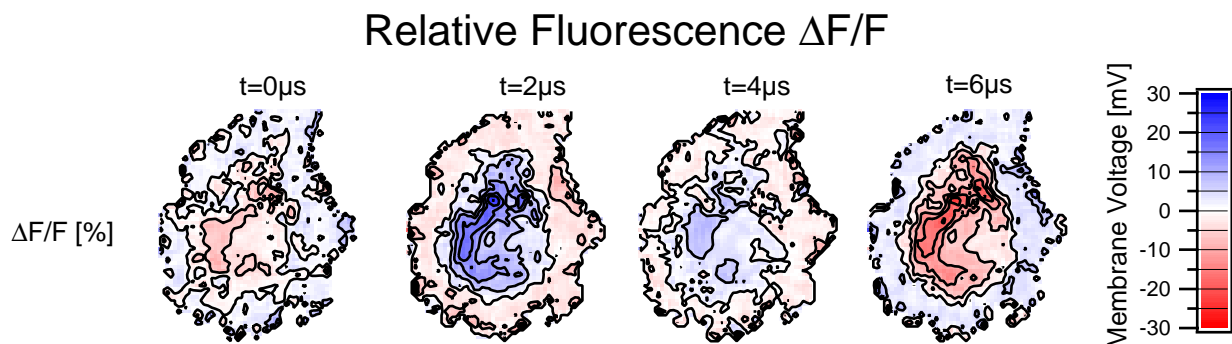


Fig 7.7 Images of relative fluorescence at $t=0,2,4,6\mu$ s. We find for the junction membrane peaks of 25% at 2μ s and -25% at 6μ s, both decaying in approximately 2μ s. The free membrane shows an inverted characteristic with a similar decaying time constant. Sensitivity is inhomogeneous, making it necessary to scale the fluorescence transients to better compare with theory.

Since the sensitivity for each pixel is already known from the area contact model, the measured transients have been scaled to the membrane potential. The result is shown in the first row of Fig 7.8 with the corresponding area contact model prediction in the second row.

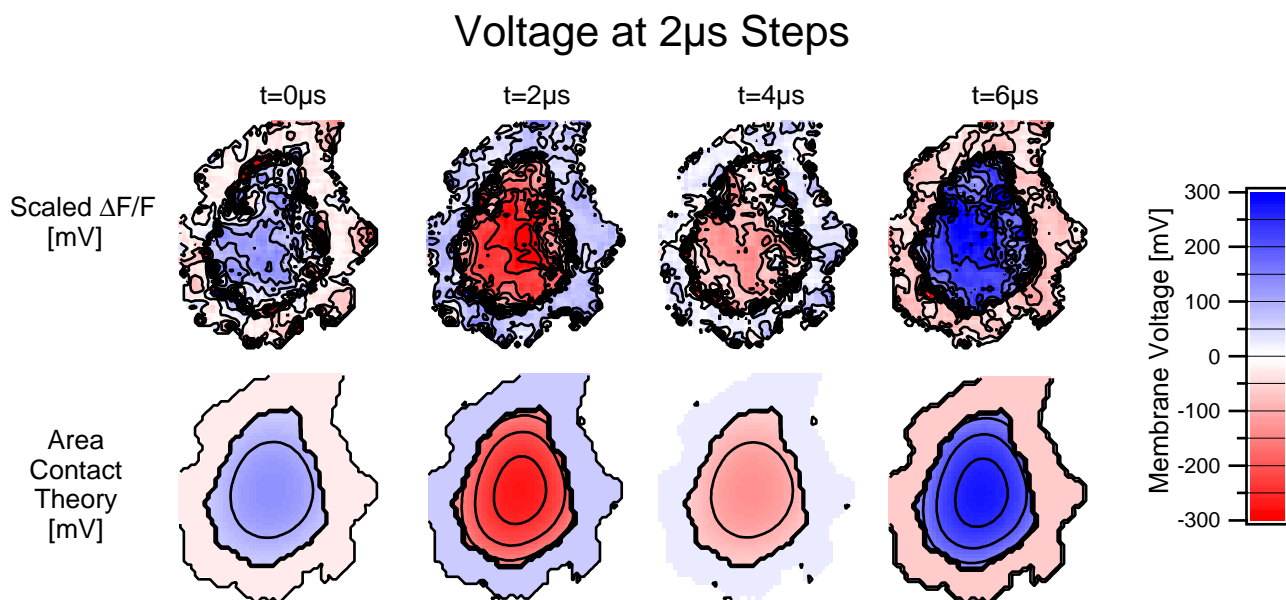


Fig 7.8 Images of scaled relative fluorescence at $t=0,2,4,6\mu$ s and of area contact theory. Transients of area contact model (second line) are used to scale relative fluorescence to membrane potential (first line).

7.1.G Voltage section versus time

Both ways of presenting the data can be combined when we considering a one dimensional section through the image. Here a vertical section along the white line in the fluorescence image of Fig 7.1 is chosen. Both the scaled measurement and the area contact model are plotted in Fig 7.9:

Voltage vs. Time along vertical Section

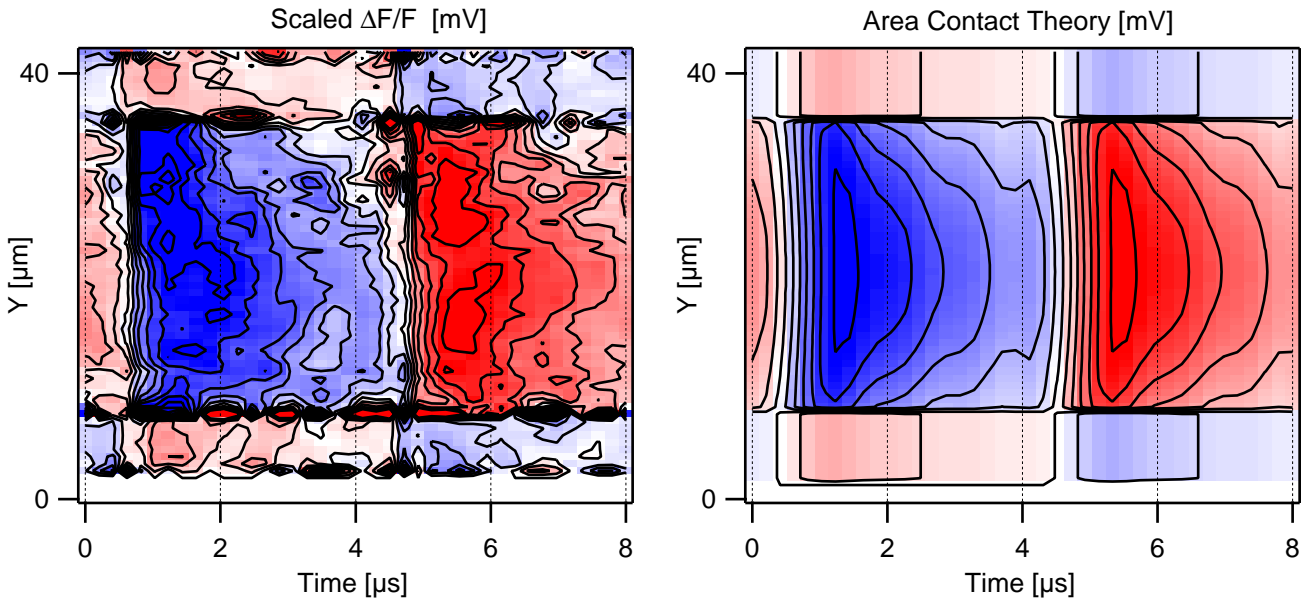


Fig 7.9 Membrane potential along a vertical section (left) as compared to the area contact model (right). The transients of the junction membrane in the center and the free membrane at the top and the bottom are described precisely.

7.2 Imaged transients of single HEK cells

Imaged transients of HEK cells confirm the area contact parameters previously obtained from lock-in measurements of the same cells. The junction time constants fitted with the point contact model cover the range of $\tau_j=1.5$ to $5\mu\text{s}$ depending on cell size.

7.2.A Spindle-shaped HEK cells

On the next two pages (Fig 7.10 and Fig 7.11) we present a transient measurement of a spindle shaped HEK cell already measured with lock-in imaging (Fig 6.14 on page 112). Model parameter were left unchanged for the calculation of transients with the area contact model. The already found junction resistance of $r_j=4.0\text{M}\Omega$ also predicts the transients. The point contact model yields a junction time constant of $2.2\mu\text{s}$ in the center and $1.3\mu\text{s}$ at the border of the junction membrane. The free membrane is fitted with a rather slow time constant of $2.7\mu\text{s}$, we would have expected from the area contact model to find a faster time constant. The lock-in phase predicted $1.5\mu\text{s}$ for the center of the junction and $1.1\mu\text{s}$ for the free membrane, therefore we find a slightly enhancement of time constants with the transient measurements at the chosen points.

Imaged Transients of spindle-shaped HEK Cell

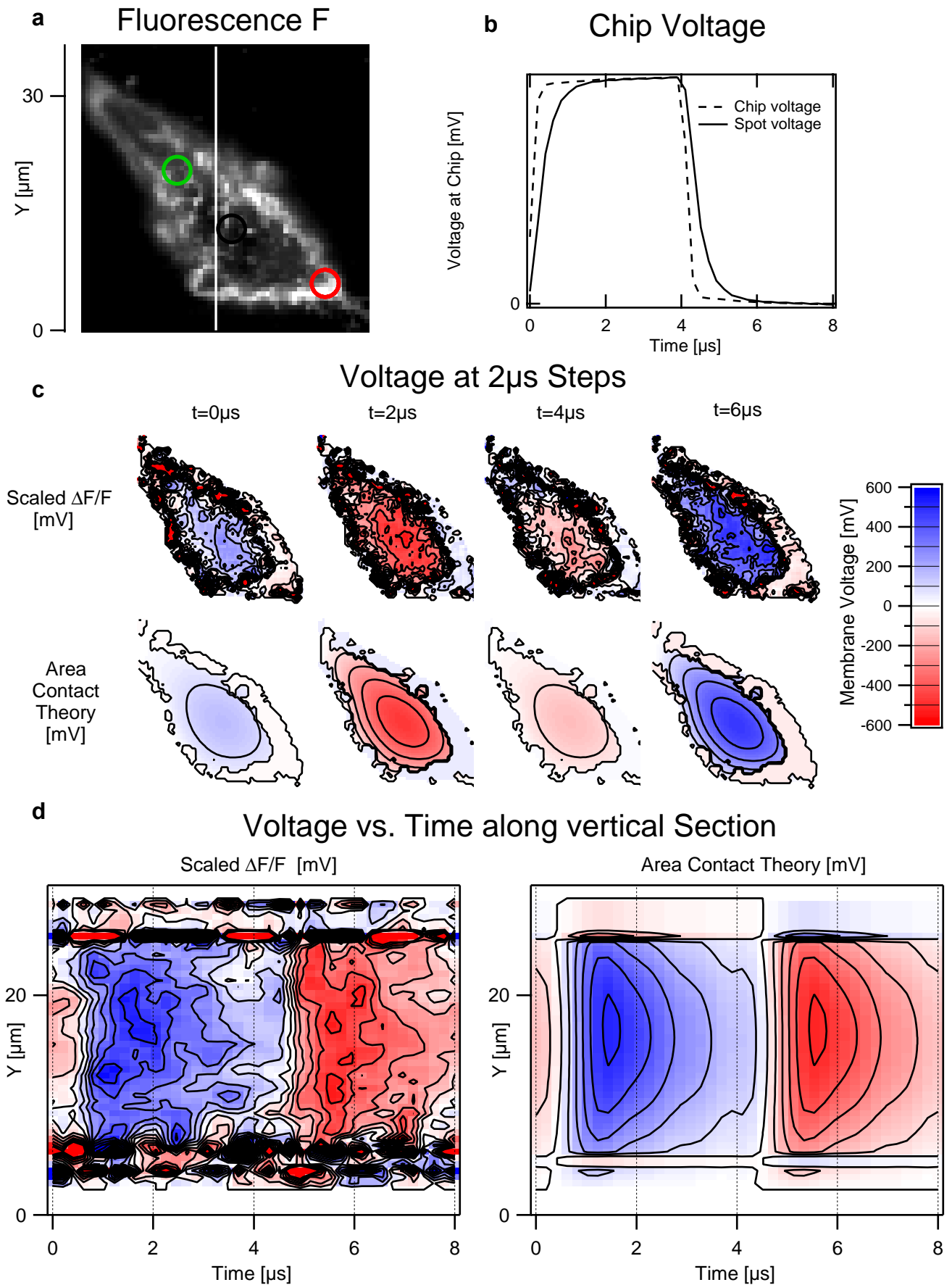


Fig 7.10 Imaged transients of a spindle-shaped HEK cell with the area contact model.

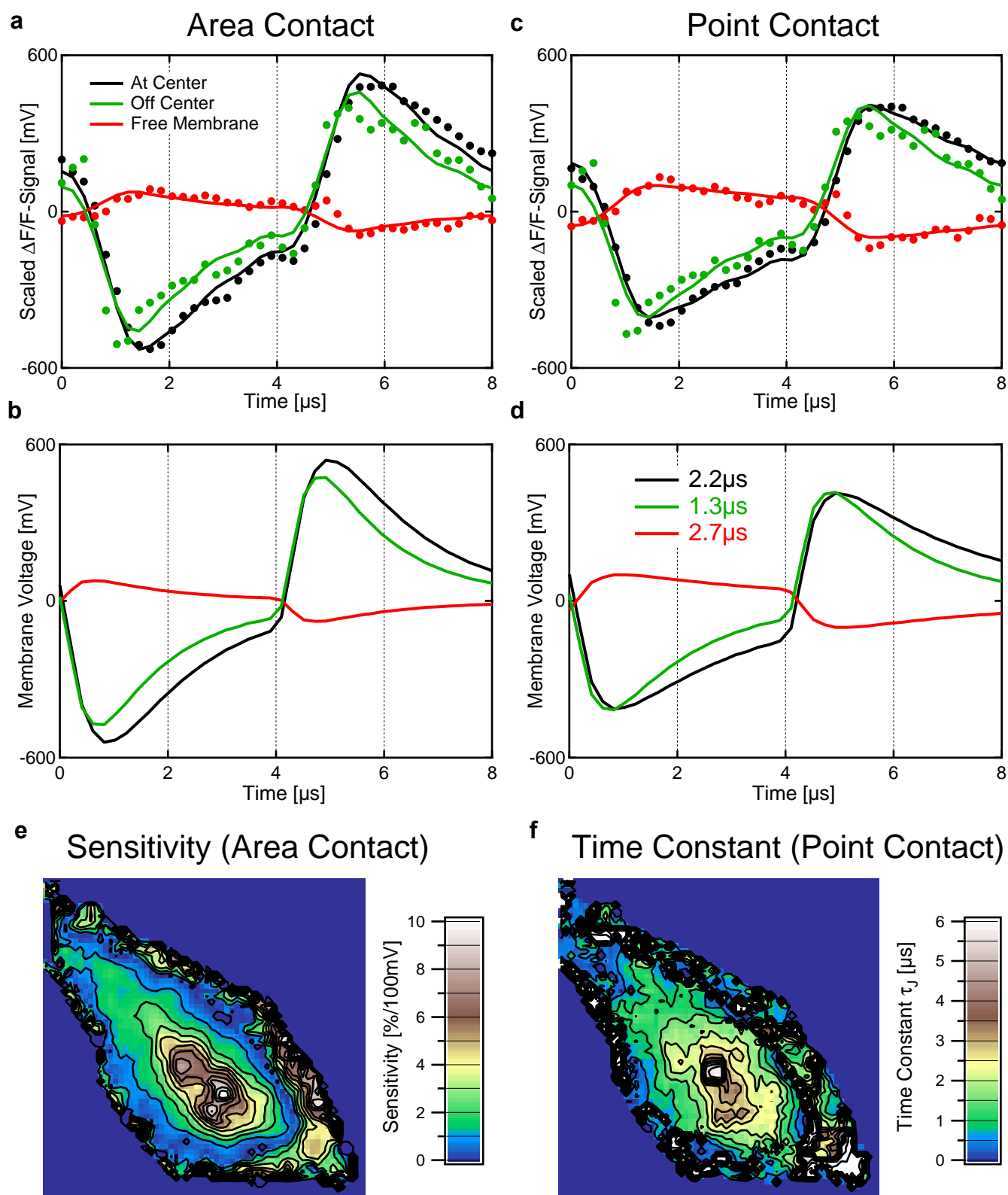


Fig 7.11 Imaged transients of a spindle-shaped HEK cell fitted with area and point contact. Single transients from the center, off the center of the junction membrane and from the free membrane fitted are with the area contact model (a,b) and the point contact model (c,d). Images of the sensitivity derived from the area contact is given in (e). The local junction time constant obtained from fitting the local point contact model is given in (f).

A drop in sensitivity at the center of the cell is found in both the lock-in and the transient measurement. The fluorescence intensity is low at this position, therefore we cannot attribute it to unspecific staining. Slightly above this position we find an extraordinary slow voltage transient with a time constant of $6.3\mu\text{s}$ as plotted in Fig 7.12a. It cannot be explained by the area contact as all the transients only $2.5\mu\text{m}$ away are described well with a time constant of $2.2\mu\text{s}$ (Fig 7.12b). This result resembles the spots in the junction of some ghosts as discussed in 6.2.B on page 99. It is paradoxical since for a local leakage in the junction membrane we would expect a lower time constant which would also be the reason for the reduction in the amplitude of the membrane potential. Only the free membrane should experience an increase in time constant as discussed in 2.4.F on page 25. The effect could have been initiated by the high peak membrane potential of around 600mV at the center of the cell. Perhaps a local cell leakage has generated a more tight junction contact. The effect did not lead to a damage of the cell within the scan time of 120s and did not show cell damage typical for electroporation as presented in 8.1 on page 158. The measured enhanced free membrane time constant is confirming the low time constant in the junction membrane as it is more or less an average of the junction membrane time constants.

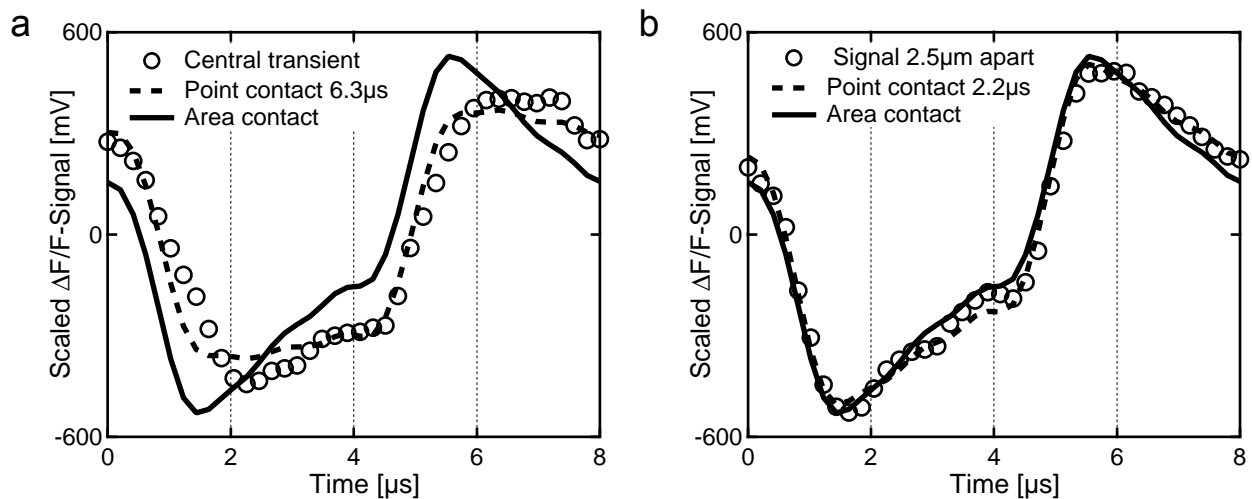


Fig 7.12 Local slow junction time constant at the center of the cell (a). Transient cannot be explained by the area contact model, but the point contact model can fit a time constant of $6.3\mu\text{s}$. The transient is slightly delayed. Only $2.5\mu\text{m}$ apart (b) the membrane potential can be precisely fit with the area contact model, yielding a time constant of $2.2\mu\text{s}$ as expected. Further discussion is found in the text.

7.2.B Epithelioid HEK cells

We have already discussed a measurement of an epithelioid HEK cell in paragraph 7.1 on page 137. Another transient measurement is presented in Fig 7.13 and Fig 7.14. This cell was already characterized by lock-In imaging in Fig 6.16 on page 115. The same model parameters of the area contact with a junction resistance of $r_j=2.0\text{M}\Omega$ also describe the transients very precisely. We find as expected and predicted from lock-in different time constants in the center of the junction ($3.3\mu\text{s}$) and towards the border ($2.0\mu\text{s}$) but again cannot distinguish between a locally fitted point contact model and the area contact model. The free membrane is fitted with a membrane time constant of $2.4\mu\text{s}$. Sensitivities of lock-in imaging and the fitted transients are almost identical.

Imaged Transients of Epithelioid HEK Cell

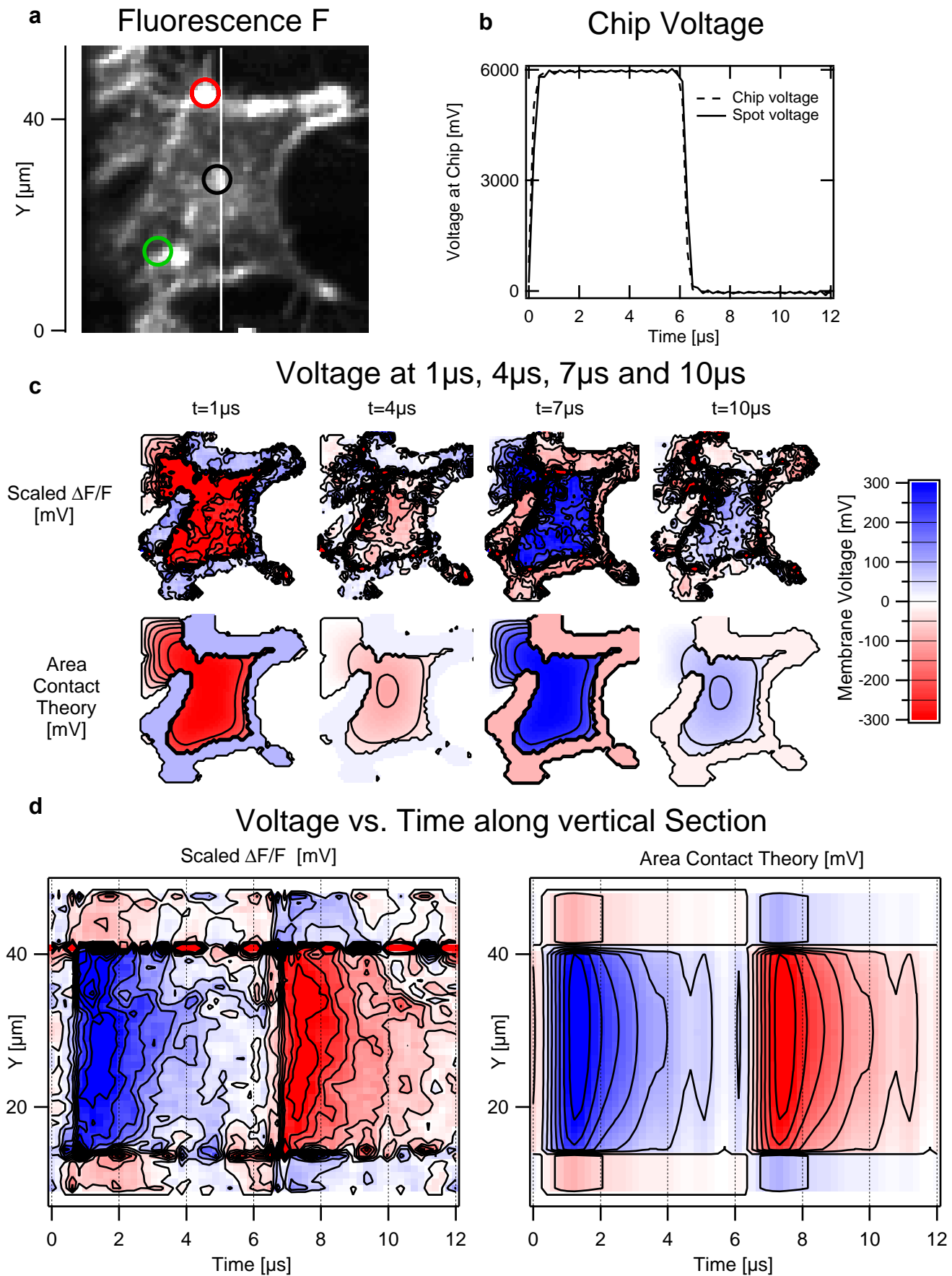


Fig 7.13 Imaged transients of epithelioid HEK cell fitted with the area contact model.

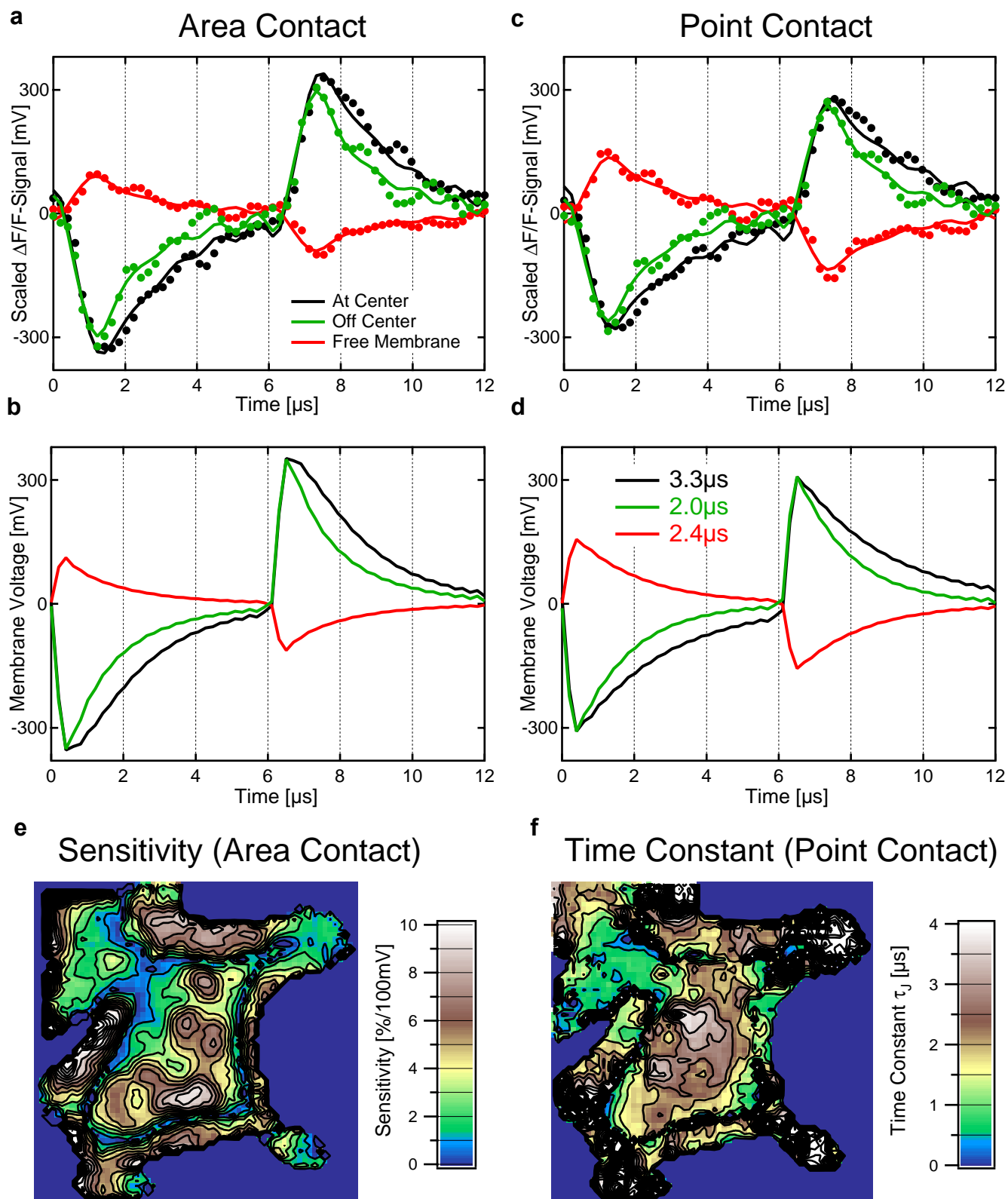


Fig 7.14 Imaged transients of a epithelioid HEK cell fitted with area and point contact. Single transients from the center, off the center of the junction membrane and from the free membrane fitted are with the area contact model (a,b) and the point contact model (c,d). Images of the sensitivity derived from the area contact is given in (e). The local junction time constant obtained from fitting the local point contact model is given in (f).

7.3 Group of HEK cells

The group of HEK cells previously measured with lock-in imaging is reexamined with transient imaging. Junction time constants of up to $6\mu\text{s}$ are confirmed.

The cell group measured with lock-in imaging (Fig 6.17 on page 118 and Fig 6.18 on page 119) was also measured with transient imaging. The same area contact model parameters were used to describe the imaged transients. The junction resistance of $r_j=3.0\text{M}\Omega$ estimated from lock-In imaging describes the transients also very precisely. Again two measurements have been made with a distance from the chip of $z=0\mu\text{m}$ (Fig 7.15 and Fig 7.17) and $z=5\mu\text{m}$ (Fig 7.16 and Fig 7.18). Both experiments are presented on opposing pages.

Also from imaged transients the cell group behaves as it was a single huge cell. The cell-cell contacts give a sufficient isolation to the bath as compared to the junction resistance between the cells and the chip. Especially the section image in Fig 7.15d and Fig 7.16d shows this fact explicitly

Values for the junction time constant in the center of the cell group show no significant z -dependence with $\tau_j=5.7\mu\text{s}$ at $z=0\mu\text{m}$ and $\tau_j=5.4\mu\text{s}$ at $z=5\mu\text{m}$. The time constants evaluated towards the boundaries of the cell group are smaller as would be expected by the area contact model. They differ with $\tau_j=2.9\mu\text{s}$ at $z=0\mu\text{m}$ and $\tau_j=4.5\mu\text{s}$ at $z=5\mu\text{m}$. But only in the right bottom of the image we find systematically smaller time constants for $z=0\mu\text{m}$ than with $z=5\mu\text{m}$ as can be seen in the time constant images of Fig 7.17f and Fig 7.18f. The reason for this is not clear.

The phase from Lock-In imaging had the tendency to yield phase values below zero in the center of the junction membrane of the cell group. But the predicted values from r_j and the area contact model with $6.8\mu\text{s}$ at the center of the cell group and $3.9\mu\text{s}$ for the free membrane are very good estimates for the time constants directly measured above.

The time constant of the free membrane was found to be $\tau_j^{\text{FM}}=4.1\mu\text{s}$ at $z=0\mu\text{m}$ and $\tau_j^{\text{FM}}=3.0\mu\text{s}$ at $z=5\mu\text{m}$ but we find in the image of time constants that this difference is not significant as values fluctuate for the free membrane within a range of $2.5\mu\text{s}..5.0\mu\text{s}$.

The transients measured prove that we are for values of $z=5\mu\text{m}$ very well at the base part of the cell-cell contact as needed in discussion of the circuit of Fig 6.19 on page 120 and subsequent measurements with confluent cell layers. Measuring and characterizing the voltage transients along the z direction in the cell-cell contact would be therefore an interesting problem. These measurements are hampered by photobleaching, but either a further increase in sensitivity or the usage of two-photon microscopes could overcome this problem.

Transients: Group of HEK Cells 0 μm above the Chip

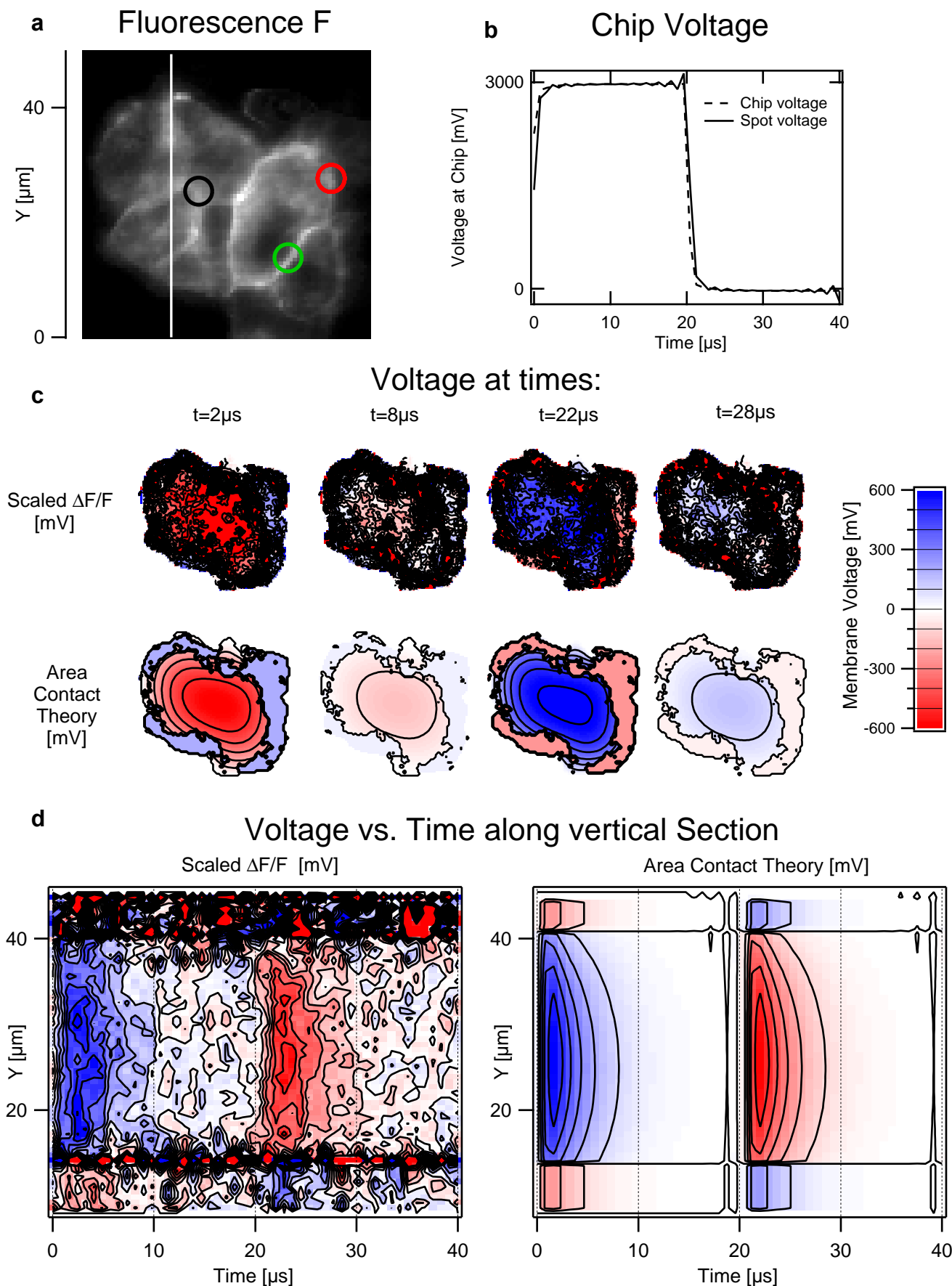


Fig 7.15 Imaged transients of a group of HEK cells at $z=0\mu\text{m}$ with the area contact model.

Transients: Group of HEK Cells 5 μm above the Chip

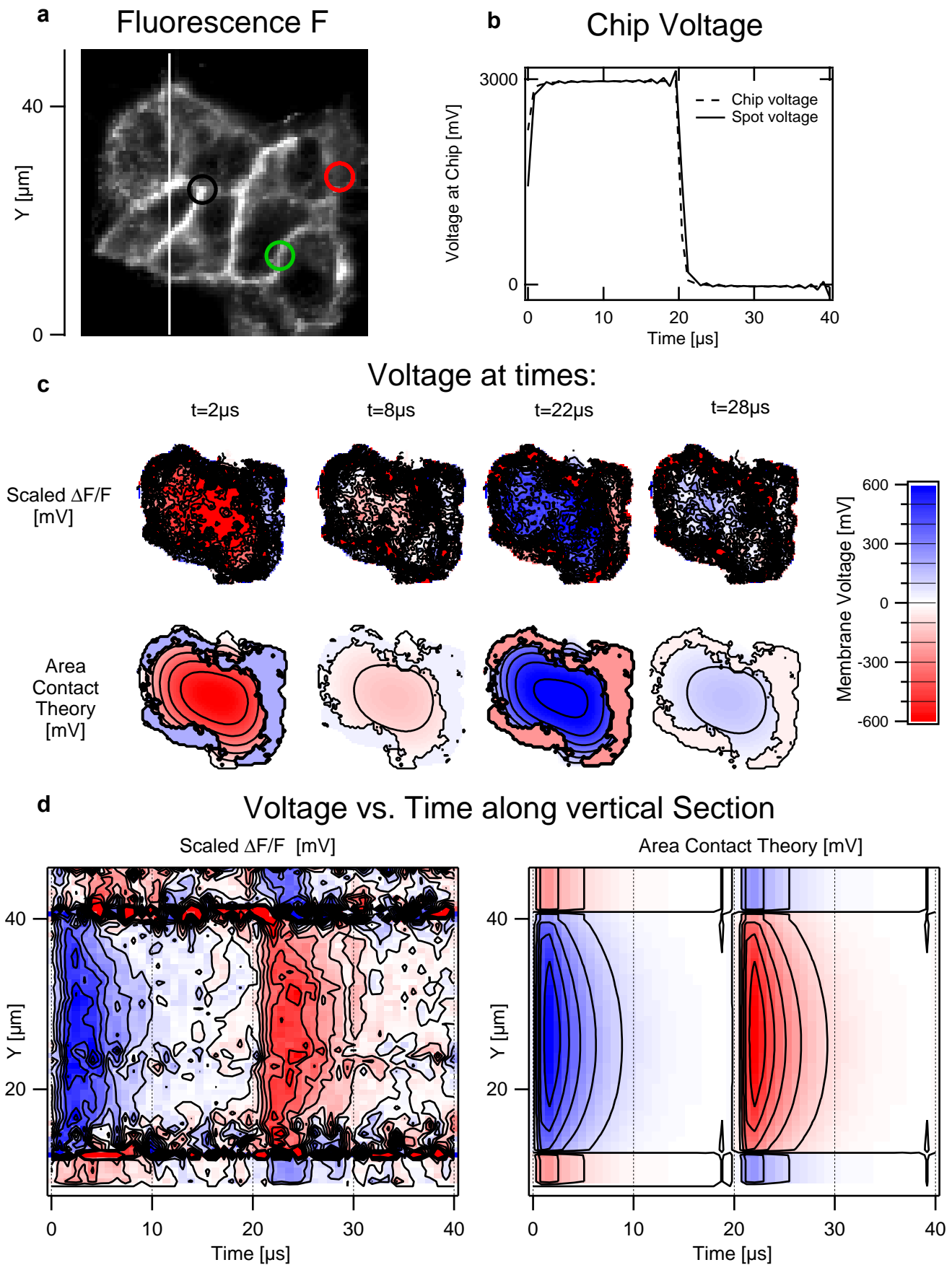


Fig 7.16 Imaged transients of a group of HEK cells at $z=5\mu\text{m}$ with the area contact model.

Transients: Group of HEK Cells 0 μm above the Chip

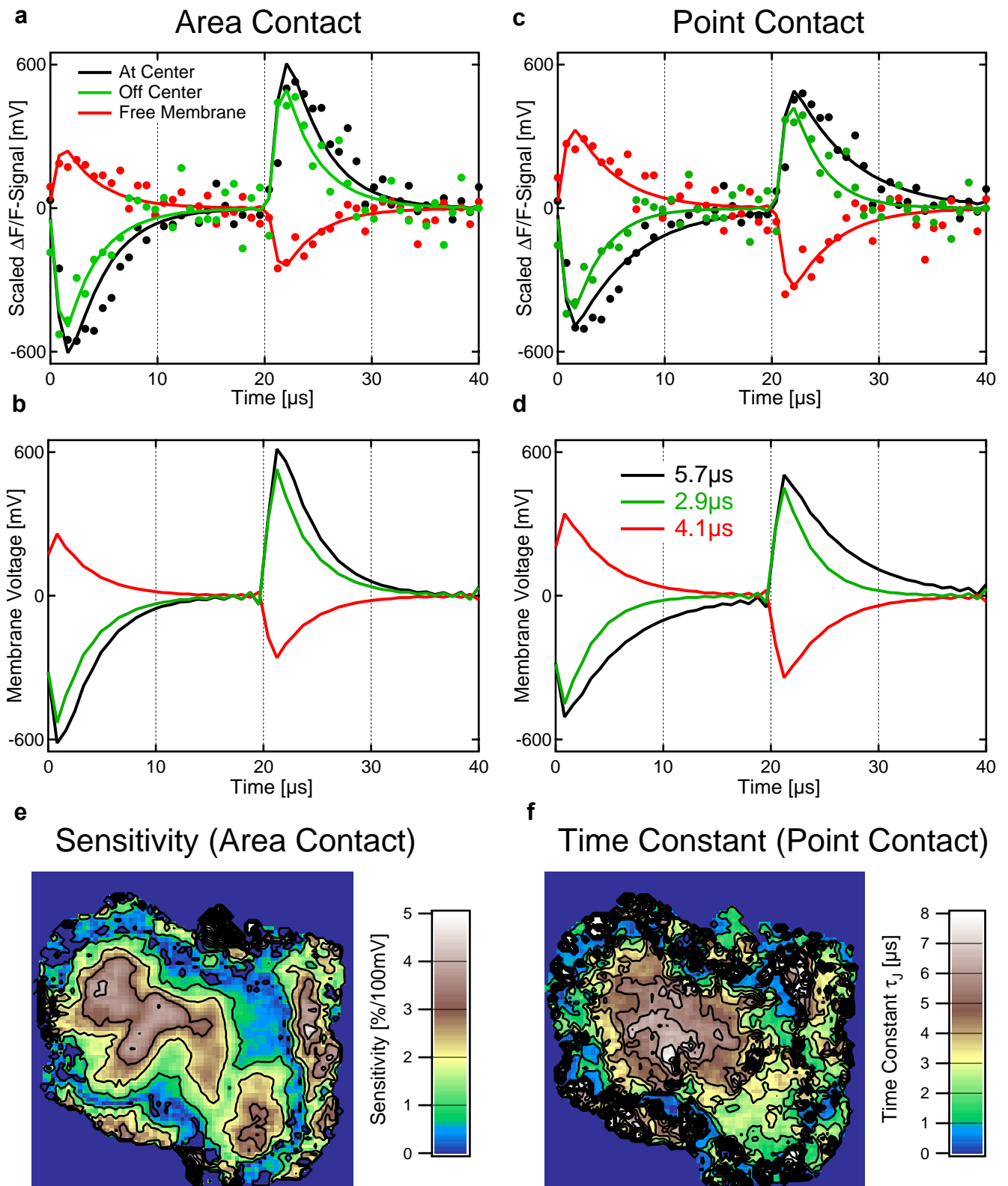


Fig 7.17 Imaged transients of a group of HEK cells 0 μm above the chip surface. Single transients from the center, off the center of the junction membrane and from the free membrane fitted are with the area contact model (a,b) and the point contact model (c,d). Images of the sensitivity derived from the area contact is given in (e). The local junction time constant obtained from fitting the local point contact model is given in (f).

Transients: Group of HEK Cells 5 μm above the Chip

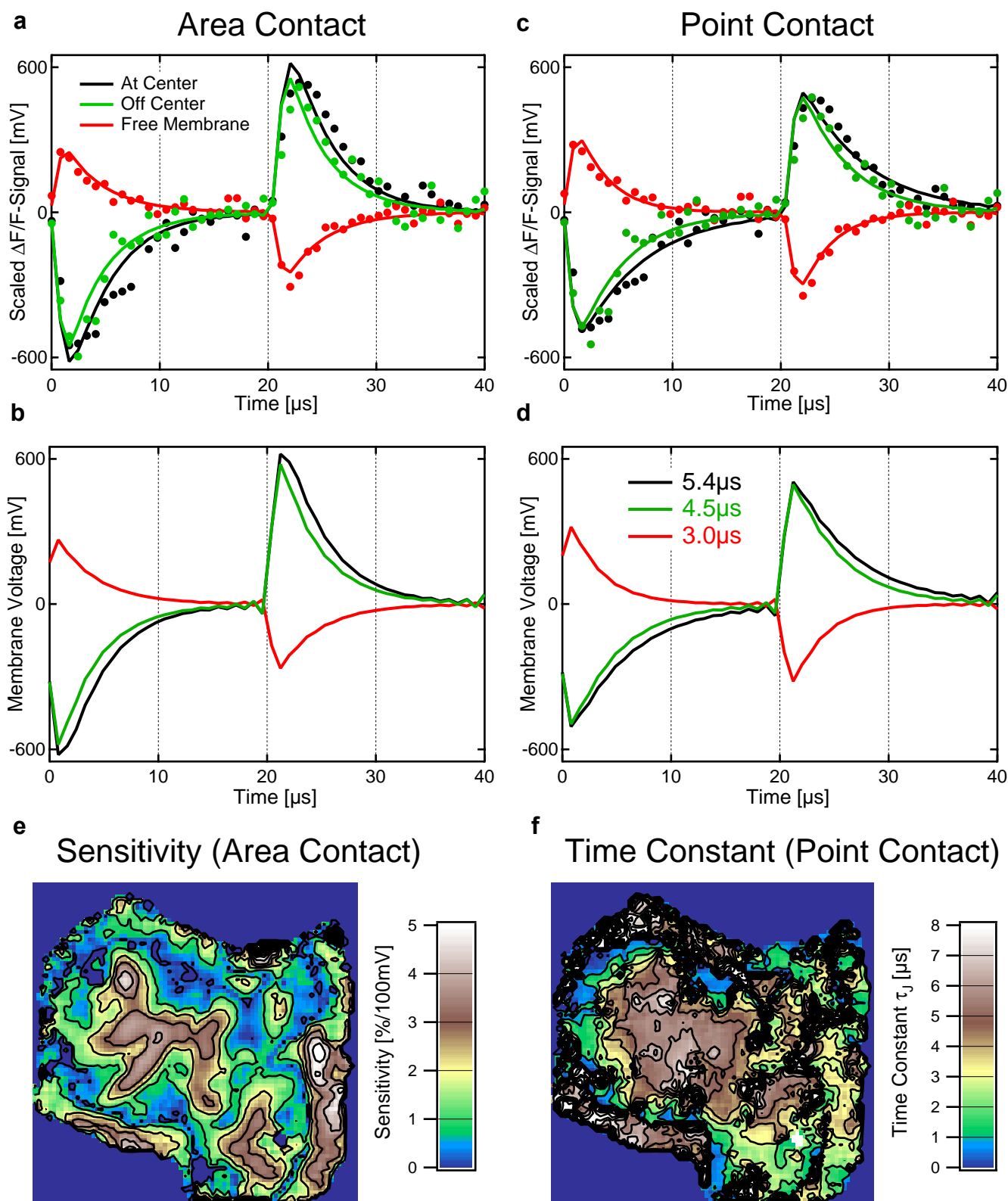


Fig 7.18 Imaged transients of a group of HEK cells 5 μm above the chip surface. Single transients from the center, off the center of the junction membrane and from the free membrane fitted are with the area contact model (a,b) and the point contact model (c,d). Images of the sensitivity derived from the area contact is given in (e). The local junction time constant obtained from fitting the local point contact model is given in (f).

7.4 Imaged transients of vesicle membrane

Imaged transients of adsorbed giant vesicle membranes confirm previous lock-in measurements. Junction time constants are limited to $>3\text{ms}$ with both methods.

We found from lock-in imaging on adsorbed giant vesicle membranes a junction resistance of $r_j > 5\text{G}\Omega$ and therefore expected junction time constants to be above 3.2ms . Transient imaging at 1kHz on the same adsorbed giant membrane as measured in Fig 6.29 on page 133 revealed the same upper limit for the junction time constant. The decay of membrane potential could not be further resolved as presented in Fig 7.19a and Fig 7.20. Scanning at lower speed was limited by fluorescence bleaching of the chromophore. The sensitivity is slightly reduced to $2.5\%/100\text{mV}$ obtained by the transient imaging (Fig 7.19b) as compared to the sensitivity of $3.75\%/100\text{mV}$ measured by lock-in imaging. The most probable reason for the decrease is photobleaching.

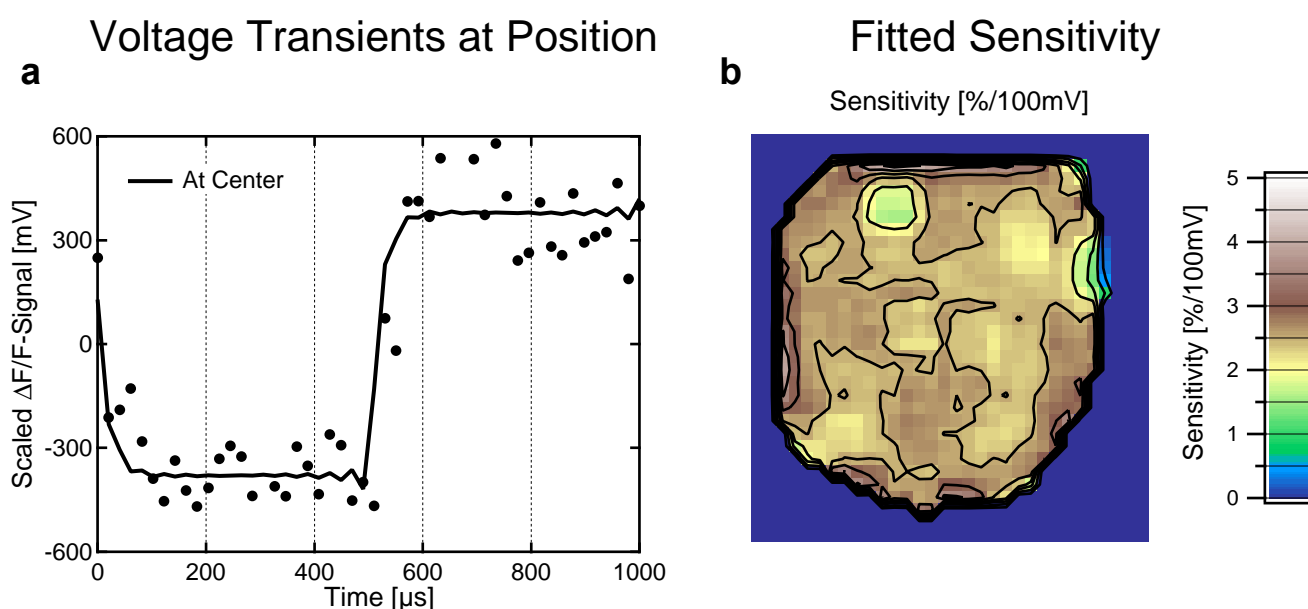


Fig 7.19 Transient imaging of an adsorbed giant vesicle membrane. (a) Transient at the center together with the area contact model fit using a junction resistance of 5GW . (b) Sensitivity is very homogeneous around $2.5\%/100\text{mV}$ and thus slightly reduced from $3.75\%/100\text{mV}$ as observed by Lock-In imaging before.

Imaged Transients of Adsorbed Vesicle Membrane

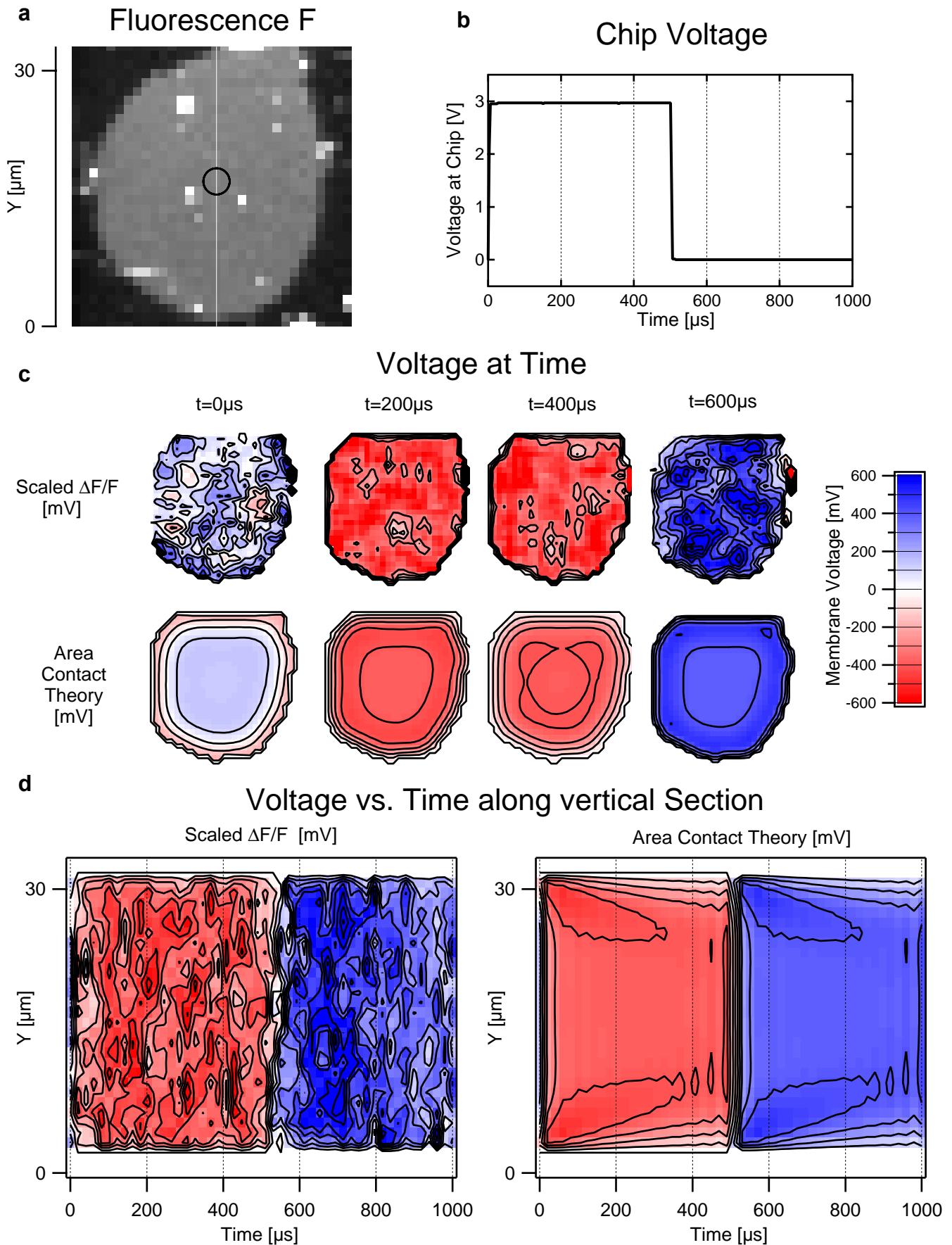


Fig 7.20 Imaged transients of adsorbed vesicle membrane with theory at resistance limi

Specials

Electroporation, Adsorbed dye and Linearity

8.1 Electroporation of junction membrane ***158***

HEK cells suffer electroporation for junction membrane potentials above 800mV easily applied with high chip voltage amplitudes.

8.2 Adsorbed dye on poly-lysine ***160***

Large voltage sensitive fluorescence above 200kHz is observed for poly-lysine coated chips after staining with the usual FCS-BNBIQ solution. This exemplifies possible extensions of the method.

8.3 Linearity of voltage sensitivity ***161***

Linearity of voltage sensitivity of BNBIQ is proved from the variation of the chip voltage.

8.1 Electroporation of junction membrane

HEK cells suffer electroporation for junction membrane potentials above 800mV easily applied with high chip voltage amplitudes.

Capacitive stimulation can elicitate very high membrane potentials if the chip voltage is increased. It can even electroporate the cells as demonstrated in two subsequent measurements in Fig 8.21 with the model and measurement parameters are given in Table 8.1.

Image=60 μ m	f=125kHz=13f ₀
Pixel=0.94 μ m	V _{Chip} =1.5V
Binning=3x3	α =0.34 (10nm)
A _{JM} =400 μ m ²	β =0.5

TABLE 8.1 Measurement and model parameter for single HEK before electroporation in Fig 8.21. By applying area contact model we find r_J=4.0M Ω . The junction voltage of 400mV is further doubled at a second scan where electroporation destroys the cell (Fig 8.22).

Area contact Model		Point contact Model	
r _J =4.0M Ω	d _J =50nm	Phase _{JM} =0°	Phase _{FM} =-165°
ρ_J =20 Ω cm	Sens.=6%/100mV	---	τ_J^{FM} =4.8 μ s
g _J ^{JM} =110mS/cm ²	g _J ^{FM} =190mS/cm ²	---	g _J ^{FM} =220mS/cm ²
V _{JM} =400mV	V _{FM} =130mV	---	V _{FM} =165mV

A junction resistance of r_J=4M Ω is fitted in the first scan (Fig 8.21). The phase hammock profile is precisely described by the area contact model. With a dye sensitivity of 6%/100mV also a good correspondence of the relative fluorescence amplitude is found. Junction membrane potential reaches values of 400mV in the center of the junction with the typical amplitude fluctuations. When the chip voltage is doubled in a subsequent scan to 3.0V, resulting in a junction membrane potential of 800mV, electroporation of the junction membrane sets in. The cells often generate membrane vesicles aside from the junction after some 10-20s. In our case the cell totally detached while the scanning time of 60s, still generating a voltage sensitive signal in the first lines (Fig 8.22).

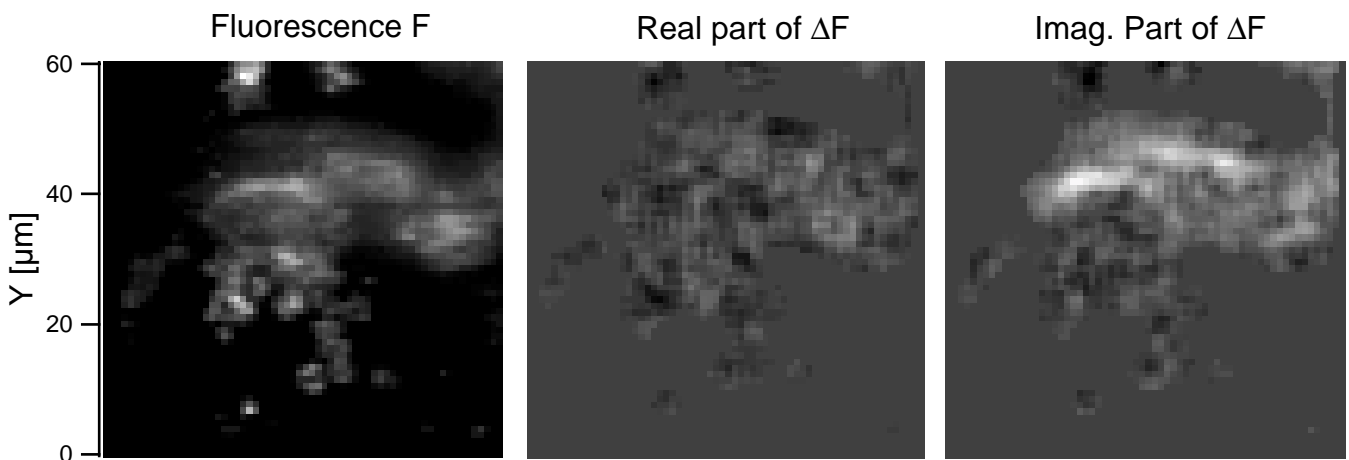


Fig 8.22 Electroporation of a HEK cell at a junction membrane potential of 800mV. The cell is destroyed while scanning the picture.

HEK Cell before Electroporation

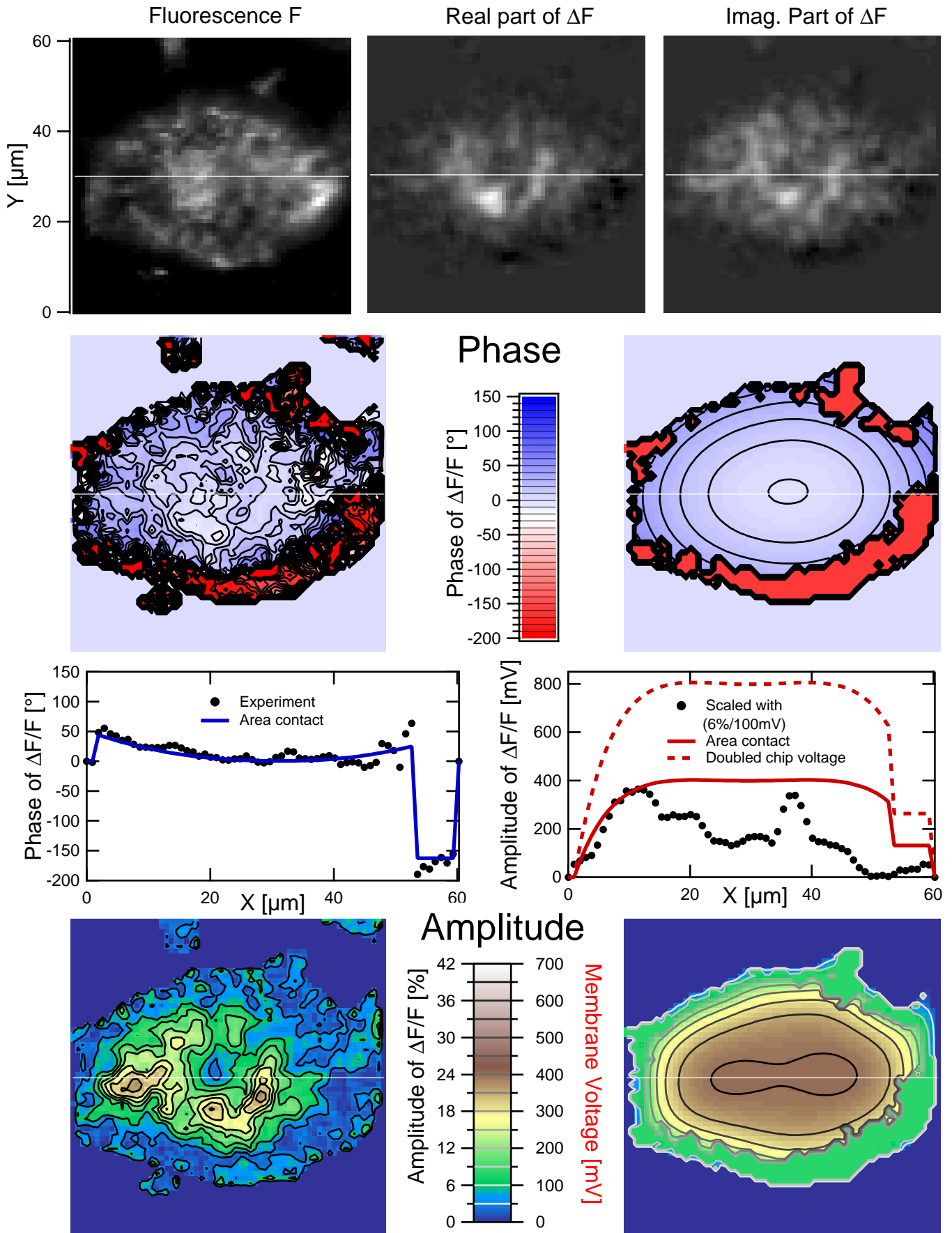


Fig 8.21 HEK cell before electroporation with theory. Parameters from Table

8.2 Adsorbed dye on poly-lysine

Large voltage sensitive fluorescence above 200kHz is observed for poly-lysine coated chips after staining with the usual FCS-BNBIQ solution. This exemplifies possible extensions of the method.

To give a possible extension of the method we will show fluorescence signals obtained at high stimulation frequencies on the free chip surface of an erythrocyte ghost preparation. As described in 6.2.A on page 99 the chip is cleaned and coated with a thin layer of poly-lysine. After settling of the ghosts, the solution is stained with a BNBIQ-FCS-mixture (4.1.C on page 61). It is very probable that the enzymes from the fetal calve serum (FCS) are adsorbed on the chip. A very small fluorescence intensity is found next to the ghosts directly on the chip. This probably originates from dye which is still adsorbed on the FCS-Enzymes. A voltage sensitive fluorescence amplitude with a high relative amplitude is found at frequencies of 400kHz and above on the 10nm thick oxide stimulation spot. This signal must originate from the stimulation of the chip as its amplitude is proportional to the applied chip voltage at 416kHz as shown in Fig 8.23:

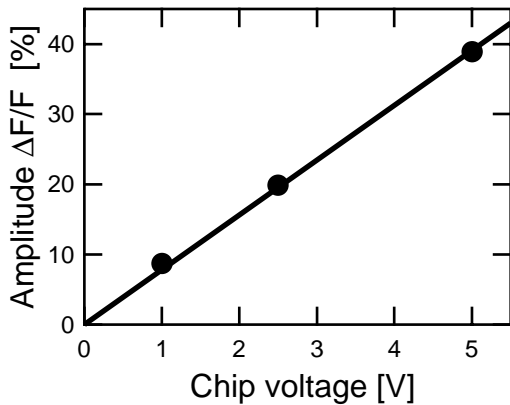


Fig 8.23 Relative fluorescence amplitude at 416kHz depending linearly on chip voltage. Probably the enzymes of the staining FCS-BNBIQ solution is adsorbed on the poly-lysine coated chip together with the dye. Signal amplitudes are very high.

The amplitude and phase spectrum of this adsorbed dye is still more complicated, especially the frequency characteristic is nonlinear in the amplitude as no signal can be detected for stimulation frequencies below 200kHz. For a chip voltage amplitude of 2.5V we obtain the frequency characteristics of amplitude and phase in Fig 8.24:

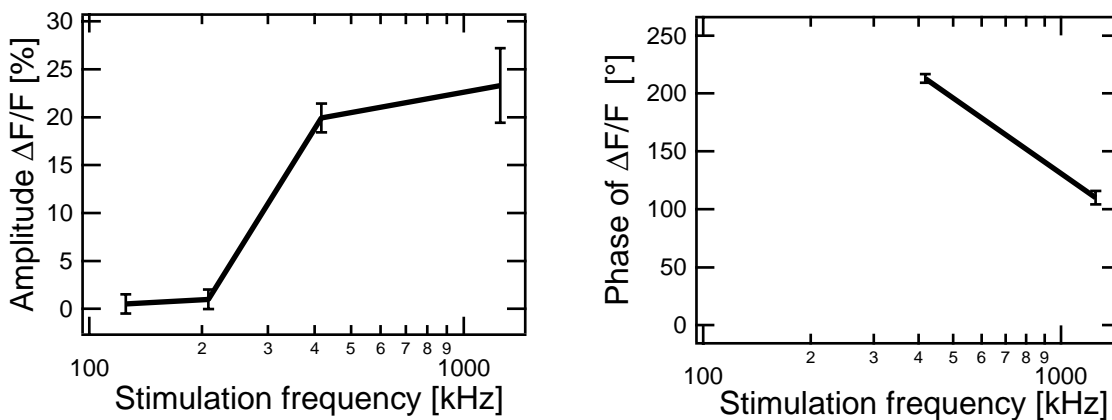


Fig 8.24 Frequency characteristic of adsorbed dye. Signal amplitudes are very high at frequencies above 200kHz.

Many speculations could be given for this result, we give the example only to exemplify a possible extension of the method to other fluorescence measurements.

8.3 Linearity of voltage sensitivity

Linearity of voltage sensitivity of BNBIQ is proved from the variation of the chip voltage.

Thus far we did not comment on the linearity of voltage sensitive dyes. As the signal mostly is generated by a stokes shift of the excited state and the shift of fluorescence spectra is rather small, we would expect that the dye gives a linear voltage to fluorescence intensity characteristic. The linearity of BNBIQ up to 150mV is known from the detection of action potentials in [Fromherz 1993a]. Voltage sensitivity inside thin PMMA films as measured by [Ostertag 1998] proved the linearity up to much higher voltage.

Within our measurement scheme it is easily possible to prove the linearity by detecting the voltage sensitive fluorescence versus the applied chip voltage. A group of HEK cells was chosen being very similar to the measurement in Fig 6.17 on page 118. The amplitude of voltage sensitive fluorescence is detected from the unbinned signal between two cells of the cell group. We take into account the point contact parameters of $\epsilon=0.34$ and $\beta=0.7$ together with a junction time constant of $\tau_j=5\mu\text{s}$ derived from the phase of the signal at a stimulation frequency of 125kHz. With these parameters a point contact transfer function from stimulation spot voltage to junction membrane of $g=0.21$ is found. The transfer function is not very sensitive to variations of β and the stimulation frequency. The voltage amplitude applied to the chip was varied from 0V to 2.5V. Taking into account the transfer function, we find a nearly perfect linear relationship with a sensitivity of 2.9%/100mV in Fig 8.25. Therefore the voltage sensitivity of BNBIQ is proved to be linear up to a membrane potential of 520mV:

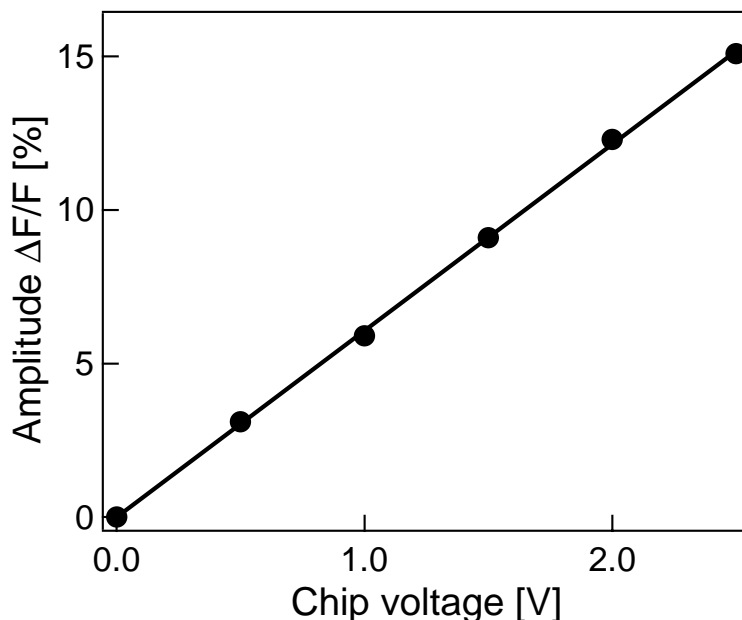


Fig 8.25 Test of linearity of the voltage sensitivity of the dye. Relative fluorescence between two cells in a cell group is plotted versus the applied voltage to the chip. From the transfer function of the point contact model we derive a sensitivity of 2.9%/100mV. The linearity of the voltage sensitive relative fluorescence signal is very good up to a membrane potential of 520mV.

Summary and Outlook

A *Advances in methods*

- The transfer function from the stimulation electrode to the cell membrane is imaged confocally with voltage-sensitive fluorescence. chapter 6 on page 91
- Membrane potential transients in response to rectangular voltage steps are imaged confocally with voltage-sensitive fluorescence. chapter 7 on page 135
- Within LabView a software interface is developed to control the Olympus confocal microscope. 5.2.B on page 83
- FLIC microscopy is extended to confocal microscopes. 4.3 on page 66
- A 2-lambda FLIC method not relying on oxide steps is proposed. 4.4 on page 71
- Design and fabrication of a backbonded stimulation chip with large stimulation spots and backside spring contacts is accomplished. chapter 3 on page 37

B *Advances in theory*

- The core-coat conductor model of the area contact was refined to an integral-differential equation to account for the free membrane. 2.2 on page 13
- The description of the junction and the free membrane by four point contact models is proposed. The transition from the area to the point contact model is found to depend on the area ratio β . 2.5.E on page 31
- Membrane potential transients are fitted with a local point contact model. 7.1.D on page 141
- The area contact model is calculated using the actual geometry of the junction area. It fits both imaged transients and lock-in images. 2.3 on page 18

C *Confirmations of the area contact model*

- The phase of the junction membrane potential has a hammock shape around zero for stimulation frequencies above the reference frequency of the junction. 6.2 on page 99
- The difference between the phase in the center of the junction membrane and the free membrane is 180° and slightly smaller for the cases of a hammock shaped junction membrane phase. 6.2 on page 99

- The membrane potential of the free membrane is smaller than the junction membrane potential depending on the ratio between the areas of free and junction membrane. 6.2 on page 99
- The junction membrane can sustain voltage values of up to 600mV. e.g. 6.3 on page 108
- Junction properties of erythrocyte ghosts confirm transistor measurements on fused erythrocyte ghosts with a seal resistance of 900M Ω . chapter 6 on page 99
- The seal resistance for HEK cells on fibronectin is 3.4 \pm 0.9M Ω . Therefore the specific junction conductance is enhanced by a factor of 4.4 \pm 1.4. 6.3 on page 108
- Confluent cell layers have a slower time constant of around 10 μ s. This value can be estimated from identical junction resistance between the cells and between the cells and the chip. Lines of leakage between the cells are imaged. 6.4 on page 116
- Neurons on poly-lysine exhibit a seal resistance of 1.5M Ω . Their membrane can be stimulated equally well through a monolayer of glia cells. 6.5.C on page 128
- Voltage transients are fitted precisely and fitted with time constants of 2 μ s depending on the junction membrane area. The measured transients confirm the model fits based on the phase of the lock-in image. chapter 7 on page 135
- Local enhancement of the junction membrane time constant at high membrane potential was detected. 7.2.A on page 144
- Electroporation can be induced with high chip voltages. 8.1 on page 158
- The membrane potential is linear with respect to the stimulation. 8.3 on page 161

D Outlook

The electrical coupling between single mammalian nerve cells and capacitors is very weak because of the small junction time constant of 2 μ s measured in this work. Previous work on FLIC microscopy focussed on reducing the width of the cleft between cell and substrate in order to improve coupling. As shown in this work, an enhancement of the specific conductance within the cleft has to be taken into consideration. Since this method directly measures the electrical properties of the junction, it may help in further optimizing the coupling parameters. It is superior to transistor or metal electrode methods in three aspects: it is highly sensitive, the cells do not have to be positioned above a small detector and it precisely detects the junction area.

Moreover, this method of optically imaging transfer functions or transients following electrical stimulation can also be applied to confluent monolayers or even to tissue. The stimulation and the detection of electrical signals have corresponding properties. Therefore the method is suited to gain microscopic insight into passive voltage spread within tissue. Moreover it provides electrical parameters needed to improve the detection of membrane potentials.

Since the contact models of capacitive stimulation were confirmed, it would be very interesting to investigate the junction properties of cells grown on the widely used metal electrodes. It is expected that their enhanced surface capacitance results in an increased junction time constant.

References

[Born 1980]

Born M., Wolf E., *Principles of optics: electromagnetic theory of propagation, interference and diffraction of light*, 6.Edition, Oxford-Pergamon 1980, ISBN 00-08-026482-4

[Banker 1977]

G.A. Banker, W.M. Cowan: *Brain Res.* 126, 397 (1977)

[Braun 1995]

Braun D., *Dotieren im Centrotherm-Ofen*, Internship at the Department of Membrane- and Neurophysics, MPI for Biochemistry, Martinsried, 1995

[Braun 1996]

Braun D., *Untersuchung der Struktur der Silizium-Neuron-Kopplung durch Fluoreszenzfarbstoffe*, Diploma thesis, Technische Universität München, 1996

[Braun 1997]

Braun D., Fromherz P., *Fluorescence interference-contrast microscopy of cell adhesion on oxidized silicon*, *Appl. Phys. A* 65 (1997) 341-348

[Braun 1998]

Braun D., Fromherz P., *Fluorescence Interferometry of Neuronal Cell Adhesion on Microstructured Silicon*, *Phys. Rev. Lett.* 81 (1998) 5241-5244

[Burns 1995]

N.L. Burns, J.M. Van Alstine, J.M. Harris: *Langmuir* 11, 2768 (1995)

[Bullen 1997]

Bullen A., Patel S.S., Saggau P., *High-Speed, Random-Access Fluorescence Microscopy: I. High-Resolution Optical Recording with Voltage-Sensitive Dyes and Ion Indicators*, *Biophysical Journal* 73: 477-491 (1997)

[Bullen 1999]

Bullen A., Saggau P., *High-Speed, Random-Access Fluorescence Microscopy: II. Fast Quantitative Measurements With Voltage-Sensitive Dyes*, *Biophysical Journal* 76: 2272-2287 (1999)

[Crank 1975]

Crank J., *The Mathematics of diffusion*, Oxford 1975, ISBN 0-19-853411-6

[Dertinger 1998]

Dertinger S., *Kontrolle des neuronalen Wachstums durch elektrische Felder auf chemisch mikrostrukturier-tem Silizium*, PhD thesis, Technische Universität München 1998.

[Dimitrov 1988]

D.S. Dimitrov, M.I. Angelova: *Bioelectrochem. Bioenerg.* 253, 323 (1988)

[Ephardt 1993]

Ephardt H., Fromherz P., *Fluorescence of Amphiphilic Hemicyanine Dyes without Free Double Bonds*, *Journal of Phphysical Chemistry* 97:4540-4547 (1993)

[Figger 1999]

Figger C., *Optimierung der kapazitiven Stimulation indivi-dueller Neuronen mit Halbleiter Mikrostrukturen*, Diploma thesis, Technische Universität München, 1999

[Fromherz 1991a]

Fromherz P., Offenhäuser A., Vetter T., and Weis J., *A neuron-silicon junction: a Retzius-cell of the leech on an insulated-gate field-effect transistor*, *Science* 252:1290-1293 (1991)

[Fromherz 1991b]

Fromherz P., Dambacher K.H., Ephardt H., Lambacher A., Müller C.O., Neigl R., Schaden H., Schenk O., Vetter T., *Fluorescent Dyes as Probes of Voltage Transients in Neuron Membranes*, *Ber. Bunsenges. Phys. Chem.* 95:1333-1345 (1991)

[Fromherz 1993a]

Fromherz P., Müller C.O., *Voltage-sensitive fluorescence of amphiphilic dyes in neuron membrane*, *Biochimica et Biophysica Acta*, 1150: 111-122 (1993)

[Fromherz 1993b]

Fromherz P., Müller C.O., Weis R., *Neuron-transistor: electrical transfer function measured by the patch-clamp technique*. Phys. Rev. Lett. 71:4090-4082 (1993)

[Fromherz 1995a]

Fromherz P., Stett A., *Silicon-Neuron Junction: Capacitive Stimulation of an Individual Neuron on a Silicon Chip*. Phys. Rev. Lett. 75:1670-1673 (1995)

[Fromherz 1995b]

Fromherz P., *Monopole-Dipole Model for Symmetrical Solvatochromism of Hemicyanine Dyes*. J. Phys. Chem., 99:7188-7192 (1995)

[Fromherz 1996]

Fromherz P., *Interfacing Neurons and Silicon by Electrical Induction*, Ber. Bunsenges. Phys. Chem. 100: 1093-1102 (1996)

[Fromherz 1999]

Fromherz P., Kiessling V., Kottig K., Zeck G., *Membrane-Transistor with Giant Lipid Vesicle Touching a Silicon Chip*, Appl. Phys. A 69, 571-576 (1999)

[Giaever 1995]

Giaever I., *Impedance analysis of MDCK cells measured by electric cell-substrate impedance sensing*, Biophysical Journal 69 (1995) 2800-2807 and references therein.

[Graham 1977]

Graham F.L., Smiley J., Russel W.C., Nairn R., *Characteristic of a human cell line transformed by DNA from human adenovirus type 5*, J. gen. Virol. 36:59-72 (1977)

[Görler 1999]

Görler K., Braun D., Meyer E., Fromherz P., *Messungen zum Abstand der Zelllinie HEK 293 und von Neuronen des Hippocampus mit Hilfe der Fluoreszenzinterferenzkontrast (FLIC)-Mikroskopie*, Internship at the Department of Membrane- and Neurophysics, MPI for Biochemistry, Martinsried, 1999.

[Hecht 1987]

Eugene Hecht, *Optics*, 1987 Addison-Wesley

[Hibino 1991]

Hibino M., Shigemori M., Itoh H., Nagayama K., Kinoshita K. Jr, *Membrane conductance of an electroporated cell analyzed by submicrosecond imaging of transmembrane potential*, Biophysical Journal 59(1): 209-220 (1991)

[Hibino 1993]

Hibino M., Itoh H., Kinoshita K. Jr, *Time course of cell electroporation as revealed by submicrosecond imaging of transmembrane potential*, Biophysical Journal 64(6): 1789-1800 (1993)

[Hilleringmann 1996]

Hilleringmann U., *Silizium-Halbleitertechnologie*, Teubner-Verlag Stuttgart 1996; ISBN 3-519-00149-7

[Kießling 1995]

Kießling V., *Struktur und elektrische Eigenschaften von Lipidmembranen auf oxidiertem Silizium*, Diploma thesis, Universität Ulm 1995

[Kießling 1999]

Kießling V., *Zelladhäsion als Kern-Mantel-Leiter: Charakterisierung mit Transistoren und extrazellulär angelegter Wechselfspannung*, Dissertation 1999 Technische Universität München

[Kießling 2000]

Kießling V., Müller B., Fromherz P., *Extracellular Resistance in Cell Adhesion measured with a Transistor Probe*, Langmuir in press

[Knisley 1995]

Knisley S.B., *Transmembrane voltage changes during unipolar stimulation of rabbit ventricle*, Circulation Research 77(6): 1229-39 (1995)

[Kottig 2000]

Kottig K., *Fluoreszenz-Korrelations-Spektroskopie an Lipidvesikeln auf oxidiertem Silizium*, PhD thesis, Technische Universität München, 2000

[Kuhn 1996]

Kuhn B., *Modulation zweidimensionaler Fluoreszenzspektren durch das elektrische Feld in einer Nervenmembran*, Diploma thesis Universität Ulm, 1996

[Lambacher 1994]

Lambacher A., *Fluoreszenz-Interferenzkontrast-Mikroskopie von Membranen auf Silizium*. PhD-Thesis, Universität Ulm, 1994

[Lambacher 1996]

Lambacher A., Fromherz P., *Fluorescence interference-contrast microscopy on oxidized silicon using a monomolecular dye layer*, Appl. Phys. A 63 (1996) 207-216

[Lambacher 2000]

Lambacher A., Fromherz P., in preparation.

[Mathivet 1996]

L. Mathivet, S. Cribier, P.F. Devaux: *Biophys. J.* 70, 1112 (1996)

[Meyer 1997]

Meyer E., Müller C.O., Fromherz P., *Cable properties of dendrites in hippocampal neurons of the rat mapped by a voltage-sensitive dye*, Eur. J. Neurosci. 9: 778-785 (1997)

[Numerical recipes in C 1992]

Press, Teukolsky, Vetterling, Flannery: *Numerical recipes in C*, 2nd edition, Cambridge University Press 1992

[Ostertag 1998]

Ostertag G., *Stark-Spektroskopie von Hemicyaninfarbstoffen in viskoser polarer Matrix*, PhD thesis, Technische Universität München, 1998.

[Prinz 1996]

Prinz A., *Optische Detektion der elektrischen Signalausbreitung in Neuronen*, Diploma thesis, Universität Ulm 1996

[Schwoch 1973]

Schwoch G., Passow H., *Mol. Cell. Biochem.* 2, 197 (1973)

[Stett 1992]

Stett A., *Extrazelluläre Reizung von Blutegel-Neuronen mit Silizium-Elektroden*, Diploma thesis, Universität Ulm 1992

[Stett 1995]

Stett A., *Extrazelluläre kapazitive Stimulation und Detektion elektrischer Signale individueller Nervenzellen mit planaren Silizium-Mikrostrukturen*, PhD-Thesis, Universität Ulm 1995

[Stett 1997]

Stett A., Müller B., Fromherz P., *Two-way silicon-neuron interface by electrical induction*, *Physical Review E* 55:1779-1782 (1997)

[Takashima 1988]

Takashima S., Asami K., Takahashi Y., *Frequency Domain Studies of Impedance Characteristics of Biological Cells Using Micropipette Technique*. *Biophys. J.* 54: 995-100 (1988)

[Vassanelli 1997]

Vassanelli S., Fromherz P., *Neurons from rat brain coupled to transistors*, *Appl. Phys. A* 65:85-88 (1997)

[Vassanelli 1998]

Vassanelli S., Fromherz P., *Transistor records of excitable neurons from rat brain*, *Appl. Phys. A* 66:459-463 (1998)

[Vassanelli 1999]

Vassanelli S., Fromherz P., *Transistor Probes Local Potassium Conductances in the Adhesion Region of Cultured Rat Hippocampal Neurons*, *J. Neurosci.* 19:6767-6773 (1999)

[Weis 1996]

Weis R., Müller B., Fromherz P., *Neuron Adhesion on a Silicon Chip probed by an Array of Field-Effect Transistors*, *Phys. Rev. Lett.*, 76:327-330 (1996)

[Windisch 1995]

Windisch H., Ahammer H., Schaffer P., Müller W., Platzner D., *Optical multisite monitoring of cell excitation phenomena in isolated cardiomyocytes* *Pflügers Archiv - European Journal of Physiology* 430(4): 508-18 (1995)

[Wolf 1985]

Wolf D.E., *Biochemistry* 24 (1985) 582

[Zeck 1997]

Zeck G., *Adhäsion von Lipidvesikeln auf Siliziumchips*, Diploma thesis, Technische Universität München 1997

Acknowledgements

I would like to thank

Prof. Fromherz for posing the interesting problem, for long and helpful discussions and for the chance to combine so many techniques developed so far in the department. Karsten Kottig for discussions and his expertise with lasers and teaching me how to make vesicles. Helge Vogl for servicing and building the well equipped clean room with so much commitment. Doris Eckerlein for preparing the rat neurons very reliably. Martin Jenkner for teaching me how to become a good LabView programmer and the good mood he's spreading. Bernd Kuhn for his expertise in staining techniques and the two-dimensional BNBIQ spectrum. Christian Figger for drawing the masks, discussions and good collaboration in the clean room. Armin Lambacher for laborious discussions in FLIC theory and its implementation. Fred Stett for initial discussions long long ago. Yoriko Iwanaga for her help with the english language. Heidi Simeunovic for preparing many solutions. Erich Neusser and Walter Wagner for making and discussing the tiny fine mechanical interfaces. Gerd Hübener, Birgit Haringer and Michaela Morawetz for their chemical assistance. Since the BNBIQ supply dates back to Ulmer times, I thank Heinz Ehardt, Andrea Heilemann and Carola Kemper for the synthesis.

And all the other members of the department of Membrane- and Neurophysics for the nice time.

... and the dear one really not only for the corrections
and your notorious advice to remove some pages :)